Technische Universität München

Fakultät für Informatik

Global Braginskii turbulence simulations across the edge and scrape-off layer of diverted tokamaks

Wladimir Zholobenko

Vollständiger Abdruck der von der Fakultät für Informatik der Technischen Universität München zur Erlangung des akademischen Grades eines

Doktors der Naturwissenschaften
(Dr. rer. nat.)

genehmigten Dissertation.

Vorsitzender:	Prof. Dr. Hans-Joachim Bungartz
Prüfer der Dissertation:	1. Hon.-Prof. Dr. Frank Jenko
	2. Prof. Dr. Ulrich Stroth

Die Dissertation wurde am 22.09.2021 bei der Technischen Universität München eingereicht und durch die Fakultät für Informatik am 10.12.2021 angenommen.

"There is no value in anything until it is finished."
- Genghis Khan

Global Braginskii turbulence simulations across the edge and scrape-off layer of diverted tokamaks

Wladimir Zholobenko

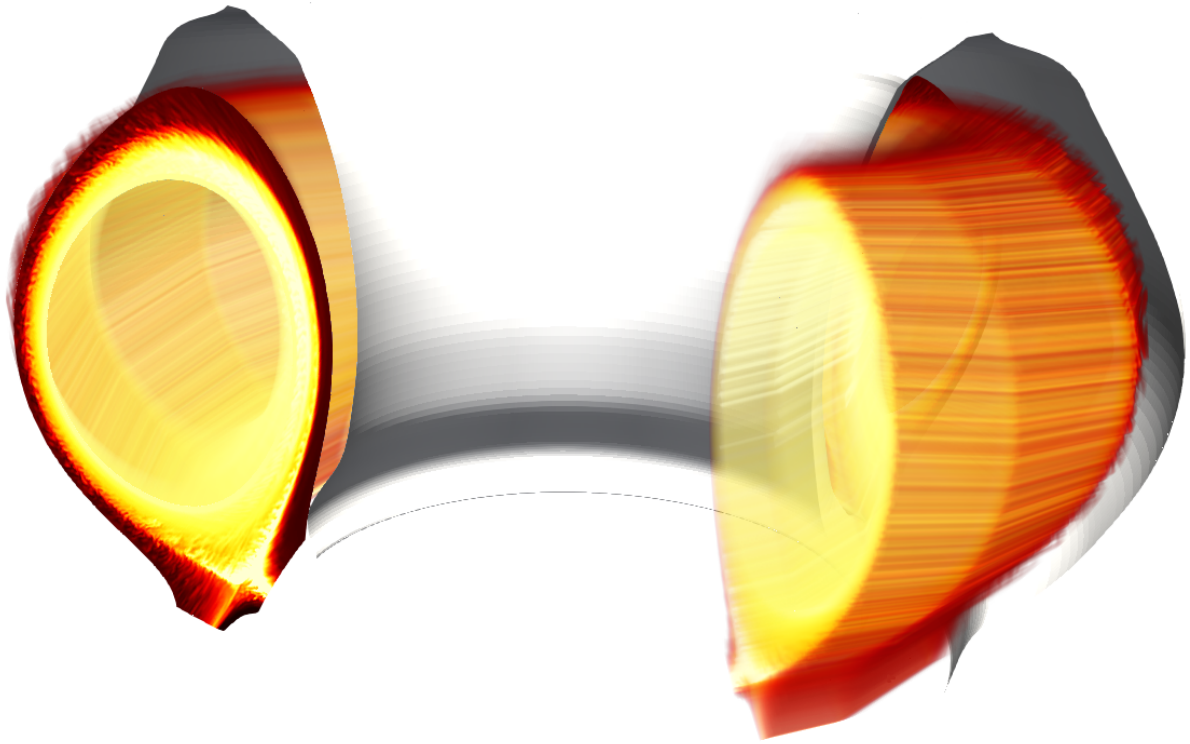

Max-Planck-Institut
für Plasmaphysik

Abstract

Magnetic confinement fusion is an attractive source of energy. The tokamak is close to net energy production, but there remain difficulties preventing commercial use. Among the key design goals for fusion reactors are manageable heat and particle exhaust at optimal confinement. It is determined by transport across the magnetic field due to electromagnetic turbulence: multi-scale fluctuations of electric and magnetic fields, triggered by microscopic instabilities. Turbulence is among the most intriguing phenomena in nature. Therefore, its study is both interesting and crucial for the successful operation of tokamaks. To this end, numerical simulations constitute a powerful tool.

This thesis, based on the publications [1–4], investigates turbulent transport from the edge of the confined plasma to the tokamak wall. The transition region between closed field lines and those impinging on material surfaces in the scrape-off layer (SOL) is of particular interest: harbouring the steepest gradients, it largely determines the performance of the whole machine. But it also poses a number of particular challenges: a complex geometry with a magnetic separatrix, large turbulent fluctuations, interaction of the plasma with the wall, neutral gas and impurities. The GRILLIX code is developed to tackle these challenges. It is built on a novel numerical scheme, the flux-coordinate independent (FCI) approach, that allows efficient 3D edge turbulence simulations in realistic (diverted) tokamak geometry. This thesis focuses on extensions of the physical model: the dynamics of the electron and ion temperatures in the Braginskii equations, the plasma-wall interaction and neutral gas models. Arbitrarily large fluctuation amplitudes are permitted and all non-linear parametric dependencies are considered. Necessarily, model extensions are accompanied by optimisations of the numerical scheme, the computational implementation and performance.

Results are obtained for the Alcator C-mod and ASDEX Upgrade tokamaks. Focusing on the latter, a close match to a selected experimental discharge is achieved. Thereby, we emphasize the role of the neutral gas: its ionization is the major plasma density source, it cools the SOL and increases the collisionality there. Different turbulence driving instabilities are identified: drift waves, ballooning and ion temperature gradient modes. On the microscopic sound Larmor radius scale, drift waves initiate an inverse cascade of energy, generating machine scale zonal flows. Particular attention is put on the interaction between turbulence generated and mean field flows. We show that the latter result from the curvature of the toroidal magnetic field and inflow of toroidal momentum from the SOL, while poloidal rotation is dissipated by ion viscosity. A non-trivial stationary radial electric field results. This in turn leads to shearing of turbulence, particularly at the separatrix, regulating it.

Such realistic global turbulence simulations across the plasma edge and SOL of a diverted tokamak, validated against a state-of-the-art experiment, have been performed for the first time. This paves the road towards a more complete understanding of tokamaks and their optimisation. Yet we also emphasize the restrictions of the used fluid model and steps for near future improvements.

Zusammenfassung

Die Fusion mittels magnetischen Einschlusses ist eine attraktive Energiequelle. Der Tokamak ist kurz davor, netto Energie produzieren zu können. Es verbleiben jedoch Probleme, die eine kommerzielle Nutzung bisher verhindern. Zu den wichtigsten Zielen eines Fusionsreaktors gehören beherrschbare Wärme- und Teilchenabfuhr unter optimalem Einschlussverhalten. Dies wird durch den Transport senkrecht zum Magnetfeld aufgrund von elektromagnetischer Turbulenz bestimmt: Fluktuationen elektrischer und magnetischer Felder auf vielen Skalen, verursacht durch mikroskopische Instabilitäten. Turbulenz gehört zu den faszinierendsten Phänomenen in der Natur. Sie zu untersuchen ist daher sowohl interessant als auch wichtig, um Tokamaks erfolgreich zu betreiben. Zu diesem Zweck stellen numerische Simulationen ein mächtiges Werkzeug dar.

Die vorliegende Doktorarbeit, die auf den Publikationen [1–4] basiert, untersucht den turbulenten Transport vom Rand des eingeschlossenen Plasmas zur Wand des Tokamaks. Der Übergangsbereich zwischen geschlossenen Flussflächen und solchen die auf Materialoberflächen in der Abschälschicht treffen ist von besonderem Interesse: da er die steilsten Gradienten beherbergt, bestimmt er zum großen Teil die Leistung der gesamten Anlage. Dieser Bereich stellt jedoch auch eine Reihe von besonderen Herausforderungen: eine komplexe Geometrie mit einer magnetischen Separatrix, große turbulente Fluktuationen, die Interaktion des Plasmas mit der Wand, dem Neutralgas und den Verunreinigungen. Der Code GRILLIX ist dazu entwickelt worden, diese Herausforderungen anzugehen. Er baut auf einem neuartigen numerischen Verfahren, dem Fluss-Koordinaten-unabhängigen Ansatz (FCI), der effiziente 3D Randturbulenz-Simulationen in realistischer Divertorgeometrie eines Tokamaks ermöglicht. Die vorliegende Arbeit richtet sich auf die Erweiterung des physikalischen Modells: die Dynamik der Elektronen- und Ionentemperatur gemäß den Braginskii-Gleichungen, die Plasma-Wand-Wechselwirkung und das Neutralgas-Modell. Fluktuationsamplituden beliebiger Größe sind zulässig und alle nicht-linearen Parameterabhängigkeiten sind berücksichtigt. Die Modellerweiterungen werden notwendigerweise begleitet von Optimierungen des numerischen Schemas, der Computerimplementierung und der Performance.

Es wurden Resultate für die Tokamaks Alcator C-mod und ASDEX Upgrade erzielt. Für den letzteren wurde eine weitgehende Übereinstimmung mit einer ausgewählten experimentellen Entladung erreicht. Dabei heben wir insbesondere die Rolle des Neutralgases hervor: dessen Ionisation ist die dominante Quelle der Plasmadichte, es kühlt die Abschälschicht und erhöht dort die Kollisionalität. Als Treiber der Turbulenz wurden unterschiedliche Instabilitäten identifiziert: Driftwellen, Ballooning-Moden und Ionen-Temperatur-Gradient-Moden. Auf der mikroskopischen Skala eines Schall-Larmor-Radius lösen Driftwellen eine inverse Energiekaskade aus, die zu zonalen Strömungen auf der Maschinen-Skala führt. Besondere Aufmerksamkeit wurde der Interaktion zwischen diesen Strömungen gewidmet, die durch Turbulenz verursacht werden, und der mittleren Strömung. Wir zeigen, dass die mittlere Strömung zum einen aus der Krümmung des toroidalen Magnetfeldes resultiert, und zum anderen aus dem Zufluss des toroidalen Impulses aus der Abschälschicht, während die poloidale Rotation durch Ionenviskosität dissipiert wird. Dies führt zu einem nicht-trivialen stationären elektrischen Feld. Dieses wiederum verschert, insbesondere an der Separatrix, die Turbulenz, wodurch sie reguliert wird.

Solche realistischen globalen Turbulenzsimulationen über den Plasmarand und die Abschälschicht eines Divertor-Tokamaks, validiert gegen ein hochmodernes Experiment, wurden erstmalig durchgeführt. Dies ebnet den Weg zu einem umfassenden Verständnis des Tokamaks und dessen Optimierung. Wir betonen jedoch auch die Einschränkungen im angewendeten Fluid-Modell sowie Schritte zu Verbesserungen für die nahe Zukunft.

Acknowledgments

I would like to begin by thanking Frank Jenko for easily convincing me to join his group, by fueling my interest for plasma turbulence and magnetic fusion devices by his own fascination. He mastered the art of continuously supporting his students in all matters while allowing them a lot of freedom, swiftly responding to upcoming issues, providing substantial resources and motivating everyone to great accomplishments. The success of this thesis and myself is owed to a large degree to Andreas Stegmeir. It was a pleasure to work together with him on the code that he created. He supported the project in every scientific aspect, and he cordially supported me on a personal level, earning my deepest gratitude. Many thanks go to David Coster, who significantly shaped the project by his sound advise both on major strategic decisions as well as on small but important technical details, in particular regarding mean field and neutral gas physics. In terms of physics, Peter Manz has been an inexhaustible source of wisdom, especially regarding the turbulence. His sincere enthusiasm was contagious and sparked many pivotal ideas. I enjoyed many discussions with him, also on personal matters. I also thank Detlev Reiter, my former supervisor, for encouraging me to follow this path.

It is a great pleasure to work at the Max Planck Institute for Plasma Physics, not only because of the limitless scientific opportunities, but also because of the staggering number of highly competent colleagues, many of whom have greatly enriched my journey. A prime example is Emanuele Poli, with whom I enjoyed many enlightening discussions, but who would also always help in private issues – like lending a mattress to sleep on while waiting for many weeks for the delivery of a bed. Particular gratitude is owed to Omar Maj, who took much time to extensively discuss mathematical problems, fostering their solutions. In the time before corona (b.c.), lunch was an extraordinary opportunity to meet and consult experts such as Alberto Bottino, Garrard Conway, Clemente Angioni and Giovanni Tardini – perhaps I have somewhat abused this opportunity, but I thank these people for many conversations also after noon. Further, I am grateful for the chance to learn from Andreas Bergmann, Alex Chankin, Roberto Bilato, Thomas Eich, Elisabeth Wolfrum, Marco Wischmeier, Matthias Hölzl, Tobias Görler and Per Helander. I thank Michael Griener for helping with the non-trivial access to the experimental data.

The interactions with fellow students were also very enriching. I believe the close symbiotic collaboration with Thomas Body was the key to our success. Many crucial discussions took place in our shared office with him, Matthias Bösl and Dominik Michels, and on our joint trips to summer schools and conferences. Dominik Michels was a source of inspiration for numerics and computing strategies. The debates about fluid models with Andres Cathey-Cevallos and Sergei Makarov, and those about kinetic models with Thomas Hayward-Schneider, Paul Crandall, Dominik Michels, Matthias Bösl and Robert Brzozowski have been useful and inspiring. Many others whom I cannot name individually have enhanced my journey in many ways.

I also want to thank colleagues outside of IPP. Most of all, the collaboration with Ben Zhu from the Lawrence Livermore National Laboratory was a crucial ingredient to this thesis, both in person and in extensive e-mail conversations. Very important contributions have been also made by Manaure Francisquez from MIT. Further, I want to thank Joaquim Loizu and Vladimir Rozhansky for highly useful and interesting discussions.

Finally, I want to thank my family and friends for their support. The greatest gratitude goes to my significant other Denise Naltsas. She lovingly supported me in every matter, in good times and in bad times, sweetening each success and alleviating each defeat. Not only did she preserve my mental health, she also physically supported me during the recovery from multiple accidents, particularly during the emotional resettlement to Bavaria, making this thesis feasible in the first place. I cannot thank her enough.

Contents

Part I

Introduction and Methodology

Chapter 1

Introduction

While energy consumption in Europe stagnates due to efforts for higher energy efficiency, energy consumption world wide grows, as depicted in figure 1.1. It is also expected to continue growing due to developing countries, and because it is the natural way to improve ones standard of living. At the same time, the usage of fossil fuels must be urgently reduced to limit the greenhouse gas emission and its impact on climate change [5, Paris Agreement]. Therefore, more than ever it is due time for the development of new energy sources complementing volatile renewable wind and sun energy, that have prospects to provide unlimited, safe and clean energy on demand – such as nuclear fusion [6–8].

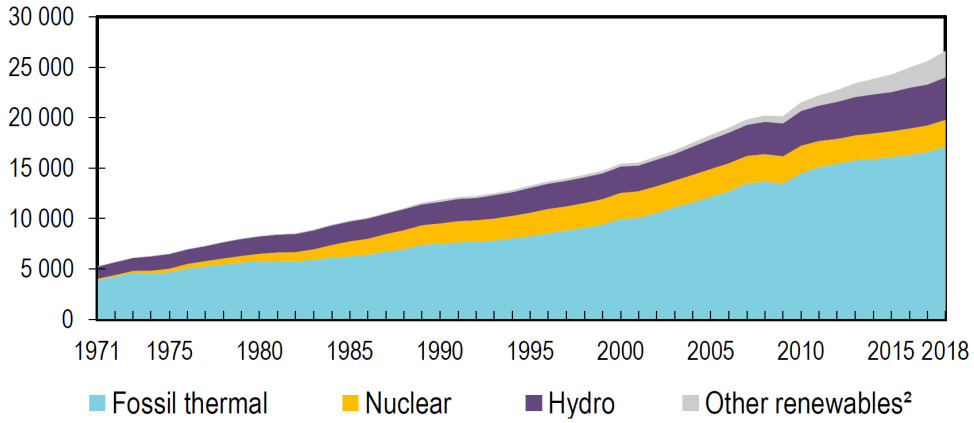

Figure 1.1: World electricity generation from 1971 to 2018 by fuel (TWh), IEA, Key World Energy Statistics 2020 [9]. Other renewables includes geothermal, solar, wind, tide/wave/ocean, biofuels, waste, heat and other.

The most successful concept to date for harnessing nuclear fusion for energy production is the tokamak [10]. The plasma is confined in a magnetic field created by means of toroidally symmetric external coils, nowadays superconductors, as shown in figure 1.2. The toroidal magnetic field is strongest on the inside of the tokamak, where toroidal field coils are closer together, and weaker on the outside. To compensate the radially-outward drift of the plasma due to the curvature and gradient of the toroidal magnetic field, a toroidal plasma current driven by a transformer and a vertical coils arrangement create a helical twist of magnetic field lines, such that they trace out closed magnetic flux surfaces. Due to the toroidal symmetry of the tokamak, a poloidal cross section of flux surfaces as shown on the right of figure 1.2 remains symmetric in toroidal direction (the plasma does not move toroidally but rather helically though, following magnetic field lines). Closed red lines indicate closed magnetic flux surfaces. The bold red line, the separatrix, indicates the boundary between closed and open field lines that intersect device walls in the scrape-off layer (SOL). This geometry is called diverted. It is created on purpose by additional external field coils to separate the plasma-wall interaction in the divertor chamber from the confined plasma in the main chamber, thereby substantially improving the heat, particle and impurity management of the device [11, 12].

Progress in magnetic confinement nuclear fusion has been remarkable in the last 50 years, as demonstrated in figure 1.3. To start a nuclear fire, the fusion reaction, in a mixture of deuterium and tritium, three criteria must be fulfilled: the plasma should be at least 100 million degrees hot, have a least 10^{20}

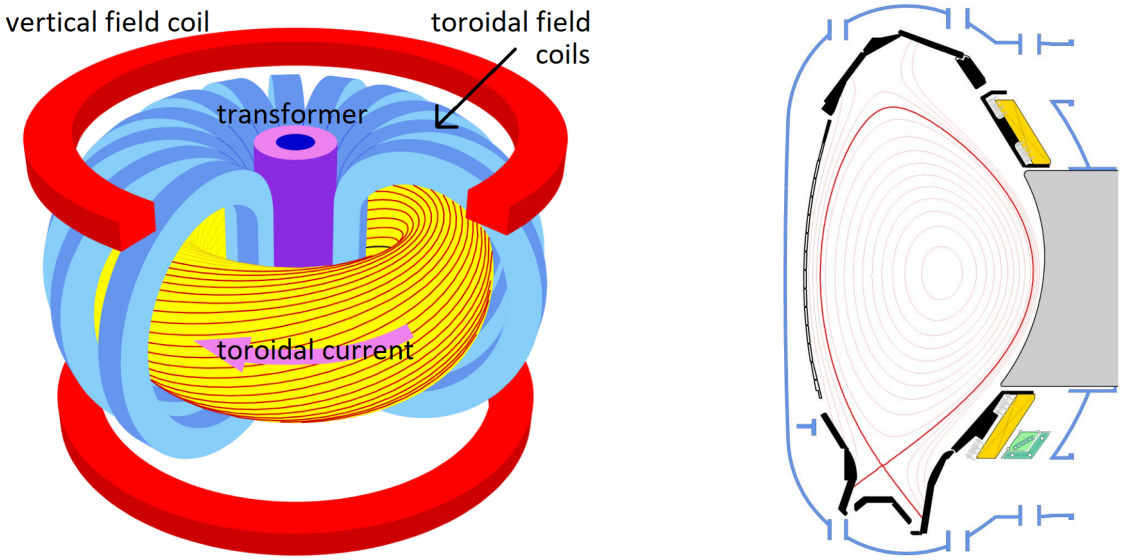

Figure 1.2: Schematic representation of a tokamak (left) and one poloidal cross section with flux surfaces in diverted geometry (right), adapted from [13].

particles per cubic meter density and a confinement time of about two seconds, the time in which the plasma stored energy diffuses outward. For the temperature, there is an optimum. Overall, the progress towards a burning plasma is quantified in a triple product of these three quantities, known as the Lawson criterion [14], and the European JET tokamak was already merely a factor 6 away from ignition in 1992 [15]. In the beginning of the 21st century the progress has stagnated because experiments have reached a size that made it cumbersome for universities or individual public research institutions to make progress, while economic prospects were still too thin to attract significant investments from the private sector. However, the attractiveness of the approach has led to an unprecedented project – ITER [8] – a collaboration of all major industrial nations in the quest for energy. With its size and complexity, ITER is becoming one of the largest physics experiments to date. Its goal is to demonstrate the technological feasibility of magnetic confinement fusion for energy production, specifically to reach an energy amplification factor of 10. Simultaneously, it turned out to be a global quest for peace, uniting nations to a common goal.

Being a first of its kind, huge physics experiment, ITER has no economic relevance yet and will not produce electricity for public usage. To demonstrate economic feasibility, yet another, even larger reactor is envisaged – DEMO [16]. On the other hand, it is clear today that not all challenges towards commercial fusion energy can be addressed in ITER, requiring further activity in both technology and physics [17]. One of the most urgent questions is how power loads on reactor walls can be maintained at manageable levels ($\lesssim 10$ MW/m^2) at steady state reactor conditions – i.e. at maximum fusion power gain [18]. A great number of solutions to these questions have been proposed with varying complexity, for example advanced divertor concepts (ADCs) [19], non-inductive current drive [20], tokamaks with a negative triangularity [21] and non-axisymmetric devices (stellarators) [22]. However, the challenge is to assess these proposals under reactor relevant conditions without building gigantic and costly experiments. To this end, numerical simulations have become a very handy tool.

1.1 Motivation

To investigate remaining challenges towards commercial fusion, dedicated miniature experiments (compared to DEMO) are being built, such as IFMIF for researching materials under heavy neutron irradiation [23], the Divertor Tokamak Test (DTT) facility for improving the heat exhaust at the divertor [24] and the SPARC tokamak for exploring higher magnetic fields with high-temperature superconductors [25]. Also existing experiments are being adapted, e.g. ASDEX Upgrade to investigate alternative divertor concepts [26] and DIII-D to study the prospects of negative triangularity [21].

Additionally, numerical simulations have become an immensely useful tool: while experimental

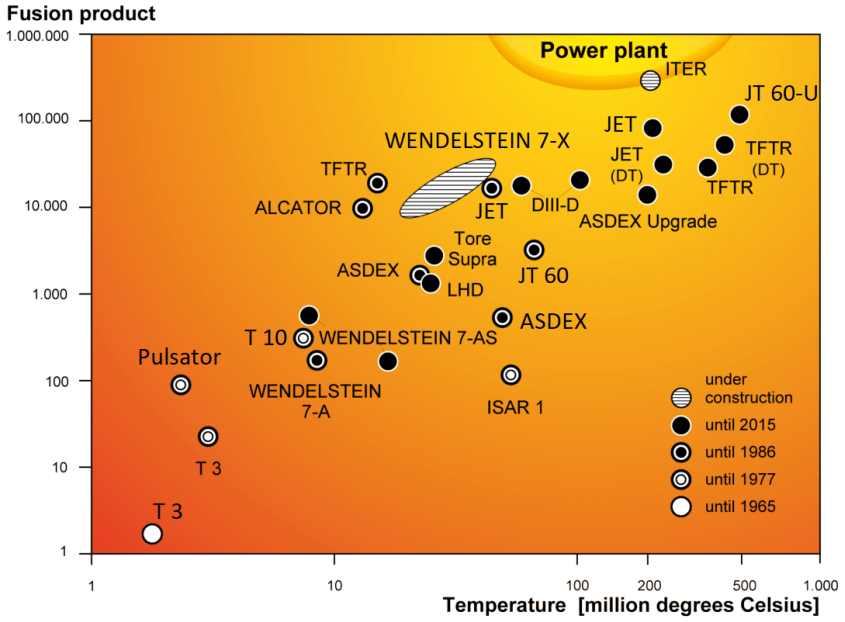

Figure 1.3: Fusion product [$\frac{\text{kg}}{\text{m}\cdot\text{s}}$] = density [$\text{m}^{-3}$] $\times$ energy confinement time [s] $\times$ k_B temperature [J] versus maximum achieved plasma temperature for different magnetic confinement fusion devices. The ignition diagram shows the progress of fusion research (adapted from [13]).

validation of technological solutions remains indispensable, simulations allow to investigate new ideas on general usage supercomputers before building dedicated machines. Naturally, to do so, simulation software has to be "realistic enough", i.e. ideally it should be validated on existing experiments. This usually requires significant investments of work into the development of sufficiently complete physical models, their numerical discretisation and computational implementation into software – which only then becomes useful for the above mentioned goals. Examples of such widely used community codes are SOLPS-ITER [27] for mean-field SOL and divertor exhaust modelling, JOREK [28] for non-linear magnetohydrodynamic (MHD) modelling of the interaction between plasma flows and the self-consistent magnetic field, and GENE [29, 30] for gyro-kinetic modelling of plasma turbulence.

Among the key challenges in understanding and predicting the performance of a tokamak is the mechanism of radial particle and heat transport. The equilibrium magnetic field of a tokamak provides a topology of closed flux surfaces such that single particle trajectories within are confined, i.e. do not on average have any radial motion. Mean radial motion of the plasma can therefore only result as a collective effect: either due to particle collisions, or due to electromagnetic fields generated by the collective motion of the plasma and perturbing the equilibrium field. Collisional transport alone, studied in neoclassical theory, is usually too low to explain experimentally observed radial fluxes [31]. Magnetic perturbations studied by MHD, on the other hand, are often so large that they must be avoided for steady state reactor operation [32]. It is therefore generally believed that the confinement in tokamaks at steady-state operation is primarily limited by turbulence driven by micro-instabilities [33], primarily electrostatic in nature but interacting with both collisional transport and electromagnetic fluctuations.

The academic aspect of tokamak turbulence simulations is also of significant interest. Turbulence remains one of the big unsolved puzzles in modern physics, as even the existence of global solutions for the Navier-Stokes equations is unproven [34]. For a long time, the only robust analytical prediction has been the Kolmogorov power spectrum $P(k) \sim k^{-5/3}$ [35]. Recently, progress has been made by means of information theory [36]: it is demonstrated that "the resolved scales carry significant information about the unresolved scales", which is good news for numerical simulations. Turbulence in magnetised plasmas has the additional complexity that the variety of waves and interactions is much larger due to the coupling to Maxwell's equations. On the other hand, due to the strong guiding magnetic field turbulence is essentially two dimensional (not 3D), lying in the so called drift plane (perpendicular to $\mathbf{B}$), while parallel dynamics remain laminar [37, 38].

The primary scope of this thesis are direct numerical simulations of turbulent transport across the

edge (of the confined region) and SOL of tokamaks, by solving the global drift-reduced Braginskii equations in 3D diverted geometry. The transition between the edge and SOL, and particularly the character of turbulence therein, is least explored and of major interest. For instance, under certain conditions a narrow layer forms in the edge of the confined region where turbulence is strongly suppressed and a much larger radial pressure gradient ('pedestal') can exist [39]. Plasma confinement can be twice as large in these high confinement (H-mode) discharges, compared to low confinement (L-mode) ones. Experimentally, it is known that divertor geometry is highly beneficial for the transition, the ion heat channel is more important than the electron heat channel [40] and the radial electric field plays a crucial role [41]. The H-mode confinement improvement and pedestal control are also crucial for ITER [42] and turbulence therein is being explored [43]. Yet a definitive agreement on the mechanisms and predictive capability are still missing. Among other things, the interaction between mean-field and turbulence generated zonal flows is thought to be of high importance [44] and was explored in this thesis in chapter 5.

Another urgent issue for DEMO design is power load handling on the divertor [45], and power and particle fluxes on device walls in general [46]. The issue is tightly coupled to the understanding of improved confinement regimes, as those are the reactor relevant conditions in which the power and particle loads have to be studied, and to the turbulent transport in the SOL. But a number of additional processes become important, such as the interaction of the plasma with neutral gas in the SOL and divertor chamber, and the interaction with device walls through the plasma-sheath boundary. The neutral gas is of paramount importance for a number of reasons, in particular the pumping out of particles to control the plasma core density and remove the helium ash [47], and also for heat load control, as the extinguishment of the plasma near the device walls (ultimate detachment) provides the safest way of operation [12]. The formation of a Debye sheath at the interface between the plasma and the tokamak wall sustains a strong electric field between the plasma and the wall, confining the electrons to preserve quasi-neutrality and accelerating the plasma (ions) towards the wall [48, 49]. In chapter 3 of this thesis we studied the effect of the sheath on cooling the electrons in the SOL, and in chapter 5 we investigated the sheath sustained $E \times B$ rotation. The neutral gas leads to a higher collisionality in the SOL and particularly towards the divertor plates, as plasma temperature is decreased and density is increased due to electron impact collisions with neutral atoms [12]. This has been explored in chapter 6, finding as a result much better agreement with the ASDEX Upgrade experiment. The validation against ASDEX Upgrade builds the first step towards predictive turbulence and transport simulations across the plasma edge, SOL and in the divertor, that might help to design DEMO and other fusion reactors.

1.2 Brief review of historical and cutting-edge research

We do not know exactly which physical model is optimal for tokamak simulations, in fact presumably a framework of model hierarchies would be best – depending on the application in mind. For turbulence simulations this question is even more treacherous as turbulence is naturally a multi-scale nonlinear phenomenon, and so approximations have to be made with great care. At the same time, simply solving the most realistic model – fully kinetic (6D), coupled to Maxwell's equations in 3D – is computationally nearly impossible [50] (although progress is being made [51]). Therefore, it is impossible to discuss appropriate physical models for plasma turbulence simulations without having an eye on the computational aspect, and vice versa computational performance strongly depends on the model and its assumptions. Gyrokinetic models [52, 53] in 5D are now established as a very good approximation of tokamak dynamics at feasible cost – at least in the plasma core. However, these models remain extremely computationally expensive, particularly at the plasma edge. Plasma edge turbulence is more expensive to simulate because of the more complex magnetic geometry, as described in chapter 2.2. Further, lower plasma temperature requires a higher resolution and makes Coulomb collisions more important. The latter break the Hamiltonian structure of gyrokinetics and typically lead to significant computational cost and/or complexity [54, 55]. At the same time, the velocity-space structure tends towards a Maxwellian distribution function – hence why fluid models (in 3D) become attractive. Classical fluid models for magnetised plasmas almost always go back to the work of Braginskii [56], introduced in chapter 2.1. As the fluid closure is performed over the full kinetic equation, the resulting model (together with full Maxwell's equations) yet contains phenomena over too many orders of magnitude in time and in space,

including light waves and electron cyclotron modes. We are interested in turbulent flows of guiding center drifts on transport time scales, so fast dynamics such as cyclotron motion are eliminated from the equations by the drift-reduction procedure [38, 57, 58], introduced in chapter 2.1.1, with the goal of not having to resolve them numerically.

Codes based on sub-sets of drift-reduced Braginskii equations, partly linearised for small fluctuation amplitudes, have been very popular since the 80s, after Hasegawa and Wakatani [59, 60] have demonstrated in their pioneering work, among others, that plasmas exhibit two-dimensional (resistive) drift-wave turbulence with Bohm type diffusion $D \sim T/eB$. Additionally, the curvature of the tokamak magnetic field leads to interchange (ballooning) modes [61]. Among the different types of interchange modes, a prominent one is the ion temperature gradient (ITG) mode [62], since perturbations of the ion temperature cannot be effectively balanced by the parallel electron current and therefore lead to significant cross-field transport. Generally, non-linear drive and saturation are at least as important as linear instabilities though, as drift-wave turbulence can be self-sustained even without a linear instability [63–65]. Among other saturation processes, an interesting one is the absorption of turbulence into a large scale stationary zonal flow, typical of 2D turbulence [44, 66, 67]. Braginskii models allowed to characterise the parameter space of tokamaks, with first indications for the mechanisms behind the L-H transition and the density limit [68].

However, it was also acknowledged that kinetic effects play a major role in actual tokamaks [69–71], particularly as collisionality is never large enough for the particles to actually thermalize [72]. To date, the work horse for tokamak core turbulence simulations is gyro-kinetic theory, whereby two principal approaches for the discretisation of the velocity space should be distinguished: grid based [29, 30] and particle based (particle-in-cell, PIC) [73, 74], as well as hybrids [75, 76]. For example, recent focus is on the interplay with neoclassical (collisional, mean-field) physics [77] and on fast particles [78], in tokamaks and in stellarators [79]. To mimic kinetic effects with fluid equations (that are still numerically cheaper to solve), the kinetic dispersion relation, i.e. linear response, was approximated [80–82]. This gyro-fluid approach allows to approximate kinetic effects (in the collisionless limit) such as gyro-averaging, pressure anisotropy, Landau damping and trapped particles. However, care has to be taken nonetheless compared to the more rigorous gyro-kinetic theory in non-linear simulations [33]. In principle, even non-linear kinetic dynamics can be approximated by a fluid closure [83], but the resulting equations become arbitrarily complicated, loosing the computational advantage compared to gyro-kinetic codes. Naturally, gyro-fluid models have been extended to the plasma edge by taking collisionality into account [84, 85], with the exception of trapped particle effects [86].

In the plasma edge and particularly the SOL, however, fluctuation amplitudes can be up to 100% of the background [87–89]. Further, coherent large-amplitude structures are observed [90–92], called blobs or filaments. Therefore, small-amplitude approximations are not applicable, and all aforementioned models are strictly speaking invalid. The existence of such large amplitude fluctuations means that no separation between the (axisymmetric) background and turbulence can be made. Consequently, also the interaction of turbulence with mean field effects such as neoclassical physics, neutral gas and impurities becomes important. Because of that and, as discussed above, due to the more complex geometry and lower temperature (requiring higher resolution), turbulence simulations of the plasma edge are more challenging than in the tokamak core. But, on the other hand, the increased collisionality somewhat reduces the importance of kinetic effects. This led to a renaissance of drift-reduced Braginskii models.

Historically, due to the complexity of the plasma edge, it was mostly studied with mean field codes that approximate turbulent transport with diffusion coefficients but, on the other hand, take rigorously into account the interaction of the plasma with neutral gas, impurities and the wall: SOLPS [27, 93, 94], UEDGE [95], EDGE2D [96] and others in 2D, and EMC3 [26, 97] and SOLEDGE [98] in 3D. Recently, global drift-reduced Braginskii codes have emerged – in contrast to local codes used before – that evolve turbulent fluctuations simultaneously with the background (taking no low amplitude approximations) and usually simulate an extended radial domain, bridging the plasma edge of the confined region through the SOL to the device wall. Examples of such codes are BOUT++ [99, 100], GBS [101, 102], GDB [103], TOKAM3X [104, 105] and GRILLIX [3, 106, 107]. The codes vary in the details of their plasma models, taking successive steps in relaxing locality approximations towards fully global equations. They vary in the method of treating diverted geometry: from fully non-field-aligned methods [102], over flux-surface

aligned [104] to locally field aligned [103, 106] and fully aligned [99, 100]. And they take different approaches in including e.g. neutral gas physics [3, 105, 108, 109]. Work continuous also on gyro-fluid approaches, e.g. for relaxing the long-wavelength limit [110], as well as Landau closures for such global codes [100]. But also gyro-kinetic models and codes are being extended into the plasma edge and SOL. The most prominent example is the full$-f$ PIC code XGC1 [111, 112], that employs unstructured grids for diverted geometries, a multi-species grid-based collision operator [76] and a sophisticated neutral gas model [113]. But also continuum gyro-kinetic codes are bridging the gap, such as COGENT [114], Gkeyll [115] and GENE-X [116]. Thus, the field of plasma edge and SOL turbulence research is vivid and exciting, and can be expected to complete our understanding of dynamics in tokamaks and improve their predictability.

1.3 Outline of this thesis

The remainder of this publication based dissertation is organized as follows. Firstly, chapter 2 describes the methodology behind the published results: the physical model, numerical methods and computational implementation of the GRILLIX code. The focus thereby lies on a systematic overview of the concepts, and on important and novel technical details underlying the published results.

The major publications at the basis of this dissertation are contained in part II, as well as in appendix A in the original journals formatting. Chapter 3 describes the implementation of ion thermal dynamics and an implicit solver for parabolic (diffusive) terms in GRILLIX. This is used to perform Alcator C-mod simulations in circular geometry, similar to [117], finding among other things geodesic acoustic modes and a dependence of temperature profiles not just on parallel heat conductivity, but also on sheath heat transmission. Chapter 4 contains a corrigendum to that publication: a mistake in the handling of input parameters, leading to a confusion of ion and electron heat conductivities, was corrected and their distinct role was emphasized.

Building on these model extensions and the implementation of numerical equilibria [118], in chapter 5 we were able to simulate an ASDEX Upgrade L-mode discharge in the actual diverted geometry. In this work, we particularly highlight the interplay between mean field (neoclassical) $E \times B$ flows and turbulence driven (zonal) flows, their origin and impact on turbulence, transport and profiles.

Chapter 6 describes the latest, most complete simulations performed with GRILLIX. Starting from the setup in chapter 5, a neutral gas model was included, allowing to bring the simulations much closer to the actual experiment. A quantitative validation of GRILLIX simulations against experimental measurements was performed, focusing on the role of the neutral gas in improving the agreement. Also, prospects towards simulations of detached discharges were demonstrated.

A summary is given in chapter 7, particularly for the major publications building the cumulative part of this thesis, but also including a list of all peer-reviewed publications (with short explanations) and conference contributions of the author. Finally, the overall results are discussed in chapter 8, and conclusions are drawn in chapter 9.

Chapter 2

Methodology: physical model, numerical discretisation and computational implementation

In this chapter we establish the methodology for this thesis, which comprises the physical model, numerical methods and computational implementation of the GRILLIX code. Due to the cumulative character of this dissertation, the methods used to obtain the results in chapters 3-6 have been discussed therein to some degree. This chapter serves to introduce the methodology in a somewhat more systematic way, but is more illustrative than exhaustive. As this thesis is based on further developing the GRILLIX code [106, 107], it is important to point out that it builds on two previous dissertations: GRILLIX was written during the pioneering PhD thesis by Andreas Stegmeir [119], and further developed by Alexander Ross [120]. The former has laid out the numerical and computational foundation of the code, which will be discussed in chapters 2.2 and 2.3. The latter expanded the physical model from local Hasegawa-Wakatani to global Braginskii [107, 121], introduced in chapter 2.1, but yet under the cold ion approximation. The present dissertation aimed at allowing first realistic tokamak simulations. To this end, the plasma model was completed, a neutral gas model was implemented, but also numerical algorithms and their computational implementation have been improved.

2.1 The physical model: Braginskii equations, neutrals and sheath

Classical fluid models for magnetised plasmas almost always go back to the work of Braginskii [56]. He used the well known Chapman-Enskog procedure [122] to derive a set of plasma fluid equations from the plasma kinetic equation – the Vlasov equation with a Coulomb collision operator [123]. In classical (neutral) fluid mechanics this method is used to establish the connection between the microscopic kinetic Boltzmann equation and macroscopic continuum Navier–Stokes equations. The basic structure of the equations, the ideal part without dissipative terms $\mathbf{\Pi}$, $\mathbf{q}$, $\mathbf{R}$ and Q, can be directly derived from a fluid Lagrangian, i.e. from conservation laws – see e.g. [38, chapter 2.II]. The full Braginskii set of equations reads

$$\partial_t n_\mathrm{s} + \nabla\cdot(n_\mathrm{s}\mathbf{v}_\mathrm{s}) = 0, \tag{2.1}$$

$$m_\mathrm{s} n_\mathrm{s}\left(\partial_t + \mathbf{v}_\mathrm{s}\cdot\nabla\right)\mathbf{v}_\mathrm{s} + \nabla\cdot\mathbf{\Pi}_\mathrm{s} = -\nabla p_\mathrm{s} \pm e n_\mathrm{s}\left(\mathbf{E} + \frac{1}{c}\mathbf{v}_\mathrm{s}\times\mathbf{B}\right) \mp \mathbf{R}, \tag{2.2}$$

$$\frac{3}{2} n_\mathrm{s}\left(\partial_t + \mathbf{v}_\mathrm{s}\cdot\nabla\right) T_\mathrm{s} + \nabla\cdot\mathbf{q}_\mathrm{s} = p_\mathrm{s}\nabla\cdot\mathbf{v}_\mathrm{s} - \mathbf{\Pi}_\mathrm{s} : \nabla\mathbf{v}_\mathrm{s} + Q_\mathrm{s}. \tag{2.3}$$

These are (in cgs units) the equations for density n, velocity $\mathbf{v}$ and temperature T of the plasma species s. The species are usually, as in the present work, electrons and ions. This is called a simple plasma, and the Braginskii equations are limited in this regard [56]. However, extensions to plasmas with arbitrarily many ion species exist [124] and are being applied [98, 125], but are not subject of the present work. In eq. (2.2), we have $+e$ and $-\mathbf{R}$ for ions, and the opposite sign for electrons. For ions in a higher

charge state Z the charge becomes $+Ze$. m_s is the species mass, e the elementary charge, c the light speed and $p_\mathrm{s} = n_\mathrm{s} T_\mathrm{s}$ the pressure. Although the equations look identical for electrons and ions, the crucial difference are the species mass and charge in eq. (2.2), particularly as we have for a deuterium plasma $m_\mathrm{i}/m_\mathrm{e} \approx 3700$. The principal complexity of describing plasma flows in comparison to neutral fluids is the necessity to solve the above set of equations of motion coupled to Maxwell's equations for the electromagnetic fields, appearing in eq. (2.2). In section 2.1.1 below, we will introduce some further approximations to this end, but the most common and robust one for the dynamics of interest is quasi-neutrality $n = n_\mathrm{e} \approx Z n_\mathrm{i}$.

As for neutral fluids, constitutive relations must be added to describe the dynamics of the fluid precisely on the macroscopic level: the (viscous) stress tensor $\mathbf{\Pi}$, the conducted heat flux density $\mathbf{q}$, the frictional / thermal force between electrons and ions $\mathbf{R}$, and the collisional heat source Q. These can only be derived from first principles via a so called closure from the kinetic equation. Importantly, they can only be expressed as functions of the local $(n, \mathbf{v}, T)$ if the velocity space distribution function is close to a Maxwellian. This is usually only the case at very high collisionality, never quite reached in tokamaks and estimated with the electron and ion collision times

$$\tau_\mathrm{e} = \frac{3\sqrt{m_\mathrm{e}} T_\mathrm{e}^{3/2}}{4\sqrt{2\pi}\lambda e^4 Z n} = \frac{3.5 \cdot 10^4}{\lambda/10} \frac{T_\mathrm{e}^{3/2}/\mathrm{eV}}{Zn/\mathrm{cm}^{-3}} \mathrm{s}, \tag{2.4}$$

$$\tau_\mathrm{i} = \frac{\tau_\mathrm{e}}{Z^2} \left(\frac{T_\mathrm{i}}{T_\mathrm{e}}\right)^{3/2} \sqrt{\frac{2m_\mathrm{i}}{m_\mathrm{e}}}. \tag{2.5}$$

Here, λ is the Coulomb logarithm [126]. The closure is needed because the kinetic equation couples each fluid moment to the next higher one. However, one can exploit the fact that collisions drive the distribution of particles to a Maxwellian for an expansion in velocity space. The specific truncation used by Braginskii results in the Braginskii equations, or more specifically the Braginskii closure terms. For example, the parallel component of the force $\mathbf{R}$, a projection on the direction of the magnetic field $\mathbf{b} = \mathbf{B}/B$, is $R_\parallel = \mathbf{b} \cdot \mathbf{R} = R_\eta + R_T$. It consists of the friction $R_\eta = en\eta_\parallel j_\parallel$ and the thermal force $R_T = -0.71 n \nabla_\parallel T_\mathrm{e}$ (the coefficients change for $Z \neq 1$). We have introduced the Spitzer-Härm resistivity $\eta_\parallel = 0.51 m_\mathrm{e}/ne^2\tau_\mathrm{e}$, the parallel current $j_\parallel = en(u_\parallel - v_\parallel)$ with $u_\parallel = \mathbf{b} \cdot \mathbf{v}_\mathrm{i}$ and $v_\parallel = \mathbf{b} \cdot \mathbf{v}_\mathrm{e}$, and the parallel gradient $\nabla_\parallel = \mathbf{b} \cdot \nabla$. Perpendicular resistivity and thermal force are negligible – a typical anisotropy in magnetised plasmas.

As our scope are global simulations, capable of predicting turbulent transport from the confined region to the divertor target (where turbulent fluctuations can be up to 100%), we seek a model with a minimal set of simplifying assumptions, yet it must be computationally feasible. The full set of Braginskii equations coupled to Maxwell's equations contains waves spanning many different spatial and temporal scales – some of which are far separated from the turbulence and hence not of interest. We want to remove such waves – light, cyclotron and compressional Alfvén waves – from the system of equations to avoid the necessity to resolve very short time scales in numerical computations. This is discussed in the section below.

2.1.1 The drift reduction

The drift reduction has been detailed by numerous authors [38, 57, 58], so we try to be brief. On the other hand, although Braginskii equations in their drift-reduced form were widely applied to plasma turbulence simulations for decades [127], some strong approximations have been retained throughout the literature. In particular, we seek to alleviate restrictions regarding fluctuation amplitudes and the locality of turbulent saturation. This was initiated during the PhD thesis by Alexander Ross [120] and continued in the present work.

Let us first discuss the assumptions. The fastest motion resulting from eq. (2.2) is from the subset $\partial_t \mathbf{v}_\mathrm{s} = \pm \frac{e}{m_\mathrm{s} c} \mathbf{v}_\mathrm{s} \times \mathbf{B}$, which leads to gyration of the particles around field lines with the angular frequency $\omega_\mathrm{cs} = \frac{eB}{m_\mathrm{s} c}$, $\mathrm{s} \in \{\mathrm{e}, \mathrm{i}\}$. The cross product with $\mathbf{B}$ motivates separating the motion into a part along the magnetic field, and a part perpendicular to it, called the drift plane. We are, however, interested in turbulence on time scales $\partial_t \sim \omega \sim c_s/L_\perp \ll \omega_\mathrm{ci}$, caused by mean drifts of the particles – $E \times B$, diamagnetic and polarisation – not the periodic gyro-motion itself. This is why the equations are called drift-reduced.

The sound velocity $c_s = \sqrt{T_e/m_i}$ is defined without ion temperature by convention, such that the theory is applicable to cold ion conditions. $L_\perp = \bar{p}/|\nabla_\perp \bar{p}|$ is the scale length of the average pressure gradient perpendicular to the magnetic field, with $\nabla_\perp = -\mathbf{b}\times\mathbf{b}\times\nabla$. Equivalently, with the sound Larmor radius $\rho_s = c\sqrt{T_e m_i}/eB = c_s/\omega_{ci}$, we obtain the ordering parameter

$$\delta = \rho_s/L_\perp \ll 1. \tag{2.6}$$

It is used in an expansion of the perpendicular ion momentum equation (2.2) to eliminate the gyro-motion from the system.

A robust and strongly simplifying assumption in all plasma turbulence models is the flute mode ordering

$$k_\perp \gg k_\parallel, \tag{2.7}$$

which means that plasma quantities vary on spatial scales that are much larger along the magnetic field than perpendicular to it due to the fast parallel dynamics, the perpendicular motion being restricted by the Lorentz force. With the Alfvén velocity (in cgs units, replace 4π by μ_0 for SI)

$$v_A = \frac{B}{\sqrt{4\pi n_i m_i}}, \tag{2.8}$$

it follows for the frequencies ω that

$$\omega \sim k_\parallel v_A \ll k_\perp v_A, \tag{2.9}$$

i.e. we keep (parallel) shear Alfvén waves in the system while we neglect (perpendicular) compressional Alfvén waves. Condition (2.6) is sufficient for the time derivative in eq. (2.2) to be neglected to zeroth order within the drift plane (but not along $\mathbf{b}$). Condition (2.7) will rather be important for the numerical discretisation.

The last, also rather robust assumption is that the plasma is strongly magnetised, i.e. has larger magnetic than thermal pressure,

$$\beta_e = \frac{4\pi p_e}{B^2} = \frac{c_s^2}{v_A^2} \ll 1. \tag{2.10}$$

Note that the electron beta, not the total plasma beta is used here. This condition allows us to neglect magnetic field perturbations within the drift plane, i.e. the perpendicular electric field is electrostatic. The parallel electric field is not! Also, this allows us to commute the magnetic field through perpendicular derivatives.

With this, we can proceed to manipulating the equations. The electric field is expressed in terms of the potentials as

$$E_\parallel = -\frac{1}{c}\frac{\partial A_\parallel}{\partial t} - \nabla_\parallel \varphi, \qquad \mathbf{E}_\perp = -\nabla_\perp \varphi. \tag{2.11}$$

The magnetic field is assumed to consist of a fixed background $\mathbf{B}$, given by the magnetohydrodynamic (Grad-Shafranov) equilibrium, and a perturbation given by $A_\parallel$,

$$\mathbf{B}_{tot} = \mathbf{B} + \nabla \times A_\parallel \mathbf{b}. \tag{2.12}$$

The key step in drift reduction is to solve approximately the momentum balance equation (2.2) in the perpendicular plane. First, we simply rewrite it in terms of the velocity in the Lorentz force (crossed with $\mathbf{B}$),

$$B^2 \frac{en}{c}\mathbf{v}_\perp^s = \pm\nabla p_s \times \mathbf{B} + en\mathbf{E}\times\mathbf{B} \pm m_s n \frac{\mathrm{d}\mathbf{v}_s}{\mathrm{d}t}\times\mathbf{B} \pm (\nabla\cdot\mathbf{\Pi}_s)\times\mathbf{B}, \tag{2.13}$$

with $+$ for electrons and $-$ for ions. The first two terms on the right-hand side are the diamagnetic drift v_* and $E\times B$ drift v_E. Under the above assumptions, they dominate the velocity of both plasma species, i.e. to 0th order

$$\mathbf{v}_{0\perp}^{e,i} = \pm\frac{c}{enB^2}\nabla p_s \times \mathbf{B} + \frac{c}{B^2}\mathbf{E}\times\mathbf{B}. \tag{2.14}$$

For electrons, due to their small mass and hence gyro-radius, we completely ignore the other terms. For ions, the next order correction is approximated via

$$\mathbf{v}_{1\perp}^i = \mathbf{v}_\perp^i - \mathbf{v}_{0\perp}^i \approx -\frac{m_i c}{eB^2}\frac{\mathrm{d}\mathbf{v}_{0\perp}^i}{\mathrm{d}t}\times\mathbf{B} - \frac{c}{enB^2}\left(\nabla\cdot\mathbf{\Pi}_i(\mathbf{v}_{0\perp}^i)\right)\times\mathbf{B}, \tag{2.15}$$

i.e. inserting the lower order velocity into the higher order terms. This correction is called a polarisation velocity because it contains the time derivative of the electric field, but in fact it also contains other terms. The reason for including this smaller velocity in the model is that its divergence is comparable in size to that of the zeroth order drifts [38]. The $\mathrm{d}/\mathrm{d}t$ term is non-linear, as it contains advection with $\mathbf{v}^{\mathrm{i}}_{0\perp}$. Since we assume the plasma to be quasi-neutral, $n_{\mathrm{e}} = Zn_{\mathrm{i}}$, the electric field is determined not by Gauss's law, but by the quasi-neutrality condition $\nabla\cdot\mathbf{j} = 0$, where $\mathbf{j}_\perp$ is given by the drifts. In principle, the expansion can be continued to higher order by inserting the 1st order solution again into the right-hand side of (2.15), but the resulting system becomes horrible to solve, particularly due to the non-linearity. And, as it is explained in Ref. [38, chapter 13.III] and we discuss in chapter 8.3.1, the Chapman-Enskog closure itself poses limits on the expansion (for hot ions) as it assumes the smallness of $k_\perp\rho_{\mathrm{i}}$.

The remainder of the model is built by carefully inserting these perpendicular drifts into the rest of the Braginskii equations. This procedure is detailed in [37, 38, 120] and illustrated below, together with the resulting equations.

2.1.2 The global drift-reduced Braginskii equations

The drift reduction presented in the previous section is the main step from Braginskii to the drift-reduced Braginskii equations. But some further steps are required. In this section, the equation are introduced systematically. The full final set of equations is also presented in chapter 5.7, normalised according to section 2.1.7. Importantly, the model is global because no assumptions are made on the size of fluctuation amplitudes, and all parametric dependencies are retained.

Continuity equation

Let us first note that due to quasi-neutrality $n = n_{\mathrm{e}} \approx Zn_{\mathrm{i}}$, only one continuity equation is required. We choose the equation for electrons, since polarisation can be fully neglected there. Throughout this work, we assume $Z = 1$, except in the electron collision time. Simply inserting (2.14), we obtain

$$\frac{\partial}{\partial t}n + \nabla\cdot n\left(\mathbf{v}_E + \mathbf{v}^{\mathrm{e}}_* + v_\parallel\mathbf{b}\right) = 0. \tag{2.16}$$

Importantly, the diamagnetic drift enters only in a non-homogeneous magnetic field, as well as the compression of the $E\times B$ drift. Therefore, we define the curvature operator

$$C(f) = -\nabla\cdot\left(\frac{c}{B^2}\mathbf{B}\times\nabla f\right) = -\left(\nabla\times\frac{c\mathbf{B}}{B^2}\right)\cdot\nabla f, \tag{2.17}$$

and with

$$\nabla\cdot\mathbf{v}_E = -C(\varphi), \qquad \nabla\cdot(n\mathbf{v}^{\mathrm{e}}_*) = \frac{1}{e}C(p_{\mathrm{e}}), \qquad \nabla\cdot\left(n\mathbf{v}^{\mathrm{i}}_*\right) = -\frac{1}{e}C(p_{\mathrm{i}}), \tag{2.18}$$

we obtain

$$\frac{\partial}{\partial t}n + \mathbf{v}_E\cdot\nabla n + \nabla\cdot\left(nu_\parallel\mathbf{b}\right) = nC(\varphi) - \frac{1}{e}C(p_{\mathrm{e}}) + \frac{1}{e}\nabla\cdot\left(j_\parallel\mathbf{b}\right). \tag{2.19}$$

Quasi-neutrality equation

Quasi-neutrality is not maintained automatically, but we have to enforce it by evolving $e\partial_t(n_{\mathrm{i}} - n_{\mathrm{e}}) = \nabla\cdot\mathbf{j} = 0$. Therefore, it is also called the charge conservation equation. Importantly, here the polarisation velocity enters under the divergence. Inserting the drifts, we obtain

$$\nabla\cdot\left[\frac{m_{\mathrm{i}}c^2}{B^2}n\frac{d_{\mathrm{i}}}{dt}\left(\nabla_\perp\varphi + \frac{\nabla_\perp p_{\mathrm{i}}}{en}\right)\right] = -C(p_{\mathrm{e}} + p_{\mathrm{i}}) + \nabla\cdot\left(j_\parallel\mathbf{b}\right) - \frac{1}{6}C(G). \tag{2.20}$$

Here, we have introduced the material derivatives

$$\frac{d_{\mathrm{e}}}{dt} = \frac{\partial}{\partial t} + \left(\mathbf{v}_E + v_\parallel\mathbf{b}\right)\cdot\nabla, \tag{2.21}$$

$$\frac{d_{\mathrm{i}}}{dt} = \frac{\partial}{\partial t} + \left(\mathbf{v}_E + u_\parallel\mathbf{b} + \mathbf{u}_{\mathrm{pol}}\right)\cdot\nabla. \tag{2.22}$$

The diamagnetic velocity does not appear in the material derivatives due to diamagnetic cancellation with the stress tensor $\mathbf{\Pi}_\mathrm{i}$ [37, 38]. Although formally the polarisation velocity does appear, we will henceforth neglect this additional non-linearity since $\mathbf{u}_\mathrm{pol} \ll \mathbf{v}_E$ (but $\nabla\cdot\mathbf{u}_\mathrm{pol} \sim \nabla\cdot\mathbf{v}_E$). The peculiarity of the drift-reduction is that this material derivative appears under the divergence [120]. Further, following Ref. [37], we have written the viscous part of the ion stress tensor with the viscous stress function [128]

$$G = -\eta_\mathrm{i}\left[\frac{2}{B^{3/2}}\nabla\cdot\left(u_\parallel B^{3/2}\mathbf{b}\right) - \frac{C(\varphi)}{2} - \frac{C(p_\mathrm{i})}{2en}\right], \tag{2.23}$$

using the identity $3\nabla_\parallel u_\parallel - \nabla\cdot u_\parallel\mathbf{b} = 2B^{-3/2}\nabla\cdot u_\parallel B^{3/2}\mathbf{b}$ adopted from Ref. [94]. The parallel ion viscosity coefficient is $\eta_\mathrm{i} = 0.96 n T_\mathrm{i}\tau_\mathrm{i} \propto T_\mathrm{i}^{5/2}$.

Parallel momentum equation

For the parallel momentum of the plasma, we add the parallel projections of equations (2.2) for electrons and ions together. The Lorentz force and friction terms add up to zero. Due to the small electron mass, we can neglect their inertia, hence the total plasma momentum is approximately carried exclusively by the ions, $m_\mathrm{i}u_\parallel + m_\mathrm{e}v_\parallel \approx m_\mathrm{i}u_\parallel$. We then obtain

$$m_\mathrm{i} n\frac{d_\mathrm{i}}{dt}u_\parallel = -\nabla_\parallel(p_\mathrm{e}+p_\mathrm{i}) + \frac{m_\mathrm{i}p_\mathrm{i}}{e}C(u_\parallel) - \frac{2}{3}B^{3/2}\nabla_\parallel\frac{G}{B^{3/2}}. \tag{2.24}$$

The last two terms thereby stem from the ion viscosity.

Ohm's and Ampère's laws

Next, we derive an equation for the parallel current $j_\parallel = en(u_\parallel - v_\parallel)$. Due to their small mass, the parallel current is mainly carried by the faster electrons. Scaling eq. (2.2) for ions by $m_\mathrm{e}/m_\mathrm{i}$, we obtain by subtracting the ion from the electron part

$$-\frac{m_\mathrm{e}}{e}\frac{d_\mathrm{e}}{dt}\frac{j_\parallel}{en} = \eta_\parallel j_\parallel + \frac{1}{c}\frac{\partial}{\partial t}A_\parallel + \nabla_\parallel\varphi - \frac{1}{en}\nabla_\parallel p_\mathrm{e} - 0.71\frac{1}{e}\nabla_\parallel T_\mathrm{e}. \tag{2.25}$$

On the right-hand side, all terms of order $m_\mathrm{e}/m_\mathrm{i}$ have been neglected. The inertia term is important to physically limit the wave propagation speed below light speed [129]*. The resistivity $\eta_\parallel$ has been introduced above. The equation is solved for $A_\parallel$, connected to $j_\parallel$ through Ampère's law (see section 2.1.4)

$$\nabla_\perp^2 A_\parallel = -\frac{4\pi}{c}j_\parallel. \tag{2.26}$$

Temperature equations

Finally, for the temperatures we follow the derivation by Ref. [37], except that we keep the collisional heating terms, yielding

$$\begin{aligned}\frac{d_\mathrm{e}}{dt}T_\mathrm{e} = &-\frac{2}{3}\left[\frac{T_\mathrm{e}}{en}C(p_\mathrm{e}) - T_\mathrm{e}C(\varphi) + \frac{5}{2}\frac{T_\mathrm{e}}{e}C(T_\mathrm{e})\right] - \frac{2}{3}T_\mathrm{e}\nabla\cdot\left(v_\parallel\mathbf{b}\right) + \frac{2}{3}0.71\frac{T_\mathrm{e}}{en}\nabla\cdot\left(j_\parallel\mathbf{b}\right) \\ &+\frac{2}{3}\frac{1}{n}\nabla\cdot\left(\chi_\parallel^\mathrm{e}\nabla_\parallel T_\mathrm{e}\right) - \frac{2m_\mathrm{e}}{m_\mathrm{i}\tau_\mathrm{e}}(T_\mathrm{e}-T_\mathrm{i}) + \frac{2}{3}\frac{\eta_\parallel j_\parallel^2}{n},\end{aligned} \tag{2.27}$$

$$\begin{aligned}\frac{d_\mathrm{i}}{dt}T_\mathrm{i} = &-\frac{2}{3}\left[\frac{T_\mathrm{i}}{en}C(p_\mathrm{e}) - T_\mathrm{i}C(\varphi) - \frac{5}{2}\frac{T_\mathrm{i}}{e}C(T_\mathrm{i})\right] - \frac{2}{3}T_\mathrm{i}\nabla\cdot\left(u_\parallel\mathbf{b}\right) + \frac{2}{3}\frac{T_\mathrm{i}}{en}\nabla\cdot\left(j_\parallel\mathbf{b}\right) \\ &+\frac{2}{3}\frac{1}{n}\nabla\cdot\left(\chi_\parallel^\mathrm{i}\nabla_\parallel T_\mathrm{i}\right) + \frac{2m_\mathrm{e}}{m_\mathrm{i}\tau_\mathrm{e}}(T_\mathrm{e}-T_\mathrm{i}) + \frac{2}{9n\eta_\mathrm{i}}G^2.\end{aligned} \tag{2.28}$$

*Note that at arbitrarily low density (towards a vacuum), the Alfvén speed becomes arbitrarily large. For $n \leq \varepsilon_0 B^2/m_\mathrm{i}$ (in SI units) it still surpasses the light speed. This occurs at 4×10^{16} m^{-3} for $B = 4$ T, which is possible in far-SOL and private flux regions of tokamaks. The reason is that the quasi-neutrality assumption breaks down, but this can be cured by including vacuum permittivity (space charge) and the displacement current in the charge conservation equation [129].

The parallel Braginskii electron and ion heat conductivities are defined as

$$\chi_{\parallel}^{\mathrm{e}} = 3.16 \frac{n T_{\mathrm{e}} \tau_{\mathrm{e}}}{m_{\mathrm{e}}} \propto T_{\mathrm{e}}^{5/2}, \qquad \chi_{\parallel}^{\mathrm{i}} = 3.9 \frac{n T_{\mathrm{i}} \tau_{\mathrm{i}}}{m_{\mathrm{i}}} \propto T_{\mathrm{i}}^{5/2}. \tag{2.29}$$

2.1.3 Thermal dynamics: hot ions

In their global form, the drift-reduced Braginskii equations are subject of current cutting-edge research [99, 101, 104, 117]. Their understanding and implementation are not trivial, and proceed in consecutive steps, some of which were performed in this dissertation. This section stresses a particular extension of the model compared to its previous state [120] – the hot ions.

The basis for understanding turbulence in plasmas are the $E \times B$ flow dynamics and density fluctuations [60, 66]. In the experimental reality, temperature dynamics plays a crucial role though: while the plasma core has to be above 10 keV hot for ignition, the tokamak wall has to be at essentially 0 keV to survive operation. The electron and ion temperature gradients are not only a source of free energy for turbulence [29, 130]. Due to heat conduction, temperatures are also involved in qualitatively different and important dynamics [131], including Landau damping [70, 132]. Ion temperature plays a particular role: it drives one of the most important instabilities, the ITG mode [62], and is crucial in flow regulation and confinement mode transitions [40]. This is because the parallel current barely reacts to ion temperature fluctuations, and because an increasing ion Larmor radius determines the plasma viscosity.

Electron thermal dynamics has been implemented during Alexander Ross' thesis [120], but fully explicitly with the time step restrictions discussed in section 2.3.1. This has strongly limited the allowable heat conduction [107], putting electron temperature unjustly on the same footing as density. This restriction was resolved in the present dissertation, as discussed in chapters 2.2.3, 2.3.3 and 3. We also remark that the Braginskii expressions for heat conductivities (and ion viscosity) are indeed overestimated, and first kinetic corrections were implemented in chapter 6.3, as further discussed in section 8.3.1. Additionally, while $T_{\mathrm{i}} = 0$ was assumed previously [120], we have now implemented hot ion dynamics. In large parts, the implementation proceeds identically to the electron temperature equation, as can be seen in chapter 3.2. However, there are some noteworthy differences.

Diamagnetic polarisation

The ion pressure term on the left-hand side of eq. (2.20), the diamagnetic polarisation, appears due to the ion diamagnetic drift in the polarisation velocity. 'Diamagnetic cancellation', the fact that the diamagnetic velocity does not cause any actual advection except due to the inhomogeneity of the magnetic field, does not apply here as this term does not represent diamagnetic advection. Rather, as discussed in chapter 5.2.2, this term is part of the diamagnetic vorticity. It can be understood as the lowest order finite Larmor radius effect, i.e. the ions do not feel the local but rather the gyro-radius-averaged electrostatic potential [37, 72]. The main challenge in the implementation of this term is the time derivative acting on it under the divergence, i.e. the consistent time discretisation without resorting to an implicit treatment, as discussed in chapter 3.3.1. But also the $E \times B$ and parallel advection acting on it were implemented.

Electron-ion collisional heat exchange

Having now both electron and ion temperature, these two can differ due to different transport and/or sources and sinks. However, the difference is limited by collisional equilibration

$$\frac{\partial T_{\mathrm{e}}}{\partial t} \sim -\frac{2 m_{\mathrm{e}}}{m_{\mathrm{i}} \tau_e} \left(T_{\mathrm{e}} - T_{\mathrm{i}} \right), \tag{2.30}$$

with the electron collision time τ_{e} [56]. The same term appears in the ion temperature equation with the opposite sign. Although not difficult to implement, this term is often neglected in literature [101, 103] because it is not crucial for turbulence itself (acting on longer time scales due to the $m_{\mathrm{e}}/m_{\mathrm{i}}$ dependence) – but it is crucial for the correct maintenance of mean field profiles, which is key in a global code, and of course it is important in the highly collisional divertor.

Ion viscosity

Finally, due to their larger gyro-radius, viscosity is important for ions[†]: the collisional part of the stress tensor $\mathbf{\Pi}_\mathrm{i}$ in equations (2.2) and (2.3). After drift reduction, it enters the vorticity (2.20), parallel momentum (2.24) and ion temperature (2.28) equations via the viscous stress function G (2.23). The role of this term is also discussed in chapter 5, particularly with respect to neoclassical theory. The derivation mostly follows Zeiler's habilitation [37, chapter 2], with two differences: firstly, the viscous heating term in the ion temperature equation is actually implemented (Zeiler derived but then dropped the term). It did cause issues in chapter 5 due to the very low collisionality, but worked fine in chapter 6 as discussed therein. Secondly, and perhaps more importantly, the expression for viscosity in the parallel momentum equation (2.24) slightly differs. Following the argument by Bruce Scott [38], we do not commute $\mathbf{b}$ through parallel derivatives, i.e. we carefully discriminate between parallel gradients and divergences. This is because $\nabla_\parallel f = \nabla\cdot\mathbf{b}f + f/L_{B\parallel}$, with the magnetic scale length $1/L_{B\parallel} = -\nabla_\parallel B/B$ comparable to $k_\parallel$ from $\nabla_\parallel f$. But also, this distinction is important in the FCI approach to keep the continuous properties of the operators, see section 2.2.1. The final expression reads

$$\frac{\partial u_\parallel}{\partial t} = \ldots + \frac{B^{3/2}}{3m_\mathrm{i}n}\nabla_\parallel\frac{\eta_\mathrm{i}}{B^{3/2}}\left[\frac{4}{B^{3/2}}\nabla\cdot\left(u_\parallel B^{3/2}\mathbf{b}\right) - C(\varphi) - \frac{1}{en}C(p_\mathrm{i})\right]. \tag{2.31}$$

Physically, the magnetic field factors are important in toroidal geometry as they lead to the magnetic pumping effect [133, chapter 14.3.3]: due to the radial variation of the toroidal magnetic field and the resulting magnetic mirror, there is a constant competition between the anisotropy of the ion velocity distribution due to trapping, and the isotropisation due to collisions. As a result, even a rigid parallel rotation is damped due to the parallel gradient of the magnetic field, thereby heating the ions up. The first term in the bracket constitutes a parabolic (diffusion) equation for the parallel velocity, and has to be treated implicitly just like the electron and ion parallel heat conductivities, as discussed in section 2.2.3.

2.1.4 Electromagnetic effects

Electromagnetic fields are crucial in plasmas because they are tightly coupled to plasma flows, as discussed above and in chapter 5. Historically, the dynamics of the magnetic field was rather a topic of MHD as it often leads to large scale phenomena. For micro-turbulence, on the other hand, the electric field plays the crucial role. Naturally, no clear separation between small and large scales exists, and so both the electric field and the magnetic field are important in reality. This is particularly true for global turbulence simulations which naturally aim to study the interaction between small- and large-scale flows.

The electric field enters through the $E\times B$ drift and is solved for via the vorticity equation, as detailed in chapter 5. The magnetic field enters all the drifts as well as parallel motion. It is determined by currents via Ampère's law (in cgs units),

$$\nabla\times\mathbf{B} = \frac{1}{c}\left(4\pi\mathbf{j} + \frac{\partial\mathbf{E}}{\partial t}\right), \tag{2.32}$$

whereby the displacement current $\partial_t\mathbf{E}$ is usually negligible [38]. Further, as tokamaks possess a strong guiding background magnetic field (that needs to be in MHD equilibrium), we can assume that turbulent fluctuations remain aligned to it – relying on the low beta assumption $\beta_\mathrm{e} \ll 1$ in (2.10). Magnetic field perturbations are assumed to be small – but they are nonetheless important. The reason for this is the fast parallel transport, that can lead to significant perpendicular flows on a small perpendicular magnetic field perturbation. Therefore, the total magnetic field is given by $\mathbf{B}_\mathrm{tot} = \mathbf{B} + \nabla\times A_\parallel\mathbf{b}$, with the background field $\mathbf{B}$ and its unit vector $\mathbf{b}$, and the perpendicular perturbation $\tilde{\mathbf{B}}_\perp \approx \nabla\times A_\parallel\mathbf{b}$. Even more importantly, these small perturbations can strongly affect the parallel electric field via $E_\parallel = -\nabla_\parallel\varphi - c^{-1}\partial_t A_\parallel$. In this section, we will argue that the effect on $E_\parallel$ is generally crucial, while $\tilde{\mathbf{B}}_\perp$ is less important in present simulations. Therefore, we use $\mathbf{b}$ instead of $\mathbf{b}_\mathrm{tot} = \mathbf{B}_\mathrm{tot}/B$ for the remainder of this thesis, also for the simplicity of notation.

[†]The Braginskii expression for the electron heat conductivity is 35 times larger than that of ions, primarily due to the mass ratio. The ion viscosity has a similar magnitude as the ion heat conductivity – but in comparison to the electron viscosity, the mass ratio enters **inversely**, such that the electron viscosity is roughly 60 times **smaller** – it is therefore typically neglected.

Plugging $\mathbf{B}_{\text{tot}}$ into Ampère's law, and subtracting the background magnetic field and main plasma current, we obtain

$$\nabla_\perp^2 A_\parallel = -\frac{4\pi}{c} j_\parallel. \tag{2.33}$$

The parallel current $j_\parallel$, on the other hand, is determined by Ohm's law (2.25). This hyperbolic equation has to be solved together with Ampère's law (an elliptic equation), as detailed in Ref. [107]. The need for an elliptic solver with time-varying coefficients (the density in the inertia) is the practical reason why many codes neglect electromagnetic effects [102, 105, 134].

The practical reason for including $A_\parallel$ in Ohm's law, i.e. in $E_\parallel$, is that it limits the fastest dynamics in the system, the parallel electron dynamics, as discussed by various authors [38, 129, 135, 136]. The kinetic shear Alfvén velocity is

$$V_a^2 = \frac{1+k_\perp^2\rho_s^2}{\beta_\text{e}+\mu k_\perp^2\rho_s^2} c_s^2 = \frac{1+k_\perp^2\rho_s^2}{1+k_\perp^2\sigma_0^2} v_\text{A}^2, \tag{2.34}$$

with the collisionless skin depth $\sigma_0^2 = (\mu/\beta_\text{e})\rho_s^2$. This has two important limits: for large scales, $k_\perp \to 0$, we get the Alfvén velocity v_A. For small scales, $k_\perp \to \infty$, we get propagation at the thermal electron speed $c_s^\text{e} = \sqrt{T_\text{e}/m_\text{e}}$. The latter consideration justifies why for small-scale simulations, $\beta_\text{e} \approx 0$ and equivalently $A_\parallel \approx 0$ can work. However, the small scales are never separated from the larger ones, and particularly global simulations contain arbitrarily small $k_\perp$. Neglecting β_e hence leads to arbitrarily large propagation velocities. To limit the current propagation velocity to physically meaningful values, it is sufficient to include $A_\parallel$ in Ohm's law and solve it together with Ampère's law as above. This was done during the thesis by Alexander Ross [120] and published in Ref. [107]. The relevance of this to the performance of current simulations is further discussed in section 2.3.1.

Nonetheless, the induced magnetic field perturbation $\tilde{\mathbf{B}}_\perp$ is generally small compared to the background magnetic field B due to the low beta condition $\beta_\text{e} \ll 1$, in chapter 5.3.3 we found $\left|\tilde{\mathbf{B}}_\perp\right|/B < 0.1\%$. Therefore, one can still neglect the magnetic flutter $\tilde{\mathbf{B}}_\perp$ in parallel operators, i.e. neglect magnetic flutter transport. This was done in all publications with GRILLIX before this thesis [107, 121]. However, the fast parallel dynamics does not require large flutter to produce significant cross-field transport [137], so one must proceed with care. In this thesis, we have investigated magnetic flutter transport more carefully. We write

$$\nabla_\parallel f = \mathbf{b}_\text{tot}\cdot\nabla f = \frac{1}{B}\left(\mathbf{B}+\nabla\times A_\parallel\mathbf{b}\right)\cdot\nabla f = \nabla_{\parallel 0} f + \nabla_{\parallel 1} f + \nabla_{\parallel 2} f. \tag{2.35}$$

The zeroth term is just the unperturbed parallel gradient $\mathbf{b}\cdot\nabla f$. The first and second term are

$$\nabla_{\parallel 1} f = \frac{1}{B}\left(-\mathbf{b}\times\nabla A_\parallel\right)\cdot\nabla f = -\frac{1}{B}\mathbf{b}\cdot\left(\nabla A_\parallel\times\nabla f\right), \tag{2.36}$$

$$\nabla_{\parallel 2} f = \frac{1}{B}\left(A_\parallel\nabla\times\mathbf{b}\right)\cdot\nabla f = A_\parallel\left(\nabla\times\frac{\mathbf{B}}{B^2}\right)\cdot\nabla f - \frac{A_\parallel}{B^2}\mathbf{b}\cdot\left(\nabla B\times\nabla f\right). \tag{2.37}$$

The $\nabla_{\parallel 1}$ term is the main perturbation [103], [37, eq. (2.78)], [38, eq. (14.7)]. The additional correction $\nabla_{\parallel 2}$ is required to keep the total magnetic field divergence free, but it is typically neglected because it is small and somewhat artificial: the vector potential $A_\parallel$ appears without a derivative, although it is not a physically observable quantity – only its derivative, the magnetic field, is. The reason for its appearance is the approximation that the magnetic field perturbation is strictly orthogonal to the equilibrium magnetic field, $\tilde{\mathbf{B}}_\perp \approx \nabla\times A_\parallel\mathbf{b}$. It is not a complicated expression: under the usual large aspect ratio approximation $\mathbf{B} \approx B_0\frac{R_0}{R}\sigma_b\mathbf{e}_\phi$, where $\mathbf{e}_\phi$ is the toroidal unit vector and $\sigma_b = \pm 1$ is the direction of the toroidal magnetic field, we obtain

$$\nabla_{\parallel 2} f \approx -\frac{A_\parallel}{2c} C(f). \tag{2.38}$$

This term has been implemented and verified to be tiny.

The main perturbation $\nabla_{\parallel 1}$ represents perpendicular advection due to $A_\parallel$ and is written with the Poisson bracket $[g,f]_{R,Z} = \partial_R g\partial_Z f - \partial_Z g\partial_R f \approx -\sigma_b\mathbf{b}\cdot(\nabla g\times\nabla f)$ as

$$\nabla_{\parallel 1} f = \frac{\sigma_b}{B}\left[A_\parallel, f\right]_{R,Z}. \tag{2.39}$$

We can now understand magnetic flutter transport. The flutter does not lead to a flow on its own: it is rather a deformation of magnetic geometry which leads to an effective perpendicular flux due to redirection of parallel flows. For example, the parallel density flow $nv_\parallel$ (with electron parallel velocity $v_\parallel$) leads to

$$\frac{\partial n}{\partial t} = \nabla\cdot\left(\mathbf{b}_{\text{tot}} n v_\parallel\right) = \nabla\cdot\left(\mathbf{b} n v_\parallel\right) + \left[A_\parallel, n v_\parallel/B\right] = \nabla\cdot\left(\mathbf{b} n v_\parallel\right) + \nabla\cdot\left(n\mathbf{v}_\beta(v_\parallel)\right), \tag{2.40}$$

with the magnetic flutter drift due to parallel electron flow

$$\mathbf{v}_\beta(v_\parallel) = v_\parallel \frac{\mathbf{B}}{B^2}\times\nabla A_\parallel. \tag{2.41}$$

Comparing this expression to the $E\times B$ drift in eq. (2.14), we anticipate that at a comparable gradient of φ and $A_\parallel$ (which is not necessarily true!) the flutter drift is smaller by the ratio of parallel velocity to light speed $v_\parallel/c$. Indeed, in numerical simulations parallel advection typically does not lead to significant flutter transport. For this reason, also the non-linearity in Ohm's law, $\nabla_{\parallel 1} j_\parallel/n$, seems not to play a significant role in practice, compared to the electric field non-linearity in the vorticity equation.

By far the dominant magnetic flutter transport channel is due to the parallel diffusion terms from the Braginskii closure, the parallel electron and ion heat conductivities as well as ion viscosity (the first term in eq. (2.31)). For the former, an expression of the form

$$\frac{\partial T}{\partial t} \sim \sigma_b\left[A_\parallel, \frac{\chi_\parallel}{B}\left(\nabla_{\parallel 0} T + \frac{\sigma_b}{B}\left[A_\parallel, T\right]_{R,Z}\right)\right]_{R,Z} \tag{2.42}$$

is obtained, with the Braginskii heat conductivity $\chi_\parallel \sim T^{5/2}$. Note that due to magnetic flutter, parallel diffusion becomes a 3D problem, and is solved implicitly as described in section 2.2.3.

The large heat conductivity is the reason why the small magnetic field perturbation can lead to significant perpendicular heat transport [137]. Kinetically, the conductivity is due to supra-thermal particles in the tail of the velocity distribution. However, unlike the Braginskii expressions suggests, the conductivity does not become arbitrarily large at higher temperatures due to Landau damping, as discussed in chapters 6.3 and 8.3.1. With the free-streaming limited heat conductivity, we have not yet observed significant perpendicular heat flows (as noted also in chapter 5.3.3), corroborating also previous studies. Therefore, the effect was switched off, saving a factor 2 in computing time (just evaluating the operator in each iteration of the implicit solver is expensive) – for this reason, and for simplicity of notation, $\mathbf{b}$ is used instead of $\mathbf{b}_{\text{tot}}$ in the remainder of this thesis. A larger impact is expected at higher beta, presumably in H-mode simulations [43]. However, additionally, also the ion viscosity in eq. (2.31) is subject to magnetic flutter and is comparable in magnitude to the ion heat conductivity, providing a perpendicular transport mechanism for parallel momentum. Surprisingly, this completely suppresses turbulence in our simulations. Together with the findings in chapters 6.5.2 and 6.5.5, this suggests that similarly as for the Braginskii heat conductivity, the ion viscosity must be corrected in sufficiently collisionless regimes, similarly as in [94]. The mechanism is different though: the ion viscosity is determined by the friction between trapped and passing particles [31, 138], and should be corrected according to Ref. [139], as further discussed in section 8.3.1.

2.1.5 Interaction with the neutral gas

An integral goal of this PhD thesis has been to move the GRILLIX code towards reactor relevant simulations, in particular of the plasma edge and SOL of diverted tokamaks. This includes the extension of the plasma model, accompanied by numerical and computational developments. But also, it was anticipated [12, 47] and shown in chapter 6 that the interaction of the plasma with the neutral gas is of paramount importance. The primary effect thereby is on the mean plasma profiles [105], which is important in a global turbulence code that develops the mean profiles together with turbulence. A still simple, but impactful neutral gas model as described here and in chapter 6 has been implemented and indeed led to a much better agreement between the simulations and the AUG experiment.

A simple plasma consisting of one ion species and the corresponding neutral atoms are considered, ignoring molecules. They interact via three reactions, electron impact ionization and recombination, and charge exchange (CX),

$$\mathrm{e} + \mathrm{D} \longleftrightarrow 2\mathrm{e} + \mathrm{D}^+, \tag{2.43}$$
$$\mathrm{D}^+ + \mathrm{D} \longleftrightarrow \mathrm{D} + \mathrm{D}^+. \tag{2.44}$$

In a homogeneous plasma, the dynamics of the ion-neutral reactions is described by the following set of rate equations:

$$\frac{\mathrm{d}n_\mathrm{e}}{\mathrm{d}t} = \frac{\mathrm{d}n_\mathrm{i}}{\mathrm{d}t} = -\frac{\mathrm{d}N}{\mathrm{d}t} = k_\mathrm{iz} N n_\mathrm{e} - k_\mathrm{rec} n_\mathrm{i} n_\mathrm{e}, \tag{2.45}$$
$$\frac{\mathrm{d}\mathbf{p}_\mathrm{i}}{\mathrm{d}t} = -\frac{\mathrm{d}\mathbf{p}_\mathrm{N}}{\mathrm{d}t} = k_\mathrm{iz} N n_\mathrm{e} M \mathbf{v}_\mathrm{N} - k_\mathrm{rec} n_\mathrm{i} n_\mathrm{e} M \mathbf{v}_\mathrm{i} + k_\mathrm{cx} N n_\mathrm{i} M (\mathbf{v}_\mathrm{N} - \mathbf{v}_\mathrm{i}), \tag{2.46}$$
$$\frac{\mathrm{d}\mathbf{p}_\mathrm{e}}{\mathrm{d}t} = k_\mathrm{iz} N n_\mathrm{e} m_\mathrm{e} (2\mathbf{v}_\mathrm{N} - \mathbf{v}_\mathrm{e}) - k_\mathrm{rec} n_\mathrm{i} n_\mathrm{e} m_\mathrm{e} \mathbf{v}_\mathrm{e} + k_\mathrm{en} N n_\mathrm{e} m_\mathrm{e} (\mathbf{v}_\mathrm{N} - \mathbf{v}_\mathrm{e}), \tag{2.47}$$
$$\frac{3}{2}\frac{\mathrm{d}p_\mathrm{e}}{\mathrm{d}t} = -W_\mathrm{iz} N n_\mathrm{e} - W_\mathrm{rec} n_\mathrm{i} n_\mathrm{e}, \tag{2.48}$$
$$\frac{3}{2}\frac{\mathrm{d}p_\mathrm{i}}{\mathrm{d}t} = -\frac{3}{2}\frac{\mathrm{d}p_\mathrm{N}}{\mathrm{d}t} = \frac{3}{2} k_\mathrm{cx} N n_\mathrm{i} (T_\mathrm{N} - T_\mathrm{i}) + \frac{3}{2} k_\mathrm{iz} N n_\mathrm{e} T_\mathrm{N} - \frac{3}{2} k_\mathrm{rec} n_\mathrm{i} n_\mathrm{e} T_\mathrm{i}. \tag{2.49}$$

The above equations can alternatively be derived from the integration of Krook collision operators [140]. We have used here the neutral gas density N, the momentum density $\mathbf{p}_\mathrm{s} = m_\mathrm{s} n_\mathrm{s} \mathbf{v}_\mathrm{s}$ and thermal energy density $\frac{3}{2} p_\mathrm{s} = \frac{3}{2} n_\mathrm{s} T_\mathrm{s}$. The rate coefficients for ionization k_iz and recombination k_rec are obtained from collisional-radiative (CR) models, the results being available in public Amjuel [141] or OPEN-ADAS [142] data bases. The same is true for electron cooling rate coefficients $W_\mathrm{iz}, W_\mathrm{rec}$ [143, chap. 6], whereby it must be noted that the recombination cooling rate becomes negative below 1 eV. This is because three-body recombination heats up the plasma. Therefore, the database stores the always positive radiation rate coefficient due to recombination instead, and we compute $W_\mathrm{rec} = P^\mathrm{rad}_\mathrm{rec} - 13.6\ \mathrm{eV} \cdot k_\mathrm{rec}$. For charge exchange, the simple formula $k_\mathrm{cx} = 2.93 \sigma_\mathrm{cx} \sqrt{T_\mathrm{i}/m_\mathrm{i}}$ from reference [144] can be used, which makes the rather robust assumption that the cross section σ_cx is constant, i.e. does not depend on impact energy – but does not assume an exactly Maxwellian velocity distribution for the electrons, performing a more elaborate closure.

In the momentum balance, we have applied the usual approximation $m_\mathrm{e} \ll m_\mathrm{N} = m_\mathrm{i}$ and assume that momentum is exchanged similarly in both elastic and inelastic collisions. Therefore, momentum is simply exchanged between ions and neutrals at each collision, while electrons are scattered from the heavier species (including in elastic collisions with the rate coefficient k_en). While electron scattering in this approximation does not conserve energy, it is usually dissipative as $\mathbf{v}_\mathrm{e} \gg \mathbf{v}_\mathrm{i} \sim \mathbf{v}_\mathrm{N}$. However, the process is very inefficient due to the small electron mass, and therefore it will be henceforth simply neglected setting $\mathrm{d}\mathbf{p}_\mathrm{e}/\mathrm{d}t = 0$, although this might require reconsideration in a detached divertor with $N \gtrsim n$.

Similarly, ion and neutral thermal energy is simply exchanged due to collisions. While momentum dissipation is negligible for electrons, their thermal energy dissipation due to inelastic ionization and recombination is important. Firstly, during ionization thermal energy of the electron fluid is depleted to increase the bound electrons energy (internal atom energy) to the continuum level. Secondly, the neutral atoms are constantly excited and emit energy by spontaneous emission due to electron impact, radiating electron thermal energy away. Both is taken into account by the electron cooling rate coefficients.

In a non-homogeneous plasma, the rate equations (2.45)-(2.49) can be added to the right-hand side of the Braginskii equations (2.1)-(2.3) as source terms. We employ the usual approximation $n = n_\mathrm{e} = n_\mathrm{i}$, setting $Z = 1$ as we only consider pure deuterium reactions (6.1) and (6.2). Further, as detailed in chapter 6.2, the ion-neutrals momentum exchange is considered in the drift-reduction, yielding an additional ion

drift term $\mathbf{u}_{\mathrm{iN}}$, $\mathbf{v}^{\mathbf{i}}_{\perp} \approx \mathbf{v}^{\mathbf{i}}_{0\perp} + \mathbf{u}_{\mathrm{pol}} + \mathbf{u}_{\mathrm{iN}}$. In summary, we obtain the following source terms:

$$S_n = k_{\mathrm{iz}} nN - k_{\mathrm{rec}} n^2 = -S_N, \tag{2.50}$$

$$S_{u_\parallel} = N\left(k_{\mathrm{iz}} + k_{\mathrm{cx}}\right)\left(v_{\mathrm{N}\parallel} - u_\parallel\right), \tag{2.51}$$

$$S_{T_\mathrm{e}} = -\frac{2}{3}\left(W_{\mathrm{iz}} N + W_{\mathrm{rec}} n\right) - \left(k_{\mathrm{iz}} N - k_{\mathrm{rec}} n\right) T_\mathrm{e}, \tag{2.52}$$

$$S_{T_\mathrm{i}} = \left(k_{\mathrm{iz}} + k_{\mathrm{cx}}\right) N (T_\mathrm{N} - T_\mathrm{i}), \tag{2.53}$$

$$S_{T_\mathrm{N}} = k_{\mathrm{cx}} n (T_\mathrm{i} - T_\mathrm{N}) + k_{\mathrm{rec}} \frac{n^2}{N} (T_\mathrm{i} - T_\mathrm{N}), \tag{2.54}$$

$$S_\Omega = \nabla \cdot (n \mathbf{u}_{\mathrm{iN}}) = -\nabla \cdot \left[\frac{m_\mathrm{i} c^2 nN}{eB^2} \left(k_{\mathrm{iz}} + k_{\mathrm{cx}}\right) \left(\nabla_\perp \varphi + \frac{\nabla_\perp p_\mathrm{i}}{en} \right) \right]. \tag{2.55}$$

It is instructive to compare the reaction rates at this point, depicted in figure 2.1. Firstly, we note that the charge exchange rate is the largest one and has the weakest temperature dependence. Recombination is essentially irrelevant above 2 eV, outweighed by ionization. Below 1 eV, it becomes important though. Above 1 eV, the plasma is cooled by ionization, while it is heated up by three-body recombination below 1 eV. Above 20 eV, radiation becomes ineffective and the ionization cooling rate decreases again. At $k_{\mathrm{iz}} > \frac{2}{3} W_{\mathrm{iz}}/T_\mathrm{e}$, the plasma is mainly cooled simply by dilution with cold electrons from ionization rather than by energy dissipation.

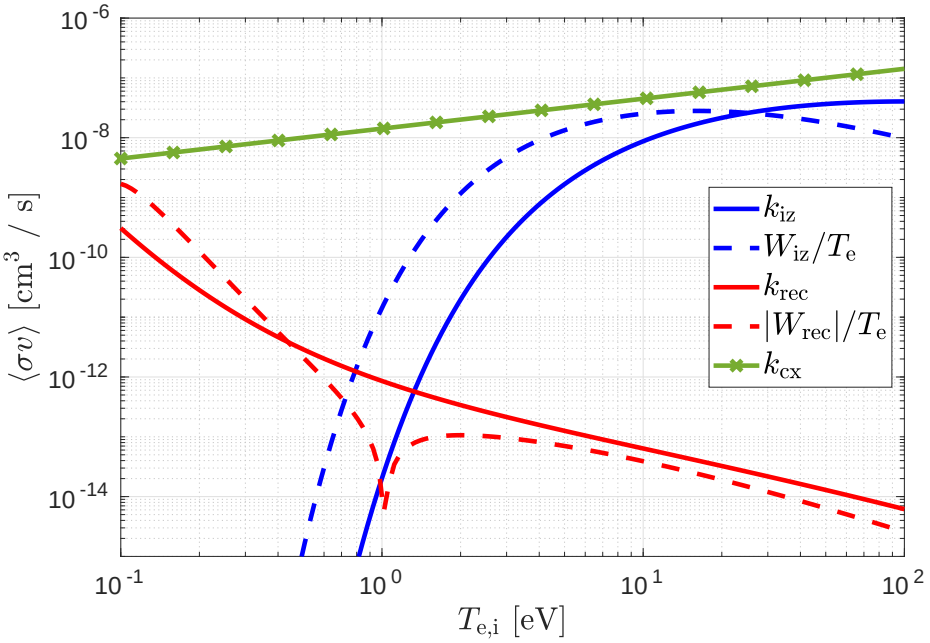

Figure 2.1: Reaction rate coefficients k_{iz} for electron impact ionization, k_{rec} for recombination (including radiative) and k_{cx} for charge exchange as a function of temperature, at constant density $n = 10^{19}$ m^{-3} (particularly recombination becomes more effective at higher density). Also shown are the electron cooling rates divided by T_e, for both ionization and recombination. For W_{rec}, the absolute value is plotted as it becomes negative below 1 eV.

It is a common approach to assume that the charge exchange reaction mixes the velocity space structure of ions and neutrals so efficiently that their temperature is essentially equal [144–146]. For simplicity, we make the same assumption for the parallel velocity, as described in chapter 6.2. We then only require an equation for the evolution of the neutrals density to complete the system, which we obtain from Ref. [145, 146] as

$$\frac{\partial N}{\partial t} = \nabla \cdot \frac{\tilde{D}_N}{T_\mathrm{i}} \nabla N T_\mathrm{i} - k_{\mathrm{iz}} nN + k_{\mathrm{rec}} n^2, \tag{2.56}$$

with the diffusion coefficient

$$D_N = \frac{c_{\mathrm{s,N}}^2}{\nu_{\mathrm{cx}}} = \frac{T_\mathrm{i}/m_\mathrm{i}}{k_{\mathrm{cx}} n}, \qquad \tilde{D}_N = \min\left(D_N, \frac{N T_\mathrm{i} c_{\mathrm{s,N}}}{|\nabla N T_\mathrm{i}|} \right). \tag{2.57}$$

Thereby, $c_{s,N} = \sqrt{T_i/m_i}$ is the neutral gas sound velocity, $m_N \approx m_i$ the neutrals mass and $\nu_{cx} = k_{cx} n$ the charge exchange frequency. The diffusivity is limited such that the resulting particle flux does not exceed sound speed, which otherwise happens in low density regions far from the recycling area, like the top of the device, see chapter 6.2 for more details. The numerical solution of this equation is discussed in section 2.2.4.

2.1.6 The Debye sheath: a boundary layer between the plasma and the wall

The sheath is a tiny region (1-10 µm) of net space charge between the main quasi-neutral plasma and the tokamak wall [49, chapter 2]: due to their small mass, the thermal motion of electrons is much faster than that of ions. Without any confining force, their flux on the tokamak wall would therefore be larger than that of ions, leading to a negative charge of the wall. This, in turn, leads to a build up of an electric field towards the wall – the confining force – accelerating ions and repelling electrons. A stationary state results with a thin layer at the device wall – the sheath – where electrons are less dense than ions, sustaining a significant electric field between the main plasma and the wall that balances electron and ion fluxes to the wall, as sketched in figure 2.2.

The Debye sheath is widely discussed in literature [48, 147–150], yet it remains a significant topic of controversy [151–155]. This is because due to its smallness and breaking of quasi-neutrality, the sheath cannot be directly resolved in codes describing the main plasma dynamics, particularly in 3D. Its effect is therefore typically prescribed via analytical boundary conditions, relying on a number of strong assumptions, but still rather complex and non-linear. Naturally, these assumptions are continuously reviewed and the boundary conditions are being refined. The GRILLIX code is based on a novel numerical scheme, discussed in section 2.2.1, that poses special difficulties in the application of boundary conditions, described in section 2.2.2. Therefore, the physical boundary conditions had to be reviewed, since the numerical discretisation and computational implementation are tightly linked to the physical model.

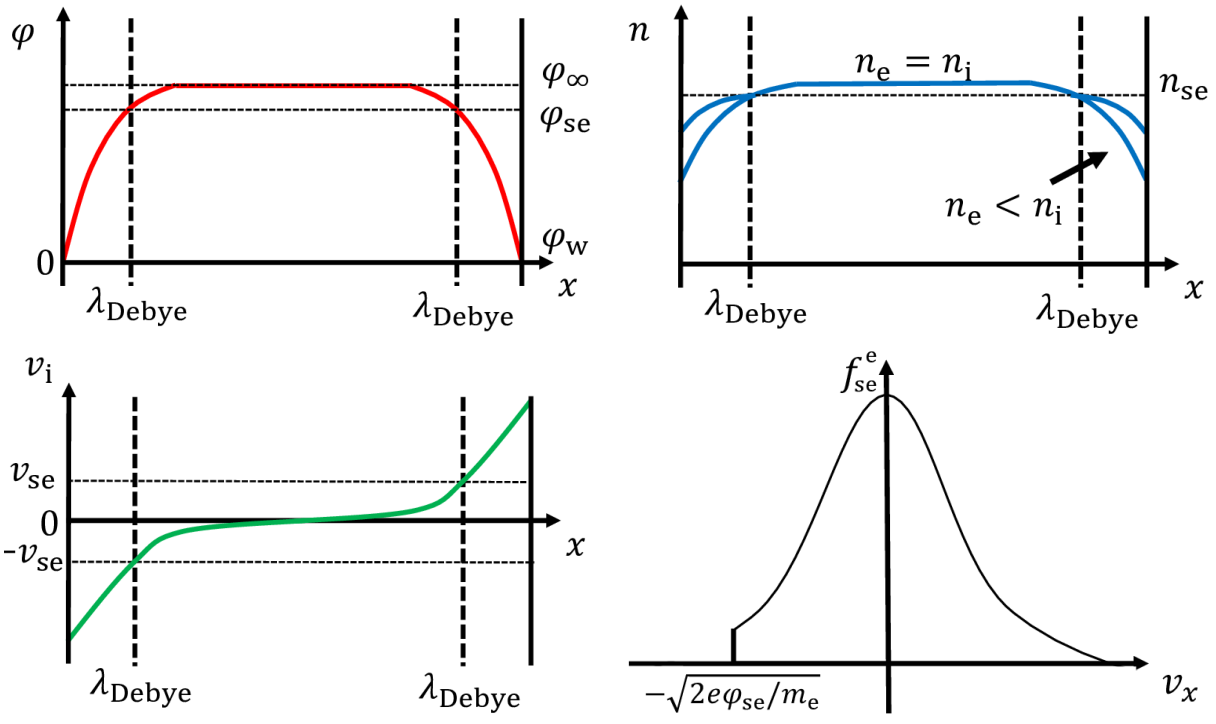

Figure 2.2: A sketch of the classical 1D sheath model: on the scale of a Debye length near a solid wall, the plasma quasi-neutrality is broken and a strong electric field is established to counter the non-ambipolar thermal fluxes of electrons and ions to the wall, accelerating the ions to above sound speed and confining the electrons, except the fast tail of their distribution function. The behaviour is more complicated in a magnetised plasma with a non-orthogonally impinging magnetic field, see text.

The usual description of the sheath is based on a number of strong assumptions: the electric field is assumed to be so strong that the dynamics essentially becomes one dimensional, which is equivalent to

the case when a magnetic field is perpendicular to the wall surface (the transition to the magnetised main plasma is discussed further below). The electric field is also assumed to be monotonic, stationary and electrostatic. Since the sheath is so thin, collisions and sources are judged to be unimportant therein. At the same time, at the interface to the collisional main plasma and due to the confining electric potential, electrons are assumed to be essentially Maxwellian. In this case, their distribution function follows

$$v_x \frac{\partial f}{\partial x} - \frac{eE}{m_\mathrm{e}} \frac{\partial f}{\partial v_x} = 0, \tag{2.58}$$

with the electric field $E = -\partial_x \varphi$. This equation is fulfilled by the solution $f = f^\mathrm{M} \exp\left(\frac{e(\varphi-\varphi_0)}{T_\mathrm{e}}\right)$, where f^M is the 1D Maxwellian distribution function

$$f^\mathrm{M} = n_0 \sqrt{\frac{m_\mathrm{e}}{2\pi T_\mathrm{e}}} \exp\left(-\frac{m_\mathrm{e} v_x^2}{2T_\mathrm{e}}\right), \tag{2.59}$$

and φ_0 is an arbitrary constant. Integrating f over v_x, we obtain the relation between electron density $n_\mathrm{e} = \int f dv_x$ and the electric potential φ,

$$n_\mathrm{e} = n_0 \exp\left(\frac{e(\varphi - \varphi_0)}{T_\mathrm{e}}\right). \tag{2.60}$$

Such electrons are called 'adiabatic'. The same result can be obtained in the fluid picture when the magnetic field, collisional terms and electron inertia are neglected in equation (2.2) or (5.28), in 1D, leaving as the dominant parts

$$0 = -\partial_x p_\mathrm{e} + e n_\mathrm{e} \partial \varphi. \tag{2.61}$$

Let us choose $\varphi_0 = \varphi_\mathrm{se}$, se meaning the sheath entrance, and $n_0 = n_\mathrm{se}$.

We consider the ions next. For simplicity, we consider cold ions with $T_\mathrm{i} \approx 0$, but discuss the generalisation to $T_\mathrm{i} \neq 0$ down below. At every point in the sheath, the steady state particle conservation equation (2.1), $\partial_x n v_\mathrm{i} = 0$, requires $n_\mathrm{i} v_\mathrm{i} = n_\mathrm{se} v_\mathrm{se}$. Further, the momentum conservation equation (2.2), $m_\mathrm{i} n_\mathrm{i} v_\mathrm{i} \partial_x v_\mathrm{i} = -e n_\mathrm{i} \partial_x \varphi$, demands the conservation of kinetic energy, $\frac{1}{2} m_\mathrm{i} v_\mathrm{i}^2 + e\varphi = \text{const}$. At a point far enough from the sheath, we have $v_\mathrm{i} = 0$ and the potential φ_∞, see figure 2.2. Therefore, we can write

$$\frac{1}{2} m_\mathrm{i} v_\mathrm{i}^2 = e\left(\varphi_\infty - \varphi\right). \tag{2.62}$$

Combining these two conservation laws, we obtain

$$n_\mathrm{i} = n_\mathrm{se} \frac{v_\mathrm{se}}{v_\mathrm{i}} = n_\mathrm{se} \sqrt{\frac{\varphi_\infty - \varphi_\mathrm{se}}{\varphi_\infty - \varphi}}. \tag{2.63}$$

Now, we can plug these expressions into Poisson's equation (in SI units)

$$\frac{\mathrm{d}^2\varphi}{\mathrm{d}x^2} = -\frac{e}{\varepsilon_0}\left(n_\mathrm{i} - n_\mathrm{e}\right) = \frac{e n_\mathrm{se}}{\varepsilon_0}\left(\exp\left[\frac{e(\varphi - \varphi_\mathrm{se})}{T_\mathrm{e}}\right] - \sqrt{\frac{\varphi_\infty - \varphi_\mathrm{se}}{\varphi_\infty - \varphi}}\right). \tag{2.64}$$

We are interested in the sheath edge, and so we expand for $\Delta = \varphi_\mathrm{se} - \varphi > 0$ around $\Delta \approx 0$, i.e. just inside the sheath,

$$\frac{\mathrm{d}^2\Delta}{\mathrm{d}x^2} = -\frac{\mathrm{d}^2\varphi}{\mathrm{d}x^2} \approx -\frac{e n_\mathrm{se}}{\varepsilon_0}\left(1 - \frac{e\Delta}{T_\mathrm{e}} - 1 + \frac{\Delta}{2(\varphi_\infty - \varphi)}\right) \tag{2.65}$$

$$= \frac{e n_\mathrm{se} \Delta}{\varepsilon_0}\left(\frac{e}{T_\mathrm{e}} - \frac{1}{2(\varphi_\infty - \varphi)}\right) = \frac{\Delta}{\lambda_\mathrm{Debye}^2}\left(1 - \frac{T_\mathrm{e}}{2e(\varphi_\infty - \varphi)}\right). \tag{2.66}$$

We have introduced the Debye length $\lambda_\mathrm{Debye} = \sqrt{\varepsilon_0 T_\mathrm{e}/e^2 n}$. The equation above describes a harmonic oscillator and only has non-oscillatory solutions of the form $\Delta(x) = \left(1 - \frac{T_\mathrm{e}}{2e\varphi_\mathrm{se}}\right) \mathrm{e}^{-x/\lambda_\mathrm{Debye}}$ if the bracket on the right-hand side is positive, $2e(\varphi_\infty - \varphi) = m_\mathrm{i} v_\mathrm{i}^2 \geq T_\mathrm{e}$. The decay of the potential with λ_Debye is the

reason why the sheath has the size of the Debye length. The positivity of the bracket, i.e. monotonicity condition, yields the well known **Bohm criterion** for the plasma (ions) exit velocity at the sheath edge,

$$v_{\mathrm{se}}^{\mathrm{i}} \geq c_s = \sqrt{\frac{T_{\mathrm{e}}}{m_{\mathrm{i}}}}, \tag{2.67}$$

where c_s is the cold ion sound speed. This means, under all the above assumptions – discussed in chapter 8.3.2 – a stationary and monotonic (non-oscillatory) sheath requires ions leaving the plasma at or above sound speed.

As discussed in [49, chapter 2.4], the above result can be generalised to hot ions, requiring for their distribution function

$$\int_0^\infty \frac{f_{\mathrm{se}}^{\mathrm{i}}(v)\mathrm{d}v}{v^2} \leq \frac{m_{\mathrm{i}}}{T_{\mathrm{e}}}. \tag{2.68}$$

The distribution function is non-Maxwellian, as there can be no backward going ions and it is centred around sound speed. Nevertheless, for their mean velocity one can derive

$$v_{\mathrm{se}}^{\mathrm{i}} \geq \sqrt{\frac{T_{\mathrm{e}} + \gamma_a T_{\mathrm{i}}}{m_{\mathrm{i}}}}. \tag{2.69}$$

A debate remains about the adiabaticity constant γ_a. For a 1D adiabatic flow – which we have assumed throughout the derivation – one should employ $\gamma_a = 3$. However, setting this as a boundary condition for a 3D fluid code usually leads to instability, so in practice all codes including GRILLIX use $\gamma_a = 1$. Experimental measurements of the ion exit velocity are available only at very low electron temperature (3 eV) and even lower ion temperature (1 eV) [151], so a definitive decision can not be made on that matter, experiments however at least do not contradict our choice.

Next, we wish to determine the sheath potential relative to the wall (the wall chosen to be at $\varphi_{\mathrm{w}} = 0$). Consider the flux of ions $\Gamma_{\mathrm{se}}^{\mathrm{i}} = n_{\mathrm{se}} c_s$ at the sheath entrance. Since ions are accelerated through the sheath, the same flux reaches the wall, $\Gamma_{\mathrm{w}}^{\mathrm{i}} = \Gamma_{\mathrm{se}}^{\mathrm{i}}$. Electrons, on the other hand, are confined, and therefore have a roughly Maxwellian velocity distribution. At the wall, all forward flowing electrons are absorbed, so their mean flux is the one-sided Maxwellian flux

$$\Gamma_{\mathrm{w}}^{\mathrm{e}} = \int_0^\infty f^{\mathrm{M}} dv_x = \frac{1}{4} n_{\mathrm{w}} \sqrt{\frac{8T_{\mathrm{e}}}{\pi m_{\mathrm{e}}}} = \frac{1}{4} n_{\mathrm{se}} \exp\left(-\frac{e\varphi_{\mathrm{se}}}{T_{\mathrm{e}}}\right) \sqrt{\frac{8T_{\mathrm{e}}}{\pi m_{\mathrm{e}}}}. \tag{2.70}$$

In the absence of a current through the wall, $\Gamma_{\mathrm{w}}^{\mathrm{e}} = \Gamma_{\mathrm{w}}^{\mathrm{i}}$, we obtain the **floating potential**

$$\frac{e\varphi_{\mathrm{se}}}{T_{\mathrm{e}}} = \Lambda = -\frac{1}{2} \ln\left[2\pi \frac{m_{\mathrm{e}}}{m_{\mathrm{i}}} \left(1 + \gamma_a \frac{T_{\mathrm{i}}}{T_{\mathrm{e}}}\right)\right] \approx 3. \tag{2.71}$$

This is used as the boundary condition for the electrostatic potential at sheath entrance throughout the rest of this thesis.

But what happens if a current does flow through the sheath? And how large is the heat flux through the sheath? To answer these questions, let us define more carefully the electron distribution function at sheath entrance. As argued above, it is roughly a Maxwellian, as electrons find themselves in a confining potential. However, fast enough electrons with $v_x > \sqrt{2e\varphi_{\mathrm{se}}/m_{\mathrm{e}}}$ can escape the confining electric field, conducting heat and current through the sheath. In the backward going tail of the distribution function, these fast electrons are therefore missing, see figure 2.2. Hence, we have

$$f_{\mathrm{se}}^{\mathrm{e}}(\vec{v}) = \begin{cases} \frac{1}{I(\sqrt{\eta_{se}})} \left(\frac{m_e}{2\pi T_e}\right)^{3/2} \exp\left(-\frac{m_e \vec{v}^2}{2T_e}\right) & \text{, if } v_x < -\sqrt{\frac{2e\phi_{se}}{m_e}}, \\ 0 & \text{, else.} \end{cases} \tag{2.72}$$

Note that this velocity distribution function is not normalised to 1, rather we have

$$I = \int_{-\infty}^{\infty}\int_{-\infty}^{\infty}\int_{-\infty}^{\infty} f_{\mathrm{se}}^{\mathrm{e}}(\vec{v})\mathrm{d}v_x\mathrm{d}v_y\mathrm{d}v_z = \frac{1 + \mathrm{erf}\left(\sqrt{\frac{e\varphi_{\mathrm{se}}}{T_{\mathrm{e}}}}\right)}{2}, \tag{2.73}$$

where erf is the error function. For $\varphi_{se} \approx 3T_e$, $I \approx 1$, but at a lower electric field it can matter. However, normalising the distribution function by I would not fulfil the kinetic equation 2.58 any more, so this approach is either way only consistent if φ_{se} is large – otherwise, the assumption of the Maxwellian is not good. On the other hand, in Ref. [152] the normalization is used as a way to connect to the situation with $\varphi_{se} \to 0$, where the Bohm condition does not apply and a large electron current to the wall results. The treatment can even be extended to electron sheaths [153], which might in fact be relevant during (turbulent) transient events. But in a steady state with a grounded wall, there should be no such large currents on average, so ion sheaths are the typical situation and we will ignore the normalisation for now.

We can now compute moments over the above specified distribution function. For the mean electron velocity, we obtain

$$\begin{aligned} v_{se}^e =< v_x >= \int_{-\sqrt{\frac{2e\varphi_{se}}{m_e}}}^{\infty} \mathrm{d}v_x \int_{-\infty}^{\infty} \mathrm{d}v_y \int_{-\infty}^{\infty} \mathrm{d}v_z v_x f_{se}^e(\vec{v}) \\ = \sqrt{\frac{T_e}{2\pi m_e}} \exp\left(-\frac{e\varphi_{se}}{T_e}\right) = c_s e^{\Lambda - \frac{e\varphi_{se}}{T_e}}. \end{aligned} \tag{2.74}$$

With the current $j = en(v_i - v_e)$, we can rewrite this as

$$e\varphi_{se} = \Lambda T_e - T_e \ln\left(\frac{v_{se}^i}{c_s} - \frac{j_{se}}{en_{se}c_s}\right). \tag{2.75}$$

If the ion velocity is around sound speed and the current is zero at sheath entrance, the second term vanishes and we recover the floating potential condition.

Taking the next moment, we obtain an expression for the heat flux

$$\begin{aligned} q_{se}^e = \int_{-\infty}^{\infty}\int_{-\infty}^{\infty}\int_{-\infty}^{\infty} (v_x n)\frac{1}{2} m_e \vec{v}^2 f_{se}^e(\vec{v}) \mathrm{d}v_x \mathrm{d}v_y \mathrm{d}v_z \\ = nc_s \exp\left(\Lambda - \frac{e\varphi_{se}}{T_e}\right)(2T_e + e\varphi_{se}). \end{aligned} \tag{2.76}$$

At $\varphi \to \infty$, the electron particle and heat flux through the sheath goes to zero. For $e\varphi = \Lambda T_e$, which is used throughout this thesis, we obtain $q_{se}^e = 5T_e nc_s$. The physically important insight here is that even in absence of a current, the sheath heat transmission significantly cools the main plasma electrons. A part of this energy, $2T_e nc_s$, reaches the wall – the rest is the energy that sustains the electric field between the sheath entrance and the wall, accelerating the ions.

To use this as a boundary condition, we need to relate this to the main plasma fluid heat flux. It consists of two pieces, the ideal or Maxwellian part

$$q_M^e = \left(\frac{5}{2}T_e + \frac{1}{2}m_e v_e^2\right) n v_e \approx \frac{5}{2} T_e n c_s, \tag{2.77}$$

where we have used $v_e \sim c_s = \sqrt{\frac{T_e + \gamma_a T_i}{m_i}}$ and hence $\frac{1}{2}m_e v_e^2 \sim \frac{1}{2}\frac{m_e}{m_i}(T_e + \gamma_a T_i) \ll T_e$. The second piece is the non-Maxwellian Braginskii heat flux

$$q_B^e = -0.71\frac{T_e}{e} j_\parallel - \chi_\parallel \nabla_\parallel T_e \approx -\chi_\parallel \nabla_\parallel T_e. \tag{2.78}$$

Here, we assume again that the (parallel) current through the sheath is zero. Note that we have used the component of the Braginskii heat flux parallel to the magnetic field, as will be clarified below.

Putting these pieces together,

$$q_M^e + q_B^e = q_{se}^e, \tag{2.79}$$

we obtain a Robin boundary condition for the temperature, with $\gamma_e = 2.5$,

$$-\chi_\parallel \nabla_\parallel T_e = \gamma_e T_e n c_s, \tag{2.80}$$

whereby the sign has to be flipped if the magnetic field points out of the wall. We note that a more detailed investigation of the sheath would allow the coefficient γ_e to vary, depending for example on the

sheath current and secondary electron emission [49, chapter 25.5]. For the ion sheath heat transmission, the situation is more complicated because their distribution function is not Maxwellian. Therefore, for the sake of simplicity, we take $\gamma_i \approx 0$.

It remains to discuss how the 1D sheath model connects to the 3D plasma model, particularly in a magnetic field that is more tangential than perpendicular to the wall surface. This has been first analysed by Chodura [48] and summarised by Stangeby [49, chapter 2.10], as depicted in figure 2.3. It was found that a new region forms between the sheath and the main plasma, the magnetic pre-sheath, that has the thickness of a few ion Larmor radii and is quasi-neutral, but where the ion gyro-motion continuously breaks down transitioning to the unmagnetised sheath.

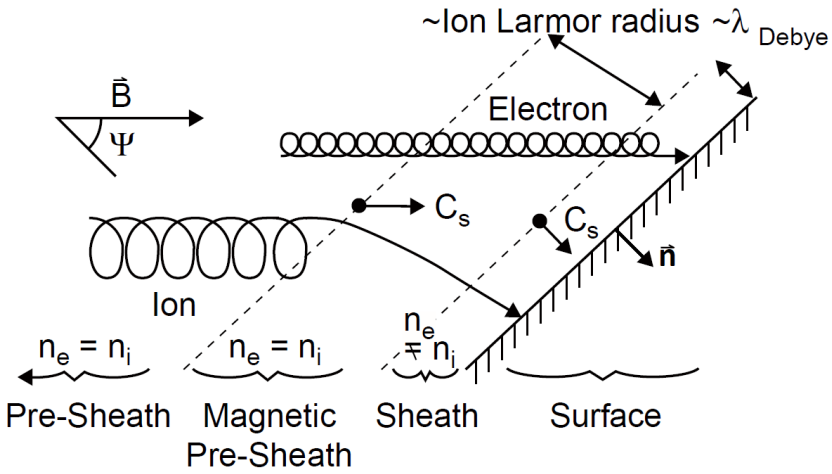

Figure 2.3: Chodura's analysis of the plasma-wall transition region for the case of **B** oblique to the surface [48], as summarised by Stangeby [49, chapter 2.10]. Adapted from [49].

As a result, sheath boundary conditions are to be applied on the flow along the magnetic field at the magnetic pre-sheath entrance, as it therein becomes the 1D sheath flow and the plasma upstream essentially does not feel whether the wall is perpendicular or oblique to the magnetic field. At the same time, the heat flux density incident on the wall can be reduced by a shallow magnetic field, hence this is the standard situation in fusion experiments. We therefore have the Bohm-Chodura boundary condition on the parallel ion flow

$$u_\parallel \mathbf{b}\cdot\mathbf{n} \geq c_s \left|\mathbf{b}\cdot\mathbf{n}\right|, \tag{2.81}$$

with the unit magnetic field vector **b** and the surface normal vector **n** (pointing outside of the domain) indicating the sign of the parallel velocity. Note that many authors, e.g. [150], require exactly sound speed at the sheath entrance – but we do not, as this is only strictly necessary in an isothermal plasma and in our experience rather leads to numerical problems.

The importance of the Bohm-Chodura condition for the main plasma is that the ion flow needs to be above some threshold for a non-oscillatory sheath potential, as oscillations on the Debye length or Larmor radius scale would be in strong contrast to the usual flute mode character of plasma fluctuations $k_\perp \gg k_\parallel$. The floating potential boundary condition $e\varphi_{se} = \Lambda T_e$ (2.71), with respect to the wall at $\varphi_w = 0$ and in absence of currents, is required to maintain the quasi-neutrality of the main plasma. And energetic consistency requires a cooling effect on the electrons, $\mp\chi_\parallel \nabla_\parallel T_e = \gamma_e T_e n c_s$ (2.80), which we already formulated for the parallel flow. The implementation of these constrains as boundary conditions in GRILLIX is discussed in section 2.2.2.

However, the exact numbers in these conditions are yet under debate [154]. Chodura himself [48] concludes that the many approximations met in the derivation are likely too strong, and the reality is more complex. In particular, he notes that so far only the 1D flow was considered (parallel to the magnetic field), and elastic collisions as well as inelastic collisions with the neutral gas were neglected. Additionally, we have remarked some caveats in the derivation above. Therefore, the discussion of sheath boundary conditions – outside the scope of the present thesis – is continued in chapter 8.3.2.

2.1.7 Normalisation

Before we proceed to the discretisation, we have to discuss the normalization of our equations. Similar as with the Reynolds number in Navier-Stokes equations, it serves to identify the minimal set of dimensionless physical parameters governing the system. Normalising the equations eliminates unnecessary variations in the magnitude of quantities, leaving only the actual physical disparity. Computationally, this has the benefit that numerical rounding errors are minimized.

For the plasma, the normalisation has been discussed in previous publications, and lastly summarised in chapter 5.7. Here, we will focus on the neutrals model, but it is not independent from the plasma. Firstly, some reference values are chosen (in CGS units),

$$\mathbf{B} = B_0\hat{\mathbf{B}}, \qquad n = n_0\hat{n}, \qquad T_\mathrm{e} = T_{\mathrm{e}0}\hat{T}_\mathrm{e}, \qquad T_\mathrm{i} = T_{\mathrm{i}0}\hat{T}_\mathrm{i}. \tag{2.82}$$

The hat indicates dimensionless quantities. The reference magnetic field B_0 is typically chosen at the magnetic axis, R_0 is the machine major radius and reference temperature and densities are typically chosen at the OMP separatrix. The reference values cancel out in most of the terms in the equations, leaving only dimensionless quantities and some dimensionless parameters. Next, we define a reference (sound) velocity, the reference sound Larmor radius, and with them the reference time and space scales:

$$c_{s0} = \sqrt{\frac{T_{\mathrm{e}0}}{m_\mathrm{i}}}, \qquad \rho_{s0} = \frac{c_{s0}}{\omega_\mathrm{ci}} = \frac{c\sqrt{T_{\mathrm{e}0}m_\mathrm{i}}}{eB_0}, \qquad t = \frac{R_0}{c_{s0}}\hat{t}, \qquad x_\parallel = R_0\hat{x}_\parallel, \qquad \mathbf{x}_\perp = \rho_{s0}\hat{\mathbf{x}}_\perp. \tag{2.83}$$

Proceeding like this (also for the electromagnetic fields, see chapter 5.7) results in essentially six dimensionless plasma parameters: the drift scale $\delta_0 = R_0/\rho_{s0}$, the dynamical plasma beta $\beta_0 = 4\pi n_0 T_{\mathrm{e}0}/B_0^2$, the electron to ion mass ratio $\mu = m_\mathrm{e}/m_\mathrm{i}$, the temperature ratio $\zeta = T_{\mathrm{i}0}/T_{\mathrm{e}0}$, and the electron and ion collisionalities $\nu_0^{\mathrm{e,i}} = R_0/(c_{s0}\tau_0^{\mathrm{e,i}})$. For the latter, the collision times τ_e defined in (2.4) and τ_i in (2.5) are evaluated at reference temperature and density and normalised to R_0/c_{s0}.

Note that the choice of B_0 and R_0 is machine specific, and constitutes important input parameters. The choice of a reference density and temperature, on the other hand, is arbitrary in a global code since the non-linearity of all parameters is fully retained: dimentionless quantities simply change in accordance with the dimentionless parameters. The only exception is the Coulomb logarithm, whose spatial and temporal variation is not taken into account, but is usually very small. Nonetheless, a reasonable choice of n_0 and T_0 usually helps with the simulation setup, as the calculated parameters point towards the expected dynamics, and minimizes rounding errors.

For the neutrals, we adapt the normalization to the plasma. For instance, we choose the same reference density, $N = n_0\hat{N}$. The plasma-neutrals interaction terms are normalized as

$$\sigma = \frac{\hat{\sigma}}{R_0 n_0}, \qquad \langle\sigma v\rangle = k = k_0\hat{k} = \frac{c_{s0}}{R_0 n_0}\hat{k}, \qquad W = W_0\hat{W} = \frac{c_{s0}}{R_0}\frac{T_0}{n_0}\hat{W}. \tag{2.84}$$

Importantly, there are two peculiarities. Firstly, the atomic databases prescribe specific units for input and output: density in cm^{-3} (cgs), temperature in eV and rate coefficients in cm^3/s. Therefore, while the equations inside GRILLIX are dimensionless, 4 inputs must be provided for the interface to the databases: n_0 [cm^{-3}], $T_{\mathrm{e}0}$ [eV], k_0 [cm^3/s] and W_0 [eV cm^3/s]. Additionally, to facilitate future applications to other plasmas than deuterium, the CX cross section has to be provided – but in normalised units, $\hat{\sigma} = \sigma R_0 n_0$. Lastly, for the calculation of the recombination cooling rate from the radiation rate, $W_\mathrm{rec} = P_\mathrm{rec}^\mathrm{rad} - E_\mathrm{iz}\cdot k_\mathrm{rec}$, the ionization energy E_iz must be provided in eV (13.6 for deuterium).

The second peculiarity is the fact that unlike the plasma, the neutral gas diffuses isotropically according to equation (2.56), as it is not influenced by the magnetic field. However, the spatial directions perpendicular and parallel to the magnetic field are normalized differently in GRILLIX. This is physically important: as explained in the following sections, due to the anisotropy in the plasma dynamics its motion is highly field-aligned, facilitating a great grid sparsification in the parallel, respectively in GRILLIX in the toroidal direction – while the perpendicular / poloidal grid has to resolve the Larmor radius scale. Even though the neutrals are not field aligned, we expect them to follow the plasma to some degree. Therefore, it is justified to treat them on the same grid, hence discriminating between the poloidal and the toroidal directions. Nonetheless, since the motion is isotropic we only need to normalise the diffusion coefficient to the parallel motion as $D_N = R_0 c_{s0}\hat{D}_N$. This is further discussed in section 2.2.4.

2.2 The numerical discretisation

GRILLIX aims at global predictive turbulence simulations for fusion experiments and reactors in general, and particularly for tokamaks. One of the key pathways for tokamak optimisation is the shaping of the magnetic field **B**, and thus it is crucial to perform turbulence simulations in a faithful representation of the experimental magnetic geometry. For simulations of the plasma boundary, this means in particular that the magnetic separatrix between the confined plasma and open field lines must be respected.

At the same time, plasma dynamics is highly anisotropic due to the Lorentz force ($\mathbf{v} \times \mathbf{B}$) in eq. (2.2). Analytically, in section 2.1.1 we have taken advantage of the dominance of this term by drift-reduction, approximately solving eq. (2.2) in the plane perpendicular to **B**. The flute mode character $k_\perp \gg k_\parallel$ of plasma turbulence, the fact that dynamics along the magnetic field is much faster than in the drift plane, manifests in structures highly elongated along **B**. Numerically, this can be exploited by an anisotropic grid: choosing coordinates such that one of the three spatial directions is aligned with the magnetic field, the grid can remain sparse in that direction, since only small gradients are expected [156]. The advantage in computational cost is at least quadratic in the parallel grid resolution, as will be shown below.

However, field alignment of the computational grid for general magnetic geometries is a non-trivial task and requires some special numerical techniques. Luckily, we can build on the ground-breaking work by Andreas Stegmeir [119], as explained in the following section 2.2.1. During the present dissertation, the numerical tool kit of GRILLIX was extended by a general matrix-free 3D iterative solver, as detailed in section 2.2.3 and chapter 3, allowing to treat parts of the parallel dynamics implicitly and computationally efficiently within the FCI approach. A persistent challenge in boundary plasma modelling in general, and GRILLIX in particular, is the treatment of boundary conditions, as discussed in section 2.2.2. Finally, the numerical discretisation is verified via the method of manufactured solutions (MMS), presented in section 2.2.5.

2.2.1 The FCI approach

Field-aligned simulations of turbulence in magnetised plasmas are being performed since the 90s [157, 158] and continuously refined [159]. However, only since the 2013 pioneering work by Hariri and Ottaviani [160] the field-aligned approach could be extended to arbitrary magnetic geometries with X-points, where the poloidal magnetic field becomes zero, called the flux-coordinate independent (FCI) field-aligned approach. The basic idea is to choose the toroidal angle as the field-aligned coordinate instead of the poloidal angle, that becomes ill defined if the poloidal magnetic field vanishes, i.e. sparsifying the toroidal direction of the grid.

In detail though, as discussed in [119, appendix A], globally field-aligned coordinates must be abandoned because the safety factor q can not be computed at the separatrix. Instead, parallel derivatives in GRILLIX are computed directly via a local field line map [161]: for every point in a poloidal plane k, as shown in figure 2.4, its neighbours on adjacent planes are found via field-line tracing and derivatives are computed via finite differences across these points. Abandoning globally field-aligned coordinates, within the poloidal plane a simple Cartesian mesh can be used, the grid overall being cylindrical with the toroidal angle φ. In general, neighbouring points along a field line do not lie on the Cartesian grid though, requiring a combination of interpolation and integration techniques to map between field lines and the grid. Spurious perpendicular diffusion is thereby suppressed by careful construction of adjoint operators $\nabla_\parallel^\dagger = -\nabla \cdot [\mathbf{b}\circ]$, such that the eigenvalue spectrum of parallel diffusion is kept real [161, 162]. Importantly, diffusive stabilisation of parallel advection schemes must also be done explicitly via support operators. The field line map procedure is equivalent to choosing a locally field-aligned coordinate system on plane k [116]. Note that the resulting coordinate system is not orthogonal, i.e. the poloidal plane does not exactly correspond to the drift plane perpendicular to **B**. However, for $B_{\text{tor}} \gg B_{\text{pol}}$ this is a good approximation that is kept throughout our work.

GRILLIX was one of the first codes that successfully adapted the FCI approach for efficient turbulence simulations in diverted geometry. It is now able to treat arbitrary axisymmetric numerically prescribed equilibria [118], and its physical model is continuously extended, allowing by now realistic simulations of e.g. ASDEX Upgrade, see chapter 6. But the FCI approach is becoming more and more popular, and is adapted in various other codes. The FELTOR code combines discontinuous Galerkin

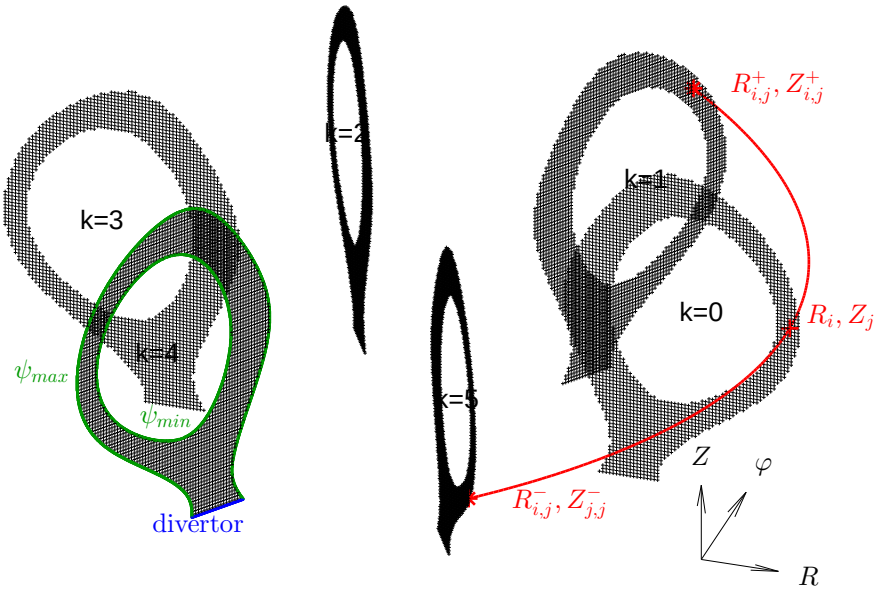

Figure 2.4: Illustration of the flux-coordinate independent (FCI) field-aligned discretisation, taken from [106].

methods with FCI parallel discretisation [163] for e.g. gyro-fluid blob propagation studies [164]. GDB implements FCI only in circular geometry, but in return it has a very efficient computational implementation with 3D MPI decomposition, allowing highly resolved simulations [103]. Unlike for tokamaks, axisymmetry cannot be assumed for stellarators, and indeed it must not be with FCI – this has been explored in BOUT++ with the extension BSTING [165][‡]. Also continuum gyrokinetic codes are starting to adapt FCI[§]. GENE-X is even built on the same framework as GRILLIX, sharing a lot of the code structure, including e.g. parallel operators and elliptic solvers [116]. GYSELA is combining FCI with semi-Lagrangian methods [166]. Finally, COGENT combines FCI with a flux surface aligned multiblock grid, allowing to somewhat sparsify also the poloidal direction [114]. Therefore, we can conclude that in recent years the FCI methods has evolved from a numerical experiment to the standard discretisation method for continuum turbulence simulations in the plasma edge.

2.2.2 Boundary conditions

A set of partial differential equations describes the dynamics of a system within a spatial and temporal domain, but requires additional constrains at the domain boundaries. The initial state, i.e. boundary conditions in time, is described in chapter 5.3.1. In a code designed for dealing with arbitrarily complex geometries, the enforcement of complex boundary conditions in space constitutes a particular challenge. This section describes the boundary conditions we chose for GRILLIX simulations in chapters 3-6.

There is a number of difficulties in choosing the boundary conditions in space, probably the most severe of which is that the set of partial differential equations we solve is non-linear and contains elliptic, parabolic and hyperbolic parts, such that it is not even clear what the set of boundary conditions should exactly comprise of, i.e. which quantities require boundary conditions and which do not. For example, in linear advection problems there should be no boundary conditions at the domain boundary towards which the flow velocity points, i.e. advective outflow of a fluid depends only on the fluid velocity itself.

The approach currently taken in GRILLIX is to prescribe boundary conditions on each dynamic quantity, plus the quantities in elliptic equations: plasma density, vorticity, parallel velocity, parallel current, electron and ion temperatures, electrostatic and parallel electromagnetic vector potentials, see appendix 5.7 in chapter 5. In all three directions in space, i.e. parallel and perpendicular to the magnetic field, either Dirichlet, Neumann or Robin (a combination of Dirichlet and Neumann) boundary conditions are prescribed on these eight quantities.

[‡]It must be noted that for tokamak geometry, even in divertor configurations, BOUT++ continuous to employ standard field-aligned grids [100], even though the X-point must be treated as an exceptional point.

[§]Field-alignment is less of an issue in particle-in-cell (PIC) simulations, where particle motion is discretised by statistical sampling and a spatial grid is required only for the fields.

A challenge in choosing boundary conditions at physical boundaries is that between the quasi-neutral plasma our drift-reduced fluid equations describe and the device walls, we expect the existence of a Debye sheath, see section 2.1.6. There, all our assumptions on the main plasma dynamics break down. Therefore, boundary conditions are in truth applied not at device walls, but at the entrance to the magnetic pre-sheath. The effect of the sheath on the confined plasma is described by non-linear boundary conditions on parallel plasma velocity, current and electrostatic potential. But, as the physics of the sheath is an open field of research, there remains room for experimentation and improvements, as discussed in section 8.3.2.

The second challenge lies in the complex geometry of a tokamak. In mean field modelling, significant efforts are spent in a realistic wall shape representation [98, 167]. But in turbulence simulations, we bypass this complexity for now by limiting the domain radially at some flux surface not touching the wall, see figure 2.5. Radial boundary conditions are applied at that flux surface, but since it does not radially intersect the wall, sheath boundary conditions are not exactly applicable (see also [49, chapter 25.2]). Sheath boundary conditions are instead used where the grid intersects the wall in parallel direction, at the divertor, that is assumed to be the main location of plasma-wall interaction. At the radial boundaries, we simply want to avoid fluxes through it and redirect the plasma to the parallel boundary. But this is not an easy task. A buffer zone with strong diffusion (near the CFL limit) is used near radial boundaries, such that fluxes are mostly governed by this diffusion and can be set radially to zero by homogeneous Neumann boundary conditions,

$$\partial_\rho n = 0, \qquad \partial_\rho T_{\mathrm{e,i}} = 0, \qquad \partial_\rho u_\parallel = 0, \qquad \partial_\rho j_\parallel = 0, \qquad A_\parallel = 0, \qquad \Omega = 0. \tag{2.85}$$

Vorticity is set to zero to damp turbulence.

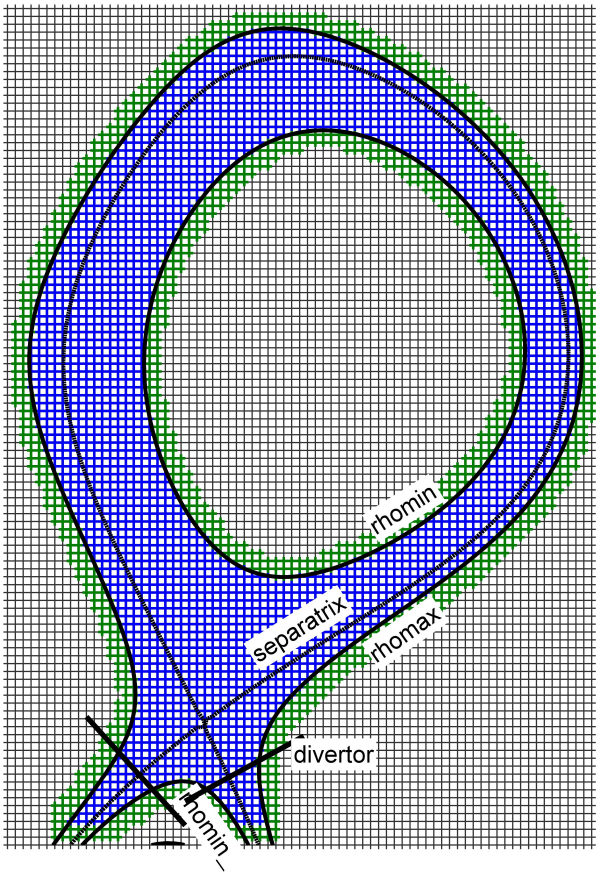

Figure 2.5: The Cartesian poloidal grid in GRILLIX. The actual grid (blue) is obtained from the logical rectangular grid (grey) by keeping only points within limiting flux surfaces (rhomin, rhomax). The perpendicular ghost grid (green) surrounds the actual grid up to a certain depth (here, 2 points). Note that the grids also extend beyond divertor plates as parallel boundaries are realized via the penalisation approach. Depicted by courtesy of Andreas Stegmeir, personal communication, May 2021.

The electrostatic potential deserves a dedicated discussion. The largest velocity in the system is

typically the $E \times B$ velocity, that can be still significant even in a buffer zone. Yet, physically, it is not obvious what the potential should be at radial boundaries. A radial $E \times B$ flux can be avoided if a poloidally constant Dirichlet boundary condition is set on the potential. However, what should the value be at the artificial core boundary? The self-consistent global evolution of the electric field is less inhibited with a Neumann boundary condition, but this can lead in turn to spurious fluxes through the boundary. The solution is a zonal Neumann boundary condition [103],

$$\partial_\rho \langle \varphi \rangle_\theta = 0 \text{ and } \varphi = \langle \varphi \rangle_\theta . \tag{2.86}$$

First, homogeneous Neumann boundary conditions are applied locally within the elliptic solve. The value of the electrostatic potential is then averaged over the core boundary and used as a Dirichlet boundary condition in a second solve. At the outer radial boundary, we assume that the flux surface is close enough to the actual wall such that the potential is roughly given by sheath boundary conditions. The isolating sheath floating potential $\varphi = \Lambda T_\mathrm{e}$ is not necessarily exactly constant over the flux surface, but due to the fast parallel electron heat conduction and buffer diffusion the resulting poloidal potential gradient is typically small enough such that the $E \times B$ flux through the radial boundary can be neglected.

For parallel sheath boundary conditions at the divertor, recall figure 2.4: parallel operators are computed via interpolation between poloidal grid points on neighbouring poloidal planes along the intersection of magnetic field lines. As discussed in the previous section, our goal is to use as few poloidal planes as possible to save computational resources. However, the resulting grid anisotropy means that the divertor is never locally intersected by parallel operators, but rather there is a significant jump of the parallel stencil over the divertor location deeper into the divertor leg, where in reality the wall resides.

Generally, this is not a numerical problem because those points behind the divertor (in parallel direction) could be used as ghost points, not physical points: they could be simply set such that certain boundary conditions are fulfilled exactly at the divertor location. This implementation was indeed used back in 2017 [162]. However, technically the implementation is rather cumbersome because parallel stencils are usually computed via interpolation to the poloidal grid, i.e. involving multiple grid points, and because the location of the divertor boundary between poloidal planes (in parallel direction) strongly varies between grid points, often resulting in a small set of points with a badly balanced (too short) stencil. An exceptional treatment is possible, but hard to generalise for automatic grid creation. Additionally, the usage of staggered grids for parallel advection [106] leads to a decoupling between neighbouring field lines depending on whether the divertor boundary is crossed between full and staggered, or staggered and full grid. We will skip the details of these issues at this point and only present the applied solution: the volume penalisation technique [103, 168].

Penalisation is applied in GRILLIX since 2019 and is described in detail in Ref. [107]. The evolution equations of all dynamic quantities and potentials are modified according to

$$\frac{\partial}{\partial t} f = (1 - \chi_p) F_f + \frac{\chi_p}{\varepsilon_p} (f_p - f) . \tag{2.87}$$

F_f is thereby the original right-hand side of the equation and χ_p is a mask function that is 0 inside the actual computational domain and 1 at the boundary, i.e. behind the divertor leg. ε_p is a small number, hence strong damping is applied on f inside the penalisation region forcing it towards the penalisation value f_p. It is easy to apply Dirichlet boundary conditions in this way, but also Neumann boundary conditions can be and are applied [107]. Using a smooth χ_p that transitions from 0 to 1 not across one, but a few poloidal planes also solves the problem with staggered grids decoupling, but smears the application of sheath boundary conditions out in the poloidal direction (see figure 5.1). The drawback of the approach is that a numerical error of order $O(\Delta s, \Delta t)$ is introduced in the application of boundary conditions, i.e. linear in time and parallel grid resolution. The time error is decreased with ε_p, but a finite time step is only stable with a finite ε_p. Further, at a finite χ_p width, a too small ε_p increases the error as it forces f towards f_p too early in front of the divertor. The space error is a severe issue for the FCI approach, because it only goes down with a larger number of poloidal planes – exactly the opposite of what we are trying to do with FCI. Nonetheless, considering also the inherent physical uncertainties of sheath boundary conditions, a stable and satisfactory method is obtained that is flexible and simple,

which allows to set sheath boundary conditions (in normalised form)

$$u_\parallel \gtrless \sqrt{T_\mathrm{e}+T_\mathrm{i}}, \quad j_\parallel = 0, \quad \varphi = \Lambda T_\mathrm{e}, \quad \nabla_\parallel T_\mathrm{e} = -\frac{\gamma_\mathrm{e}}{\left(\chi_{\parallel \mathrm{e}0} T_\mathrm{e}^{5/2}\right)} T_\mathrm{e} n u_\parallel, \quad \nabla_\parallel T_\mathrm{i} = 0, \quad \nabla_\parallel n = 0, \quad \nabla_\parallel \Omega = 0. \tag{2.88}$$

In comparison to experimental measurements and other codes, our simulations produce rather satisfying results even close to the divertor targets [155], indicating that the numerical error introduced by the penalisation method is reasonably small compared to other more important mechanisms.

2.2.3 Semi-implicit time discretisation for the parallel diffusion terms

As discussed in section 2.3.1, the parabolic part of the equations sets the most severe constrains on an explicit time step. The strongest constraint comes from the electron heat conductivity in equation (2.27),

$$\frac{\partial T_\mathrm{e}}{\partial t} \sim \frac{2}{3}\frac{\chi_{\parallel \mathrm{e}0}}{n} \nabla \cdot \left(T_\mathrm{e}^{5/2} \mathbf{b} \nabla_\parallel T_\mathrm{e} \right). \tag{2.89}$$

Note that all quantities are normalised. However, a high temporal resolution of parallel diffusion is unnecessary. Therefore, an efficient implicit treatment of these terms is attractive. Their discretisation has been concisely discussed in chapter 3, while this chapter aims to provide a few more important background and technical details.

The drift-reduced Braginskii set of equations is interesting and challenging to solve because it contains hyperbolic, elliptic and parabolic terms. The parabolic terms results from the Braginskii fluid closure rather than from the fluid Lagrangian. These are obviously the parallel electron and ion heat conductivities and ion viscosity. But also, in the electrostatic limit (low β and electron inertia), the Ohm's law (2.25) inserted into the vorticity equation (2.20) gives a diffusion term for the electrostatic potential due to resistivity. At finite β, this does not restrict the time step though. As parabolic operators have some strong and important properties, such as a real eigenvalue spectrum, it is important to keep these properties on the discrete level. While this is often automatically achieved in simple discretisation schemes on regular domains, e.g. finite differences in a Cartesian slab, the FCI approach requires some additional work – the support operator method [106, 161, 162].

Also the time discretisation must be chosen with care. GRILLIX employs the Karniadakis scheme [169], a variant of Adams-Bashforth / BDF3. It evolves a quantity f, subject to $\partial_t f = F(f)$, from time t to $t+1$ according to

$$f^{t+1} - \frac{6}{11}\Delta t F_\mathrm{im}^{t+1} = \frac{6}{11}\Delta t \left(3F_\mathrm{ex}^{t} - 3F_\mathrm{ex}^{t-1} + F_\mathrm{ex}^{t-2}\right) + \frac{18}{11} f^t - \frac{9}{11} f^{t-1} + \frac{2}{11} f^{t-2}, \tag{2.90}$$

The scheme was introduced to edge turbulence simulations by Naulin [170] and is suggested by Scott [171] due to the very good conservation properties in combination with the Arakawa scheme for drift-plane advection [172], having minimal intrinsic numerical dissipation and hence allowing precise control of dissipation via hyper-diffusion. Being a third order multi-step scheme, it has a relatively high order of convergence while requiring only one evaluation of the right-hand side (RHS) per time step, and the multiple stored time steps provide a good initial guess for elliptic solvers by extrapolation. The scheme is semi-implicit: hyperbolic parts of the equations can be advanced explicitly, while parabolic parts can be solved implicitly (see also chapter 3.3). However, the scheme is less stable than e.g. 4th order Runge-Kutta for the explicit part, requiring a factor 3-4 smaller time-step (balanced out computationally by a factor 4 fewer RHS evaluations per time step). For the implicit part, the scheme is not A-stable, so only small imaginary eigenvalues are tolerated. The real eigenvalue spectrum of the parabolic terms must be therefore preserved, achieved via the support operator method.

Then, discretising the heat diffusion equation (2.89) essentially yields the linear system

$$\left[1 - \frac{6}{11}\Delta t \frac{\chi_{\parallel 0}}{n^t} \nabla \cdot \left(T^t\right)^{5/2} \mathbf{b} \nabla_\parallel \right] T^{t+1} = \frac{18}{11} T^t - \frac{9}{11} T^{t-1} + \frac{2}{11} T^{t-2} + \frac{6}{11}\Delta t \left[3F_\mathrm{ex}^t - 3F_\mathrm{ex}^{t-1} + F_\mathrm{ex}^{t-2}\right] \tag{2.91}$$

to be solved, as discussed in chapter 3.3. Furthermore, basically the same linear system is solved not just for electron and ion parallel heat conduction, but also for parallel viscosity, the first part of the bracket in eq. (2.31), except that the parallel gradient and parallel divergence are swapped and $B^{3/2}$ factors appear. The system can also be written as $\mathbf{A}\mathbf{T}^{t+1} = \mathbf{R}$, with the vector $\mathbf{T}^{t+1}$ containing discrete temperature values at the next time step. $\mathbf{A}$ corresponds to the operator on the left-hand side of (2.91), $\mathbf{R}$ contains the explicit RHS. However, additionally it is crucial to correctly enforce boundary conditions, which is not trivial with FCI. As discussed in chapter 2.2.2 and Ref. [107], parallel boundary conditions at the sheath entrance at the divertor are enforced via the penalisation method, eq. (2.87). The term $(1-\chi_p)$ enters both the explicit and implicit RHS, $\frac{\chi_p}{\varepsilon_p}T_p$ is absorbed in the explicit RHS $F_mathrmex^t$ or $\mathbf{R}$, and $-\frac{\chi_p}{\varepsilon_p}T$ is treated implicitly. Note that T_p for electrons non-linearly depends on T, which we take explicitly from the previous time step. Also, the resulting steep parallel T_e gradient tends to deteriorate the condition number of $\mathbf{A}$. Then, $\mathbf{A}$ becomes

$$\mathbf{A} = 1 + \frac{6}{11}\Delta t\frac{\chi_p}{\varepsilon_p} - \frac{6}{11}\Delta t(1-\chi_p)\frac{\chi_{\parallel 0}}{n^t}\nabla\cdot(\mathbf{T}^t)^{5/2}\mathbf{b}\nabla_\parallel. \tag{2.92}$$

Additionally, ghost points must be set at perpendicular (poloidal) boundaries [106]. For a grid with k inner points and m ghost points, $\mathbf{A}$ has dimension $k\times(k+m)$ and the k rows correspond to the discrete linearised operator on the left-hand side of (2.91). The other m rows of the linear system are prescribing perpendicular boundary conditions, Dirichlet or Neumann, according to $\mathbf{B}^{(\mathbf{D},\mathbf{N})}\mathbf{T}^{t+1} = \mathbf{T}^{(0,1)}_{\partial V}$, with connectivity matrices $\mathbf{B}^{(\mathbf{D},\mathbf{N})}$ of size $m\times(k+m)$ and Dirichlet values or Neumann gradients $\mathbf{T}^{(0,1)}_{\partial V}$. To simplify notation, we will use from here on $\mathbf{A}$ for the whole $(k+m)\times(k+m)$ system, including perpendicular boundary conditions, and not just (2.92).

Note that unlike in field-aligned codes [100], with FCI the parallel diffusion problem (even with fixed $\mathbf{b}$) cannot be treated as a multi-1D problem, because the operators $\nabla_\parallel$ and $\nabla\cdot\mathbf{b}\circ$ have a non-trivial connectivity, so $\mathbf{A}\mathbf{T}^{t+1} = \mathbf{R}$ requires a 3D solve. With electromagnetic flutter, $\mathbf{b}\to\mathbf{b}+\tilde{\mathbf{b}}$, parallel diffusion anyway becomes a 3D problem though. However, the matrix $\mathbf{A}$ is sparse, and the number of toroidal planes and hence the problem size remain bounded thanks to FCI. Nonetheless, matrix-free iterative methods as discussed in section 2.3.3 are preferable because the 3D matrix is very large even in sparse formats.

2.2.4 Neutrals dynamics

Among the key extensions implemented in GRILLIX during this thesis is a neutral gas model and its interaction with the plasma, as discussed in chapters 6 and 2.1.5. Compared to the plasma, there are a few peculiarities in the discretisation of the neutrals due to their different behaviour, in particular due to their insensitivity to electromagnetic fields. This becomes clear starting with the normalisation in section 2.1.7: although the neutrals diffusion equation is isotropic, due to the field aligned character of the plasma motion the parallel and perpendicular directions, respectively poloidal and toroidal in GRILLIX, are normalized differently. Therefore, the neutrals diffusion equation in dimensionless units, dropping the hats for clarity, becomes

$$\frac{\partial N}{\partial t} = \frac{\delta_0^2}{R}\nabla_\perp\cdot R\frac{D_N(n,T_\mathrm{i})}{T_\mathrm{i}}\nabla_\perp NT_\mathrm{i} + \frac{1}{R^2}\partial_\varphi\frac{D_N(n,T_\mathrm{i})}{T_\mathrm{i}}\partial_\varphi NT_\mathrm{i} - k_\mathrm{iz}(n,T_\mathrm{e})nN + k_\mathrm{rec}(n,T_\mathrm{e})n^2. \tag{2.93}$$

We have introduced here the cylindrical coordinate system as depicted in figure 2.4: $\nabla_\perp = \mathbf{e}_R\partial_R + \mathbf{e}_Z\partial_Z \approx -\mathbf{b}\times\mathbf{b}\times\nabla$ is the gradient in the poloidal plane, which for the plasma approximates the drift-plane gradient perpendicular to the magnetic field. Correspondingly, ∂_φ is the derivative in the toroidal direction (it is in fact only implemented specifically for the neutrals). The factors of R, the radial coordinate normalised to the major radius R_0 (not ρ_{s0}), appear due to the Jacobian. The factor of δ_0^2 appears due to the isotropic normalisation $D_N = R_0 c_{s0}\hat{D}_N$, but a different normalisation of $\nabla_\perp$ and ∂_φ.

Internally, many perpendicular operators in GRILLIX in fact use only the normalisation to R_0 (not ρ_{s0}) due to the global geometry in R,Z. This is why the normalisation of D_N to R_0 is in fact sufficient. However, physics wise the normalisation of perpendicular scales to ρ_{s0}, the appearance of the δ_0^2 factor and the splitting between poloidal and toroidal dynamics is important: in plasma turbulence simulations,

we need to resolve the ρ_s scale in the poloidal plane, but only the R_0 scale toroidally. Therefore, the δ_0^2 factor indicates that for the typically resolved scales, the effective diffusion is δ_0^2 times larger in the poloidal plane than in the toroidal direction. Or without the normalisation, we realise that the isotropic diffusion of neutrals acts on a much finer poloidal grid than toroidally. In chapter 6, we had $\delta_0 = 2854$.

This insight is important because the neutrals diffusion coefficient itself is rather large, modelling ballistic motion of neutrals only inhibited by charge exchange collisions. As discussed in section 2.3.1, diffusion leads to a CFL criterion quadratic in the grid resolution, limiting the explicit time step. In the foregoing section 2.2.3, we have discussed that for the plasma, stiff diffusion terms appear in the parallel direction, with the remedy of solving them implicitly. For the neutrals, the diffusion is isotropic and large, but much smaller than parallel plasma diffusion. Therefore, an explicit discretisation is sufficient in the toroidal direction – but due to the grid anisotropy, an implicit treatment is required within the poloidal plane.

Note that only the diffusion of N has to be treated implicitly, while the T_i part can remain fully explicit. Let us introduce the time discretisation and boundary conditions. Note that the neutrals do not diffuse parallel to the magnetic field but toroidally, which is a periodic direction, hence boundary conditions only need to be applied in the poloidal plane. Nonetheless, we treat them consistently with the plasma, applying Dirichlet boundary conditions N_p at the divertor plate via penalisation, and the typical radial boundary conditions everywhere else. As described in chapter 2.2.3, equation (2.90), we split the right-hand side in an explicit and an implicit part:

$$F_\mathrm{im} = (1-\chi_p)\,\frac{\delta_0^2}{R}\nabla_\perp \cdot RD_N^t \nabla_\perp N^{t+1} - \frac{\chi_p}{\varepsilon_p} N^{t+1}, \tag{2.94}$$

$$F_\mathrm{ex}^t = (1-\chi_p)\left\{\frac{\delta_0^2}{R}\nabla_\perp \cdot RD_N^t N^t \nabla_\perp \ln T_\mathrm{i}^t + \frac{1}{R^2}\partial_\varphi \frac{D_N^t}{T_\mathrm{i}^t}\partial_\varphi N^t T_\mathrm{i}^t - k_\mathrm{iz}^t n^t N^t + k_\mathrm{rec}^t (n^2)^t\right\} + \frac{\chi_p}{\varepsilon_p} N_p, \tag{2.95}$$

where ln is the natural logarithm. The implicit part contains the neutrals density at the next time step $t+1$, the explicit part is evaluated at time step t. Then, we use the Karniadakis time-stepping scheme (2.90), obtaining

$$\begin{aligned}&\left(1 + \frac{6}{11}\Delta t \frac{\chi_p}{\varepsilon_p} - \frac{6}{11}\Delta t (1-\chi_p)\frac{\delta_0^2}{R}\nabla_\perp \cdot RD_N^t \nabla_\perp\right) N^{t+1} \\ &= \frac{18}{11}N^t - \frac{9}{11}N^{t-1} + \frac{2}{11}N^{t-2} + \frac{6}{11}\Delta t\left(3F_\mathrm{ex}^t - 3F_\mathrm{ex}^{t-1} + F_\mathrm{ex}^{t-2}\right).\end{aligned} \tag{2.96}$$

Next, we identify in eq. (2.96)

$$\begin{aligned}\lambda &= 1 + \frac{6}{11}\Delta t \frac{\chi_p}{\varepsilon_p}, \\ \xi &= \frac{6}{11}\Delta t (1-\chi_p)\frac{\delta_0^2}{R}, \\ c &= RD_N^t, \\ b &= \frac{18}{11}N^t - \frac{9}{11}N^{t-1} + \frac{2}{11}N^{t-2} + \frac{6}{11}\Delta t\left(3F_\mathrm{ex}^t - 3F_\mathrm{ex}^{t-1} + F_\mathrm{ex}^{t-2}\right),\end{aligned} \tag{2.97}$$

such that we can write (2.96) as the Helmholtz equation

$$\lambda N^{t+1} - \xi \nabla_\perp \cdot \left[c \nabla_\perp N^{t+1}\right] = b. \tag{2.98}$$

This equation is solved by the same 2D multigrid algorithm [173] that is applied in GRILLIX for the electromagnetic fields [107].

2.2.5 Verification via the method of manufactured solutions

Discretising and implementing a complex physical model in a computer code is prone to errors. Most errors can be avoided by carefully verifying the implementation, i.e. ensuring that the equations are

solved correctly, to the precision expected from the numerical method. However, complex models rarely have analytical solutions for comparison, motivating the numerical approach in the first place.

The method of manufactured solutions (MMS) [174] provides a simply genius systematic verification procedure, without relying on analytical solutions that can only be constructed in rare and extremely simplified cases. It exploits the fact that while finding a solution is difficult, it is easy to verify some given solution. Consider the equation

$$\frac{\partial f}{\partial t} = F\left(f, \frac{\partial f}{\partial x}, \frac{\partial f}{\partial y}, \frac{\partial^2 f}{\partial x^2}, \ldots\right). \tag{2.99}$$

The function F can be arbitrarily complex and non-linear. We can choose an arbitrary function f_{MMS} and compute analytically $\partial_t f$ and F, using e.g. Mathematica [175], finding that these two do not balance. The difference we simply define as a source,

$$S_{\mathrm{MMS}} = \partial_t f_{\mathrm{MMS}} - F(f_{\mathrm{MMS}}), \tag{2.100}$$

and add it to the right-hand side of eq. (2.99). Thereby, we obtain analytical expressions for a solution f_{MMS} and a source S_{MMS} for which eq. (2.99) is fulfilled.

Providing these expressions to GRILLIX, we can then test whether the actual implementation also solves (2.99). Numerically, errors in the discretisation are expected, but they should reduce with increasing space and time resolution at the expected order of convergence: e.g. third order in time for the Karniadakis scheme, and second order in space for our centred finite differences. Note that this method of verification is only as general as the chosen test function f_{MMS}. So far, it was implemented for the whole Braginskii set of equations in slab and in circular geometry. A typical convergence test in slab geometry is shown in figure 2.6. The error between the analytical MMS and numerical solution is quantified for all 8 dynamic fields, solved simultaneously, by the L_2 and L_∞ norms. Towards finer resolution, the expected second order convergence is obtained.

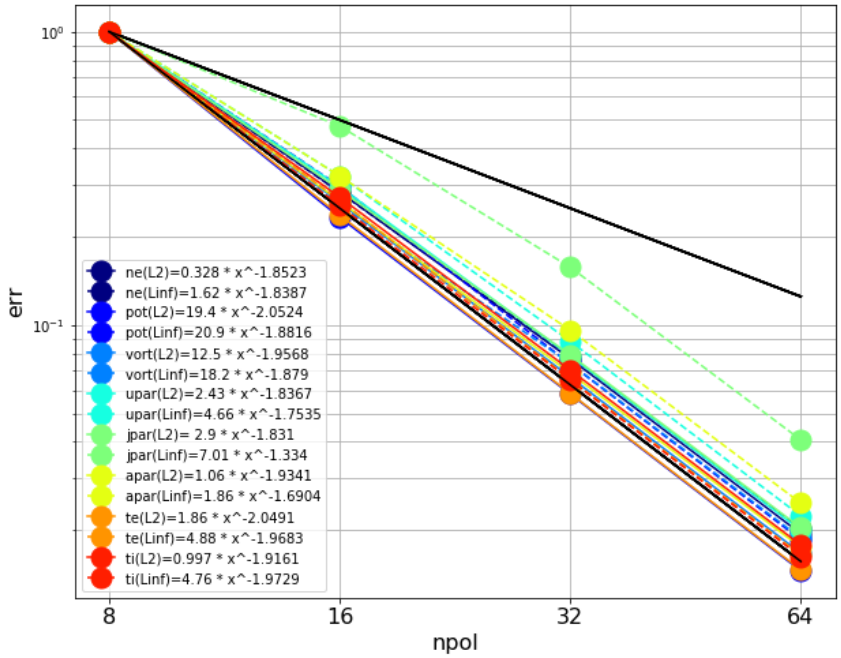

Figure 2.6: Convergence results for the whole Braginskii system under the method of manufactured solutions in slab geometry, in L_2 and L_∞ norms. The x-axis shows the number of poloidal planes, i.e. toroidal resolution is increased – poloidal and time resolution are increased by the same amount simultaneously. The black lines show precisely first order (upper line) and second order convergence (lower line) for reference.

2.3 The computational implementation and performance

Since turbulence is a complex multi-scale problem, computational efficiency naturally emerges as a critical goal for resolving turbulence in numerical simulations. Computational efficiency can never be

fully separated from the physical model and numerical discretisation: fluid models for instance can be much cheaper to simulate than kinetic models due to the reduced dimensionality (from 5-6D to 3D). Then, for a given model (fluid in our case), a smart and efficient numerical discretisation can be another major cost factor: for example, taking into account the known property of drift wave turbulence to develop flute mode structures with $k_\parallel \ll k_\perp$, while at the same time only locally aligning the operators to the magnetic field with the FCI method, allows to greatly reduce the necessary resolution in one of the three spatial dimensions, even in complex magnetic geometry, and as a result also increase the time step. Still, taking advantage of all that, direct numerical simulations of turbulence in large fusion reactors remain a very challenging task and require state-of-the-art computational methods. While the focus of this thesis lies on extensions of the physical model and applications to relevant experimental scenarios, this in turn can not be done separately from computational aspects of code development – essentially trying to make it run as fast as possible – which we aim to highlight in this chapter.

We begin by discussing in section 2.3.1 the limitations on domain size, space and time resolution due to the physical model and numerical discretisation. We highlight thereby the role of the FCI method and illustrate the restrictions for the relevant cases from recent publications. For a given grid size and time step, the computational challenge lies in executing each time step in a minimal amount of real time. To this end, firstly one has to reduce the amount of arithmetic computations and memory accesses to the bare minimum, and to structure them in an optimal way for a given computer architecture. For example, arranging the computations over whole arrays without inter-element dependencies allows to significantly reduce the arithmetic intensity by vectorisation, or single instruction, multiple data (SIMD) operations [176].

Ultimately, even if optimally utilised, a single processing unit is rarely sufficient for relevant applications – rather, applications of interest tend to be arbitrarily complex and utilize the maximum of available resources. To make more resources available, high-performance computing (HPC) substantially relies on parallelisation, i.e. splitting of the computing task among as many processing units as possible. This is discussed in section 2.3.2.

The optimisation of HPC software is complicated by the intricate entanglement between numerical algorithms, their implementation and the available computer architecture. Different architectures prefer different algorithms, depending on their implementation, and vice versa. An example for this are explicit and implicit time discretisations: the latter offer a computational benefit by allowing much larger time steps (provided these time steps are sufficient for resolving the physical dynamics), but they require a (linear) system solver in every time step. There is a great variety of linear solver algorithms, but all of them tend to become less efficient towards larger system sizes – in particular on parallel computers. This challenge is discussed in section 2.3.3 on the example of the 3D solver for parallel heat conduction and ion viscosity.

Finally, it is important to realize that scientific software has to be steadily evolving, to adapt to improving physics models, numerical algorithms and computer architectures. It is therefore important to write understandable, modular and extendable code – but also to re-write it from time to time. GRILLIX is currently in the process of refactoring, with the author of this dissertation being involved, which we discuss in section 2.3.4.

2.3.1 Space and time resolution

The boundaries for the computational performance of any computer simulation are set by physics and its numerical discretisation: they define the domain of interest, space and time scales to be resolved and the size of grid cells and time steps that provide the required resolution. Note that the drift approximation in section 2.1.1 removes fast time scales that are not of interest, such as the cyclotron motion. A successful execution of the program also requires stability in every time step, limiting its size. In this chapter, we explore the resolution requirements and stability boundaries of our simulations, with particular attention to the benefits of the FCI field-aligned approach.

We expect turbulence to take place on scales around or larger than the sound / ion gyro-radius in the drift plane. It scales with temperature and magnetic field, but can be assumed rather similar across the edge of devices of different size. The computational challenge stems from our goal to perform global turbulence simulations on the scale of the actual machine R, so the drift-/poloidal plane resolution scales

roughly like ρ/R. For comparison, for ASDEX we have $R \approx 1.65$ m, $B \approx 2.5$ T and at the separatrix $T \approx 70$ eV, resulting in $\rho/R \approx 3 \times 10^{-4}$. Resolving a box of the size R^2 would require $(R/\rho)^2 \approx 12 \times 10^6$ points per poloidal plane, but limiting the domain to the plasma edge as in chapter 5 and resolving only $2.5\rho_s$ reduced that number to ca. 500 000 points. Nonetheless, bigger devices are more expensive to resolve: for ITER with $B \approx 3.4$ T and $R \approx 3$ m (and $T \approx 70$ eV still), roughly 6 times more points are required per poloidal plane, and even more for DEMO. Even if the actual computing time would scale linearly with the number of points, considering that simulations in chapters 5 and 6 already took 3-6 month for ASDEX, that would make ITER size simulations prohibitive if no speed-up could be achieved.

The above considerations lead us to the first quantitative estimate why field-alignment is beneficial: in the worst case, a non-aligned code would have to resolve also the parallel / toroidal direction on gyro-radius scale. For ASDEX, that would mean roughly $2\pi \times 1.65$ m$/0.5$ mm $= 20000$ points in toroidal direction (or 8000 points at 2.5 ρ_s resolution) – for each poloidal grid point! This has to be compared to 16 toroidal planes used in chapters 5 and 6 thanks to the FCI approach and the flute mode character of turbulence. This proportion becomes even worse for larger machines.

The second computational constraint is the time discretisation. As it was found in chapter 5, global saturation is reached on time scales of around 3-4 ms – only then profiles and fluctuation levels can be compared to the real world experiment at steady state conditions. The time step in an explicit algorithm, on the other hand, is limited by the fastest dynamics in the system – in our case, the shear Alfvén waves speed [38, 129] $v_\mathrm{A} = B/\sqrt{\mu_0 n m_\mathrm{i}}$ (in SI units). The Courant–Friedrichs–Lewy stability condition is

$$\Delta t \leq \frac{\min(\Delta s)}{\max(v_\mathrm{A})} \approx \frac{2\pi R_\mathrm{min}}{n_\mathrm{pol} B_\mathrm{max}} \sqrt{\mu_0 m_\mathrm{i} n_\mathrm{min}}. \tag{2.101}$$

The time step is limited by the smallest parallel grid distance in the system $\min(\Delta s)$, that can be estimated by the (always smaller) toroidal grid distance with the number of poloidal planes n_pol and the inner torus radius R_min. It is also limited by the largest Alvén velocity in the system, estimated with maximum magnetic field B_max and the minimum density n_min. Note that B_max and R_min are both on the inner side of the torus, so that is where the time step is usually limited rather than at the outboard mid-plane, except if the density would be much smaller there. For the simulations in chapter 5 and 6, we have $R_\mathrm{min} \approx 1$ m, $B_\mathrm{max} \approx 4$ T, $n_\mathrm{pol} = 16$, $m_\mathrm{i} = 2m_\mathrm{p}$ (with the proton mass m_p) and $n_\mathrm{min} = 3 \times 10^{17}$ m^{-3}: this yields $\Delta t \leq 3.5$ ns or 15×10^{-5} in normalised units. This means at least 10^6 time steps are required to even reach the saturated state. In practice, in non-linear simulations the time step is chosen at least a factor 2 below the CFL limit, 5×10^{-5} in chapters 5 and 6[¶].

Under the above considerations, the second benefit of field-alignment becomes apparent: as the shear Alfvén dynamics takes place in the parallel direction to the magnetic field, the parallel or approximately the toroidal grid distance enters the respective CFL limit (2.101). Therefore, keeping the parallel grid distance large not only reduces the total number of grid points, but also increases the limit on the time step. Hence, the benefit of field-alignment is in fact quadratic in the savings in parallel grid resolution, that is $(R/\rho_s)^2$.

Finally, there is an additional strong stability / time step constraint stemming from the parabolic fluid closure terms, heat conductivity and ion viscosity in equations (2.27), (2.28) and (2.24). It is essentially parallel diffusion with diffusivity $D = 2\chi_{\parallel \mathrm{e}0} T_\mathrm{e}^{5/2}/3n$, resulting in the (explicit) time step restriction

$$\Delta t \leq \frac{\Delta s^2}{2D} = \frac{3n\Delta s^2}{4\chi_{\parallel \mathrm{e}0} T_\mathrm{e}^{5/2}} \approx \frac{3n(2\pi R_\mathrm{min})^2}{4\chi_{\parallel \mathrm{e}0} n_\mathrm{pol}^2 T_\mathrm{e}^{5/2}}. \tag{2.102}$$

Again, we notice that the problem becomes **quadratically** worse as the parallel resolution (n_pol) is increased. But also, the restriction scales with the minimum density and maximum temperature, becoming a problem in remote SOL regions with low density but high temperature, but even more so towards the

[¶]The time step is also limited by other numerical constrains, such as perpendicular hyper-diffusion $\partial f \sim \nu_\perp \Delta_\perp^3 f$ required to dissipate turbulent energy at the grid scale, with the CFL limit $\Delta t \lesssim \Delta x^6/100\nu_\perp$, Δx being the grid distance in the poloidal plane. The constant $\nu_\perp$ is usually reduced as $\sim \Delta x^6$, so the relevant quantity is $\nu_\perp/\Delta x^6$: it is ultimately determined by the turbulent energy cascade to the grid scale and can exceed the Alfvén limit in some cases, but not typically.

plasma core as the temperature dependence is non-linear. For example in chapter 5, with $R_{\min} = 0.6$ (normalised to $R_0 = 1.65$ m), $n_{\text{pol}} = 16$ and $\chi_{\parallel e0} = 940$, we have at the plasma core boundary ($\rho_{\text{pol}} = 0.9$) $n = 2$ [10^{19} m^{-3}] and $T_e = 3.5$ [100 eV], resulting in $\Delta t \leq 4 \times 10^{-6}$, an order of magnitude larger restriction than the shear Alfvén waves. The restriction is more severe for the electron than ion heat conductivity by $\chi_{\parallel e0}/\chi_{\parallel i0} \approx 35$, and for the G term in parallel momentum balance (ion viscosity) it is roughly a factor 2 smaller than for ion heat conductivity.

There is a major physical difference between these diffusive terms and Alfvén waves: the latter are directly coupled to drift-wave turbulence [38], a hyperbolic non-linear wave system, so it is desirable to resolve them in time. The parabolic (diffusive) heat conduction and viscosity are just damping mechanisms on parallel disturbances and can therefore be treated implicitly in time.[‖] This allows to ignore the time step restrictions from these terms for the price of having to solve a system of (non-linear) equations in each (super-)time-step. The implementation of a 3D linear solver to this end is one of the major technical achievements in this thesis, detailed in sections 2.2.3, 2.3.3 and 3.3.2.

2.3.2 Parallelisation strategy

At the restrictions discussed in the previous section, our goal is to execute each time step in a minimal amount of real time. Beyond writing smart and efficient algorithms, this is primarily achieved by parallel computing. The parallelisation strategy in GRILLIX is still the same as in the original implementation by Andreas Stegmeir [119]: a combination of MPI [177] and OpenMP [178], written in modern Fortran. Recall figure 2.4: each poloidal plane k consists of a 2D cartesian grid in (R,Z). The MPI domain decomposition goes over these planes: each MPI process with rank k owns the data on one poloidal plane k for all dynamic fields (density, potential etc.). Care has to be taken with toroidal staggering [106], as for flux variables like parallel velocity and current the plane is actually shifted by π/N_k, with the number of planes N_k. Each process k communicates with its neighbours at least once per time step, receiving data from k+1 and k-1. This domain decomposition is simple due to toroidal symmetry, further decomposition in (R,Z) on the other hand would involve complex communication patterns along magnetic field lines between domains. The decomposition is fixed but also optimal, reducing the computational cost per compute node and hence time for executing a time step for full torus computations by up to N_k if the execution of the program is limited by arithmetic intensity, or $N_k/3$ if it is limited by memory storage and access. It limits the execution of GRILLIX to parallel machines though, since at least N_k processes are required, and prohibits strong scalability tests.

For each process of rank k, that can take a fraction or a whole compute node, the rest of the computation is parallelised over OpenMP threads. The data are stored in logically unstructured 1D arrays, so most computations are done in single do loops. OpenMP allows to split the work in those loops over all CPUs of a compute node (threads). All threads have the same main memory access, which makes programming easier (but also more error prone), but CPUs also load data into their individual cache. Since memory access is faster for the CPU cache than for the main memory, one route of OpenMP performance optimisation lies in data layouts that reduce data loads between main memory and cache. Further, it is important that organisation and splitting of work between threads involves latencies. Therefore, it is important to arrange enough work for each parallel region (do loop) to make it worth. This requires both a large enough problem size and a smart algorithm implementation that minimizes serial bits between do loops.

Table 2.1: OpenMP scaling on Marconi A3 SKL. Benchmark was performed with 32 poloidal planes (= #MPI processes) on 32 nodes, each having 48 CPUs, with ∼1.6 million points per plane.

threads	1	2	6	12	24	48
time (s) / Δt	10.59	5.78	2.32	1.61	1.54	1.40
speed-up	1.00	1.83	4.56	6.58	6.88	7.56

[‖]On the (gyro-)kinetic level, the Vlasov equation itself is purely hyperbolic (pure advection). The only parabolic part enters due to the Coulomb collisions, a diffusion in velocity space. Indeed, this diffusion also needs to be treated implicitly [54, 76]. In the fluid closure, this diffusion translates to real space diffusion.

As an example for the benefits and limitations of parallelisation, table 2.1 shows the OpenMP scaling of a typical GRILLIX program on the Marconi A3 SKL supercomputer. The computer has 48 CPUs per node, which gives the upper bound of threads as OpenMP requires a continuous memory access. The ideal speed-up would be linear to the number of threads, which we do not achieve. With 12 threads, a reasonable speed-up of a factor 6 is achieved, but a further increase of threads does not make sense. The reasons behind this performance are discussed in section 2.3.4.

2.3.3 3D iterative matrix-free Krylov subspace solver

As we have discussed in section 2.3.1, one of the key technical achievements of this thesis is the implementation of a 3D linear solver [179] for the parabolic (diffusive) terms in the Braginskii equations: parallel heat conductivity and ion viscosity. On one hand, this allowed to run the Braginskii model in relevant parameter regimes without restrictions on the size of the time step. On the other hand, however, the solver itself can consume up to 95% of the total CPU time in each time step, becoming the major performance bottleneck depending on the parameters. It is therefore important to discuss the implementation in some more detail than in chapter 3.3.2, as well as the resulting performance in different regimes.

Recall section 2.2.3: the implicit parallel diffusion problem can be written as a "linear" system $\mathbf{A}\mathbf{T}^{t+1} = \mathbf{R}$. Importantly, the system is actually non-linear since the diffusion coefficient in $\mathbf{A}$ depends on $T^{5/2}$, but it is linearised by treating this dependency explicitly, i.e. taking $(T^t)^{5/2}$. Still, this is the main reason for the need of an iterative solver: the LU decomposition of a direct solver would need to be re-computed in every time step due to the changing diffusivity. The iterative solver, on the other hand, can converge relatively quickly as a good initial guess can be provided by T^t. With the Karniadakis time-stepping scheme, the previous two time steps are also stored, providing an even better initial guess via $T_{\text{guess}} = 3T^t - 3T^{t-1} + T^{t-2}$.

Next, we note that the parallel diffusion operator $\nabla \cdot (T^t)^{5/2}\mathbf{b}\nabla_\parallel$ connects the whole 3D grid, but sparsely. Therefore, a 3D solver is required that must respect the MPI domain decomposition and communication. Let us visualise the connectivity of $\mathbf{A}\mathbf{T}^{t+1} = \mathbf{R}$,

$$\begin{pmatrix} \mathbf{A}_{11} & \mathbf{A}_{12} & 0 & 0 & \dots & \mathbf{A}_{1N_\mathrm{k}} \\ \mathbf{A}_{21} & \mathbf{A}_{22} & \mathbf{A}_{23} & 0 & \dots & 0 \\ 0 & \mathbf{A}_{32} & \mathbf{A}_{33} & \mathbf{A}_{34} & \dots & 0 \\ 0 & 0 & \mathbf{A}_{43} & \mathbf{A}_{44} & \dots & 0 \\ \vdots & \vdots & \vdots & \vdots & \ddots & \vdots \\ \mathbf{A}_{N_\mathrm{k}1} & 0 & 0 & 0 & \dots & \mathbf{A}_{N_\mathrm{k}N_\mathrm{k}} \end{pmatrix} \cdot \begin{pmatrix} \mathbf{T}_1 \\ \mathbf{T}_2 \\ \mathbf{T}_3 \\ \mathbf{T}_4 \\ \vdots \\ \mathbf{T}_{N_\mathrm{k}} \end{pmatrix} = \begin{pmatrix} \mathbf{R}_1 \\ \mathbf{R}_2 \\ \mathbf{R}_3 \\ \mathbf{R}_4 \\ \vdots \\ \mathbf{R}_{N_\mathrm{k}} \end{pmatrix}. \tag{2.103}$$

Each entry $\mathbf{T}_\mathrm{k}$ is a vector of all the temperature values (to be solved for) on poloidal plane k, owned by MPI rank k. Each matrix $\mathbf{A}_{ml}$ is in this sense 2D in (R,Z). The RHS, containing among other things the explicit part of the system, is decomposed the same way. The parallel diffusion operator is local on plane k, coupling it only to its neighbours k+1 and k-1. The full matrix $\mathbf{A}$ is therefore block tridiagonal, plus the entries $\mathbf{A}_{1N_\mathrm{k}}$ and $\mathbf{A}_{N_\mathrm{k}1}$ appearing due to toroidal periodicity. Due to toroidal symmetry, all matrices $\mathbf{A}_{ll}$, $\mathbf{A}_{l,l+1}$ and $\mathbf{A}_{l,l-1}$ are also identical. On each rank k we compute

$$\sum_{l=\mathrm{k}-1}^{\mathrm{k}+1} \mathbf{A}_{\mathrm{k}l}\mathbf{T}_l^{t+1} = \mathbf{R}_\mathrm{k}. \tag{2.104}$$

The involved matrices (operators) are the same on each rank k. The data $\mathbf{T}_{\mathrm{k}-1}$ and $\mathbf{T}_{\mathrm{k}+1}$ need to be communicated via MPI though. The 3D solve is required because (2.104) needs to be solved for each k simultaneously. A block tridiagonal matrix algorithm with a series of 2D solves is also thinkable, though.

Although $\mathbf{A}$ is bloack tridiagonal, its elements $\mathbf{A}_{ml}$ operating on T_l are not. Firstly, each poloidal plane does not represent a full rectangular Cartesian plane but contains cuts at the limiting flux surfaces. At those cuts, the stencil is replaced by the application of perpendicular boundary conditions via $\mathbf{B}^{(\mathbf{D},\mathbf{N})}\mathbf{T}_l^{t+1} = \mathbf{T}_{\partial V}^{(0,1)}$**, changing the connectivity. Even more importantly, the connectivity is complicated because it follows the intricate field line trajectory, plus interpolation due to the FCI method

**Due to toroidal symmetry, the matrices $\mathbf{B}^{(\mathbf{D},\mathbf{N})}$ are the same in each plane k. Note that explicit application of perpendicular boundary conditions rather involves the inverse problem. Parallel boundary conditions only concern the diagonal on $\mathbf{A}_{ll}$ via penalisation.

[106, 161, 162], plus magnetic flutter [††]. This is the reason why $\mathbf{T}_l$ is stored simply in a 1D unstructured array. Therefore, the matrices A_{ml} are significantly more complicated and more dense than a tridiagonal matrix: each parallel operator, gradient and divergence, can be represented by a sparse matrix in our discretisation – but their product, the diffusion operator, is more dense. All this motivates a matrix-free method for the solution of the whole system.

Since $\mathbf{A}\mathbf{T}^{t+1} = \mathbf{R}$ constitutes an elliptic problem, Krylov subspace iterative methods [179] provide a good solution, with the significant benefit of being applicable as a black box. Specifically, we use the Parallel Iterative Methods (PIM 2.3) library [180] which offers a number of iterative methods at choice. The implementation is matrix-free with a reverse communication interface: the matrix $\mathbf{A}$ is never built, but the user has to implement the matrix-vector product (2.104). This is easily done with the standard parallel operators in GRILLIX (with some care about boundary conditions). Additionally, the user provides global MPI parallelised summation and norm routines.

The best Krylov subspace method is the conjugate gradient (CG) method, because it converges monotonically and only applies one matrix-vector product per iteration. Unfortunately, it did not converge in our case because the matrix seems to be not positive-definite. Both Bi-CGSTAB and GMRES worked though, similarly well. Due to slightly better performance, the choice ultimately fell on the GMRES method [181]. The method has the drawback that until convergence, each consecutive iteration n applies n^2 matrix-vector products (plus global reductions). The performance is significantly improved by restarting the algorithm after a number of iterations – our choice is typically 10 – although this requires more iterations overall.

The performance of the solver depends on the condition number of $\mathbf{A}$ and therefore varies. Primarily, it is determined by the diffusivity $D = 2\chi_{\parallel 0} T^{5/2}/3n$. The condition number is also impaired by a large time step and small parallel grid distance, such that the solver benefits from the sparse toroidal resolution permitted by the FCI approach. Further, magnetic flutter adds connectivity and arithmetic intensity, introducing new terms such as (2.42). This makes the solver generally more expensive, although convergence and stability are not affected because one still solves a parabolic diffusion equation, just along a perturbed magnetic field. Finally, boundary conditions matter: for instance, we observe that convergence significantly deteriorates with increasing sheath heat transmission γ_e.

2.3.4 Performance and refactoring

Finally, we can discuss the overall performance of the code and prospects for improvement. A good overview is achieved simply by timing individual routines. For the reference simulation in the latest publication in chapter 6, AUG with neutrals, table 2.2 depicts the typical outcome for a total run time of 0.25 τ, or 6 µs of the simulation. The simulation ran in total to 440 τ, or 10.5 ms.

The table shows code regions, a total number of their calls during those 0.25 τ (or 6 µs), total time spent in each region, time per number of calls and relative to the total time step. The first row shows the most important information: the whole time step for the Braginskii model was executed 5000 times, taking 0.99 s per time step on average. For 440 τ or 10.5 ms total simulation time, this results in 100 days of constant run time. 8 compute nodes on the Marconi A3 SKL supercomputer have been used, with 48 CPUs each: having 16 poloidal planes, the absolute maximum was 16, but it did only provide a 10% speed-up due to limited OpenMP performance.

Next, we find 7 regions for the 8 fields evolved in time, with $j_\parallel$ and $A_\parallel$ timed together. This indicates how the time stepping is organized: the quantities are evolved consecutively, one (equation) after the other. Partly, this is due to the structure of the equations: for instance, as detailed in chapter 3.3.1, the density has to be evolved first to provide n^{t+1} for the elliptic solver.

Comparing each region's timings to the full time step, we find significant differences: while the advancement of density takes only 5%, for the electron temperature it takes 30%. The reason for this is the PIM solver for the 3D diffusion problem discussed above: it is applied for the parallel diffusion in the T_e, T_i and $u_\parallel$ equations. The diffusion in T_e is most stiff due to the large electron heat conductivity and sheath heat transmission. The solver converges only after 1 restart, i.e. more than 10 iterations in total.

[††] In the electrostatic case, the 3D connectivity from the purely parallel operator results from the perpendicular interpolation due to the FCI method – in a field aligned code, $\mathbf{A}_{ml}$ would be trivial. However, since we generally must include electromagnetic fluctuations $\tilde{\mathbf{b}}$ in the parallel operators, the problem is generally 3D even without FCI interpolation.

Table 2.2: Timings for the computational performance of GRILLIX in chapter 6 on the Marconi A3 SKL supercomputer.

region	#calls	time [s]	time/#calls	rel.time [%]
timestep	5000	4955.96692	0.99119	100.00000
density	5000	244.43333	0.04889	4.93210
T_e	5000	1414.92344	0.28298	28.54990
T_i	5000	556.32924	0.11127	11.22544
$u_\parallel$	5000	580.37264	0.11607	11.71058
vorticity	5000	390.74477	0.07815	7.88433
potential	5000	467.13532	0.09343	9.42571
$j_\parallel, A_\parallel$	5000	626.05418	0.12521	12.63233
PIM	15000	1530.13372	0.10201	30.87458
multigrid	25000	1095.48438	0.04382	22.10435
neutrals	5000	641.42264	0.12828	12.94243
diagnostics	25	87.78870	3.51155	1.77137
snapshot	1	0.40758	0.40758	0.00822

This is generally decent convergence, but it involves more than 400 matrix-vector computations **AT**, including MPI communication in each step, hence the computational cost. For T_i and $u_\parallel$, convergence occurs before the first restart. Note that in this simulation, magnetic flutter was disabled and ion and electron heat conduction was limited by the free-streaming flux according to chapter 6.3. With magnetic flutter, the time step takes 1.25 s, primarily because the PIM solve for T_e takes 0.47 s instead of 0.28 s. The number of solver iterations remains similar, and also other parts of the code with parallel operators (like the density equation) become more expensive by up to 50%, while the multigrid solver in (R,Z) converges somewhat faster – we therefore conclude that rather than the MPI communication, the cost of the repeated matrix-vector multiplications $\mathbf{A}_{ml}\mathbf{T}_l$ within the solver is very expensive.

Finally, we find that the multigrid solver [107] for the 2D elliptic problem is invoked a total of 5 times: twice for the electrostatic potential due to zonal Neumann core boundary conditions, twice for $A_\parallel$ due to penalisation and once for the neutrals. Overall, although the multigrid takes a significant fraction of the compute time, but it is not dominating it. For the neutrals, the computational cost is dominated by the multigrid but remains reasonable.

The physics problem studied in chapter 6 is typical and relevant, it is also by far not small – but still much smaller than the most interesting cases for nuclear fusion reactors. Firstly, reactors must be significantly larger than AUG, requiring a roughly 10 times larger simulation domain. Secondly, the grid resolution in chapter 6 was barely sufficient, while there is significant interest in much smaller scales. However, already these AUG simulations take each on the order of 100 days to complete, while we want to be actually able to perform parameter scans quickly. Therefore, the improvement of computational performance is among the top priorities.

There are multiple ways to proceed. Firstly, as 2D and 3D linear solvers play an important role across the time step, improving their convergence is key – but this is already being done to the best of our knowledge. Secondly, one can optimise the performance on current architectures, including the improvement of the OpenMP scalability. The MPI scalability could be extended beyond the 1D toroidal domain decomposition – this is however not trivial due to the arising complex communication patterns. But also, taking advantage of recently developed accelerator machines, one could extend or replace the OpenMP parallelisation by utilising graphics processing units (GPUs) via e.g. OpenACC [182].

The difficulty is that there is no single obvious bottleneck in the current code, with all the regions performing similarly. Even if both solvers would be further optimised, the rest of the time step is still taking already half of the computing time. This is owed, however, in parts to the chosen code structure – evaluating the physical equations consecutively, instead of decomposing the code into different operators, communicators and parallel regions, and grouping them accordingly. Let us examine the system of equations in chapter 5.7: we notice that many operators appear repeatedly throughout the equations, for example $\nabla\cdot(j_\parallel\mathbf{b})$ and $C(p_\mathrm{e})$ appear 4 times. On the other hand, each equation contains a mixture

of all kinds of operators. While perpendicular operators rely solely on OpenMP parallelisation, parallel operators require MPI communication each time. As a results, the time step contains a vast number of small but very different, alternating computing steps, including OpenMP regions and MPI communication. Not only are many operators computed more often than required, and MPI communication is often redundant (data storage is thereby minimized though, but it is usually not the bottleneck). Each operator also contains only a limited amount of work, making the overhead from barrier synchronisations and latencies a significant factor. Partly, this code design emerged from GRILLIX originally implementing the Hasegawa-Wakatani equations [119], where much fewer operators appear.

Therefore, it was decided that a major refactoring of the time step routine (and the whole code around it) was required. The main goal is performance optimisation, but also maintainability is being improved by making the code more readable, modular, and introducing automated unit and integration tests. The preservation of functionality is ensured by MMS. For performance, the idea was to minimize the amount of MPI and to improve the communication pattern, separating it from OpenMP regions as far as possible. This allows more work to be done in the latter, avoids redundant operator evaluation and simplifies their profiling. The minimisation of latencies is also thought to be a major prerequisite for a reasonable GPU implementation, since they become even larger there due to the transfer between main and device memory. A preliminary result from refactoring is shown in figure 2.7.

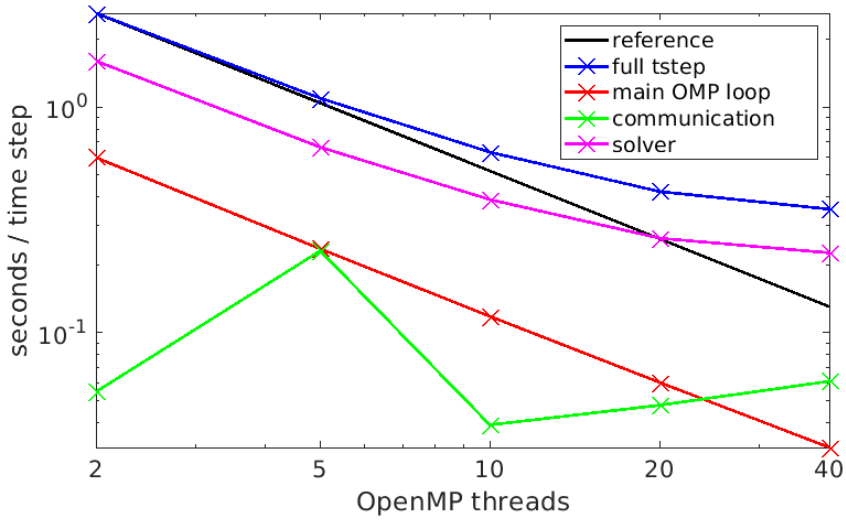

Figure 2.7: OpenMP scaling of the refactored GRILLIX version on the Cobra supercomputer of the Max-Planck Computing and Data Facility (each node containing 40 Intel SkyLake Processors).

The test case is a circular C-mod simulation, similar to chapter 3, with 350000 grid points per poloidal plane, but with a reduced heat conduction and no 3D solver. Even though the test case is not exactly comparable to table 2.1, some improvement can be seen – in particular, we can now better diagnose what is happening. Most importantly, the whole MPI communication now happens in only two places during the time step: the 8 fields are simply exchanged and stored in halo data, with parallel derivatives operating on these data without additional MPI communication. This allows to quantify the computational cost of MPI communication separately. As one would expect, it becomes important towards larger number of OpenMP threads, as the work per thread is reduced while the amount of communication stays the same. The fluctuations in the MPI communication cost also indicate how large the latencies can become with too much synchronisation.

The rest of the work is largely separated in one single OpenMP loop, containing all the operators for all the equations, and the elliptic solver for the electromagnetic fields. Consequently, with so much work the OpenMP loop scales perfectly to 40 threads, becoming irrelevant for the remaining computational cost. The elliptic solver now remains as the clear bottleneck, which can be further optimised. The 3D solver has also been just recently ported and was not yet benchmarked. With the code already being slightly faster than the previous GRILLIX version, significant performance improvement for reactor scale simulations seems feasible now.

Part II

Own publications

Chapter 3

Thermal dynamics in the flux-coordinate independent turbulence code GRILLIX

W. Zholobenko, A. Stegmeir, T. Body, A. Ross, P. Manz, O. Maj, D. Coster, F. Jenko, M. Francisquez[1)], B. Zhu[2)], B. N. Rogers[3)]

Max-Planck-Institut für Plasmaphysik, D-85748 Garching, Germany
[1)] MIT Plasma Science and Fusion Center, Cambridge, Massachusetts 02139, USA
[2)] Lawrence Livermore National Laboratory, 7000 East Avenue, Livermore, CA 94550, USA
[3)] Department of Physics and Astronomy, 6127 Wilder Laboratory, Dartmouth College, Hanover, New Hampshire 03755, USA

Email: Wladimir.Zholobenko@ipp.mpg.de

Appeared in: Zholobenko W, Stegmeir A, Body T, et al. Thermal dynamics in the flux-coordinate independent turbulence code GRILLIX. *Contributions to Plasma Physics.* 2020; 60:e201900131.
https://doi.org/10.1002/ctpp.201900131
Presented at: 17th International Workshop on Plasma Edge Theory in Fusion Devices, August 19-21, 2019, University California San Diego, La Jolla, USA
Original publication [1] and detailed disclaimer are included in the appendix.

A corrigendum has been published to this article, see chapters 4 and A.2.

Abstract GRILLIX employs the flux-coordinate independent approach (FCI), which allows us to study boundary plasma turbulence in realistic diverted configurations. Recently, the physical model in GRILLIX has been extended to a global drift reduced Braginskii model, without any separation between background and fluctuations. It includes electromagnetic and thermal dynamics with hot ions, relaxation of the Boussinesq approximation and non-linear parametric dependencies. This contribution presents solutions to associated issues, i.e. the ion diamagnetic polarisation and the stiff parallel heat conduction. Simulations based on parameters characteristic for the Alcator C-Mod tokamak were carried out. In circular geometry, the self-consistent electric field contains zonal flows and geodesic acoustic modes in the confined region. In the scrape-off layer the electron parallel heat conduction and its boundary condition determine the temperature and electric field, leading to sheared flows at the LCFS.

3.1 Introduction

A fundamental issue investigated with turbulence codes like GRILLIX [107] is the competition between the turbulent perpendicular heat flux and the parallel one in the scrape-off layer (SOL), which determines the SOL width and the survival of the wall components of future fusion power plants. A comprehensive and self-consistent physical model is required that describes both effects in realistic and experimentally relevant magnetic geometries. The latter is discussed in a separate contribution to these proceedings [118], while the physical model and its implementation is discussed herein.

The global drift reduced Braginskii model, described in section 3.2, does not separate between background and fluctuations, which is shown to be important for the edge plasma [99, 101, 104, 107, 117]. Alternatively, global gyrokinetic [183] or gyrofluid [149] models are being developed. In GRILLIX, we recently implemented the crucial ion temperature dynamics and an implicit treatment of (electron) parallel heat conductivity. The consistent time discretization with the 3rd order Karniadakis [169] scheme is detailed in section 3.3, as well as the matrix-free parallelized solution of the resulting system of equations by the PIM library [180].

We demonstarate the importance of the newly implemented thermal effects by performing Alcator C-mod like L-mode simulations in circular geometry, illustrated in section 3.4. Compared to previous work [117], we confirm that the turbulence is stabilized by higher temperature and destabilized by higher density. The electric field in the confined region exceeds the ion pressure gradient and contains zonal flow as well as geodesic acoustic mode (GAM) components. In the SOL, it follows the electron temperature and its profile is strongly dependent on the electron parallel heat conductivity, while the ion conductivity plays a minor role. A sheared electric field at the last closed flux surface (LCFS) results. This is also summarized in section 3.5.

3.2 Physical model

The drift reduced Braginskii model [56, 57] describes edge and SOL turbulence in the low frequency regime $\omega \ll \frac{eB}{M_i c}$. In the following, time scales are normalised to R_0/c_{s0}, with R_0 the major radius and $c_{s0} = \sqrt{T_{e0}/M_i}$ the sound speed at reference electron temperature T_{e0}. Perpendicular scales are normalised to the sound Larmor radius $\rho_{s0} = c\sqrt{T_{e0}M_i}/(eB_0)$ and parallel scales to R_0. The dynamical fields evolved in GRILLIX are the density n normalised to a reference density n_0, the electrostatic potential ϕ normalised to T_{e0}/e, the parallel ion velocity $u_\parallel$ normalised to c_{s0}, the electron and ion temperatures T_e and T_i normalised to reference values T_{e0} respectively T_{i0}, the parallel current $j_\parallel$ normalised to en_0c_{s0} and the parallel component of the perturbed electromagnetic potential $A_\parallel$ normalised to $(\beta_0 B_0 \rho_{s0})^{-1}$ with $\beta_0 = 4\pi n_0 T_{e0}/B_0^2$:

$$\frac{d}{dt}n = nC(\phi) - C(p_e) + \nabla\cdot\left[\left(j_\parallel - nu_\parallel\right)\mathbf{b}\right], \tag{3.1}$$

$$\nabla\cdot\left[\frac{n}{B^2}\left(\frac{d}{dt}+u_\parallel\nabla_\parallel\right)\left(\nabla_\perp\phi+\tau\frac{\nabla_\perp p_i}{n}\right)\right] = -C(p_e+\tau p_i) + \nabla\cdot\left(\mathbf{b}j_\parallel\right), \tag{3.2}$$

$$\left(\frac{d}{dt}+u_\parallel\nabla_\parallel\right)u_\parallel = -\frac{\nabla_\parallel\left(p_e+\tau p_i\right)}{n}, \tag{3.3}$$

$$\begin{aligned}\frac{3}{2}\left(\frac{d}{dt}+v_\parallel\nabla_\parallel\right)T_e = T_eC(\phi) - \frac{T_e}{n}C(p_e) - \frac{5}{2}T_eC(T_e) + 0.71\frac{T_e}{n}\nabla\cdot\left(\mathbf{b}j_\parallel\right) + \left(\frac{\eta_{\parallel 0}}{T_e^{3/2}}\right)\frac{j_\parallel^2}{n} \\ + \frac{1}{n}\nabla\cdot\left[\left(\chi_{\parallel e0}T_e^{5/2}\right)\mathbf{b}\nabla_\parallel T_e\right],\end{aligned} \tag{3.4}$$

$$\begin{aligned}\frac{3}{2}\left(\frac{d}{dt}+u_\parallel\nabla_\parallel\right)T_i = T_iC(\phi) - \frac{T_i}{n}C(p_e) + \frac{5}{2}\tau T_iC(T_i) - T_i\nabla\cdot\left(\mathbf{b}v_\parallel\right) + \frac{T_i}{n^2}j_\parallel\nabla_\parallel n \\ + \frac{1}{n}\nabla\cdot\left[\left(\chi_{\parallel i0}T_i^{5/2}\right)\mathbf{b}\nabla_\parallel T_i\right],\end{aligned} \tag{3.5}$$

$$\beta_0\frac{\partial}{\partial t}A_\parallel + \mu\left(\frac{d}{dt}+v_\parallel\nabla_\parallel\right)\frac{j_\parallel}{n} = -\left(\frac{\eta_{\parallel 0}}{T_e^{3/2}}\right)j_\parallel - \nabla_\parallel\phi + \frac{\nabla_\parallel p_e}{n} + 0.71\nabla_\parallel T_e, \qquad \nabla_\perp^2 A_\parallel = -j_\parallel, \tag{3.6}$$

where we have introduced as auxiliary variables the parallel electron velocity $v_\parallel = u_\parallel - j_\parallel/n$ and the electron and ion pressures $p_e = nT_e$ respectively $p_i = nT_i$, The parallel gradient is defined as $\nabla_\parallel := \mathbf{b}\cdot\nabla$ with $\mathbf{b} = \mathbf{B}/B$ the unit vector of the static background magnetic field. The advective derivative is defined as $\frac{d}{dt} := \frac{\partial}{\partial t} + \delta_0\left(\frac{\mathbf{B}}{B^2}\times\nabla\phi\right)\cdot\nabla$ and the curvature operator as $C(f) := -\delta_0\left(\nabla\times\frac{\mathbf{B}}{B^2}\right)\cdot\nabla f$. The dimensionless parameters of the system are the drift scale $\delta_0 := R_0/\rho_{s0}$, the dynamical plasma beta β_0 defined above, the electron to ion mass and temperature ratios $\mu := m_e/M_i$ respectively $\tau := T_{i0}/T_{e0}$, the normalised parallel resistivity $\eta_{\parallel 0} := 0.51\frac{R_0}{\tau_{e0}c_{s0}}\frac{m_e}{M_i}$ and normalised parallel electron and ion heat conductiv-

ities $\chi_{\parallel e0} := 3.15 \frac{\tau_{e0} c_{s0}}{R_0} \frac{M_i}{m_e}$ respectively $\chi_{\parallel i0} := 3.9 \frac{\tau_{i0} c_{s0}}{R_0} \frac{T_{i0}}{T_{e0}}$, where τ_{e0} and τ_{i0} are the electron respectively ion collision times evaluated at reference. The equations are supplemented by sources for density, electron and ion temperature and by numerical dissipation terms.

Insulating Bohm sheath boundary conditions [49] are applied at the limiter/divertor target plates:

$$u_\parallel \gtrless \sqrt{T_e}, \quad j_\parallel = 0, \quad \phi = \Lambda T_e, \quad \nabla_\parallel T_e = -\frac{\gamma_e}{\left(\chi_{\parallel e0} T_e^{5/2}\right)} T_e n u_\parallel, \quad \nabla_\parallel T_i = 0, \quad \nabla_\parallel n = 0, \tag{3.7}$$

where $\Lambda \approx 0.5 \ln \frac{M_i}{2\pi m_e}$ is the sheath floating potential and $\gamma_e \approx 2.5$ is the electron sheath transmission coefficient. Additionally, the simulation domain is bounded by inner and outer limiting flux surfaces, where homogeneous Neumann boundary conditions are applied to n, T_e, T_i, $u_\parallel$ and homogeneos Dirichlet boundary conditions to $A_\parallel$. At the outer radial boundary ϕ is set to ΛT_e, and in order to allow the potential to float at the inner boundary a zonal homogeneous Neumann boundary condition is applied, i.e. $\partial_\rho \langle \phi \rangle_\theta = 0$ and $\phi - \langle \phi \rangle_\theta = 0$, with $\langle \rangle_\theta$ denoting the flux surface average and ρ a coordinate perpendicular to flux surfaces.

We note that the model is global, which is reflected in the fact that all parametric dependencies are kept and the routinely employed Boussinesq approximation is not applied. In comparison to the previous version [107], GRILLIX was extended by ion thermal dynamics. However, magnetic flutter terms, as well as terms arising from the viscous part of the ion stress tensor, e.g. magnetic pumping terms, are not yet implemented in the GRILLIX model.

3.3 Numerical implementation

GRILLIX is based on the flux-coordinate independent approach [160, 161] (FCI), which avoids the common singularities of flux-coordinates [184] at the separatrix and X-point(s). A cylindrical grid is used, where parallel operators are discretised via a field line map between adjacent poloidal planes. For a comprehensive description of GRILLIX and the FCI implementation we refer to Stegmeir *et al.* [107], and we discuss here numercal techniques of the most recent extensions, i.e. ion thermal dynamics and the implicit treatment of the parallel heat conduction.

3.3.1 Ion diamagnetic polarisation

The main difficulty in the implementation of ion thermal dynamics is the calculation of the electrostatic potential in presence of the ion diamagnetic polarisation term in Eq. (5.26), where one has to take into account the time derivatives correctly. The time-stepping scheme in GRILLIX is based on a 3rd order backward differentiation formula (BDF3), where a quantity f, subject to $\partial_t f = F(f)$, is evolved in time according to

$$f^{t+1} - \frac{6}{11}\Delta t F^{t+1} = \frac{18}{11} f^t - \frac{9}{11} f^{t-1} + \frac{2}{11} f^{t-2}, \tag{3.8}$$

with time-step Δt and $F^{t+1} = F(f^{t+1})$. BDF3 is an implicit scheme that modifies to an explicit scheme (Karniadakis [169]) via approximating $F^{t+1} \approx 3F^t - 3F^{t-1} + F^{t-2}$. For the temporal discretisation of the vorticity equation we define the generalised vorticity at time-step t

$$\Omega_j^t := \nabla \cdot \left[\frac{n^{t+1}}{B^2} \left(\nabla_\perp \phi^{t+j} + \tau \frac{\nabla_\perp p^{i+j}}{n^{t+j}} \right) \right], \tag{3.9}$$

where the index j is only attached to quantities that the time derivative acts on. Integrator (3.8) applied to (5.26) yields

$$\Omega_{+1}^t = \frac{18}{11}\Omega_0^t - \frac{9}{11}\Omega_{-1}^t + \frac{2}{11}\Omega_{-2}^t + \frac{6}{11}\Delta t \left(3F^t - 3F^{t-1} + F^{t-2}\right), \tag{3.10}$$

where the F terms contain advection and the right hand side terms of eq. (5.26), which can be computed explicitely. We note that before this step the continuity equation (5.25) has already been advanced and

therefore $\Omega^t_{0,-1,-2}$ can be computed directly as n^{t+1} is available. The electrostatic potential at time $t+1$ is finally obtained by solving

$$\Omega^t_{+1} - \tau\nabla\cdot\left(\frac{1}{B^2}\nabla_\perp p_i^{t+1}\right) = \nabla\cdot\left(\frac{n^{t+1}}{B^2}\nabla_\perp\phi^{t+1}\right), \tag{3.11}$$

where p_i^{t+1} is also available due to the prior advancement of the ion thermal equation (5.30). Therefore, eq. (3.11) is a two-dimensional elliptic equation for ϕ^{t+1} and is solved in GRILLIX via an efficient geometric multigrid solver within each poloidal plane separately [107]. We note that the final implementation of the model with ion-thermal dynamics was verified successfully with the Method of Manufactured Solutions [174], which is continuously integrated in GRILLIX.

3.3.2 Semi-implicit non-linear parallel heat conduction

With the Braginskii closure for the 3-moment fluid equations [56], the resulting parabolic heat conduction term leads to a severe restriction on the allowed time step if treated with the same high order explicit scheme as the hyperbolic rest of the system. In a global model this constraint depends on temperature and density and therefore on space and time, so that either the time step or the heat conductivity have to be significantly reduced [107]. However, due to its crucial role in setting the SOL temperature profile [107] and symmetrizing the temperature profile on closed flux surfaces [117] a remedy had to be found.

A natural solution is to treat this term implicitly. This can be done consistently within the Karniadakis time stepping scheme by splitting the equations into an explicit and an implicit part, $F(f) = F_{ex}(f) + F_{im}(f)$, and approximating only the explicit part by $F_{ex}^{t+1} \approx 3F_{ex}^t - 3F_{ex}^{t-1} + F_{ex}^{t-2}$. The implicit part contains only the parabolic heat conduction terms for electrons and ions (as well as penalisation terms [103, 107] for parallel boundary conditions, omitted here for brevity), while the rest of the system of equations is treated explicitly. This results in two non-linear 3D elliptic problems (for T_e and T_i) that have to be solved at every time step,

$$\left[1 - \frac{6}{11}\Delta t\frac{\chi_{\parallel 0}}{n^t}\nabla\cdot(T^*)^{5/2}\mathbf{b}\nabla_\parallel\right]T^{t+1} = \frac{18}{11}T^t - \frac{9}{11}T^{t-1} + \frac{2}{11}T^{t-2} + \frac{6}{11}\Delta t\left[3F_{ex}^t - 3F_{ex}^{t-1} + F_{ex}^{t-2}\right]. \tag{3.12}$$

T^* in the brackets has to be T^{t+1} according to the Karniadakis scheme, requiring Newton iterations for the solution of the non-linear system of equations. However, the $O(\Delta t)$ linearisation $T^* = T^t$ (or higher order approximations) can be used without impact on the stability of the scheme.

In FCI, the grid can be toroidally sparse, keeping the condition number of the linear system low. The Karniadakis scheme (BDF3), however, is not A-stable, and therefore large enough imaginary eigenvalues would make it unstable. The continuous diffusion operator is self-adjoint and has only real eigenvalues, but this is not generally given on the discrete level in FCI - in GRILLIX, these properties are preserved by the support operator method [106, 161].

To solve the linear system we use the Parallel Iterative Methods (PIM 2.3) library [180], particularly the well scalable restarted GMRES algorithm [181], with a matrix-free implementation. This is useful because the matrix for parallel operators is somewhat complex in FCI, has to be distributed among MPI processes and recomputed every time step due to the non-linearity. With PIM, no matrix is ever built and (3.12) is simply defined by existing operators, saving memory space, computational cost and effort.

3.4 C-mod L-mode in circular geometry

The setup is based on [117], although we use a very different implementation, most notably a fully non-field-aligned grid. The normalization parameters are: major radius $R_0 = 68$ cm, minor radius $a = 22$ cm, equilibrium toroidal magnetic field $B_0 = 4.1$ T, deuterium ion mass $M_i = 2m_p$, density $n_0 = 8\times10^{13}$ cm^{-3} and temperature $T_0 = 30$ eV. For electron collisions, we use the effective charge state $Z = 1.5$. This results in dimensionless parameters: $\delta = 3520$, $\beta_0 = 2.88\times10^{-5}$, $\mu = 2.72\times10^{-4}$, $\tau = 1$, $\eta_{\parallel 0} = 6.03\times10^{-2}$, $\chi_{\parallel e0} = 26.6$, $\chi_{\parallel i0} = 1.15$. We define the normalized radial coordinate $\rho = \sqrt{(R-R_0)^2 + Z^2}$, then the safety factor $q(\rho) = 4/\left(1 - 3.71(\rho - 0.305)\right)$ defines the poloidal magnetic field profile.

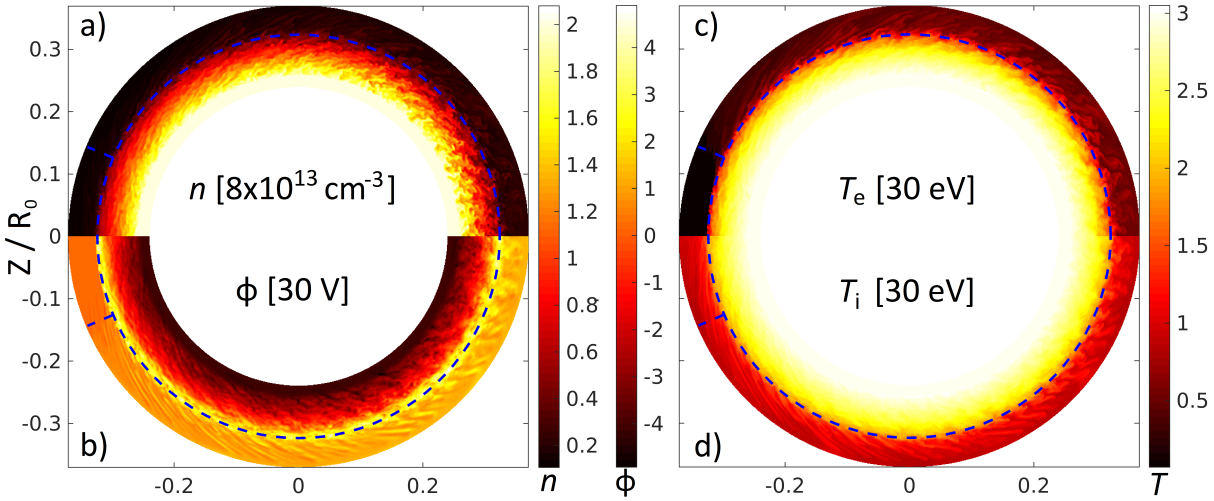

Figure 3.1: Poloidal snapshot of a) density, b) potential, c) electron and d) ion temperature at $t = 1.44$ ms. The horizontal coordinate is $(R - R_0)/R_0$. The average profiles are (nearly) up-down symmetric, hence only half the plane is shown. The blue dashed line indicates the limiter location on the inboard midplane (parallel sheath boundary region) and the LCFS.

The grid consists of 16 poloidal planes and a uniform poloidal resolution of $3 \times \rho_{s0} \approx 0.58$ mm. The time step is $\Delta t = 5 \times 10^{-5} \frac{R_0}{c_{s0}} \approx 0.9$ ns. The simulation domain is $\rho \in (0.2412, 0.3685)$, with LCFS at $\rho = 0.3235$. In total, the grid consists of circa 5.4×10^6 points. In order to test the resolution a simulation with 16×10^6 points was run until $t = 0.6$ ms and showed no significant difference in the profiles. A sixth order hyperviscosity $4000\nabla_\perp^6$ was applied in perpendicular direction on all fields to cut off turbulent spectra on grid scale, as well as regular diffusion $0.05\nabla \cdot (\mathbf{b}\nabla_\parallel)$ on n, Ω and $u_\parallel$ in parallel direction.

The reference simulation has as initial condition $(n, T_e, T_i) = (2, 3, 3)$ at the core boundary and $n = T_e = T_i = 0.2$ in the SOL, with a smooth transition in the edge region. The initial temperature profile is shown in figure 3.2. An adaptive source keeps the profiles fixed at the core boundary and $n > 0.03$, $T_e > 0.07$ and $T_i > 0.03$. Otherwise they are free to evolve in the rest of the domain, with a sink given by sheath boundary conditions at the limiter boundary. Other fields are set to stabilize the initial profile, i.e. an electric field balances the ion diamagnetic polarisation and Pfirsch-Schlüter currents balance the pressure gradient. Additionally, one simulation with $n = 4$ at the core (double density) and one with $T_e = T_i = 6$ (double temperature) were carried out, as well as scans with parallel heat conductivity $\chi_{\parallel 0}$ at reference core parameters.

Simulations were run until $t = 80 \frac{R_0}{c_{s0}} \approx 1.5$ ms (for circa 9 days on the Marconi-A3 SKL partition, on 8 nodes with 2 MPI processes per node times 24 cores). The resulting poloidal profiles of n, ϕ, T_e and T_i at $t = 1.44$ ms are displayed in figure 3.1. All profiles except T_i are saturated, with T_i still rising at $t > 3$ ms [117]. Averaged toroidally and in time over $10 \frac{R_0}{c_{s0}} \approx 0.2$ ms (40 snapshots), profiles and fluctuation amplitudes $\sigma_f^2 = \langle f^2 \rangle - \langle f \rangle^2$ at the outboard midplane are shown in figure 3.2.

With the updated voriticity equation, the electric field in the confined region is proportional to the ion pressure gradient, exceeding it by circa 50%. On the other hand, due to sheath boundary conditions the potential in the SOL is following $\phi = \Lambda T_e$. A potential maximum results at the separatrix, leading to a jump in the electric field and consequently sheared $E \times B$ flows. The potential oscillations in the confined region contain a strong poloidally and toroidally symmetric part at acoustic frequencies, indicating the presence of GAMs [185]. Figure 4.2 shows the frequency spectrum. The radial profile of the acoustic frequency $\hat{f} \approx \frac{\sqrt{2}}{2\pi}\sqrt{T_e + T_i}$ is shown as a reference, $f = \frac{c_{s0}}{R_0}\hat{f} = 56\,\text{kHz} \times \hat{f}$ in physical units.

We confirm the results by Zhu *et al.* [117] in that the turbulence is enhanced with increasing density and suppressed with increasing temperature, most visible in T_i which is shown in figure 4.3. However, investigating the different behaviour of electron and ion temperature, we find a surprising dependence on parallel heat conductivity, discussed in the following section.

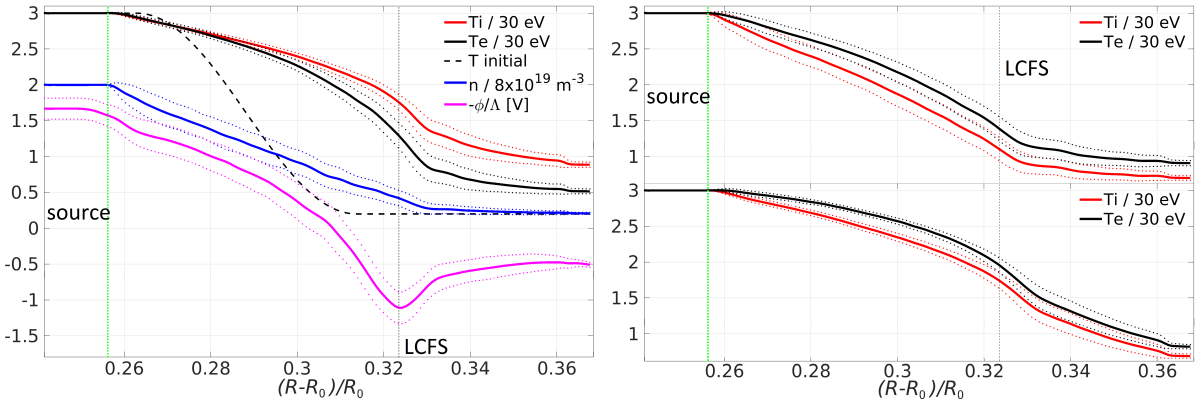

Figure 3.2: Mean radial profiles (T_i, T_e, T initial, $n, -\phi/\Lambda$ from top to bottom) at the outboard mid-plane at $t \approx 1.4$ ms. Dotted lines indicate the $\pm\sigma_f$ fluctuation level. The negative potential $-\phi$ and its fluctuation level are devided by $\Lambda = 2.69$. LCFS and source region are marked. Left: reference simulation with $\chi_{\parallel e0} = 26.6$, $\chi_{\parallel i0} = 1.15$, $\gamma_e = 2.5$. Top right: $\chi_{\parallel e0} = \chi_{\parallel i0} = 1.15$ and $\gamma_e = 0.1$ (case 2); bottom right: $\chi_{\parallel e0} = 26.6$, $\chi_{\parallel i0} = 1.15$, $\gamma_e = 0$ (case 1, see section 3.4.1).

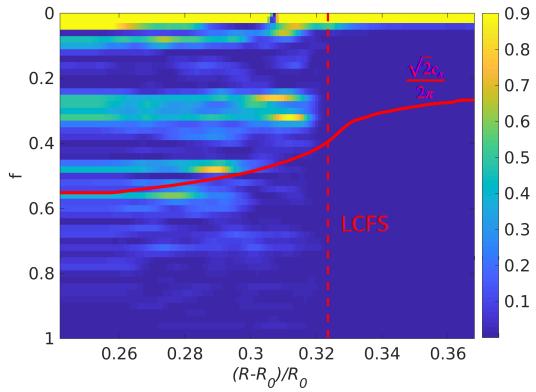

Figure 3.3: Frequency spectrum of poloidally and toroidally averaged electrostatic potential fluctuations.

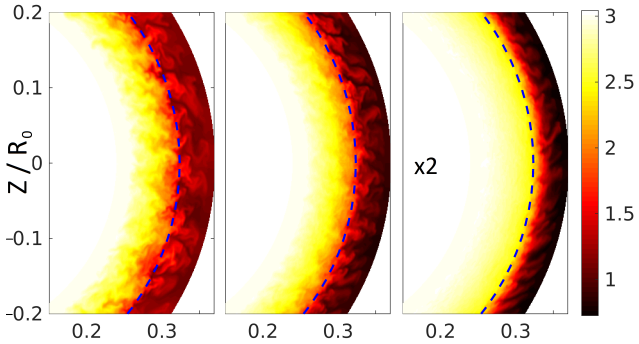

Figure 3.4: Outboard mid-plane ion temperature snapshot at 1.44 ms in: double density, reference, double temperature (left to right). Horizontal axis is $(R - R_0)/R_0$. LCFS marked by blue dashed line.

3.4.1 Parallel heat conduction

To test the relevance and effect of the parallel heat conduction, four additional simulations were carried out. Comparing to the reference ($n|_{core} = 2$, $T|_{core} = 3$) with $\chi_{\parallel e0} = 26.6$, $\chi_{\parallel i0} = 1.15$ and $\gamma_e = 2.5$ these have

1. $\chi_{\parallel e0} = 26.6$, $\chi_{\parallel i0} = 1.15$, $\gamma_e = 0$
2. $\chi_{\parallel e0} = \chi_{\parallel i0} = 1.15$ and $\gamma_e = 0.1$
3. $\chi_{\parallel e0} = \chi_{\parallel i0} = 0.1$ and $\gamma_e = 0.01$
4. $\chi_{\parallel e0} = 26.6$, $\chi_{\parallel i0} = 30$, $\gamma_e = 2.5$

T_e and T_i for cases 1 and 2 are shown in figure 3.2 on the right. In the reference run, and also double n and double T, ions are hotter in the SOL then electrons, as expected from experiments. This is due to the electron heat sheath transmission. Without this boundary condition (case 1), electrons are hotter. This trend extends into the confined region. A lowered electron heat conductivity (case 2) also requires a reduced γ_e to avoid unphysical gradients at the sheath, and hence also has the same effect. Additionally, a reduced electron heat conductivity increases the T_e and T_i fluctuation level and flattens profiles, likely due to the lowered flux surface symmetrization and fluctuation damping.

Further reducing both heat conductivities (case 3) has no effect on neither the profiles nor fluctuation levels at the outboard mid-plane. However, the up-down asymmetry becomes more visible, as in the results of Zhu *et al.* [117].

The difference in heat conductivity between electrons and ions **does not** explain the different saturation time of T_e and T_i. In fact, setting $\chi_{\parallel i0} = 30$ (case 4) or lowering it to 0.1 has barely any influence

on the profiles at all. The electron heat conductivity has a much higher impact on both electron and ion transport - only T_e enters Ohm's law and sheath boundary conditions, thereby setting the SOL potential and currents.

3.5 Conclusion

The thermal model in GRILLIX was extended by ion temperature dynamics, including the ion diamagnetic polarisation drift, leading to a self-consistent electric field with zonal flows and GAMs. In circular geometry simulations, the electric field on closed field lines balances the ion pressure gradient, somewhat exceeding it. In the SOL the electric potential follows the electron temperature due to sheath boundary conditions and Ohm's law. This leads to a maximum in the electrostatic potential at the LCFS and a jump of the electric field. Turbulence is destabilized by higher density, while higher temperature is somewhat stabilizing.

A 3D iterative implicit solver now allows for a realistically large parallel heat conductivity without affecting the time step and hence simulation time. The electron parallel heat conductivity, together with sheath heat transmission boundary conditions, largely determines the SOL temperature profile - for both electrons and ions. In the confined region it leads to flux surface symmetrization and fluctuation reduction. The ion heat conductivity, on the other hand, plays a much smaller role.

Acknowledgements

This work has been the framework of the EUROfusion Consortium and has received funding from the Euratom research and training program 2014–2018 and 2019–2020 under Grant Agreement No. 633053. The views and opinions expressed herein do not necessarily reflect those of the European Commission.

Chapter 4

Corrigendum: Thermal dynamics in the flux-coordinate independent turbulence code GRILLIX

W. Zholobenko, A. Stegmeir, T. Body, A. Ross, P. Manz, O. Maj, D. Coster, F. Jenko, M. Francisquez[1)], B. Zhu[2)], B. N. Rogers[3)]

Max-Planck-Institut für Plasmaphysik, D-85748 Garching, Germany
[1)] MIT Plasma Science and Fusion Center, Cambridge, Massachusetts 02139, USA
[2)] Lawrence Livermore National Laboratory, 7000 East Avenue, Livermore, CA 94550, USA
[3)] Department of Physics and Astronomy, 6127 Wilder Laboratory, Dartmouth College, Hanover, New Hampshire 03755, USA

Email: Wladimir.Zholobenko@ipp.mpg.de

Appeared in: Zholobenko W, Stegmeir A, Body T, et al. Corrigendum: Thermal dynamics in theflux-coordinate independent turbulence code GRILLIX. *Contributions to Plasma Physics.* 2020; 60:e202000056.
https://doi.org/10.1002/ctpp.202000056
Original publication [2] and detailed disclaimer are included in the appendix.

We have discovered that one of the original articles [1] findings, that the actual choice of the dimensionless parameter $\chi_{\parallel i0}$ for the ion heat conductivity* seemed to play no role for the simulation results, was not physical. Instead, due to a mistake in the handling of input parameters, $\chi_{\parallel i0}$ was actually not used in the code - the dimensionless electron heat conductivity $\chi_{\parallel e0}$ was used instead. Hence, the results in chapter 4 and the conclusions are correct only if $\chi_{\parallel i0} = \chi_{\parallel e0}$. For the reference case, this means $\chi_{\parallel i0} = \chi_{\parallel e0} = 26.6$ was used†, instead of what we thought was $\chi_{\parallel i0} = 1.15$ and $\chi_{\parallel e0} = 26.6$. The rest of the code and model is correct.

We have fixed the error, verified the code and rerun all the simulations. The main conclusion is that the dimensionless ion heat conductivity $\chi_{\parallel i0}$ plays as much of a role for the equilibrium ion temperature profile T_i as the electron heat conductivity $\chi_{\parallel e0}$ for the electron profile T_e. Further, with the correct heat conductivity $\chi_{\parallel i0} = 1.15$, T_i saturates faster - after $t \gtrsim 50\frac{R_0}{c_{s0}} \approx 0.9$ ms - while it was still not saturated at 1.5 ms with the wrong $\chi_{\parallel i0} = \chi_{\parallel e0} = 26.6$. The saturation time for the plasma density n and electron temperature T_e remain the same - $t \gtrsim 30\frac{R_0}{c_{s0}} \approx 0.5$ ms.

Figure 4.1, left, shows the saturated radial profiles for the reference simulation. We find that in comparison to the mistakenly used $\chi_{\parallel i0} = 26.6$, the proper, lower ion heat conductivity $\chi_{\parallel i0} = 1.15$ increases the stationary ion temperature gradient $\partial_r T_i$ in the confined region, leading to $T_i < T_e$ at the separatrix. The T_i profile and fluctuation level are now similar to those of the plasma density n. The T_e and n profiles remain unaffected. The stationary profile of the electrostatic potential ϕ flattens in

*$\chi_{\parallel i0}$ is obtained by normalizing the Braginskii ion parallel heat conductivity to $\chi_\parallel^i = \chi_{\parallel i0} n_0 c_{s0} R_0 \hat{T}_i^{5/2}$, with $\hat{T}_i = T_i/T_{i0}$.
†We have for deuterium $\chi_{\parallel i0}/\chi_{\parallel e0} = 23 \neq 35$ because the electron collision frequency was calculated with $Z_{\text{eff}} = 1.5$.

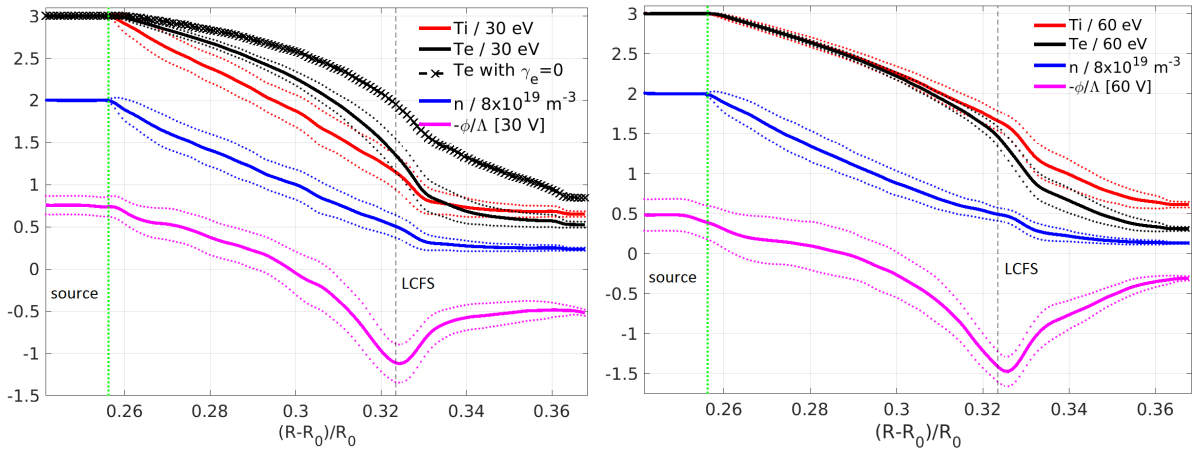

Figure 4.1: Mean radial profiles (T_i, T_e, n, $-\phi/\Lambda$) at the outboard mid-plane in saturated state. Dotted lines indicate the $\pm\sigma_f$ fluctuation level. The negative potential $-\phi$ and its fluctuation level are divided by $\Lambda = 2.69$. LCFS and source region are marked. Left: reference case with $T_e = T_i = 90$ eV at the core boundary, with additionally the T_e profile from the simulation with no sheath heat conduction (case 1 from chapter 4.1, $\gamma_e = 0$). Right: simulation with double the temperature.

the confined region due to the lower T_i, while it remains the same in the SOL following T_e. In the far SOL, $T_i > T_e$ is found due to electron sheath heat transmission - unlike in the case without this boundary condition ($\gamma_e = 0$). We note that the previously observed result, $T_i > T_e$ also at the separatrix, is recovered again at higher temperature, see double temperature case in figure 4.1, right.

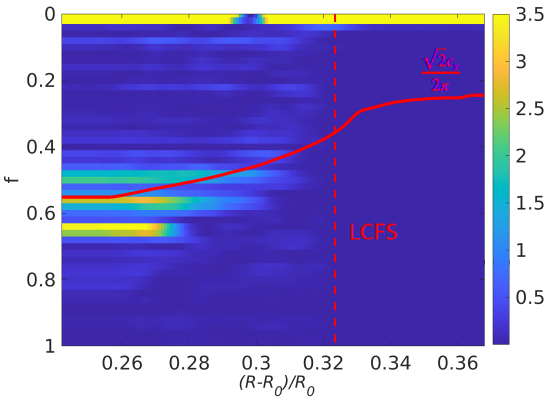

Figure 4.2: Frequency spectrum of poloidally and toroidally averaged electrostatic potential fluctuations.

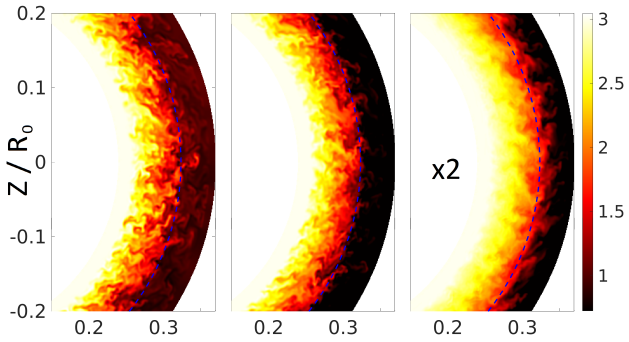

Figure 4.3: Outboard mid-plane ion temperature snapshot at 1.44 ms in: double density, reference, double temperature (left to right). Horizontal axis is $(R - R_0)/R_0$. LCFS marked by blue dashed line.

Other results of the original article [1] hold true, at least qualitatively. The GAM frequency spectrum, shown in 4.2, is somewhat different quantitatively. With the lower ion heat conductivity $\chi_{\parallel i0}$, the ion temperature fluctuates more, but overall the turbulence is nonetheless enhanced with increasing density and suppressed with increasing temperature, see figure 4.3. In cases 2 and 3 from chapter 4.1, we already had $\chi_{\parallel i0} = \chi_{\parallel e0}$ (and case 4 was actually nearly the same as the reference scenario), so the result holds that reducing $\chi_{\parallel i0}$ and $\chi_{\parallel e0}$ below 0.1 has no impact on outboard midplane profiles.

We additionally remark that the Bohm sheath boundary conditions (7) for parallel velocity should contain T_i, $u_\parallel \gtrless \sqrt{T_e + T_i}$. Also, there is a mistake in the indexes in equation (9): instead of $\nabla_\perp p^{i+j}$, it should read $\nabla_\perp p_i^{t+j}$.

Acknowledgements

This work has been carried out within the framework of the EUROfusion Consortium and has received funding from the Euratom research and training programme 2014-2018 and 2019-2020 under grant agreement No 633053. The views and opinions expressed herein do not necessarily reflect those of the European Commission.

Chapter 5

Electric field and turbulence in global Braginskii simulations across the ASDEX Upgrade edge and scrape-off layer

W. Zholobenko, T. Body, P. Manz, A. Stegmeir, B. Zhu[1)], M. Griener, G. D. Conway, D. Coster, F. Jenko, and the ASDEX Upgrade Team[a)]

Max-Planck-Institut für Plasmaphysik, D-85748 Garching, Germany
[1)] Lawrence Livermore National Laboratory, 7000 East Avenue, Livermore, CA 94550, USA
[a)] see author list of H. Meyer *et al* 2019 *Nucl. Fusion* **59** 112014

Email: Wladimir.Zholobenko@ipp.mpg.de

Appeared in: W Zholobenko *et al* 2021 *Plasma Phys. Control. Fusion* **63** 034001,
https://doi.org/10.1088/1361-6587/abd97e
Presented as an invited talk at: Joint Varenna-Lausanne International Workshop on the Theory of Fusion Plasmas 2020, October 12-16, Lausanne, Switzerland
Original publication [3] and detailed disclaimer are included in the appendix.

Abstract Turbulence simulations in diverted geometry across the edge and scrape-off layer (SOL) of ASDEX Upgrade are performed with the GRILLIX code [107]. The underlying global (full-f) drift-reduced Braginskii model allows to concurrently study the self-consistent dynamics of the turbulence and the background as well as the evolution of toroidal and zonal flows. Different contributions to the radial electric field are identified. The dominant contribution on closed flux surfaces comes from the ion pressure gradient, due to the diamagnetic drift in the curved magnetic field. Large deviations can be induced, in particular, by the polarization particle flux, leading to zonal flows. The latter are driven by small-scale eddies, but do not exhibit much impact on the overall transport which is driven by ballooning modes at larger scales. Ion viscosity is found to be important in damping poloidal rotation through adjusting of the parallel velocity profile, but not via direct vorticity damping. The zonal flow drive peaks at the separatrix, where a strong shear layer forms due to the sheath-induced counter-propagating SOL flow, allowing for the formation of a transport barrier. The temperature profile across the separatrix is determined by the competition between cross-field transport and outflow in the SOL, the latter being largely controlled by the parallel heat conductivity.

5.1 Introduction

The radial electric field and the resulting $E \times B$ flows are of central importance in determining magnetic confinement properties of tokamaks [41, 186, 187]. In the confined region, the electric field consists of mean-field (neoclassical) contributions as well as of zonal flows generated by the turbulence [44]. The latter result from the interaction of poloidal and radial fluctuations through the Reynolds stress [66], but can also be amplified by the anomalous Stringer drive [188, 189]. A review of zonal flow

experiments can be found in Ref. [67]. In the scrape-off layer (SOL), on the other hand, in the absence of closed flux surfaces, the electric field is primarily determined by dynamics parallel to the magnetic field, and particularly by the sheath boundary conditions [49, 150]. The interface between closed and open field lines is of central interest. Different mechanisms act on the two sides of the separatrix, leading to electric fields of different signs. Therefore, the electric field changes abruptly across a narrow region and produces strongly sheared $E \times B$ flows [190]. This shearing is thought to act as a turbulence suppression mechanism [191, 192], playing a key role in the transition to improved confinement regimes.

To study the formation of the electric field and its back-reaction on turbulent transport, involving both mean and zonal flows, a global (full-f) turbulence model is required. While gyrokinetic models [77, 193] can be more realistic if collisions and electromagnetic effects are taken into account, fluid models are attractive due to their significantly lower computational cost. In the present work, we present theoretical and computational results based on the global version of the drift-reduced Braginskii two-fluid model [56, 57], which is widely used for both direct turbulence simulations [99, 102, 104, 194] and simplified transport studies [94, 195]. Although restricted (strictly speaking) in its validity to sufficiently collisional regimes, important insights can be gained. More refined studies may become possible in the future with the help of gyrofluid models employing appropriate closure schemes [72, 196], with full-f formulations currently still under development [110]. The study of the tokamak edge is further complicated by the relatively complex magnetic geometry. As diverted geometry is beneficial for confinement [111, 197, 198] and impurity exhaust [11], theoretical and computational studies must adapt to that geometry. A computationally feasible implementation is achieved through the flux-coordinate independent (FCI) approach [160, 161], implemented in the code GRILLIX [107].

In the present study, we report on the first global turbulence simulations in diverted geometry across the edge and SOL of ASDEX Upgrade (AUG), based on the L-mode discharge #36190. The results illuminate many aspects of tokamak edge physics, such as high and intermittent fluctuation levels, up to 10% at the separatrix and of order unity in the SOL. Turbulent vortices in the confined region develop a mean poloidal rotation in the electron diamagnetic drift direction, as the radial electric field balances the ion pressure gradient. Due to the sheath at the divertor, the flow is in the ion diamagnetic drift direction in the SOL. A shear layer develops at the separatrix in which vortices are strained out and decorrelated. Zonal flows are driven by drift waves and damped by the geodesic acoustic mode. However, this barely affects the ballooning driven transport. Ion viscosity is found to be important for damping poloidal rotation. The competition between perpendicular and parallel transport leads to the formation of a temperature pedestal due to the high parallel heat conduction. Nevertheless, we note that the validity of our fluid model might be yet restricted due to the low collisionality in the plasma edge, and lack of neutral gas recycling and impurities in the SOL.

The remainder of the manuscript is organized as follows. In Sec. 5.2 we illustrate the key components of the model that lead to the formation of the multi-scale electric field (the full set of equations is detailed in Appendix 5.7). Sec. 5.3 describes the performed ASDEX Upgrade simulations: the setup, saturation, input power, equilibrium profiles, and fluctuation levels. The electric field is presented and analysed in Sec. 5.4, with its determining contributions and its impact on the turbulence. A separate discussion on the role of fluid closure terms – ion viscosity and heat conductivities – is presented in Sec. 5.5. Finally, conclusions and an outlook are given in Sec. 5.6.

5.2 The electric field in drift-reduced Braginskii models

The radial electric field E_r in a tokamak is commonly explained by the radial force balance. It is derived from the Braginskii ion momentum conservation equation [56] by neglecting inertia, viscosity and friction (electron momentum is assumed to be small in this regard). This yields in the SI unit system

$$E_r = \frac{\partial_r p_\mathrm{i}}{en} - (\mathbf{v} \times \mathbf{B}) \cdot \mathbf{e}_r = \frac{\partial_r p_\mathrm{i}}{en} + v_\phi B_\theta - v_\theta B_\phi, \tag{5.1}$$

where $\partial_r p_\mathrm{i}$ is the radial component of the ion pressure gradient, n the plasma density, e the elementary charge and $\mathbf{B}$ the magnetic field. The fluid velocity $\mathbf{v}$ with its poloidal (v_θ) and toroidal (v_ϕ) component is in this expression yet undetermined, but depends implicitly on the electric field and other parameters

in a non-trivial way. Therefore, this force balance equation is illustrative, but insufficient to actually determine the electric field. To do that we require additionally at least the ion particle balance equation, and further charge and momentum balance equations.

Following the drift reduction procedure we assume that the dynamics of interest is slow compared to the gyro-motion, $\omega \ll \Omega_\mathrm{i} = eB/(M_\mathrm{i}c)$. Applying an ordering expansion to the perpendicular momentum balance, plasma motion can be expressed via perpendicular drift velocities and parallel streaming $u_\parallel$ along magnetic field lines. For ions, this reads

$$\mathbf{v}^\mathrm{i} = \mathbf{v}_E + \mathbf{v}^\mathrm{i}_* + \mathbf{u}_\mathrm{pol} + u_\parallel \mathbf{b}, \tag{5.2}$$

where $\mathbf{b} = \mathbf{B}/B$ is the unit vector of the magnetic field. The perpendicular drifts are to leading order the $E \times B$ velocity $\mathbf{v}_E = \mathbf{E} \times \mathbf{B}/B^2$ and the diamagnetic velocity $\mathbf{v}^\mathrm{i}_* = \mathbf{B} \times \nabla p_i/(enB^2)$, i.e. the inverse of (5.1) in terms of $\mathbf{v}$. The polarisation velocity $\mathbf{u}_\mathrm{pol}$ includes the first order correction effects in the radial force balance which have been neglected in eq. (5.1), namely inertia and viscosity. It is responsible for the emergence of turbulence in our model, as detailed in section 5.2.2. The obtained expression for the ion velocity (5.2) is inserted into the ion continuity equation yielding

$$\frac{\partial n}{\partial t} + \nabla \cdot n \left(\mathbf{v}_E + \mathbf{v}^\mathrm{i}_* + \mathbf{u}_\mathrm{pol} + u_\parallel \mathbf{b} \right) = S_n, \tag{5.3}$$

with S_n a source term.

The diamagnetic particle flux can be rewritten as

$$n\mathbf{v}^\mathrm{i}_* = -\nabla \times \left(\frac{p_\mathrm{i}}{eB^2} \mathbf{B} \right) + \frac{p_\mathrm{i}}{e} \nabla \times \frac{\mathbf{B}}{B^2} \approx -\nabla \times \left(\frac{p_\mathrm{i}}{eB^2} \mathbf{B} \right) + \frac{2p_\mathrm{i}}{eB^3} \mathbf{B} \times \nabla B, \tag{5.4}$$

which due to $\nabla \cdot \nabla \times \mathbf{A} = 0$ shows that it is 'nearly divergence-free' [49, chapter 18.7], in the sense that its divergence is non-zero only in a curved magnetic field. The last equality requires $\nabla \times \mathbf{B} \ll \mathbf{b} \times \nabla B$.

It is convenient to introduce here the curvature operator

$$C(f) = -\nabla \cdot \left(\frac{\mathbf{B}}{B^2} \times \nabla f \right) = -\left(\nabla \times \frac{\mathbf{B}}{B^2} \right) \cdot \nabla f, \tag{5.5}$$

which represents advection of a field f along the magnetic field curvature.* It allows us to write

$$\nabla \cdot (n\mathbf{v}_E) = \mathbf{v}_E \cdot \nabla n - nC(\varphi), \tag{5.6}$$

$$\nabla \cdot (n\mathbf{v}^\mathrm{i}_*) = -\frac{1}{e} C(p_\mathrm{i}), \tag{5.7}$$

where we express the electric field component orthogonal to the magnetic field via the electrostatic potential $\mathbf{E}_\perp = -\nabla_\perp \varphi$, neglecting electromagnetic effects in the drift plane. We notice that due to the diamagnetic particle flux being 'nearly divergence-free', it does not cause any advection, an effect known as 'diamagnetic cancellation'. The pressure gradient enters only through magnetic curvature.

In quasi-steady state $\left\langle \frac{\partial n}{\partial t} \right\rangle = 0$, the ion particle balance equation (5.3) for the background profiles becomes

$$\left\langle \mathbf{v}_E \cdot \nabla n - nC(\varphi) - \frac{1}{e} C(p_\mathrm{i}) + \nabla \cdot (n\mathbf{u}_\mathrm{pol}) + \nabla \cdot (nu_\parallel \mathbf{b}) - S_n \right\rangle = 0, \tag{5.8}$$

where the brackets $\langle \ldots \rangle$ denote a suitable ensemble average, either in time, in space, or both. This equilibrium particle balance is central in determining the electric field on closed field lines.

It is sufficient to consider only the ion continuity equation as the electron particle balance is tied to it by the quasi-neutrality condition $e\partial_t(n_\mathrm{e} - n_\mathrm{i}) = \nabla \cdot \mathbf{j} = 0$. We illustrate results using the ion particle balance, but it is equivalent and in fact numerically advantageous to solve the electron continuity (5.25) and the quasi-neutrality (5.26) equations instead, see also section 5.2.2 and appendix 5.7. However, this approach constrains our model to a single ion species – for a drift-reduced multi-species model see e.g. Ref. [125].

*Alternatively, one could replace the diamagnetic velocity by $\tilde{\mathbf{v}}^\mathrm{i}_* = \frac{2T_\mathrm{i}}{eB^3} \mathbf{B} \times \nabla B$ for a flux conservative formulation [104, 199].

5.2.1 The equilibrium (static) electric field on closed flux surfaces

In the confined region, to lowest order, we can assume $\langle \mathbf{v}_E \cdot \nabla n \rangle = 0$ since for the background we have only a radial density gradient and no radial $E \times B$ advection. For now, let us also neglect any flows, i.e. $\left\langle \nabla \cdot n(\mathbf{u}_{\text{pol}} + u_\parallel \mathbf{b}) \right\rangle = 0$. In absence of stationary sources S_n, the balance for the stationary fields becomes

$$n\nabla \cdot (\mathbf{v}_E) + \nabla \cdot (n\mathbf{v}_*^{\text{i}}) = -nC(\varphi) - C(p_{\text{i}})/e = 0. \tag{5.9}$$

As there are no background poloidal gradients along closed flux surfaces, $\partial_\theta f \approx 0$, the balance is fulfilled by the static equilibrium radial electric field

$$E_r = \frac{\partial_r p_{\text{i}}}{en}. \tag{5.10}$$

We expect the dominant contribution to the radial electric field on closed flux surfaces to be this balance between $E \times B$ and diamagnetic compression of ion density along the curved magnetic field [41, 186]. Corrections, especially in L-mode, can be significant though – see section 5.4.1. It is worth pointing out that under this equilibrium electric field, the background plasma is at rest (i.e. static), but fluctuations are $E \times B$ advected. Deviations from eq. (5.9), on the other hand, also impact the background.

5.2.2 Anomalous electric field

Besides the lowest order equilibrium electric field (5.10), additional contributions arise from polarisation and parallel particle fluxes contained in eq. (5.8). Obtaining closed form analytical expressions for their stationary contributions is not possible. In this section we discuss the form and role of the ion polarisation velocity and viscosity, while numerical simulation results will be presented in section 5.4.

As noted at eq. (5.2), the polarisation velocity is the correction to the perpendicular ion velocity which contains inertia and viscosity. However, the latter depend themselves on the perpendicular ion velocity in a non-trivial way. Therefore, in reduced fluid models, the polarisation velocity is approximated to first order by inserting the zero order approximation $\mathbf{v}_{\perp 0}^{\text{i}} = \mathbf{v}_E + \mathbf{v}_*^{\text{i}}$ into inertia and viscous stress. Since the divergence of the zeroth order velocities is of the same order as the divergence of the polarisation velocity, $\nabla \cdot \left(n\mathbf{u}_{\text{pol}}\right) \sim \nabla \cdot \left(n\mathbf{v}_{\perp 0}^{\text{i}}\right)$, it has to be retained for divergence terms [37, 38]. Explicitly, the expression reads

$$\nabla \cdot \left(n\mathbf{u}_{\text{pol}}\right) = \nabla \cdot \left[-\frac{nM_{\text{i}}}{eB^2} \left(\frac{\partial}{\partial t} + \mathbf{v}_E \cdot \nabla + u_\parallel \nabla_\parallel \right) \left(\nabla_\perp \varphi + \frac{\nabla_\perp p_{\text{i}}}{en} \right) \right] - \frac{1}{6e} C(G), \tag{5.11}$$

where the first term on the right hand side represents inertia, and the second viscosity. We can also write

$$\nabla \cdot \left(n\mathbf{u}_{\text{pol}}\right) = \nabla \cdot \left(n\mathbf{u}_{\text{pol}}^{\text{in}}\right) - \frac{1}{6e} C(G). \tag{5.12}$$

The viscous stress function [128] is

$$G = -\eta_0^{\text{i}} \left[\frac{2}{B^{3/2}} \nabla \cdot \left(u_\parallel B^{3/2} \mathbf{b} \right) - \frac{1}{2} \left(C(\varphi) + \frac{1}{en} C(p_{\text{i}}) \right) \right], \tag{5.13}$$

with the dominant Braginskii viscosity coefficient $\eta_0^{\text{i}} = 0.96 p_{\text{i}} \tau_{\text{i}}$ and ion collision time τ_{i}.

Due to the time derivative in the inertial part, the direct implementation of the ion continuity equation is cumbersome. Instead, in drift-reduced Braginskii codes like GRILLIX, the electron continuity equation is used – where the polarisation velocity can be neglected due to the small electron mass – together with the quasi-neutrality, or vorticity, equation $e\partial_t(n_{\text{e}} - n_{\text{i}}) = \nabla \cdot \mathbf{j} = 0$. The latter reads

$$e\nabla \cdot \left(n\mathbf{u}_{\text{pol}}\right) = C(p_{\text{e}} + p_{\text{i}}) - \nabla \cdot (j_\parallel \mathbf{b}), \tag{5.14}$$

with the parallel current $j_\parallel = en(u_\parallel - v_\parallel)$ and parallel electron velocity $v_\parallel$. If the right hand side of (5.14) balances, i.e. the diamagnetic charge separation is balanced by a parallel current, we obtain the Pfirsch-Schlüter current [138, chapter 8.4]. However, we will see in section 5.4 that the divergence of the polarisation flux is not necessarily small.

Equation (5.14) is typically called vorticity equation because under some (too) strong approximations, regarding the size of density fluctuations and homogeneity of the magnetic field, one can rewrite

$$\nabla \cdot \left[\frac{n}{B^2} \frac{\mathrm{d}}{\mathrm{d}t} \left(\nabla_\perp \varphi + \frac{\nabla_\perp p_\mathrm{i}}{en} \right) \right] \sim \frac{n_0}{B} \frac{\mathrm{d}}{\mathrm{d}t} \mathbf{b} \cdot \nabla \times \left(\mathbf{v}_E + \mathbf{v}_*^\mathrm{i} \right). \tag{5.15}$$

The quantity on the right hand side is the 2D fluid vorticity $\Omega_\mathrm{F} = \mathbf{b} \cdot \nabla \times \left(\mathbf{v}_E + \mathbf{v}_*^\mathrm{i} \right)$, not to be confused with the generalised vorticity defined in appendix 5.7. Note that while the diamagnetic velocity is 'nearly divergence-free', it is not rotation-free.

The inertial part of the vorticity equation is central to fluid plasma turbulence models, particularly the non-linearity $\mathbf{v}_E \cdot \nabla \mathbf{E}_\perp$, as it is ultimately responsible for the turbulent inverse energy cascade [200]. This term also contains the Reynolds stress, responsible for zonal flow drive [66]. We note that a rigorous decomposition into mean field and fluctuating flows in a global model is quite complex, e.g. one requires the Favre instead of the Reynolds average [201]. Further, a second Reynolds stress term contained in $u_\parallel \nabla_\parallel \nabla_\perp \varphi$ couples 2D turbulence to parallel dynamics [202]. This decomposition will not be further detailed here. In the steady-state, we must have $\left\langle \partial_t \left(\nabla_\perp \varphi + \frac{\nabla_\perp p_\mathrm{i}}{en} \right) \right\rangle = 0$. Therefore, we will use $\left\langle \nabla \cdot \left(n \mathbf{u}_\mathrm{pol}^\mathrm{in} \right) \right\rangle$ as a measure of the stationary Reynolds stress.

5.2.3 The role of ion viscosity and poloidal rotation

In this section we summarize some key insights from neoclassical theory [138] for the confined plasma. The main difference to our model is that inertia, and hence the polarisation velocity $\mathbf{u}_\mathrm{pol}$ from the previous chapter, is neglected. In this case it is then a good assumption that pressure and electrostatic potential are constant along closed flux surfaces ψ. With $\partial_r f = R B_p \partial_\psi f$, one obtains the relation [138, chapter 8.5]

$$E_r = \frac{1}{en} \frac{\partial p_\mathrm{i}}{\partial r} + u_\parallel B_\theta \frac{B}{B_\phi} - v_\theta \frac{B^2}{B_\phi}. \tag{5.16}$$

v_θ is the flux surface averaged poloidal rotation. An important result is then that according to the Braginskii fluid closure, poloidal rotation is damped to zero due to the ion viscosity [138, chapter 12.3]. The reason is that in a flux surface average over the parallel momentum equation (5.27), one finds the condition

$$\langle \mathbf{B} \cdot \nabla \cdot \Pi_\mathrm{i} \rangle_S = 3 \eta_0^\mathrm{i} \left\langle \left(\nabla_\parallel B \right)^2 \right\rangle_S v_\theta = 0. \tag{5.17}$$

Π_i is thereby the Braginskii ion viscous stress tensor. We will write this with the viscous stress function G defined above in eq. (5.13),

$$\mathbf{B} \cdot \nabla \cdot \Pi_\mathrm{i} = \frac{2}{3} B^{5/2} \nabla_\parallel \frac{G}{B^{3/2}}. \tag{5.18}$$

The situation is more complicated, however, when turbulent transport is considered (i.e. $\mathbf{u}_\mathrm{pol}$) – see also [138, chapter 13.1] – as will be detailed in section 5.4.1 on the basis of numerical simulations. Note, as the viscous stress function G appears in Braginskii's ion temperature equation (5.30), this flow damping acts as a heating mechanism for ions known as 'magnetic pumping'.

5.2.4 The (simple) scrape-off layer electric field

In the SOL, due to the absence of closed flux surfaces, parallel dynamics and boundary conditions take a more important role [49, 150]. The electrostatic Ohm's law – used here for simplicity, although our full model is electromagnetic, see appendix 5.7 – reads

$$\eta_\parallel j_\parallel = -\nabla_\parallel \varphi + \frac{\nabla_\parallel p_\mathrm{e}}{en} + \frac{0.71}{e} \nabla_\parallel T_\mathrm{e}, \tag{5.19}$$

with resistivity $\eta_\parallel$. We have insulating sheath boundary conditions $j_\parallel = 0$ at the divertor. And in present simulations, without any neutral particles or impurities, there are no significant sources or sinks for any terms in the above equation. This results in flat parallel gradients (in an average over turbulent

fluctuations). Therefore, T_e is roughly equal at the outboard mid-plane and at the divertor, and resistivity is negligibly small. At the divertor, the insulating sheath boundary condition

$$\varphi = \Lambda T_e \tag{5.20}$$

for the potential applies, with $\Lambda = -\frac{1}{2}\ln\left[\left(2\pi\frac{m_e}{M_i}\right)\left(1+\frac{T_i}{T_e}\right)\right] \approx 2.69$. Hence, due to $\nabla_\parallel \varphi \approx 0$, we expect $\varphi = \Lambda T_e$ to also hold at the outboard mid-plane. Having $E_r \sim \partial_r p_i / en$ in the confined region (5.10) and $E_r \sim -\Lambda \partial_r T_e$ in the SOL, we expect a jump of the electric field across the separatrix, and contra-rotating poloidal flows inside and outside of it [190].

It should be noted that in reality, contrary to our yet simplified model, the presence of neutral gas and impurities in the SOL leads to more complex parallel gradients, even in attached conditions. Furthermore, the sheath can conduct significant currents. Therefore, the SOL dynamics itself can be much more involved, particularly in detached plasmas [203].

5.3 ASDEX Upgrade simulations

It is not possible to solve analytically the full set of equations detailed in appendix 5.7, and particularly the non-linear polarisation discussed in section 5.2.2. Therefore, we employ the code GRILLIX [107]. For the first time, global numerical simulations are performed in a diverted magnetic equilibrium and at experimental parameters based on an ASDEX Upgrade discharge (#36190), without any down-scaling. The setup is presented in Sec. 5.3.1 and results are summarized in subsequent sections. The reference simulation can be seen in supplementary movie 1 (available online at (stacks.iop.org/PPCF/63/034001/mmedia)). It shows the initial evolution of plasma density within the poloidal plane, as well as outboard mid-plane pressure and radial electric field profiles. Further, supplementary movie 2 shows the dynamics of density fluctuations relative to the background, in the saturated state of the simulation with increased poloidal resolution (see text below).

We note that these simulations are very computationally demanding, consuming each between 0.4-2 MCPUh and 2-5 months of run time, as described in the next section.

5.3.1 The simulation setup

This section details the setup of the simulations – namely geometry, parameters, initial state, resolution and computational cost – guided by the AUG discharge #36190 at time $t = 2$-4 s. In this discharge the toroidal magnetic field was $B_{tor} = -2.5$ T, i.e. in favourable configuration with $\mathbf{B}\times\nabla B \sim -\hat{\mathbf{e}}_Z$ towards the X-point. The plasma current was $I_p = 0.8$ MA[†] resulting in $q_{95} = 4.4$, and the average triangularity was $\delta = 0.21$. Further important inputs are the measured $T_e \approx 350$ eV and $n_e \approx 2\times10^{19}$ m^{-3} at $\rho_{pol} = 0.9$, and $T_e \approx 50-80$ eV and $n_e \approx 1\times10^{19}$ m^{-3} at the separatrix. The total heating power in the discharge was roughly 800 kW: 550 kW neutral beam injection, 500 kW ohmic heating and subtracting 250 kW radiation losses.

The geometry is illustrated in figure 5.1 by the poloidal flux function Ψ. The separatrix and machine walls are highlighted. The simulation domain extends beyond the divertor legs due to the implementation of parallel boundary conditions via penalisation [107]. We define the normalized poloidal flux radius as $\rho_{pol} = \sqrt{\frac{\Psi-\Psi_0}{\Psi_X-\Psi_0}}$, with Ψ_0 and Ψ_X the poloidal magnetic flux at magnetic axis and separatrix, respectively. Simulations are performed for $\rho_{pol} > 0.9$, since our fluid model is not valid in the plasma core, and the reduced domain saves computational cost. The outer most flux surface is chosen at the location where the HFS main chamber wall acts as a plasma limiter, at $\rho_{pol} = 1.05$.

Our choice of reference values is guided by parameters and measurements in AUG discharge #36190: major radius $R_0 = 1.65$ m, magnetic field on axis $B_0 = 2.5$ T, density $n_0 = 10^{19}$ m^{-3}, electron and ion temperatures $T_{e0} = T_{i0} = 100$ eV, $Z_{eff} = 1.3$ and deuterium ion mass $M_i = 2m_p$. We note that in a

[†]One difference between experiment and simulation is the choice of the helicity of the poloidal magnetic field: in the experiment, the plasma current flows in the opposite direction to the toroidal magnetic field, while we chose them to be parallel in most of our simulations, i.e. the poloidal magnetic field rotates in the opposite direction. However, we have repeated the reference simulation (defined below) with the correct helicity and found no physical difference except the direction of toroidal rotation – within a poloidal plane, nothing changes at all.

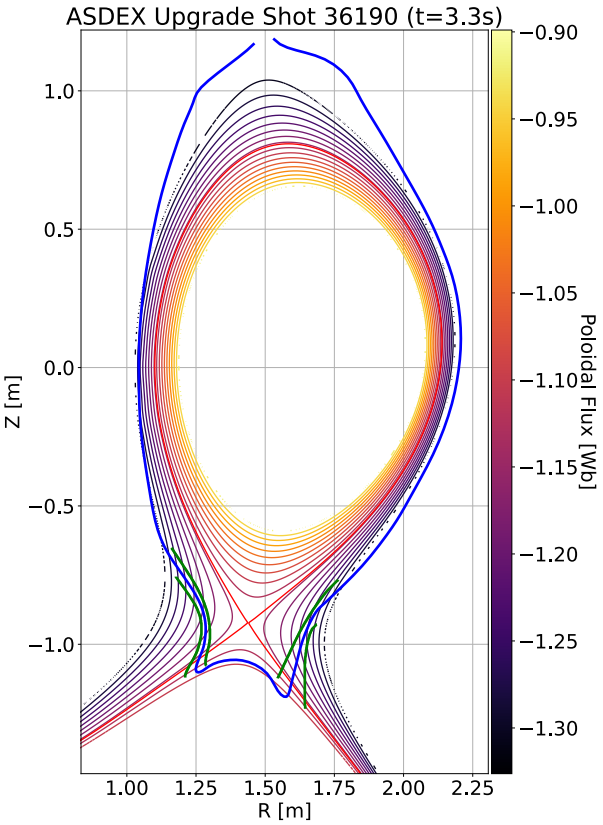

Figure 5.1: (Left) Flux surfaces of the equilibrium used for the simulation. The red line marks the seperatrix. The blue line gives the first wall and divertor. The simulation domain extends beyond the divertor legs due to the implementation of parallel boundary conditions via penalisation [107], with the penalisation transition area bounded by the two green lines.

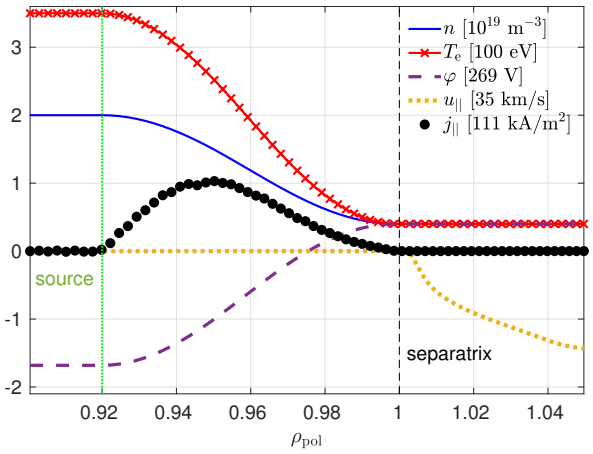

Figure 5.2: Initial normalized outboard mid-plane ($Z = 0$) profiles in the reference simulation.

global model, reference density and temperature are only required for the normalization of the equations, to write them in dimensionless form as in appendix 5.7, and have no physical relevance. They are chosen only on the order of measured separatrix values, since their exact choice does not matter. Z_{eff} is considered only in the calculation of the electron collision frequency. The resulting dimensionless collisionless parameters of the system – see appendix 5.7 for their definition – are $\delta = 2854.2$, $\beta_0 = 3.227 \times 10^{-5}$, $\mu = 2.723 \times 10^{-4}$ and $\zeta = 1$. The collisional parameters are $\nu_{e0} = 12.30$, $\eta_{\|0} = 0.0017$, $\chi_{\|e0} = 940$, $\chi_{\|i0} = 35.35$ and $\eta_{i0} = 8.70$. The Braginskii heat conductivity is known to be inappropriate at low collisionality [94, 204, 205]. For instance, it becomes arbitrarily large as $\sim T^{5/2}$ due to the lack of kinetic flux limiting effects, such as Landau damping. In this work, we use a simple flux limiter which reduces the stiffness and therefore computational expense of the parallel heat conduction: $\chi_{\|e,i0} T_{e,i}^{5/2} \leq 940$. For the chosen reference values, we obtain as reference drift scale and ion Larmor radius

$$\rho_{s0} = \frac{\sqrt{M_i T_{e0}}}{eB_0} = \rho_{i0} = \frac{\sqrt{M_i T_{i0}}}{eB_0} = 0.578 \text{ mm}. \tag{5.21}$$

Note that the local Larmor radius varies with magnetic field and temperature. E.g., at reference temperature, it is larger by 25% at the outboard mid-plane due to the reduced local magnetic field of $B \approx 2$ T.

In diverted geometry and in absence of neutral gas ionization, we find that density can drop arbitrarily low in the far SOL and private flux region. This contradicts the experimental observation that density can even rise in the far SOL [206], i.e. the simulations are missing the necessary mechanism, e.g. neutral gas ionization. It also makes the solution of the equations unnecessarily expensive, since in particular the parabolic part becomes very stiff at low collisionality. As a simple solution we apply an adaptive source to keep the density above 3×10^{17} m^{-3}, and temperatures above 3 eV. This source does not hinder cross-field inflow but limits parallel outflow in the far SOL, starting to act above $\rho_{\text{pol}} = 1.02$ in the reference simulation, but e.g. only above $\rho_{\text{pol}} = 1.04$ in the simulation in section 5.5.2. For simplicity, respectively due to the unphysical core boundary at $\rho_{\text{pol}} = 0.9$, simulations are adaptively flux driven: the heat and particle sources at the core boundary are adapted in time such as to hold density and temperature fixed there – while in the rest of the domain they evolve freely.

In a global code, background profiles are not chosen but rather evolve freely in accordance with turbulent fluxes. Nonetheless, an initial state must be chosen for the simulation. The most trivial choice

would be a flat, or even zero, background profile - which then evolves due to sources at the core boundary. However, in our experience the saturated state is reached faster the closer the initial state is to the final. We choose as initial state for density and temperatures the simple profile as function of ρ_{pol}

$$f(\rho) = \begin{cases} f_{\text{ped}} & \text{for: } \rho < \rho_{\text{ped}}, \\ -A\sin(a\cdot\rho + b) + B & \text{for: } \rho_{\text{ped}} \leq \rho \leq \rho_{\text{sep}}, \\ f_{\text{sep}} & \text{for: } \rho_{\text{sep}} < \rho, \end{cases} \tag{5.22}$$

with

$$A = \frac{f_{\text{ped}} - f_{\text{sep}}}{2}, \qquad B = f_{\text{ped}} - A, \qquad a = \frac{\pi}{\rho_{\text{sep}} - \rho_{\text{ped}}}, \qquad b = -\frac{\pi}{2}\frac{\rho_{\text{sep}} + \rho_{\text{ped}}}{\rho_{\text{sep}} - \rho_{\text{ped}}}.$$

In present simulations, we chose $\rho_{\text{ped}} = 0.92$ and $\rho_{\text{sep}} = 0.999$. The value f_{ped} is held constant between $\rho = 0.9$ and $\rho = 0.92$ by an adaptive source. In the SOL, the initial profile is flat and equal to f_{sep}.

The core boundary respectively pedestal top values are chosen in accordance to the experiment as $n_{\text{ped}} = 2\times10^{19}$ m^{-3} and $T^{\text{e,i}}_{\text{ped}} = 350$ eV. The separatrix and SOL initial values are less relevant because they adapt in the course of the simulation. An important restriction comes from the choice of flat SOL profiles: simulations saturate faster with f_{sep} as low as possible, since it also initialises lower far SOL values. On the other hand, ideal ballooning stability of the initial profiles prohibits large radial gradients in the confined region, which is correlated with the Greenwald density limit [207]. Our choice for the reference case is $n_{\text{sep}} = 4\times10^{18}$ m^{-3}, $T^{\text{e}}_{\text{sep}} = 40$ eV and $T^{\text{i}}_{\text{sep}} = 50$ eV. In the confined region, electrostatic potential and current are chosen such that the initial pressure profile is stable: $\partial_r\varphi = -\partial_r p_{\text{i}}/(en)$ according to (5.10), resulting in $\mathbf{u}_{\text{pol}} = G = \Omega = 0$ (no vorticity and polarisation velocity), and $\nabla\cdot(j_{\parallel}\mathbf{b}) = eC(p_{\text{e}} + p_{\text{i}})$ according to (5.14). The parallel velocity is chosen as zero. In the SOL, the initial state is chosen such that it fulfils the Bohm boundary conditions (5.34). Particularly, the parallel velocity is $u_{\parallel} = \pm\sqrt{(T_{\text{e}} + T_{\text{i}})/M_{\text{i}}}$ at each divertor plate, with a linear dependence on distance between the plates. The initial outboard mid-plane profiles are illustrated in figure 5.2. To trigger an instability and consequent turbulence, random noise of magnitude 10^{-5} is added to the density and temperature profiles.

For the reference simulation, we choose as poloidal resolution $h_f = 2.5\rho_{s0} = 1.45$ mm. Toroidally, we resolve 16 planes. The time step is chosen slightly below the stability limit as $\Delta t = 5\times10^{-5}R_0/c_{s0} = 1.2$ ns. Due to the limited resolution, the turbulent spectrum must be cut at the poloidal grid scale. To this end, third order hyperviscosity is applied as detailed in appendix 5.7, with $\nu_{\perp} = 3350$ for all fields. Being able to resolve even smaller scales is highly desirable, particularly in a global code. Eventually, our choice of resolution is a compromise, restricted by the allowable computational expense. Nevertheless, we also performed convergence tests with $h_f = 1.67\rho_{s0}$, and a separate test with 24 planes at $2.5\rho_{s0}$. For the $1.67\rho_{s0}$ simulation, hyperviscosity was reduced to 300. For the 24 planes simulation, the timestep had to be reduced to 0.7 ns.

It is worth mentioning the computational cost of these simulations, and how it scales. The reference case with $2.5\rho_{s0}$ poloidal resolution and 16 toroidal planes (~ 7 million points) required for simulating 1 ms of the discharge 9 days on 384 processor cores (8 nodes) of the Marconi-A3 SKL partition. As we find saturation only after $t \gtrsim 5$ ms, at least roughly 0.4 MCPUh and 2 months of patience were required per simulation. Increasing poloidal resolution to $1.67\rho_{s0}$ raised both the number of grid points and the cost and duration of the simulation by a factor of 2. Increasing toroidal resolution raises the cost quadratically with the number of planes as the maximum allowed timestep is inversly proportional to toroidal resolution, i.e. 24 instead of 16 poloidal planes roughly doubles the cost.

We find no large differences in heat transport with increasing resolution, suggesting that it is mostly captured by the reference case. In detail, however, ion heat transport slightly increases with toroidal resolution, and zonal flows increase with poloidal resolution, as detailed in sections 5.3.2 and 5.4, respectively.

5.3.2 Input power and saturation

In current simulations, fixed density and temperature are prescribed at an artificial core boundary at $\rho_{\text{pol}} = 0.9$ – held constant by an adaptive heat and particle source. In figure 5.3 we show how the

input power $\langle P_{\mathrm{e,i}} \rangle_V = 3/2 \langle T_{\mathrm{e,i}} S_n + n S_{T_{\mathrm{e,i}}} \rangle_V$ for the reference simulation varies in time – with particle and temperature sources S_n and $S_{T_{\mathrm{e,i}}}$ averaged over the whole volume. In the same plot, we show the globally averaged electrostatic potential oscillations (in units of 25 V) – this is due to the geodesic acoustic mode (GAM), which is always present in global edge simulations [111]. It is important that flux-surface-symmetric potential oscillations like the GAM are permitted up to the core boundary through the implementation of the zonal Neumann boundary condition (see appendix 5.7). But the GAM also leads to an up-down asymmetric pressure oscillation [208], while the adaptive source acts to hold pressure constant – and therefore follows the GAM with the same frequency, damping the pressure oscillation at the core boundary. While the oscillation of the source is a numerical artifact, on average $\langle P_{\mathrm{e,i}} \rangle_V$ saturates at $t \gtrsim 5$ ms on a reasonable level: 192 ± 29 kW for electrons and 224 ± 36 kW for ions, with one standard deviation quantifying the oscillations. This is roughly half the input power in AUG discharge #36190.

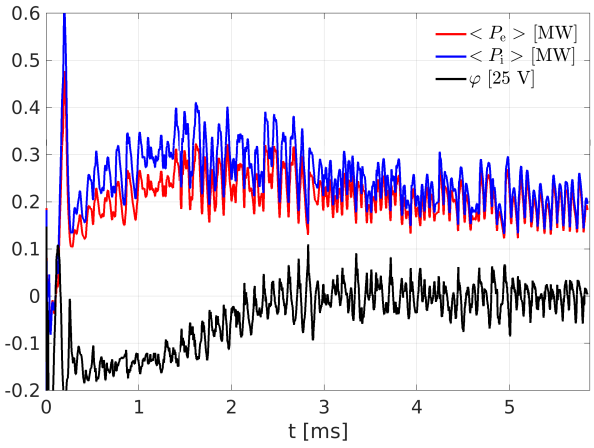

Figure 5.3: Total electron and ion heating power input in the simulation as a function of time. The globally averaged potential in units of 25 V is also shown. The input power oscillates following the GAM. At later times, it saturates at 196 kW for electrons and 236 kW for ions.

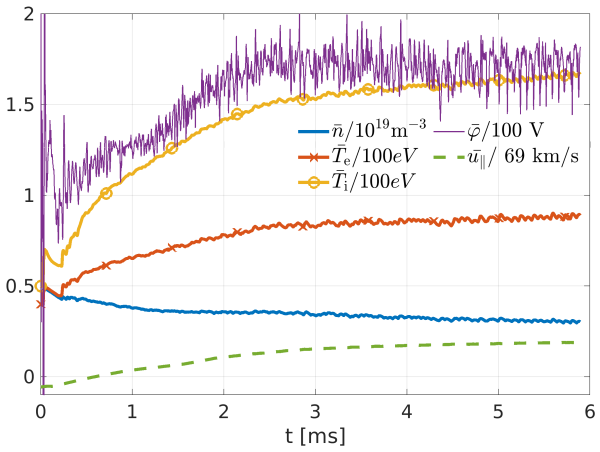

Figure 5.4: Zonally averaged separatrix density, electron and ion temperatures, and electrostatic potential in normalized units. The parallel velocity shown, averaged over the whole domain, is a measure of toroidal rotation.

In figure 5.4, we show zonally averaged separatrix values for density, electron and ion temperatures and electrostatic potential. As indicated by the input power, in the confined region turbulence, and largely also profiles, saturate within 3 ms of simulation time. Further outside, however, time scales are longer due to lower temperatures – particularly in the SOL, where the transit time is of the order 1 ms (as can be estimated from ~ 50 m connection length and 60 km/s flow velocity from figure 5.5). Turbulence at this time is locally saturated, but globally profiles vary predominantly due to the outflow in the SOL, as we started from flat profiles there. Therefore, for the confined region, the separatrix values are a good criterion for saturation. In the following, we will use the data from $t > 4$ ms for our statistcal analysis, although temperatures are still very slowly evolving. Additionally, the globally averaged parallel velocity is shown which is a measure of toroidal rotation. It saturates at 13 km/s in the direction of the plasma current – a reasonable value for ASDEX Upgrade [209].

In unfavourable configuration, i.e. with $\mathbf{B} \times \nabla B \sim +\hat{\mathbf{e}}_Z$ away from the X-point, the input power is slightly lower: 187 ± 29 kW and 204 ± 33 kW for electrons and ions, respectively. The simulation with 24 toroidal planes (higher toroidal resolution) has 176 ± 26 kW for electrons and 221 ± 32 kW for ions, respectively. For the $1.67\rho_{s0}$ simulation (higher poloidal resolution), we get 187 ± 13 kW for electrons and 221 ± 17 kW for ions – i.e. no significant difference to the reference case with $2.5\rho_{s0}$. This is remarkable as zonal flows (a radial modulation of the electric field, pressure and parallel velocity) are much more pronounced in the $1.67\rho_{s0}$ simulation, as discussed in section 5.4, suggesting that overall thermal transport seems to be barely affected by zonal flows. The reduced oscillation amplitude also indicates a less pronounced GAM. There are no other qualitative differences between the reference simulation and the simulations with higher poloidal or toroidal resolution, as profiles and fluctuation levels remain very similar. Therefore, we conclude that thermal transport is largely resolved in the reference simulation. Increasing resolution further is desirable, but requires a significant speed-up of the code.

5.3.3 Quasi-steady state profiles, fluctuation levels and transport

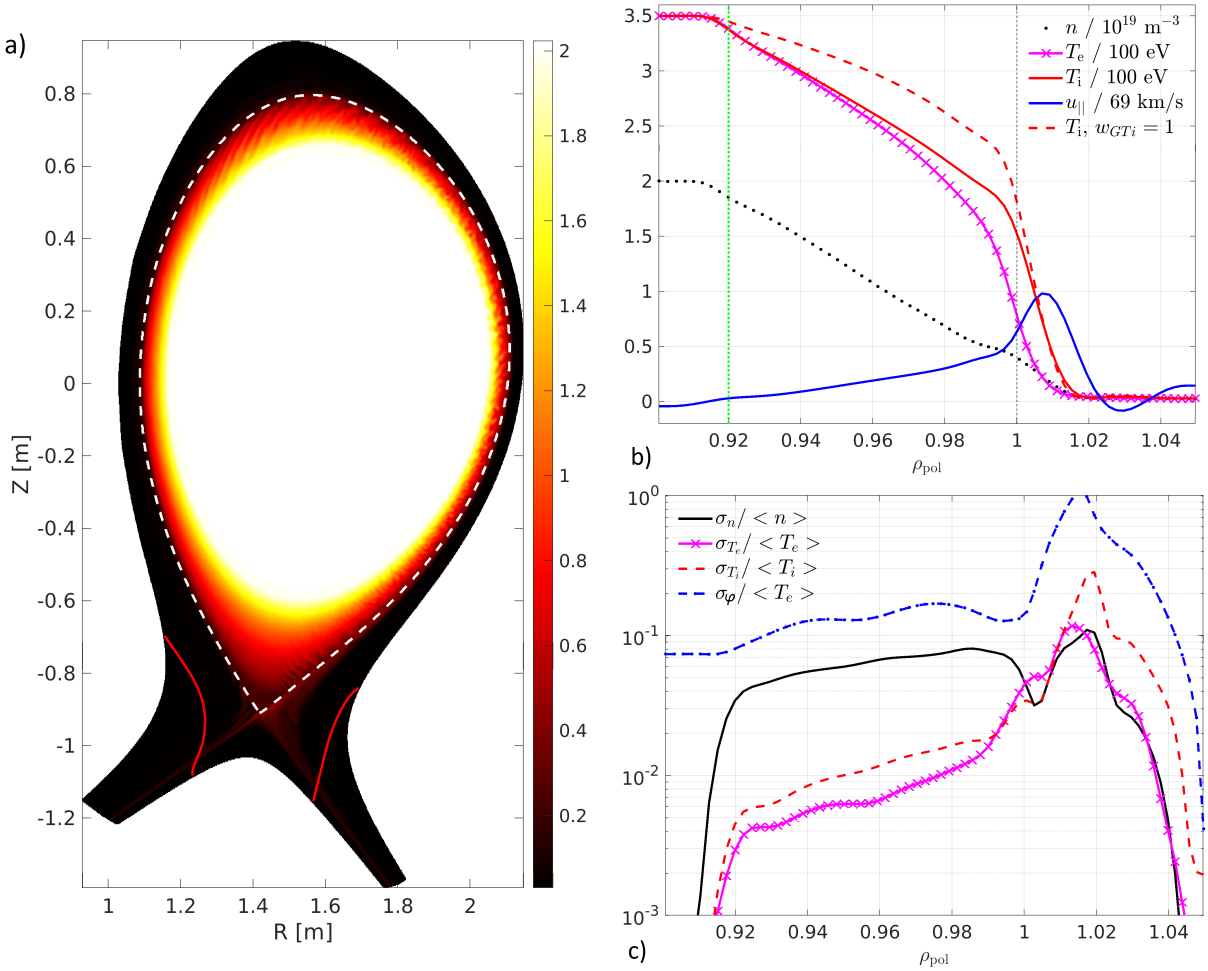

Figure 5.5: a) 2D density profile in the poloidal cross section for the quasi-steady state at 7347 μs simulation time for the reference case. The separatrix is shown with a dashed white line, the divertor boundary with a red line. b) Outboard mid-plane ($Z = 0$) background profiles, averaged in time over 1 ms and toroidally over 16 planes. '$w_{GTi} = 1$' means with viscous ion heating in the confined region, see also text. c) OMP fluctuation level, with mean $\bar{f} = \langle f \rangle_t$ and variance $\sigma_f^2 = \langle f^2 \rangle_t - \langle f \rangle_t^2$.

Figure 5.5a shows a snapshot of the plasma density in a poloidal plane, in quasi-steady state at $t = 308 R_0/c_{s0} \approx 7$ ms for the reference simulation. Figure 5.5b displays profiles at the outboard mid-plane ($Z = 0$), averaged toroidally and in time over 1 ms, for density, temperature and parallel velocity. While the density profile is rather flat, we see steep pedestals in temperatures around the separatrix – the reason is high heat conductivity, as discussed in section 5.5.2. Experimentally, pedestals are observed in L-mode at low density, particularly for T_e [210].

We see some penetration of parallel velocity into the confined region, much less than without ion viscosity in figure 5.11 though. '$w_{GTi} = 1$' stands for active viscous ion heating (in eq. (5.30)) in the confined region – ions are significantly hotter in that case. It was not possible to run stable simulations with this effect active also in the SOL, hence why the reference simulation is without viscous ion heating – this is further discussed in section 5.5.1. If active also in the SOL, the heating is even stronger there, leading to non-monotonous T_i profiles peaking in the SOL and unstable simulations.

Figure 5.5c shows fluctuation levels at the outboard mid-plane. The potential fluctuations are normalised to background (mean) electron temperature, and are the largest in the system. As we have $\sigma_\varphi/\bar{T}_e \gtrsim 2\sigma_n/\bar{n}$ in the confined region, with T_e and T_i fluctuations an order of magnitude smaller, this indicates that turbulence in the confined region is ballooning driven [65, 211]. Around the separatrix, there is a local minimum in $\sigma_n/\bar{n}$ and $\sigma_\varphi/\bar{\varphi}$, indicating some level of turbulence suppression due to the sheared $E \times B$ flow. In the SOL, fluctuation amplitudes peak around $\rho_{\rm pol} \approx 1.01 - 1.02$, at the bottom

of the steep gradients. We have here $\sigma_\varphi/\bar{T}_\mathrm{e} \gg \sigma_n/\bar{n}$, roughly an order of magnitude, but also rather high $\sigma_{T_\mathrm{i}}/\bar{T}_\mathrm{i}$ and a steep ion temperature gradient. This suggests a combination of the Kelvin-Helmholtz instability [212, table I] and ITG drive.

The induction of a perturbed magnetic field, $\beta_0 \partial_t A_\parallel$, is crucial for the dynamics of the parallel electric field and current, and therefore electrostatic turbulent transport. The perturbation $\tilde{\mathbf{B}} = \nabla \times A_\parallel \mathbf{b}$ does not necessarily lead to significant additional electromagnetic transport, though: in current simulations, we have $\left|\tilde{\mathbf{B}}\right|/B < 0.1\%$. In principle, the additional electromagnetic transport can be nonetheless large, depending on the efficiency of parallel (heat) transport along the perturbed magnetic field [137]. However, we have verified that the effect is small in present low-β simulations by additional tests that included electromagnetic flutter (that is therefore otherwise disabled to save a factor 2 in computational time).

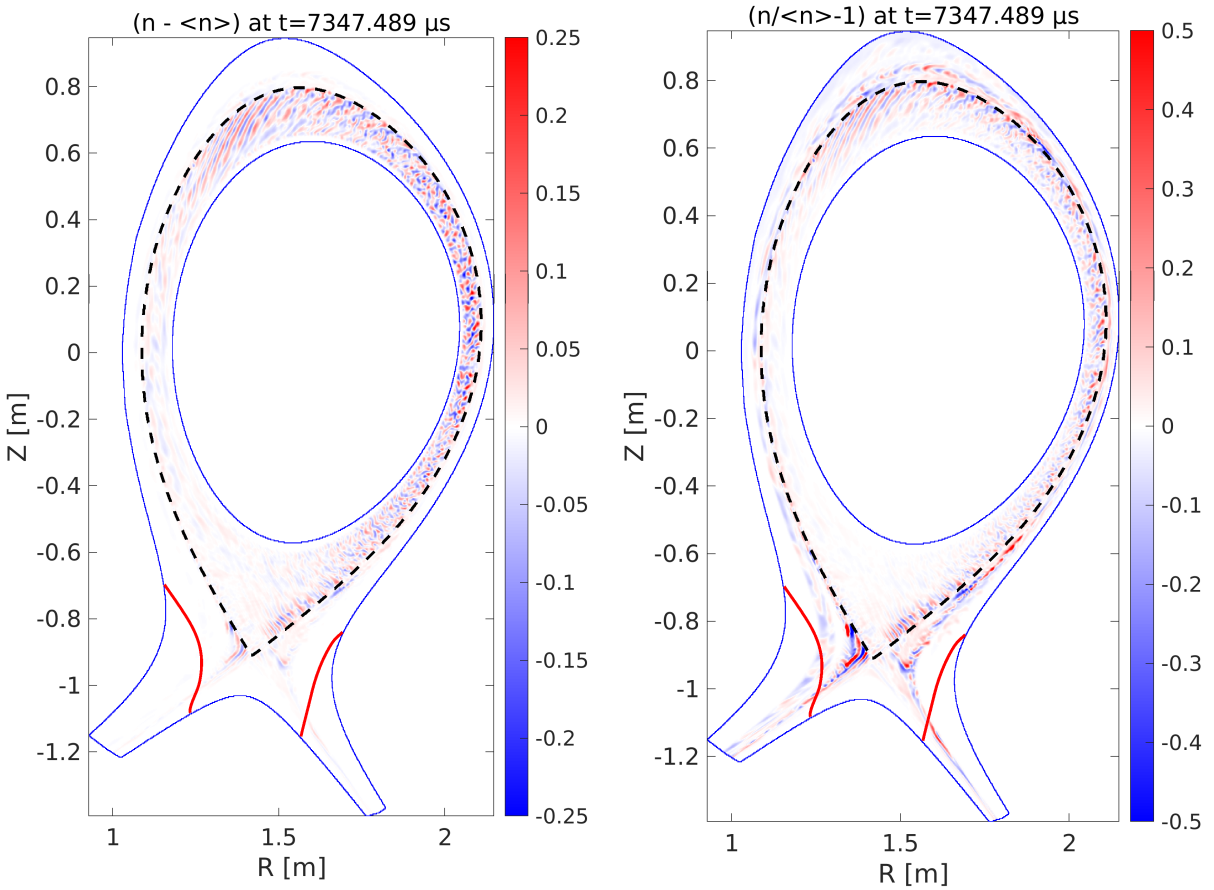

Figure 5.6: Density fluctuations at a snapshot in quasi-steady state state, at circa 7.3 ms simulation time. Left: $n - \langle n \rangle$ in units of 10^{19} m^{-3}, right: normalized to the local mean density $(n - \langle n \rangle)/\langle n \rangle$. The separatrix is marked with a dashed black line, the divertor with a red line and poloidal domain boundaries with a blue line. See supplementary movie 2 for the dynamics.

Figure 5.6 shows the difference between one snapshot's density and mean background density – in absolute units of 10^{19} m^{-3} (left), as well as normalized to the local mean density (right). Fluctuations are much more prominent on the LFS than on the HFS, which is typical for ballooning modes. In absolute units, fluctuations are negligible in the SOL compared to the confined region – relative to the small local background density, however, SOL fluctuations are much larger, reaching up to 100%, particularly in the region around the X-point where the poloidal magnetic field is weak.

While figure 5.6 clearly demonstrates poloidal asymmetries in the transport, we can still compute average radial diffusivities in quasi-steady state. For $E \times B$ particle and heat fluxes

$$\Gamma_r = \langle \mathbf{v}_E \cdot \mathbf{e}_r n \rangle \,, \qquad Q_r^{\mathrm{e,i}} = \left\langle \frac{3}{2} \mathbf{v}_E \cdot \mathbf{e}_r T_{\mathrm{e,i}} n \right\rangle \tag{5.23}$$

we define diffusivities as suggested by Ref. [213] via

$$D_\perp = \frac{\Gamma_r}{|\langle \partial_r n \rangle|}, \qquad \chi_\perp^{\mathrm{e,i}} = \frac{Q_r^{\mathrm{e,i}} - 1.5 T_{\mathrm{e,i}} \Gamma_r}{\langle n \rangle |\langle \partial_r T_{\mathrm{e,i}} \rangle|}. \tag{5.24}$$

In the global average $\langle\rangle_{r,\theta,\phi,t}$ we obtain for the confined region $D_\perp = 0.18$ m^2/s, $\chi_\perp^{\mathrm{e}} = 0.27$ m^2/s and $\chi_\perp^{\mathrm{i}} = 0.46$ m^2/s – reasonable values for AUG experiments [94]. $\chi_\perp^{\mathrm{i}} > \chi_\perp^{\mathrm{e}}$ might imply the presence of the ITG mode – scans of the parallel electron heat conductivity in section 5.5.2, however, show that this is an effect from diffusive heat flux damping rather than linear instability drive. $\chi_\perp^{\mathrm{e}} = 2/3 D_\perp$ corroborates the finding that turbulence is driven by ballooning modes [213, 214]. Further evidence could be gained by Fourier analysis in field aligned coordinates, particularly from the parallel envelope and the relative phase shifts between the potential, density and temperatures [65, 211] – but this analysis is complicated for us due to the non-field-aligned grid, and will be deferred to future work.

The presented results also hold in the 1.5 times higher resolution simulations (even higher was not yet computationally feasible, as explained in section 5.3.1). But it should be remarked, as detailed in the next section, that at higher poloidal resolution the increased zonal flow leads to a radial modulation of profiles and fluctuation levels – a staircase structure [215]. However, in present simulations, this has no impact on overall transport (and profiles, disregarding the modulation) as described in section 5.3.2.

5.4 The radial electric field

According to our theory developed in section 5.2, in collisional drift-reduced Braginskii models the equilibrium electric field is determined by the ion particle balance (5.8) in the confined region and by the sheath boundary conditions (5.20) in the SOL. We begin by showing in figure 5.7 the simulated radial electric field in comparison to the ion pressure gradient (and parallel rotation) at the outboard mid-plane ($Z = 0$) in quasi-steady state. In the SOL, the electrostatic potential follows the electron temperature profile, $E_r \sim -\Lambda \partial_r T_\mathrm{e}$, producing a positive electric field. In the confined region, the electric field is negative, which produces counter-propagating flows at the separatrix.

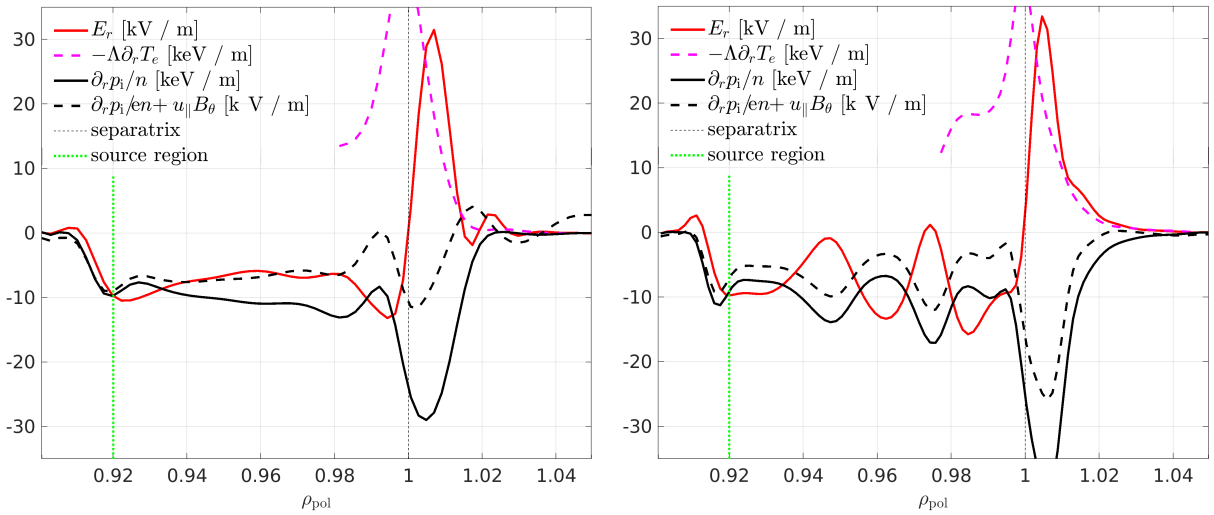

Figure 5.7: Radial electric field profile vs. ion pressure gradient at the outboard mid-plane, in quasi-stationary phase ($t \gtrsim 4$ ms), averaged in time over 1 ms and toroidally over 16 planes. The $2.5\rho_{s0}$ reference simulation is shown on the left and the $1.67\rho_{s0}$ simulation on the right.

The deviation from $E_r = \frac{\partial_r p_\mathrm{i}}{en}$ indicates that the equilibrium balance from the diamagnetic compression (5.9) is accompanied by a contribution from toroidal or turbulence driven zonal flows. In the next section we will show that poloidal rotation is small. If zonal flows are small, too, one can use equation (5.16), $E_r = \partial_r p_\mathrm{i}/en + u_\parallel B_\theta$, to understand the electric field. In a large aspect ratio tokamak, $B \approx B_\phi \gg B_\theta$, and so toroidal rotation is mostly given by the parallel velocity. In the left figure 5.7, in the domain $\rho_\mathrm{pol} \in (0.94, 0.98)$, this equality is indeed quite well fulfilled. The deviation, however, is

caused by the zonal flow, which becomes even more pronounced with increased poloidal resolution in the right figure.

Zonal flows [66, 208] are typically static in time, but can be overlaid by the geodesic acoustic mode oscillation (discussed in sec. 5.3.2) and, naturally, turbulent oscillations. They are constant over flux surfaces and have a typical mesoscale radial wavelength [67]. Importantly, we find that high poloidal resolution is necessary to properly resolve the zonal flow production at ρ_s scale [208, 216] – which is why results throughout this section are compared between the reference simulation at $2.5\rho_{s0}$ and $1.67\rho_{s0}$ resolution.[‡] On the other hand, equilibrium profiles and input power are nearly identical at both resolutions – see section 5.3.2. Thus the turbulent transport is barely affected by these zonal flows.

The zonal flow drive is very sensitive to adiabaticity. Only at high adiabaticity the zonal flow drive is efficient [217]. The low wavenumber region responsible for the transport and driving the turbulence is characterized by interchange turbulence, which is less adiabatic. Therefore, this region is less susceptible to the zonal flow. The more drift-wave dominated region around $k_\perp \rho_s = 1$ is responsible for the zonal flow drive, but due to its higher adiabaticity it is not the main driver of the transport. In ASDEX Upgrade, low-frequency zonal flows have been not observed so far, not even around the L-H transition [186]. With respect to typical ASDEX Upgrade L-mode parameters the present simulations are at particularly low densities and high electron temperatures. Under these conditions the plasma is highly adiabatic, which is beneficial for the generation of zonal flows. However, as we have $T_\mathrm{i} > T_\mathrm{e}$, finite Larmor radius effects should stabilize the region around $k_\perp \rho_s = 1$, which in drift-reduced Braginskii models is taken into account only to lowest order. This might lead to an over-prediction of the zonal flow activity.

5.4.1 Particle, charge and momentum balance on closed field lines

In this section we want to investigate the composition of the mean radial electric field on closed flux surfaces. Zonal flows will be explained by the dominant contributions to the ion particle balance equation (5.8), averaged in time and over the flux surface. Additionally, the dominant term in the parallel momentum balance – the ion viscous stress (5.17) – will reveal a non-trivial contribution from the parallel flow. It is important to note that at any single point in time and space, without averaging, $\partial_t n$ and $\mathbf{v}_E \cdot \nabla n$ are by far the dominant terms in the continuity equation (and similarly for $u_\parallel$ in the parallel momentum equation), but become less important in a large enough ensemble average, consistent with the neoclassical ordering.

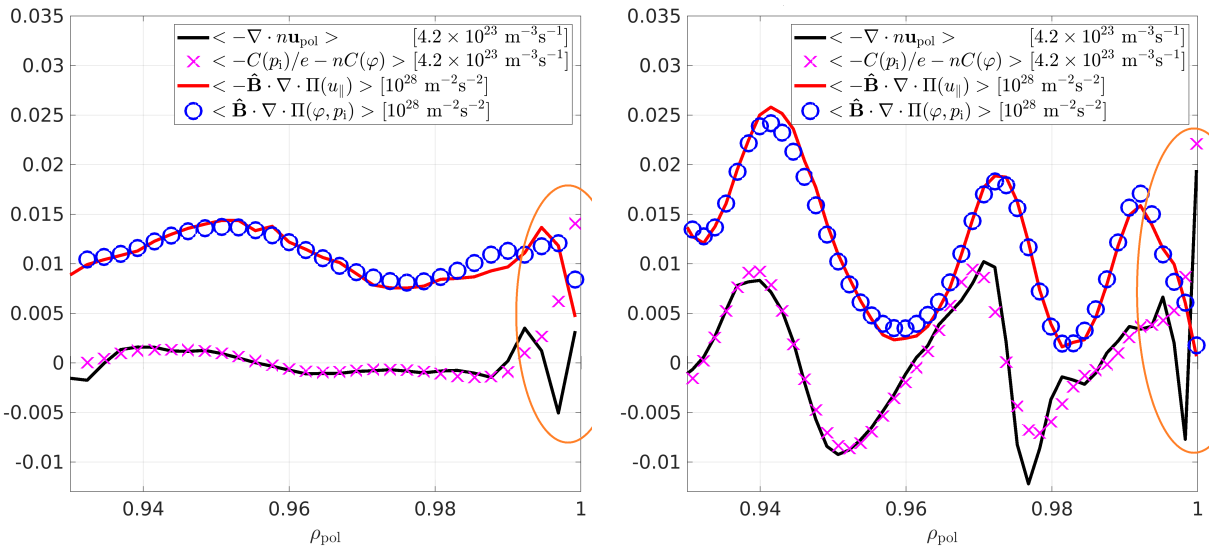

Figure 5.8: Flux surface averaged dominant terms in the ion particle balance equation (black line and magenta crosses) and in the parallel momentum balance equation (red line and blue circles), also averaged in time over 1 ms, in the $2.5\rho_{s0}$ reference simulation on the left and $1.67\rho_{s0}$ simulation on the right. Dominant terms in the ion momentum balance are the parts of the stress tensor Π_i, whereby $\hat{\mathbf{B}} = \mathbf{B}/B_0$.

[‡]Note that in a global computation the local Larmor radius ρ_s changes strongly throughout the domain – refer to section 5.3.1 for a detailed description of the simulation setup for both cases.

As pointed out in the previous section, the electric field is mostly negative in the confined region, as it mainly follows the ion pressure gradient according to $E_r \sim \partial_r p_\mathrm{i}/en$ due to the static equilibrium balance $nC(\varphi) \sim -C(p_\mathrm{i})/e$ (see eq. (5.9)). We are interested in deviations from this balance, and so we show the residue $-C(p_\mathrm{i})/e - nC(\varphi)$ by magenta crosses in figure 5.8. This residue has to be balanced by other terms in the ion particle balance (5.8). In the flux surface average, parallel derivatives are annihilated, i.e. $\left\langle \nabla\cdot(nu_\parallel \mathbf{b})\right\rangle_S = 0$, and the $E\times B$ advection $\mathbf{v}_E\cdot\nabla n$ is mostly small. Therefore, the residue is mostly balanced by the black curve, which is the divergence of the polarisation particle flux $\nabla\cdot n\mathbf{u}_\mathrm{pol}$ defined in eq. (5.11). In the average, it is a measure of the Reynolds stress. We therefore conclude that the zonal flow can be understood as the residue between $E\times B$ and diamagnetic compression which is sustained by the ion polarisation flux (or equivalently the Reynolds stress),

$$\langle enC(\varphi) + C(p_\mathrm{i})\rangle_{S,t} \approx \left\langle \nabla\cdot(en\mathbf{u}_\mathrm{pol})\right\rangle_{S,t}.$$

As explained in the previous section, the zonal flow is driven by near-adiabatic drift waves on Larmor radius scale, and is therefore more pronounced in the higher resolved simulation (but does not necessarily impact overall transport).

The remaining deviation between the two curves is explained by hyperviscosity $\mathscr{D}_\Omega$, which is the grid scale numerical dissipation defined in appendix 5.7. It is, however, not just a numerical artifact. As hyperviscosity only acts on grid scale (the value of $\nu_\perp$ is reduced from 3350 to 300 between the $2.5\rho_{s0}$ and the $1.67\rho_{s0}$ resolution simulations), it dissipates the energy arriving there due to the turbulent cascade. This process is enhanced by shear layers, and so dissipation is even stronger in the higher resolution simulation. The separatrix deserves particular attention in this regard, since the $E\times B$ shear peaks there, as discussed in the next section. Close to to the separatrix, as marked by the yellow ellipse, this results in a peak of $\nabla\cdot(n\mathbf{u}_\mathrm{pol})$ as well as $\mathscr{D}_\Omega$, and also $\mathbf{v}_E\cdot\nabla n$ largely balanced by $\mathscr{D}_n$.

It is interesting that the divergence of the polarisation particle flux can in fact be conveniently computed from the quasi-neutrality equation (5.14). In the flux surface average, $\left\langle \nabla\cdot j_\parallel \mathbf{b}\right\rangle_S = 0$, hence $\left\langle \nabla\cdot\left(n\mathbf{u}_\mathrm{pol}\right)\right\rangle_{S,t} = \langle C(p_\mathrm{e}+p_\mathrm{i})/e - \mathscr{D}_\Omega\rangle_{S,t}$. This means that the zonal flow results in $< C(p) >_S \neq 0$, i.e. a (predominantly up-down) pressure asymmetry [218]. Additionally, ballooned transport leads to an inboard-outboard asymmetry [117, 218]. Therefore, neither pressure nor the electrostatic potential can be assumed to be constant along a flux surface ψ (thereby $C(p_\mathrm{e}) \approx C(p_\mathrm{i})$).

Let us now discuss the role of ion viscosity. Strictly speaking, the Reynolds stress is only contained in the inertial part of the polarisation particle flux $\nabla\cdot(n\mathbf{u}^\mathrm{in}_\mathrm{pol})$ (see section 5.2.2). However, we find that the viscous part $C(G)$ is always more than two orders of magnitude smaller than the other contributions in the particle balance, i.e. negligible. This means that in present simulations, viscosity does not directly damp the zonal flow. It does, however, efficiently damp poloidal rotation. To see this, we multiply the parallel momentum balance equation (5.27) by density n and the magnetic field strength B and average it in time and over flux surfaces. By this, the parallel pressure gradient is annihilated, $\left\langle B\nabla_\parallel p\right\rangle_S = 0$. The remaining dominant contribution is from the viscous stress function G, or more precisely from its constituents. We have defined the ion viscous stress tensor Π_i in terms of G in section 5.2.3. We now compare the part of it containing the parallel velocity, plotted in red in figure 5.8, with the remaining part containing the static equilibrium balance $C(\varphi) + C(p_\mathrm{i})/en$, plotted in blue. As the two parts mostly balance, we conclude that poloidal rotation is near zero according to eq. (5.17),

$$\langle \mathbf{B}\cdot\nabla\cdot\Pi_\mathrm{i}\rangle_{S,t} = 3\eta_0^\mathrm{i}\left\langle \left(\nabla_\parallel B\right)^2\right\rangle_{S,t} v_\theta \approx 0.$$

A small deviation is sustained by $n\mathbf{v}_E\cdot\nabla u_\parallel$ and $p_\mathrm{i}C(u_\parallel)$. Importantly, this condition is fulfilled also in spite of pronounced zonal flows in the high resolution simulation – both parts of the viscous stress tensor are modulated, but cancel each other. This means that while viscosity does not directly damp the zonal flow via $C(G)$, it does damp the resulting mean poloidal rotation by adjusting the parallel velocity $u_\parallel$!

An important observation is that in the lower resolution simulation ($2.5\rho_{s0}$), the zonal flow is small, but on average over the radial domain constituents of the stress tensor in the parallel momentum balance are the same. In fact, both simulations develop the same mean toroidal rotation (which is roughly the same as parallel rotation in a large aspect ratio tokamak). Although not strictly valid due to the above mentioned necessary asymmetries along a flux surface, eq. (5.16) suggests that parallel velocity also

modifies the electric field locally, which seems to be more important than zonal flows in the low resolution case, figure 5.7 left, at $\rho_{\text{pol}} \in (0.94, 0.98)$. The generation, transport and saturation of toroidal rotation are outside the scope of the present study, but a review can be found in Ref. [219]. Importantly, in absence of momentum sources in the confined region, as in our present simulations, net toroidal rotation can be only generated in the SOL (see Ref. [220]) and transported inward. This is indeed suggested by the parallel velocity profile in figure 5.5. We point out that ion viscosity seems to be important also for the saturation of this process, as discussed in section 5.5.1.

The same analysis as above can be performed in a different ensemble average, e.g. toroidal and time (poloidally resolved), as was done in Ref. [117] – but more data are required, and results are less concise (2D). A more detailed examination of the generation of mean flows can be found in Ref. [201, 221]. We find, consistent with Ref. [117], that $C(G)$ is negligible in the vorticity equation. Instead, zonal flows are damped by the GAM oscillation which in turn loses energy through the coupling to Alfvén waves and finally resistivity [208]. However, we find that this damping is not complete, perhaps because unlike electron pressure, ion pressure does not enter Ohm's law.

5.4.2 Transition to the SOL: vortex breaking and straining-out at the separatrix

We have shown that the electric field is governed by the ion particle balance in the confined region, and by sheath boundary conditions in the SOL – at least in present simulations. The separatrix has its own specific dynamics as it acts as a boundary between closed and open field lines. We can see this by examining what happens to the turbulent eddies. Figure 5.9 shows the average shearing rate vs. vortex-turn-over rate at the outboard mid-plane. The former is roughly given by $\omega_s = |\partial_R \bar{v}_\theta| \approx \left| B^{-1} \partial_R^2 \langle \varphi \rangle_{t,\phi} \right|$. The latter is estimated by one standard deviation of vorticity $\Omega_{\text{std}} = \sqrt{\langle \Omega_F^2 \rangle - \langle \Omega_F \rangle^2}$, whereby the fluid vorticity is calculated from the generalised vorticity in GRILLIX via $\Omega_F = \omega_{\text{ci0}} \hat{B} \hat{\Omega} / \hat{n}$, with $\omega_{\text{ci0}} = eB_0/M_{\text{i}}$.

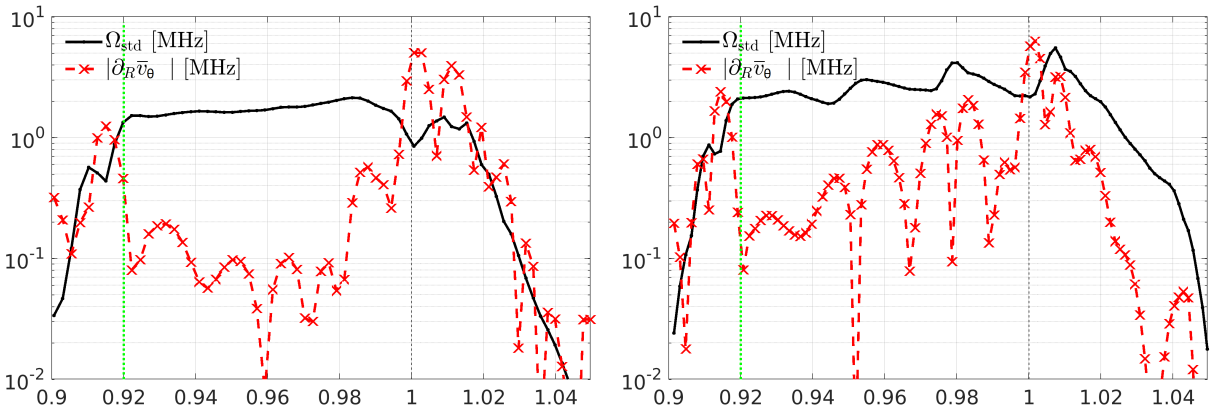

Figure 5.9: Vortex turn-over rate Ω_{std} compared to the shearing rate ω_s, see text for their definition, in the $2.5\rho_{s0}$ reference simulation on the left and $1.67\rho_{s0}$ simulation on the right.

Small vortices are elongated, thinned and finally absorbed by the shear flow [44, 216, 222] – driving the zonal flow. Stronger vorticies survive. Importantly, as stated in the last section and visible in figure 5.8, this process extends up to and peaks at the separatrix. Even though larger zonal flows do lead to somewhat higher shearing, we find that the average vortex-turn-over rate is larger than the shearing rate in the confined region at both $2.5\rho_{s0}$ and $1.67\rho_{s0}$ resolution – explaining why they have barely any effect on overall transport. At the separatrix additional shearing is provided externally due to sheath boundary conditions and the fast SOL outflow, such that the shearing rate exceeds the vortex-turn-over rate and the eddies can be torn apart. In figure 5.10, at the top of the device, the tilting of eddies is particularly visible. We highlighted one exemplary vortex breaking event (see Ref. [223] for a similar experimental finding). Ultimately, vortices are strained out by the shear flow, and dissipated at grid scale. In the particle balance this manifests as a peaked $E \times B$ advection rate balanced by dissipation. Supplementary movie 2 shows the dynamics of density fluctuations.

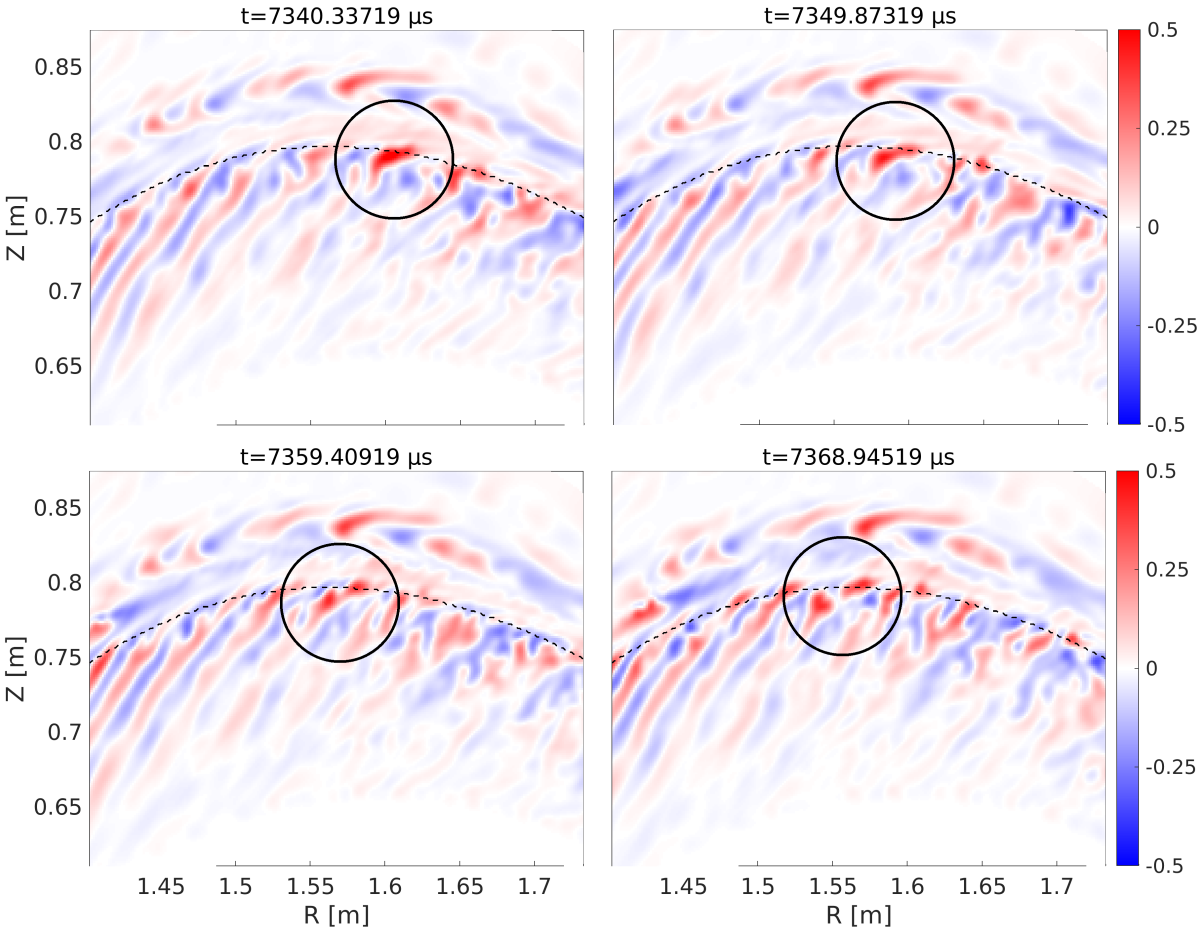

Figure 5.10: Eddy tilting, straining-out, decorrelation and a single breaking event in the $2.5\rho_{s0}$ reference simulation, at the separatrix on top of the device (compare with figure 5.6). Colour scale shows density fluctuation amplitudes relative to the background, $(n - \langle n \rangle)/\langle n \rangle$.

Note also how the far SOL structures appear to be nearly frozen in time in contrast - as temperature in hitting ~ 3 eV there, time scales are an order of magnitude slower. These structures, pronounced on the scale relative to the background, are in fact tiny due to the very low background $\bar{n} \approx 3 \times 10^{17}$ m^{-3}. Nevertheless, as transport has to saturate globally including the far SOL, its slow dynamics restricts the overall saturation of the simulations.

5.5 The role of fluid closure terms

Due to the low collisionality in fusion plasmas, the greatest limitation of our model is the collisional fluid closure. In this section we show explicitly its role. This is particularly important as towards lower collisionality, the discussed closure terms – ion viscosity and electron / ion heat conductivity – diverge as $\sim T^{5/2}$. For the current simulations, a 3D iterative solver [1] allowed us to treat these terms without constraints on the allowed time step – consuming, however, already up to 50% of the computation time. Towards less collisional, hotter regimes (H-mode) additional improvements will be therefore necessary.

5.5.1 The impact of ion viscosity

The viscosity of ions, represented by the viscous stress function G – see sections 5.2.2-5.2.3, is an important dissipation mechanism. In section 5.4.1 we found that $C(G)$, which enters the perpendicular drifts as a higher order correction, is negligible in the polarisation velocity. On the other hand, $\nabla_{\parallel} G$, which enters the parallel momentum balance at leading order, is crucial for damping poloidal rotation. We have also seen in section 5.3.3 that this damping leads to significant ion heating.

To closer investigate this, we have conducted a simulation without ion viscosity at all ($G = 0$). The results at $t = 2$ ms simulation time are shown in figure 5.11: outboard mid-plane profiles of density, temperature, parallel velocity and electric field. The density profile is very similar to the reference case in figure 5.5. The electric field is much larger and almost throughout positive, though. The temperature profiles are broader, fluctuations are larger (up to 15% in density in the confined region) and input power is much larger in this simulation – 482 ± 118 kW for electrons and 525 ± 127 kW for ions, respectively – suggesting increased turbulent transport. The larger fluctuation in input power also suggests stronger geodesic acoustic mode oscillations.

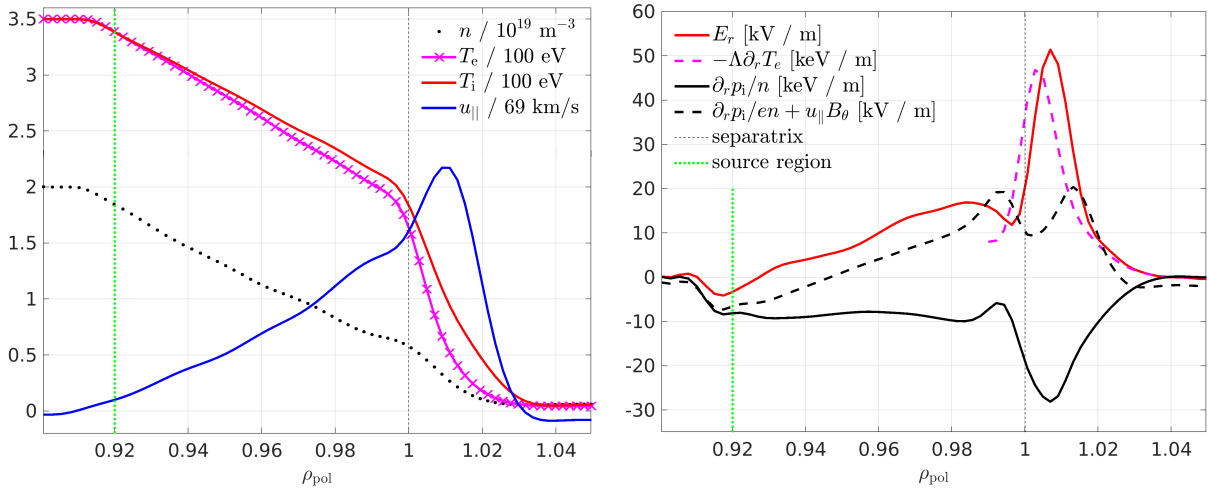

Figure 5.11: Outboard mid-plane state variables profiles (left) and radial electric field (right) without ion viscosity ($G = 0$) at $t = 2$ ms simulation time (saturated turbulence, but flows still evolving). Compare to fig. 5.5b and 5.7 (left).

The electric field is larger in the SOL due to the increased electron temperature gradient. In the confined region, we have performed the same analysis as in section 5.4.1, finding only a very small contribution from the zonal flow. Although viscosity was disabled in the simulation, we can still compute what the contribution from viscous stress in the parallel momentum balance would have been. Naturally, we find that the viscosity balance (5.17) is not fulfilled: in the reference simulation, figure 5.8 left, in an average also over the radial domain, we had $\left\langle \hat{\mathbf{B}} \cdot \nabla \cdot \Pi(u_{||}) \right\rangle_{S,t,r} = -1.07 \times 10^{26}$ m^{-2}s^{-2} and $\left\langle \hat{\mathbf{B}} \cdot \nabla \cdot \Pi(\varphi, p_i) \right\rangle_{S,t,r} = 1.10 \times 10^{26}$ m^{-2}s^{-2}. In the simulation in this section, without viscosity, one would get $\left\langle \hat{\mathbf{B}} \cdot \nabla \cdot \Pi(u_{||}) \right\rangle_{S,t,r} = -16.38 \times 10^{26}$ m^{-2}s^{-2} and $\left\langle \hat{\mathbf{B}} \cdot \nabla \cdot \Pi(\varphi, p_i) \right\rangle_{S,t,r} = 5.23 \times 10^{26}$ m^{-2}s^{-2}. This means that without viscosity, the plasma obtains a significant poloidal rotation.

At this point, $t = 2$ ms, the simulation crashes as the electric field starts having large (machine scale) oscillations. A possible reason is the Stringer instability [189, 224], which is expected at low – or absent – viscosity. As the instability is also connected to parallel [218] and toroidal [224] rotation, it is not surprising that we get $\left\langle -\hat{\mathbf{B}} \cdot \nabla \cdot \Pi(u_{||}) \right\rangle_{S,t,r} > \left\langle \hat{\mathbf{B}} \cdot \nabla \cdot \Pi(\varphi, p_i) \right\rangle_{S,t,r}$. In fact, mean toroidal rotation reaches 26 km/s already at $t = 2$ ms, compared to 13 km/s in the saturated reference simulation. However, the inflow of momentum from the SOL [219, 220] and the non-linear Reynolds stress [202] could also be important. At this point, we will not go more into details. But we can conclude that ion viscosity is a crucial mechanism – particularly for damping of poloidal rotation, but also ion heating – and has to be included in realistic tokamak simulations.

5.5.2 The impact of heat conductivity

The parallel heat conductivity largely determines the parallel heat flux in Braginskii models. Besides obvious consequences for the SOL heat exhaust, circular C-mod simulations [1,2] have previously shown that flattening of the parallel electron and ion temperature profiles in the confined region can also reduce cross-field transport. To illustrate their impact in current computations, we have repeated the reference simulation with the electron heat conduction lowered to the level of ions, i.e. $\chi_{||e0} = 35.35$ instead of 940,

and sheath heat transmission factor $\gamma_e = 0$ instead of 2.5. The resulting saturated profiles are displayed in figure 5.12 (unlike with zero ion viscosity, these simulations were running stably).

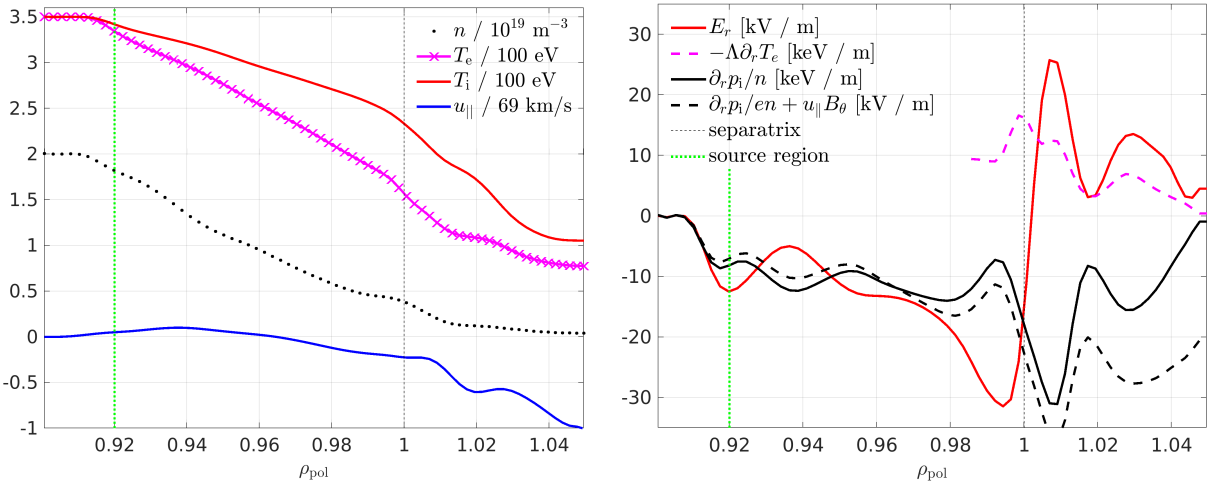

Figure 5.12: Saturated outboard mid-plane state variables profiles (left) and radial electric field (right) for $\chi_{\|e0} = \chi_{\|i0} = 35.35$ and $\gamma_e = 0$.

The most prominent feature is that electron and ion temperature profiles become much broader, including in the SOL, i.e. the pedestal disappears. This is because the profile around the separatrix is determined by the competition of perpendicular transport and parallel outflow, and reducing the heat conductivity and sheath heat transmission significantly hinders the latter. As a secondary effect, due to the increased temperature the ion viscosity increases, damping the parallel flow more strongly. Further, the electric field well deepens. Again, a similar analysis as in section 5.4.1 reveals that, in this case, this is due to the increased polarisation flux, i.e. zonal flow. This can be either due to a change in the linear instability drive [214], or due to an increased effective resolution: even though the nominal resolution is still $2.5\rho_{s0}$, the separatrix temperature has increased by roughly a factor 2, such that the effective resolution in terms of the local Larmor radius has increased by $\sqrt{2}$. Similarly as with reduced ion viscosity, the density fluctuation level increases up to $\sim 15\%$ in the confined region, and input power increases to 535 ± 232 kW for electrons and 463 ± 202 kW for ions, respectively. Noticeably, not only the fluctuations increase, but also electrons are now transporting more heat than ions. This corroborates the hypothesis that transport is driven by ballooning rather than ITG modes, except that for the reference case (with high electron heat conduction) the electron heat flux is more suppressed than the ion heat flux by parallel conductivity.

5.6 Conclusions

For the first time, global turbulence simulations (using the drift-reduced Braginskii model) have been performed across the edge and SOL of ASDEX Upgrade, in diverted geometry and at realistic parameters. Away from the inner boundary of the simulation in the core region of the plasma, the background profiles evolve freely, together with the turbulence. A quasi-steady state is reached asymptotically after about 3-4 ms. The saturated input power of about 400 kW is typical for low density AUG L-mode discharges. At the separatrix, the plasma profiles are determined by a competition between perpendicular transport and parallel outflow. A pedestal develops in the electron temperature due to high parallel heat conductivity.

Particular attention was given to the electric field. On closed flux surfaces, the radial electric field is predominantly determined by equilibrium compression, leading to $E_r = \frac{\partial_r p_i}{en}$. Additionally, we find contributions from toroidal rotation and (in particular) zonal flows. The latter absorb smaller eddies, leading to an inverse energy cascade to larger scales. In the SOL, sheath boundary conditions dominate, forcing the electric field to change sign across the separatrix. The resulting shear flow reinforces straining-out and decorrelation of vortices, leading to intermittent outbursts of up to twice the magnitude compared to the laminar background outflow in the SOL.

The stationary zonal flow, a perturbation between the electric field and pressure with a mesoscale radial wavelength, is driven by the Reynolds stress within the polarisation particle flux. A poloidal resolution scan shows that the drive happens on Larmor radius scale by near-adiabatic drift waves which do not significantly contribute to transport. On the other hand, fluctuation levels and average diffusivities suggest that transport is driven by larger scale interchange modes, i.e., coarse simulations are able to mostly capture the transport.

The role of the fluid closure terms – ion viscosity and heat conductivities – was explicitly examined. We find that ion viscosity is negligible in damping vorticity, but highly effective in damping poloidal rotation by adjusting of the parallel velocity profile, while also generating considerable ion heating through magnetic pumping. The electron and ion heat conductivities, on the other hand, are important for parallel heat fluxes, and they largely determine the pedestal and SOL temperature profiles. Both damping mechanisms, viscosity and heat conduction, affect the electric field and reduce the perpendicular transport.

A limiting factor for the simulations is their computational cost. MPI communication and OpenMP performance are currently being optimized, which should allow for faster medium-sized tokamak simulations, also including magnetic flutter (important at higher beta [43]). For larger devices like ITER and DEMO, a larger speed-up or scalability is required, by means of GPU accelaration or 3D MPI domain decomposition.

Further work is needed to extend the applicability of our model to H-mode conditions. Most pressing, as the Braginskii fluid closure loses validity towards lower collisionality regimes, Knudsen corrections [225] (modelling Landau damping [135]) will have to be introduced for heat conductivities. The ion viscosity will have to be adapted to properly model the neoclassical electric field [94,226]. In this regard, generation and damping of poloidal and toroidal rotation should be studied in more detail. Ways to include the ion orbit loss effect [227,228] should be explored, as this might explain why so far we found no significant difference between the favourable and unfavourable direction of the toroidal magnetic field. Furthermore, even in attached L-mode regimes, the applicability of our model in the SOL is yet limited. In our current simulations, the SOL electric field is determined by an isolating sheath, and the pressure profile by the competition between turbulent cross-field transport and parallel outflow. In a real SOL, the sheath can conduct significant currents, and neutral gas recycling and impurities lead to complex density and temperature profiles and flows. The resulting strong gradients between the outboard mid-plane and the divertor, and particularly plasma detachment, are of great interest for fusion reactors. Correspondingly, the incorporation of the aforementioned effects is being urgently pursued.

Acknowledgements

The authors thank E. Wolfrum, A. Bergmann, E. Poli, M. Francisquez, B. N. Rogers, E. Fable, T. Görler, A. Chankin, J. Loizu, V. Rozhansky, A. Cathey Cevallos, M. Faitsch, R. W. Brzozowski III and S. Makarov for helpful discussions. This work has been carried out within the framework of the EUROfusion Consortium and has received funding from the Euratom research and training programme 2014-2018 and 2019-2020 under grant agreement No 633053. The views and opinions expressed herein do not necessarily reflect those of the European Commission. B. Zhu is supported by the U.S. Department of Energy contract DE-AC52-07NA27344 through the Lawrence Livermore National Laboratory.

5.7 Appendix: Global drift-reduced Braginskii equations in GRILLIX

The current physical model in GRILLIX builds on its recent extension by hot ions [1]. The most important newly added terms arise from the ion stress tensor [37], particularly its viscous part. Additionally, collisional electron-ion heat exchange was added.

In the following, time scales are normalised to R_0/c_{s0}, with R_0 the major radius and $c_{s0} = \sqrt{T_{e0}/M_i}$ the sound speed at reference electron temperature T_{e0}. Perpendicular scales are normalised to the sound Larmor radius $\rho_{s0} = c\sqrt{T_{e0}M_i}/(eB_0)$ (in CGS units) and parallel scales to R_0. The dynamical fields evolved in GRILLIX are the density n normalised to a reference density n_0, the electrostatic potential φ normalised to T_{e0}/e, the parallel ion velocity $u_\parallel$ normalised to c_{s0}, the electron and ion temperatures T_e and T_i normalised to reference values T_{e0} respectively T_{i0}, the parallel current $j_\parallel$ normalised to en_0c_{s0} and

the parallel component of the perturbed electromagnetic potential $A_\parallel$ normalised to $(\beta_0 B_0 \rho_{s0})^{-1}$ with $\beta_0 = 4\pi n_0 T_{e0}/B_0^2$.

$$\frac{\mathrm{d}}{\mathrm{d}t} n = nC(\varphi) - C(p_e) + \nabla\cdot\left[\left(j_\parallel - nu_\parallel\right)\mathbf{b}\right] + \mathscr{D}_n(n) + S_n, \tag{5.25}$$

$$\nabla\cdot\left[\frac{n}{B^2}\left(\frac{\mathrm{d}}{\mathrm{d}t} + u_\parallel\nabla_\parallel\right)\left(\nabla_\perp\varphi + \zeta\frac{\nabla_\perp p_\mathrm{i}}{n}\right)\right] = -C(p_e + \zeta p_\mathrm{i}) + \nabla\cdot\left(j_\parallel\mathbf{b}\right) - \frac{\zeta}{6}C(G) + \mathscr{D}_\Omega(\Omega), \tag{5.26}$$

$$\left(\frac{\mathrm{d}}{\mathrm{d}t} + u_\parallel\nabla_\parallel\right)u_\parallel = -\frac{\nabla_\parallel\left(p_e + \zeta p_\mathrm{i}\right)}{n} + \zeta T_\mathrm{i} C(u_\parallel) - \frac{2}{3}\zeta\frac{B^{3/2}}{n}\nabla_\parallel\frac{G}{B^{3/2}} + \mathscr{D}_u(u_\parallel), \tag{5.27}$$

$$\beta_0\frac{\partial}{\partial t}A_\parallel + \mu\left(\frac{\mathrm{d}}{\mathrm{d}t} + v_\parallel\nabla_\parallel\right)\frac{j_\parallel}{n} = -\left(\frac{\eta_{\parallel 0}}{T_e^{3/2}}\right)j_\parallel - \nabla_\parallel\varphi + \frac{\nabla_\parallel p_e}{n} + 0.71\nabla_\parallel T_e + \mathscr{D}_\Psi(\Psi_m), \tag{5.28}$$

$$\begin{aligned}\frac{3}{2}\left(\frac{\mathrm{d}}{\mathrm{d}t} + v_\parallel\nabla_\parallel\right)T_e = {} & T_e C(\varphi) - \frac{T_e}{n}C(p_e) - \frac{5}{2}T_e C(T_e) - T_e\nabla\cdot\left(v_\parallel\mathbf{b}\right) + 0.71\frac{T_e}{n}\nabla\cdot\left(j_\parallel\mathbf{b}\right) \\ & + \frac{1}{n}\nabla\cdot\left[\left(\chi_{\parallel e0}T_e^{5/2}\right)\mathbf{b}\nabla_\parallel T_e\right] - 2\nu_{e0}\mu\left(\frac{n}{T_e^{3/2}}\right)\left(T_e - \zeta T_\mathrm{i}\right) + \left(\frac{\eta_{\parallel 0}}{T_e^{3/2}}\right)\frac{j_\parallel^2}{n} + \frac{3}{2}\left(\mathscr{D}_{T_e}(T_e) + S_{T_e}\right),\end{aligned} \tag{5.29}$$

$$\begin{aligned}\frac{3}{2}\left(\frac{\mathrm{d}}{\mathrm{d}t} + u_\parallel\nabla_\parallel\right)T_\mathrm{i} = {} & T_\mathrm{i} C(\varphi) - \frac{T_\mathrm{i}}{n}C(p_e) + \frac{5}{2}\zeta T_\mathrm{i} C(T_\mathrm{i}) - T_\mathrm{i}\nabla\cdot\left(u_\parallel\mathbf{b}\right) + \frac{T_\mathrm{i}}{n}\nabla\cdot\left(j_\parallel\mathbf{b}\right) \\ & + \frac{1}{n}\nabla\cdot\left[\left(\chi_{\parallel i0}T_\mathrm{i}^{5/2}\right)\mathbf{b}\nabla_\parallel T_\mathrm{i}\right] + 2\nu_{e0}\mu\left(\frac{n}{T_e^{3/2}}\right)\left(\frac{1}{\zeta}T_e - T_\mathrm{i}\right) + \frac{2w_{GTi}}{9\eta_{i0}}\frac{G^2}{nT_\mathrm{i}^{5/2}} + \frac{3}{2}\left(\mathscr{D}_{T_\mathrm{i}}(T_\mathrm{i}) + S_{T_\mathrm{i}}\right),\end{aligned} \tag{5.30}$$

$$\nabla_\perp^2 A_\parallel = -j_\parallel. \tag{5.31}$$

The normalized equations equations (5.25)-(5.31) represent electron continuity equation, vorticity equation, parallel momentum balance, Ohm's law, electron and ion temperature equations and Ampere's law. The advective derivative is defined as $\frac{\mathrm{d}}{\mathrm{d}t} = \frac{\partial}{\partial t} + \delta_0\left(\frac{\mathbf{B}}{B^2}\times\nabla\varphi\right)\cdot\nabla$ and the curvature operator as $C(f) = -\delta_0\left(\nabla\times\frac{\mathbf{B}}{B^2}\right)\cdot\nabla f$. The equation set requires a number of auxiliary quantities: The parallel electron velocity $v_\parallel = u_\parallel - j_\parallel/n$, the electron and ion pressures $p_e = nT_e$ respectively $p_\mathrm{i} = nT_\mathrm{i}$, generalized vorticity $\Omega = \nabla\cdot\left[\frac{n}{B^2}\left(\nabla_\perp\varphi + \zeta\frac{\nabla_\perp p_\mathrm{i}}{n}\right)\right]$ and generalised electromagnetic potential $\Psi_m = \beta_0 A_\parallel + \mu\frac{j_\parallel}{n}$. The ion viscous stress function G was defined in eq. (5.13) and is normalized as $G = n_0 T_{i0}\hat{G}$. The parallel gradient is defined as $\nabla_\parallel = \mathbf{b}\cdot\nabla$, with $\mathbf{b} = \mathbf{B}/B$ the unit vector of the background magnetic field. While electromagnetic induction is taken into account in eq. (5.28), transport by electromagnetic fluctuations (flutter) is implemented, but currently disabled due to significant additional computational cost.

The four dimensionless, collisionless parameters of the system are the drift scale $\delta_0 = R_0/\rho_{s0}$, dynamical plasma beta β_0 defined above, and electron to ion mass and temperature ratios $\mu = m_e/M_\mathrm{i}$ respectively $\zeta = T_{i0}/T_{e0}$. For the collisional parameters, we require τ_{e0} and τ_{i0} – the electron respectively ion collision times evaluated at reference temperature and density and normalised to R_0/c_{s0}. Then, the remaining five dimensionless collisional parameters of the system are the electron collisionality $\nu_{e0} = 1/\tau_{e0}$, normalised parallel resistivity $\eta_{\parallel 0} = 0.51\mu\nu_{e0}$, normalised parallel electron and ion heat conductivities $\chi_{\parallel e0} = 3.15\tau_{e0}/\mu$ respectively $\chi_{\parallel i0} = 3.9\tau_{i0}\zeta$, and normalized ion viscosity $\eta_{i0} = 0.96\tau_{i0}$. Additionally, via the parameter w_{GTi}, ion viscous heating which is usually dropped in literature [37] can be switched on and off.

S_n, S_{T_e} and S_{T_i} are source functions driving the system with particles and energy. For numerical reasons, respectively in order to cut the turbulent spectrum, a dissipation is added to all equations of the form

$$\mathscr{D}_f = \nu_{f\perp}\nabla_\perp^{2N} f + \nu_{f\parallel}\nabla\cdot\left(\mathbf{b}\nabla_\parallel f\right) + \nabla\cdot\left(\nu_{f,\mathrm{buffer}}\nabla_\perp f\right), \tag{5.32}$$

with constants $\nu_{f\perp}$, $\nu_{f\parallel}$ for every field. $\nu_{f,\mathrm{buffer}}$ is zero in most of the domain, but is high in the last few grid points towards the radial boundaries. For hyperviscosity, $N = 3$ is chosen.

The system is energy conserving, with the exception of numerical dissipation, neglect of polarisation velocity in perpendicular advection and boundary conditions. We note that parallel viscosity in eq. (5.27)

is treated implicitly, similarly to electron and ion heat conduction [1], while all other terms are advanced explicitly in time.

At the inner and outer limiting flux surfaces, the following homogeneous boundary conditions are applied

$$\partial_\rho n = 0, \qquad \partial_\rho T_{\mathrm{e,i}} = 0, \qquad \partial_\rho u_\parallel = 0, \qquad \Omega = 0, \qquad A_\parallel = 0, \qquad \partial_\rho j_\parallel = 0, \tag{5.33}$$

to prevent particles and energy fluxes through the boundary. For the potential, the sheath boundary condition $\phi|_{\rho_{\max}} = \Lambda T_\mathrm{e}$ is applied at the outer wall boundary. At the inner (core) boundary $\rho_{\min}$, the zonal homogeneous Neumann boundary condition $\partial_\rho \langle\varphi\rangle_\theta = 0$ and $\varphi - \langle\varphi\rangle_\theta = 0$ is applied, which allows the potential to float but prevents net $E \times B$ flux through that boundary.

At the divertor, insulating Bohm sheath boundary conditions are applied

$$u_\parallel \gtrless \sqrt{T_\mathrm{e} + T_\mathrm{i}}, \quad j_\parallel = 0, \quad \phi = \Lambda T_\mathrm{e}, \quad \nabla_\parallel T_\mathrm{e} = -\frac{\gamma_\mathrm{e}}{\left(\chi_{\parallel \mathrm{e}0} T_\mathrm{e}^{5/2}\right)} T_\mathrm{e} n u_\parallel, \quad \nabla_\parallel T_\mathrm{i} = 0, \quad \nabla_\parallel n = 0, \quad \nabla_\parallel \Omega = 0, \tag{5.34}$$

where $\Lambda = 2.69$ and $\gamma_\mathrm{e} = 2.5$.

For further numerical details on the implementation of the model in GRILLIX, e.g. the flux-coordinate independent approach and the immersed boundary technique, we refer to previous publications [1, 106, 107, 118].

Chapter 6

The role of neutral gas in validated global edge turbulence simulations

W. Zholobenko, A. Stegmeir, M. Griener, G. D. Conway, T. Body, D. Coster, F. Jenko, and the ASDEX Upgrade Team[a)]

Max-Planck-Institut für Plasmaphysik, D-85748 Garching, Germany
[a)] see author list of H. Meyer *et al* 2019 *Nucl. Fusion* **59** 112014

Email: Wladimir.Zholobenko@ipp.mpg.de

Appeared in: Wladimir Zholobenko *et al* 2021 *Nuclear Fusion*
https://doi.org/10.1088/1741-4326/ac1e61
Presented as an invited talk at: 28th IAEA Fusion Energy Conference (FEC 2020), 10–15 May 2021, Virtual Event
Original publication [4] and detailed disclaimer are included in the appendix.

Abstract To make predictions for and design fusion reactors, a multitude of physical processes must be considered. In the edge and scrape-off layer (SOL), turbulent fluctuations intertwine with the plasma background, which is largely determined by neutral gas, and magnetic geometry plays an important role. A diffusive neutrals model has now been implemented in the global Braginskii edge turbulence code GRILLIX. The code is based on the flux-coordinate independent (FCI) approach, which allows efficient turbulence simulations in diverted equilibria. We validate simulations across the ASDEX Upgrade edge and SOL against measurements in discharge #36190, and find much better agreement thanks to the neutrals. Disentangling the effects of the neutral gas, we find that it affects the plasma in several ways. Firstly, the ionization of neutrals modifies the radial profiles of plasma density and temperature, leading to a transition of the turbulence drive from general ballooning type to ion temperature gradient (ITG) type. Secondly, strong poloidal asymmetries can be induced due to divertor recycling, depending on the ionization pattern. As ballooned perpendicular plasma transport is stronger at the low-field side, neutrals penetrate deeper into the plasma at the high-field side, leading to significant ionization and radiation there. With increasing divertor neutrals density, the targets cool down while plasma density increases, more strongly at the high-field side. Much of the dynamics takes place directly around the X-point and along the separatrix, which can be resolved by the FCI approach. Potential remains in extending the model and the code, but our results build confidence that predictive capability is within reach for major design questions for fusion reactors, such as the near SOL fall-off length.

6.1 Introduction

Among the key design goals for fusion reactors are manageable heat and particle exhaust at optimal core confinement – which is only possible in divertor geometry [11]. Extrapolations from today's experiments to reactors unfortunately suggest that current solutions might not suffice [45], and advanced

divertor [18, 19], detachment [229, 230] and confinement [21, 231] concepts are required. Yet, in designing them, it is challenging to predict the complex nonlinear plasma response, and particularly the turbulent transport. The most reliable way are direct numerical simulations [50], and recently various methods have been developed in order to handle the complex diverted geometries [102, 104, 112, 114] in edge turbulence codes. Among them, GRILLIX [3, 106, 107] is able to perform turbulence simulations in any axisymmetric magnetic equilibrium [118] at moderate computational cost, thanks to the flux-coordinate independent (FCI), locally field-aligned discretisation [160, 161]. However, before reliable predictions can be made, the code should be validated against present experiments. GRILLIX was previously validated against the linear large plasma device (LAPD) [121] and was recently validated against diverted TCV experiments [155]. With the latest advances in the GRILLIX model, detailed below, we now perform a validation against an attached L-mode discharge in the ASDEX Upgrade (AUG) diverted tokamak.

It has long been recognised that at the plasma edge, recycling – i.e. neutralisation of the plasma at the wall and re-ionization of the neutral gas – plays a major role in establishing the density and temperature profiles [12]. Transport codes in 2D [94, 145, 195] and 3D [97] with sophisticated wall, neutral gas and impurity models [93, 232, 233] are routinely used to interpret and design experiments. However, the results substantially depend on the heuristic turbulent transport models. Due to large fluctuation amplitudes in the SOL [50, 88, 89], background evolution and turbulent fluctuations can not be well separated, prohibiting a straight-forward implementation of local turbulence models in those transport codes. Global turbulence codes that solve for turbulence and transport simultaneously, on the other hand, are complex and computationally expensive, and only recently began implementing neutral gas models [105, 108, 113].

In this contribution, we report on the implementation of a neutral gas model in the global turbulence code GRILLIX. Starting simple, the model defines source terms for plasma density, vorticity and electron temperature due to charge exchange (CX), ionization and recombination reactions between the plasma and one atomic neutrals species. The neutrals diffuse homogeneously, with their temperature assumed to be equal to the ions, modelling their microscopically ballistic motion inhibited only by CX collisions with the plasma. The plasma model consists of two-fluid drift-reduced [57] global Braginskii equations, as was lastly summarized in Ref. [3]. The only advancement from the Braginskii equations so far is the implementation of a limiter for the parallel heat conduction [49, 132, 135, 204, 205, 225, 234], the crudest possible model for Landau damping of the parallel heat flux at low collisionality, where the original Braginskii closure would break down.

With these extensions, GRILLIX is validated against AUG discharge #36190: we compare electron density and temperature profiles at the outboard mid-plane and at the divertor, as well as the radial electric field at the outboard mid-plane. Along with the comparison to the experiment, we stress the role of the neutral gas in these simulations. The primary effect is the plasma density source given by neutrals ionization, which has a non-trivial profile in the SOL and reaching to the separatrix around the X-point, particularly at the high-field side. The non-trivial source distribution leads to poloidal density asymmetries in the plasma edge. Compared to simulations without neutrals, a much flatter density profile results in the confined region. Consequently, the turbulence is driven not by general ballooning modes, but predominantly by ion temperature gradient (ITG) modes – characterised by large ion temperature fluctuations and larger ion than electron heat transport. Further, due to the dilution of the plasma by cold electrons from neutrals ionization and the accompanying radiation, the electron fluid is cooled down significantly towards the divertor plates. As plasma collisionality increases, its heat conduction is reduced and parallel temperature gradients establish. With reduced parallel heat outflow, the perpendicular turbulent transport flattens radial temperature profiles in the near SOL at the outboard mid-plane, resulting in much more realistic fall-off lengths. With increasing divertor neutrals density, also the far SOL plasma density rises, building ultimately a ‘density shoulder’ [235, 236].

The remainder of the manuscript is organized as follows. The neutral gas model is described in section 6.2. The implementation of the parallel heat flux limiter is documented in section 6.3. The simulation setup is summarised in section 6.4, recapitulating the basics from our previous work [3] and focusing on novel aspects concerning the neutrals and the heat flux limiter. The central results of this work – the validation of the simulations against ASDEX Upgrade and the role of neutral gas therein –

are detailed in section 6.5. Section 6.6 discusses the high-recycling regime reached at higher divertor neutrals density, and the necessary model extensions for turbulence simulations in detached conditions. Finally, conclusions and an outlook are given in section 6.7.

6.2 Neutral gas model

We consider a single ion species plasma and the corresponding neutral atoms. Molecules are currently ignored, as they are not so important in attached tokamak conditions due to the low dissociation energy of 4.5 eV*. The plasma and neutral fluids interact via the electron impact ionization and recombination reactions,

$$\mathrm{e}^- + \mathrm{D} \longleftrightarrow 2\mathrm{e}^- + \mathrm{D}^+, \tag{6.1}$$

and the charge exchange process

$$\mathrm{D}^+ + \mathrm{D} \longleftrightarrow \mathrm{D} + \mathrm{D}^+. \tag{6.2}$$

Electron impact ionization and recombination result in density exchange between the neutral (N) and ionized (n) fluids according to

$$S_n = k_{\mathrm{iz}} n N - k_{\mathrm{rec}} n^2 = -S_N. \tag{6.3}$$

This source term is added to the right hand side of the plasma continuity equation (A1) in Ref. [3]. The rate coefficients are obtained from the publicly accessible Amjuel database [141]. Note that the recombination rate is virtually irrelevant for $T_\mathrm{e} > 2$ eV.

Additionally, electron impact reactions affect the thermal energy of the electron fluid. For the pressure, we can write

$$\frac{3}{2}\frac{\mathrm{d}p_\mathrm{e}}{\mathrm{d}t} \sim -W_{\mathrm{iz}} n N - W_{\mathrm{rec}} n^2 \tag{6.4}$$

with electron cooling rates due to ionization W_{iz} and recombination W_{rec}. These contain both the thermal energy dissipation through radiation, due to electron impact excitation and radiative de-excitation, as well as the energy transfer of 13.6 eV between bound and free electrons. Note that the latter process cools the plasma during ionization and radiative recombination, but heats it up during three-body recombination, such that W_{rec} becomes negative at $T_\mathrm{e} < 1$ eV. For the electron temperature, we then obtain the source

$$S_{T_\mathrm{e}} = -\frac{2}{3}\left(W_{\mathrm{iz}} N + W_{\mathrm{rec}} n\right) - \left(k_{\mathrm{iz}} N - k_{\mathrm{rec}} n\right) T_\mathrm{e}. \tag{6.5}$$

The second bracket results from $\partial_t T_\mathrm{e} = \left(\partial_t p_\mathrm{e} - T_\mathrm{e}\partial_t n\right)/n$ and inserting S_n. $k_{\mathrm{iz}} N T_\mathrm{e}$ is in fact the dominant term at $T_\mathrm{e} > 20$ eV. It can be understood as dilution of the hot plasma by cold, newly ionized electrons.

Charge exchange involves no transfer of internal energy and is therefore elastic, mixing very efficiently the momentum and thermal energy of the neutral and ion fluids, while conserving density. Therefore, and for simplicity, we will assume that ions and neutral atoms share the same temperature $T_\mathrm{i} = T_\mathrm{N}$ (which is strictly valid only if the charge exchange mean free path is smaller than the T_i gradient length [239]). The only exception to this is right at the divertor targets: the neutrals do not thermalise instantaneously, having rather wall than plasma temperature there, $T_N \approx 0$ compared to attached plasma conditions $T_\mathrm{i} \gtrsim 10$ eV. Modelling of the neutral gas temperature in more detail is complex, as the rich chemistry (including the interaction with the wall) and the relatively large mean free path prohibit the representation of the neutrals velocity space distribution by a simple local Maxwellian – usually, either kinetic [93, 108] or multi-group fluid [240] treatments are required.

The primary importance of charge exchange in our model is that this scattering process is the only one that efficiently inhibits the ballistic motion of the dilute neutrals. Similarly as in references [145, 146, 240], we describe the motion of the neutral gas as diffusion, with the diffusion coefficient

$$D_N = \frac{c_{\mathrm{s,N}}^2}{\nu_{\mathrm{cx}}} = \frac{T_\mathrm{i}/m_\mathrm{i}}{k_{\mathrm{cx}} n}. \tag{6.6}$$

*Molecular assisted dissociation and ionization are the dominant processes [237] and should be considered as an electron cooling effect [145], but are yet negligible compared to atomic ionization and dilution. They will become important for reaching detached conditions however [12, 237, 238]: molecular assisted dissociation and ionization reduce the ionization length of particles and can lead to an up to 100% higher upstream density required to reach detachment [237], while molecular assisted recombination contributes only 10 – 20% to the total recombination rate, dominated by atoms [237, 238].

Here, $c_{s,N} = \sqrt{T_i/m_i}$ is the neutral gas sound velocity, $m_N \approx m_i$ the neutrals mass, ν_{cx} the charge exchange frequency and k_{cx} the charge exchange rate coefficient. The latter is estimated according to Ref. [144, eq. (24)] via $k_{cx} = 2.93\sigma_{cx}c_{s,N}$, with the hydrogen charge exchange cross section being roughly 7×10^{-19} m^2. Additionally, as suggested by Ref. [146, 241], the diffusion coefficient is limited to keep the neutrals flux below the sound limit (in low collisionality regions of the domain), i.e. $\tilde{D}_N = \min\left(D_N, NT_i c_{s,N}/\left|\nabla NT_i\right|\right)$.

The neutral particles conservation equation then becomes

$$\frac{\partial N}{\partial t} = \nabla \cdot \frac{\tilde{D}_N}{T_i}\nabla NT_i - k_{iz}nN + k_{rec}n^2. \tag{6.7}$$

It is important that neutrals diffuse also along the ion temperature gradient [145, 146], as they otherwise penetrate too deep into the confined plasma. An exception to this is right at the divertor, where $T_N \approx 0$ – effectively $\nabla T_i|_{div} = 0$ in eq. (6.7) – prevents local trapping of neutral gas between the neutrals density and ion temperature gradients.

Note that the motion of the neutral gas is isotropic, contrary to the strongly anisotropic plasma motion. The plasma flows very fast parallel to the magnetic field, but its motion in the perpendicular direction is strongly inhibited and described by micro turbulence. To resolve this, GRILLIX uses the FCI approach with a strongly anisotropic grid, very sparse toroidally but dense in the poloidal plane. As the neutrals move fast also within the poloidal plane, this results in a stiff 2D diffusion problem. It is solved by means of the same multigrid algorithm used for the electromagnetic fields [107], taking 5-10% of the total computing time.

We remark that the current model has little influence on the plasma parallel velocity. Due to the small electron mass, we ignore the impact of electron-neutral collisions on the momentum of the electron fluid. For the ion and neutral fluids, we assume that CX collisions are frequent enough that their parallel velocities are approximately equal and are determined by the plasma, like for the temperature. In effect, this disregards transport of parallel velocity and temperature by the neutrals. Further, the dissipation of the parallel momentum by neutrals viscosity [145], due to CX and neutral-neutral collisions, is assumed to be negligible. We expect these assumptions to be reasonable in present simulations of an attached AUG discharge, where N/n in the near-SOL does not exceed 5%. But this will need to be re-examined at higher neutrals densities, towards detachment conditions. The only effect on parallel velocity currently considered is indirect: as the temperature at the divertor drops due to the neutrals, the plasma parallel velocity at the boundaries lowers due to the Bohm sheath boundary condition.

However, we do consider the dissipation of vorticity due to the transfer of perpendicular momentum. Assuming that momentum is simply exchanged between ions and neutrals during ionization and recombination, we find the local momentum density exchange rate

$$\frac{\mathrm{d}}{\mathrm{d}t} m_i n \mathbf{v}_i \sim k_{iz} N n m_i \mathbf{v}_N - k_{rec} n^2 m_i \mathbf{v}_i + k_{cx} N n m_i (\mathbf{v}_N - \mathbf{v}_i). \tag{6.8}$$

Rewriting this in terms of $m_i n \frac{\mathrm{d}}{\mathrm{d}t}\mathbf{v}_i$, adding it to the Braginskii ion equation of motion [56] and crossing it with $\times\mathbf{B}$, we obtain for the perpendicular ion velocity (in cgs units)

$$\begin{aligned} B^2 \frac{en}{c}\mathbf{v}^{\mathbf{i}}_{\perp} = \; & - \nabla p_i \times \mathbf{B} + en\mathbf{E}\times\mathbf{B} - m_i n \frac{\mathrm{d}\mathbf{v}_i}{\mathrm{d}t}\times\mathbf{B} \\ & - (\nabla\cdot\Pi_i)\times\mathbf{B} + (k_{iz}+k_{cx})Nnm_i(\mathbf{v}_N - \mathbf{v}_i)\times\mathbf{B}. \end{aligned} \tag{6.9}$$

We readily identify the first two terms on the right-hand side of the equation as diamagnetic $\mathbf{v}^i_*$ and $E\times B$ velocity $\mathbf{v}_E$. The remaining terms depend themselves on $\mathbf{v}^{\mathbf{i}}_{\perp}$ and are approximated in terms of diamagnetic and $E\times B$ velocities following the drift-reduction procedure [57]. The third term then becomes the polarisation velocity, crucial for turbulence, together with the fourth term, the ion stress-tensor Π_i [3]. The last term on the right-hand side is perpendicular velocity exchange between ions and neutrals. Here we note that the neutrals mean free path $\lambda_N = c_{s,N}/\nu_{cx}$ is much larger than the relevant perpendicular scale for the plasma, the Larmor radius. Therefore, we have $\nabla\cdot\mathbf{v}_N \ll \nabla\cdot\mathbf{v}_i$ and can ignore the neutrals velocity here, i.e. the vorticity source due to momentum gain from neutrals [108, 242].

Finally, we obtain the vorticity sink due to momentum loss to neutrals as

$$S_\Omega = -\nabla\cdot\left[\frac{m_\mathrm{i}c^2 nN}{eB^2}\left(k_\mathrm{iz}+k_\mathrm{cx}\right)\left(\nabla_\perp\varphi+\frac{\nabla_\perp p_\mathrm{i}}{en}\right)\right]. \tag{6.10}$$

This sink is added to the right-hand side of the vorticity equation (A2), see [3, appendix]. Under a Boussinesq type approximation – which we do not apply – this is roughly $S_\Omega \approx -\frac{\nu_\mathrm{iz}+\nu_\mathrm{cx}}{\omega_\mathrm{ci}} N\Omega_\mathrm{F}$, with $\omega_\mathrm{ci} = eB/m_\mathrm{i}c$, $\nu_\mathrm{iz} = nk_\mathrm{iz}$ and the fluid vorticity $\Omega_\mathrm{F} = \mathbf{b}\cdot\nabla\times\left(\mathbf{v}_E+\mathbf{v}_*^\mathrm{i}\right)$. This vorticity sink has been found important in situations with high neutrals densities, e.g. in linear devices [243] and in detached tokamak conditions [244]. But in our simulations so far, we have not observed a significant effect yet.

As a last point, the biggest limitation of the model are boundary conditions. We currently only implement Dirichlet and homogeneous Neumann boundary conditions: zero flux at the main chamber wall, zero neutrals density at the core boundary and a fixed neutrals density N_div at the divertor. With this, N_div must be scanned to obtain global recycling, i.e. plasma density sourced to $\sim 99\%$ by neutral gas ionization, as detailed in section 6.4 (main chamber recycling is neglected, as suggested by transport studies [245]). Local recycling boundary conditions [145] will be implemented in near future, demanding adaptations to the code structure: the challenge here is that neutrals are much more mobile across flux surfaces than the plasma, requiring boundary conditions on perpendicular rather than on parallel fluxes. We note that the divertor neutrals density as a free parameter is likely to mask the general simplicity of the current neutrals model, ignoring the effects of neutrals viscosity, details of their velocity distribution, molecules and details of the plasma-wall-neutrals interaction (including gas puffing, pumping, outgassing etc.). On one hand, this avoids the problem of possibly long saturation times due to local recycling [246] and allows a relatively good match to the experiment with a very simple neutrals model, such that qualitative effects can already be studied in relevant conditions. On the other hand, predictive simulations will require a more complete model without free parameters.

6.3 Plasma model improvements

For the plasma, the global drift reduced Braginskii model is employed in GRILLIX. It can handle arbitrary fluctuation levels (no δf splitting), features electromagnetic effects and electron/ion thermal dynamics. The model has been comprehensively summarised in Ref. [3, appendix]. Here, some additional improvements are outlined.

The Braginskii heat conductivities $\chi_\parallel^\mathrm{e} = 3.16nT_\mathrm{e}\tau_\mathrm{e}/m_\mathrm{e} \sim T_\mathrm{e}^{5/2}$ and $\chi_\parallel^\mathrm{i} = 3.9nT_\mathrm{i}\tau_\mathrm{i}/m_\mathrm{i} \sim T_\mathrm{i}^{5/2}$ [56] are known to be inappropriate at low collisionality [94, 204, 205]. In this work, we will limit them by a harmonic average between the Braginskii and the free streaming heat flux, $\tilde{q} = \left(\frac{1}{|q_\mathrm{Braginskii}|}+\frac{1}{q_\mathrm{FS}}\right)^{-1}$, with $q_\mathrm{FS} = \alpha n\sqrt{T/m}T$ [49, chapter 26.2]. For the heat conduction, this can be rewritten as

$$\begin{aligned}\tilde{\chi}_\parallel^{\mathrm{e,i}} &= \chi_\parallel^{\mathrm{e,i}}\left(1+\frac{|q_\mathrm{Braginskii}|}{q_\mathrm{FS}}\right)^{-1} = \chi_\parallel^{\mathrm{e,i}}\left(1+\frac{\chi_\parallel^{\mathrm{e,i}}|\nabla_\parallel T|}{\alpha n\sqrt{T/m}T}\right)^{-1} \\ &\approx \chi_\parallel^{\mathrm{e,i}}\left(1+\frac{\chi_\parallel^{\mathrm{e,i}}}{\alpha_{\mathrm{e,i}} n\sqrt{T_{\mathrm{e,i}}/m_{\mathrm{e,i}}}R_0 q}\right)^{-1}.\end{aligned} \tag{6.11}$$

In the last expression, we have approximated $\left|\nabla_\parallel T_{\mathrm{e,i}}\right|/T_{\mathrm{e,i}} \approx 1/qR_0$ with the machine major radius R_0 and the safety factor q, to avoid the non-linearity in $\nabla_\parallel T$ in the temperature equation. To avoid issues with the diverging safety factor at the separatrix, it is set to constantly $q = 4$. Note that due to the mass factor, the limiter is more severe for ions than for electrons. This Knudsen correction [225] is frequently used in literature [135, 205, 234] and constitutes a first step towards a Landau fluid close [85, 132], but similarly to previous work [205] we will find a significant dependence of simulation results on the free parameter $\alpha_{\mathrm{e,i}}$.

Besides changing the expression for the parallel heat flux according to (6.11), we also modify the electron temperature boundary condition $\nabla_\parallel \log(T_\mathrm{e}) = -\gamma_\mathrm{e} n u_\parallel/\chi_\parallel^\mathrm{e}$ at the divertor: taking into account a

finite secondary electron emission coefficient [49] of roughly 0.75, we set $\gamma_e = 1$ (instead of 2.5). For the ions, we keep $\nabla_\parallel \log(T_i) = 0$.

Finally, we note that unlike in our previous work, viscous ion heating is less pronounced and poses no stability issues any more because of increased collisionality due to neutrals. Due to previous concerns [3], the reference simulation in the present work has also been run without viscous ion heating. But we have repeated the simulation with viscous ion heating on and found only a small effect, 7% higher ion temperature at the OMP separatrix with an otherwise identical profile.

6.4 Simulation setup

We briefly recapitulate the simulation setup, detailed in Ref. [3, sec. 3.1], and then describe the additional challenges in the present work due to the extensions discussed above. The simulations are based on and compared to ASDEX Upgrade discharge #36190 (at 2-4 s), an attached L-mode with 800 kA plasma current, $q_{95} = 4.4$ and average triangularity of $\delta = 0.21$. The toroidal magnetic field is $B_{\text{tor}} = -2.5$ T on axis, i.e. in the favourable configuration with $\mathbf{B} \times \nabla B \sim -\hat{\mathbf{e}}_Z$ towards the divertor X-point. The plasma is heated by 550 kW neutral beam injection and 500 kW ohmic heating, whereby 300 kW are radiated away by impurities.

The magnetic geometry is a lower single null diverted equilibrium, reconstructed from the AUG discharge #36190 at 3.3 s. The simulated domain extends from the core boundary at $\rho_{\text{pol}} = 0.9$ and across the separatrix to $\rho_{\text{pol}} = 1.05$. The outer radial boundary is at the last flux surface intersected by the machine main chamber wall. The artificial core boundary is chosen to be far enough away from the separatrix to not pollute the dynamics there, but not too far into the collisionless plasma core where the fluid model loses its validity. At the core boundary, an adaptive source keeps fixed density and temperature values based on the experiment ($n_{\text{ped}} = 2 \times 10^{19}$ m^{-3} and $T_{\text{ped}}^{\text{e,i}} = 350$ eV), but a zonal Neumann boundary condition allows the potential to float [1] – in the rest of the domain, plasma profiles are free to evolve self-consistently.

The difference to the previous setup is that the plasma model shown in the appendix of Ref. [3] has been extended by the diffusive neutral gas model described in section 6.2. Additionally, we have improved the limiter for the parallel conductive Braginskii heat flux, as explained in section 6.3. Both additions introduce free parameters: the divertor neutrals density N_{div}, and the free streaming parallel heat conduction limiters $\alpha_{\text{e,i}}$. The computational cost of 83 kCPUh per 1 ms simulation allows to roughly adjust these parameters, and investigate their role. However, the simulations must run for at least 3-4 ms, which takes a few months due to the yet limited parallelizability of the code (in practice, 384 Intel SkyLake CPU cores were used simultaneously per simulation). Therefore, fine tuning was not possible, and we have limited ourselves to a relatively coarse resolution of 16 poloidal planes and a grid distance of 1.45 mm within each plane, totalling 7 million grid points. We have previously found this to be sufficient to resolve the overall transport and profile evolution [3].

The neutral gas model has a major impact on the simulations. Most importantly, the dominant plasma density source is now shifted from the core boundary at $\rho_{\text{pol}} = 0.9$ to the separatrix and SOL, where neutrals are ionized. The ionization source depends on the local neutrals density, which is not obtained in a fully self-consistent way, as local recycling boundary conditions are not yet implemented: a fixed neutrals density N_{div} must be prescribed via a Dirichlet boundary condition at the divertor, the neutrals then expand into the interior domain according to the diffusion model described in section 6.2 and are ionized according to Amjuel [141] reaction rate coefficients. Recycling is then obtained in a global sense by scanning and adjusting the N_{div} parameter. Note that the adaptive source at the core boundary still holds the plasma density fixed there at 2×10^{19} m^{-3}, but the goal is that the required source strength saturates between 0-1% of the ionization source. Figure 6.1 shows the time evolution of the volume integrated core particle source S_n compared to the integrated ionization source S_{iz} in our reference simulation with $N_{\text{div}} = 5 \times 10^{17}$ m^{-3}. The initial spike in S_{iz} is due to the initial condition on the neutrals density N, which is constant in the whole domain and equal to N_{div}. After the initial transient phase, S_{iz} increases and S_n decreases as more heat is arriving at the divertor. After saturation at $t \approx 4$ ms, we have $S_n/S_{\text{iz}} \approx 0.5\%$, i.e. 99.5% recycling. For comparison, the dashed line shows the evolution of the density sources for $N_{\text{div}} = 8 \times 10^{17}$ m^{-3}. Once S_n gets too close to zero, the separatrix density becomes too high

and simulations become unstable due to resistive ballooning modes [68, 247].

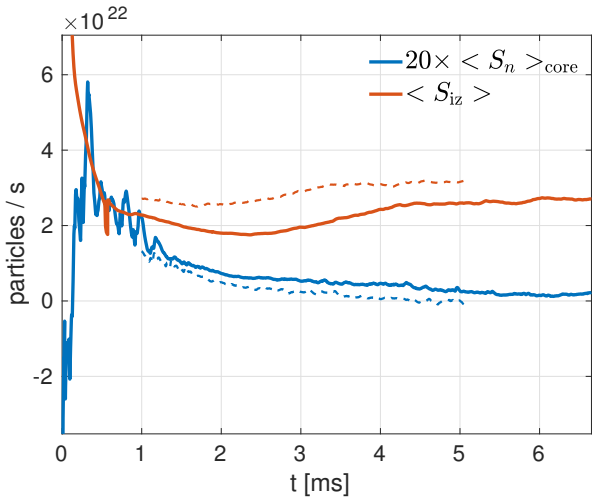

Figure 6.1: Time evolution of the volume integrated core particles source S_n magnified by 20 to be compared with the ionization particle source S_{iz}. Solid line: reference simulation with $N_{\mathrm{div}} = 5 \times 10^{17}$ m^{-3}, dashed line: $N_{\mathrm{div}} = 8 \times 10^{17}$ m^{-3}.

Figure 6.2 shows the input power at the core boundary of the simulation evolving in time, which is required to maintain the fixed pressure there due to turbulent radial heat outflow. After 4 ms in the reference simulation, it is at about 100 kW for electrons and 430 kW for ions, which is in reasonable agreement with the 750 kW net heating in the experiment (after the subtraction of the 300 kW radiated by impurities, as those are not present in the simulation). With varying divertor neutrals density, we were able to change the input power by at most 5%. However, the input power is sensitive to the free streaming limiter $\alpha_{\mathrm{e,i}}$ for the parallel conductive heat flux, introduced in section 6.3. In the reference simulation, $\alpha_{\mathrm{e,i}} = 1$ as suggested by [85, 135]. But choosing $\alpha_{\mathrm{e,i}} = 0.1$ increases the total heat transport to about 2 MW, as shown by dashed lines in figure 6.2. On the other hand, only limiting the electron and ion heat conductivities to $\chi_{\parallel}^{\mathrm{e,i}} \leq 10^{27}\mathrm{m}^{-1}\mathrm{s}^{-1}$ as was done in simulations without neutrals [3] leads to barely 34 kW electron and 26 kW ion heat transport: as noted in section 6.3, the free streaming limiter is much stronger for ions than for electrons – therefore, the simple limiter allows a particularly large parallel ion heat flux (still smaller than for electrons, though), which suppresses ITG turbulence [214]. Hence, we conclude that better agreement in net heat transport to the experiment – and potentially outboard mid-plane temperature profiles shown in figure 6.3 – might be achieved by fine tuned $\alpha_{\mathrm{e,i}}$, but reasonable results are obtained already with $\alpha_{\mathrm{e,i}} = 1$. Rather, in the future we consider further extending the fluid closure to better approximate Landau damping, as e.g. in Ref. [100].

6.5 Validation of attached L-mode AUG simulations

After discussing the recent model extensions and the simulation setup, we can now present simulation results. As in our previous work without neutrals [3], the simulations saturate after 4 ms in the sense that mean profiles do not visibly change any more, at least over the next few ms (they might change on time scales > 10 ms, but such long simulations are currently out of scope). At this stage, we can separate the mean and the fluctuating parts of the fields by time and toroidal averaging and analyse them. In the following sections, we will compare mean density, temperature and electric field profiles in the reference simulation with $N_{\mathrm{div}} = 5 \times 10^{17}$ m^{-3} to experimental measurements, as well as to simulations without neutrals and with higher divertor neutrals density. Besides analysing outboard mid-plane (OMP) and divertor pressure profiles, we discuss the 2D density profile in a poloidal plane, its asymmetry due to the ionization source distribution and consequences of the density profile on fluctuation amplitudes.

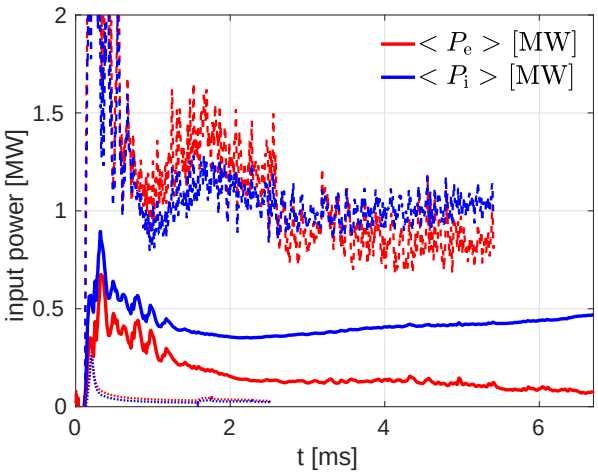

Figure 6.2: Input power at the core boundary of the simulation as a function of time. Solid lines show the reference simulation ($\alpha_{e,i} = 1$), dashed lines show the input power at $\alpha_{e,i} = 0.1$. The dotted lines show the input power without a free-streaming flux limit, but with $\chi_{\parallel}^{e,i} \leq 10^{27} \mathrm{m}^{-1}\mathrm{s}^{-1}$ (see text).

6.5.1 Outboard mid-plane profiles

Figure 6.3 shows the comparison between simulated and experimentally measured density and electron temperature at the OMP. The measured data result from integrated data analysis [248] of electron cyclotron emission, interferometry, Thomson scattering, lithium and helium beam spectroscopy at 3.25-3.35 s of AUG discharge #36190. For the simulation, we average the profiles toroidally and in time over 200 μs. We show both the simulation profiles from Ref. [3] without neutrals (blue dashed lines), as well as the new results with neutral gas ionization (in red). Although no reliable ion temperature measurements are available for this discharge, we show the simulated T_i together with T_e, as the ion heat channel is important for the L-H transition [40].

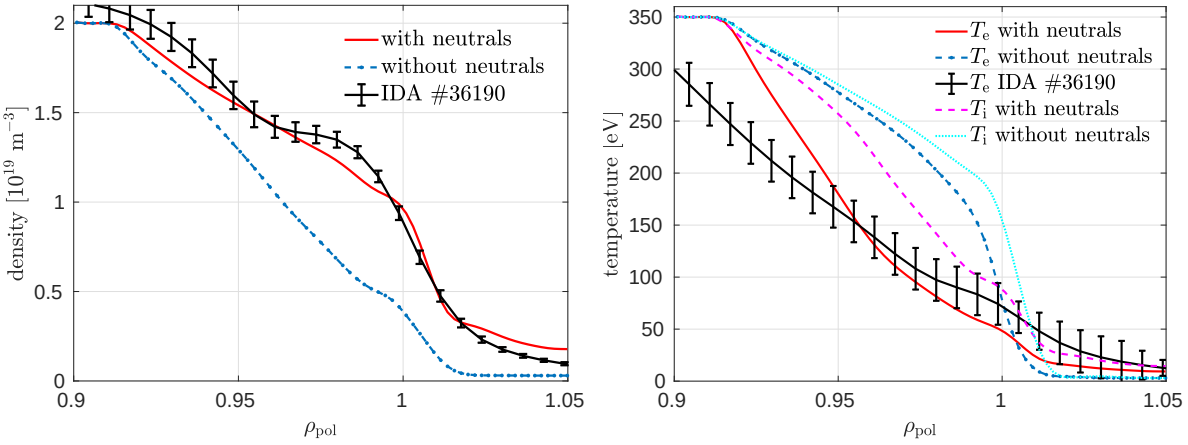

Figure 6.3: Validation of GRILLIX simulations against integrated data analysis from ASDEX Upgrade discharge #36190 (3.25-3.35 s), at the outboard mid-plane, comparing the model with neutral gas ionization ($N_{div} = 5 \times 10^{17}$ m^{-3}) against core boundary density sourcing (i.e. without neutrals) from Ref. [3]. Reliable measurement are available only for T_e, but we also show the simulated T_i.

The main observation is that both the density and electron temperature profiles become much more realistic with the neutral gas model. Without neutrals, with plasma density being sourced to 100% at the core boundary, a steep density gradient builds up as plasma is flowing out in the SOL at the divertor. With neutrals, the density source is localised around the separatrix, and a much more realistic profile results. The radial oscillation on top of the profile – observed both experimentally and in simulations – is stationary over many ms but slowly varying over hundreds of ms and explained in simulations by a zonal flow [3].

For electron temperature, it turned out in the aftermath that we chose a slightly too high core boundary temperature, 350 eV instead of 300 eV as measured experimentally. While this does result in a somewhat steeper gradient in the confined region, the profile at the separatrix is actually close to the experiment – and very different from the profile without neutrals. The reason is partly the different density profile, leading to a different turbulence drive as explained in section 6.5.4. But the neutral gas also directly influences the temperature according to equation (6.5): while recombination is virtually absent as T_e does not fall below 1 eV, ionization is effectively cooling the plasma in regions of significant neutrals density – see section 6.5.2. The colder divertor, as detailed in section 6.5.3, reduces the parallel heat conductivity, allowing for significant parallel gradients in the SOL and reducing the direct parallel heat outflow at the OMP separatrix. As the OMP temperature profile is determined by the competition between perpendicular turbulent transport and parallel conductive outflow, reducing the latter flattens the radial T_e profile and results in much more realistic SOL fall-off lengths.

6.5.2 Ionisation pattern and poloidal asymmetry

While the density profile agrees well with experimental measurements at the outboard mid-plane, it exhibits a surprising amount of poloidal asymmetry, even in the confined region. The 2D density profile in the poloidal cross section at 4 ms simulation time is displayed in figure 6.4. We see that density is higher at the high-field side (HFS) and lower at the low-field side (LFS), peaking near the X-point at the HFS. The reason for this is partly the density source distribution due to ionization: on the right of figure 6.4, we show the mean deuterium radiation density around the X-point, which has the same spacial distribution as the ionization rate. On the LFS, it peaks near the divertor target where the neutrals density is highest, and has otherwise a broad distribution around the heat channel close to the separatrix. On the HFS, ionization peaks further upstream, very close to the separatrix.

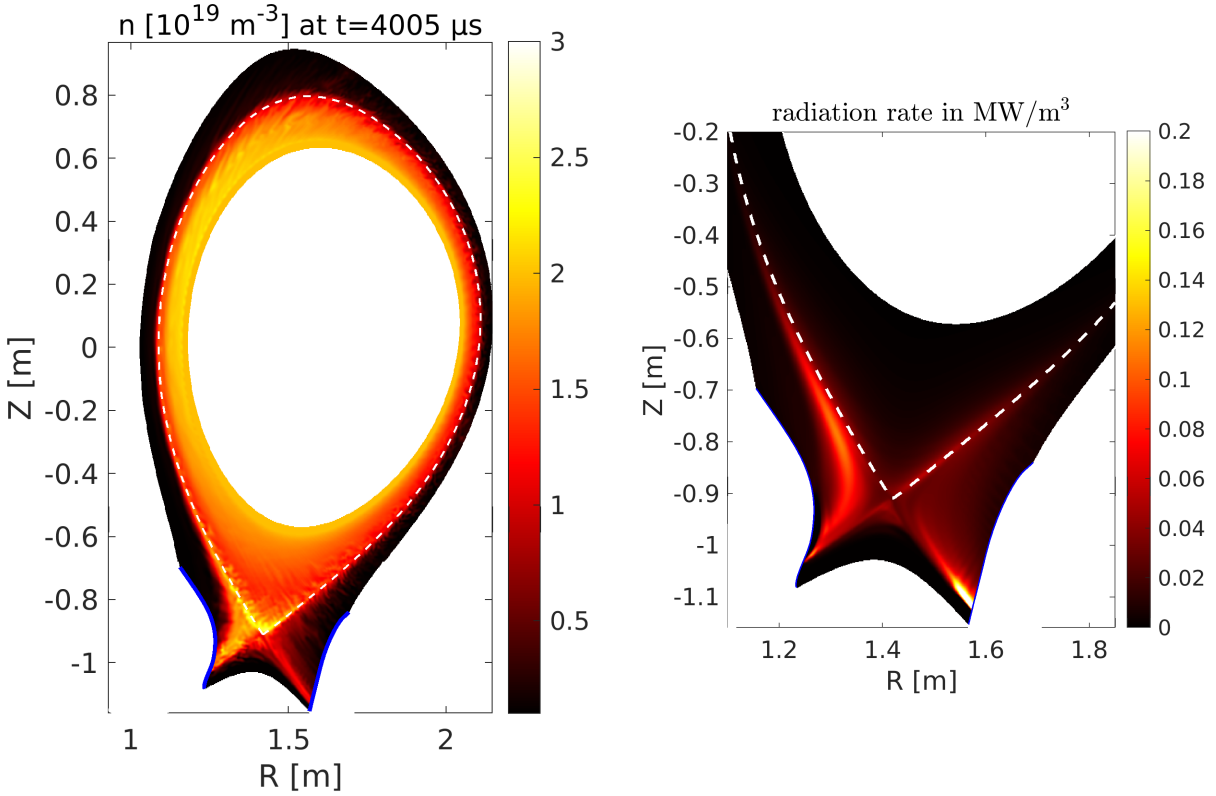

Figure 6.4: Left: 2D density snapshot in the poloidal cross section for the quasi-steady state at 4 ms of the reference simulation. Right: mean deuterium radiation density.

The difference in radiation and ionization patterns between LFS and HFS is due to the ballooned perpendicular turbulent transport being much stronger at the LFS, broadening the SOL profile there and leading to significant fluxes to the LFS divertor. On the HFS, much less power crosses the separatrix at

the inboard mid-plane, allowing the neutrals to penetrate deeper into the plasma. They are then ionized slightly below the separatrix as the confined plasma is slightly shifted downwards due to the $\mathbf{B} \times \nabla B$ drift. This becomes particularly clear from a comparable simulation in unfavourable configuration, where the plasma is shifted upward and barely any heat at all reaches the HFS divertor and the neutrals front extends into the confined region.

The density profile is determined not only by the HFS-LFS and up-down asymmetric source distribution, but also by transport between sources and sinks. Around the X-point, the density gradient in the confined region is reversed, i.e. ascending towards the separatrix, and a mean radial $E \times B$ flow brings density from the source region into the confined plasma. Plasma density peaks at the X-point, accumulating there due to the long parallel connection length. As we discuss in section 6.5.5, the mean poloidal $E \times B$ rotation in the anti-clockwise direction (enhanced by the poloidally asymmetric density source from ionization) brings density from the X-point to the outboard mid-plane. Along the way, ITG driven turbulent transport (see section 6.5.4) tends to eject density together with the heat again, resulting in a descending density slope at the outboard mid-plane as shown in figure 6.3. In a zonal average, however, the outward transport is only as strong as to keep the zonal average density gradient flat, hence the overall ITG transport. Overall, this results in a somewhat higher density at the HFS outboard mid-plane than on the LFS. This asymmetry might be overestimated though, as the parallel ion flow might be too strongly damped by the Braginskii ion viscosity [72]. Also, these results are not fully self-consistent yet, as equal neutrals density is prescribed at both divertor plates. Therefore, while current simulations show that poloidal asymmetries can arise from the ionization source distribution, the details must be more closely investigated in future work. Nevertheless, the relatively good agreement between measured and simulated density profiles at the OMP is encouraging.

6.5.3 Divertor target profiles

In section 6.5.1 we have seen relatively good agreement with the experiment at the outboard mid-plane thanks to our neutrals model. However, recycling is implemented only in a global sense, with a constant divertor neutrals density N_{div} across both divertor plates. Therefore, less good agreement is expected at the target plates. Nevertheless, figure 6.5 generally shows a significant improvement with the neutrals model.

Without neutrals the density is below 2×10^{18} m^{-3}, and the parallel temperature profile in the SOL is flat resulting in nearly identical radial profiles at HFS, LFS and OMP with a peak temperature of 70 eV. With neutrals, due to dilution of the plasma and radiation, the divertor temperature decreases. At the same time, the plasma density increases, sourced by neutrals ionization. The increased collisionality and therefore decreased parallel heat conduction reduce the parallel heat flux and allow turbulence to spread the heat further radially, broadening the temperature profile at both the divertor targets and OMP. Remarkably, even at identical neutrals density of $N_{\text{div}} = 5 \times 10^{17}$ m^{-3} at both divertor plates, we find an in-out asymmetry: as neutrals are ionized deeper in the plasma at the HFS, the plasma density increases more strongly there, while electron temperature falls lower than at the LFS.

Experimentally, an even larger in-out asymmetry is observed, suggesting that neutrals should have a higher density at the HFS than at the LFS divertor. The mismatch in the plasma density profiles also indicates that the neutrals density might be inhomogeneous across the target plates, motivating the implementation of local recycling boundary conditions. However, the profiles are closer to experimental ones than without neutrals at all, most remarkably the peak density at the HFS and the temperature at the LFS. Turbulent fluctuations of up to 40% in the simulations also partly explain the fluctuations in experimental measurements, particularly close to the separatrix, while experimental uncertainties in the far SOL might still be affected by noise.

A simulation with higher $N_{\text{div}} = 3 \times 10^{18}$ m^{-3} improves the match in the HFS temperature profile, corroborating that HFS divertor neutrals density should be higher than at the LFS, but it impairs the LFS temperature comparison and produces too high plasma density. As discussed above, N_{div} had to be scanned to achieve global recycling, but high neutrals density simulations were also an attempt to reach detached conditions, though they did not run stable to saturation as will be discussed in section 6.6.

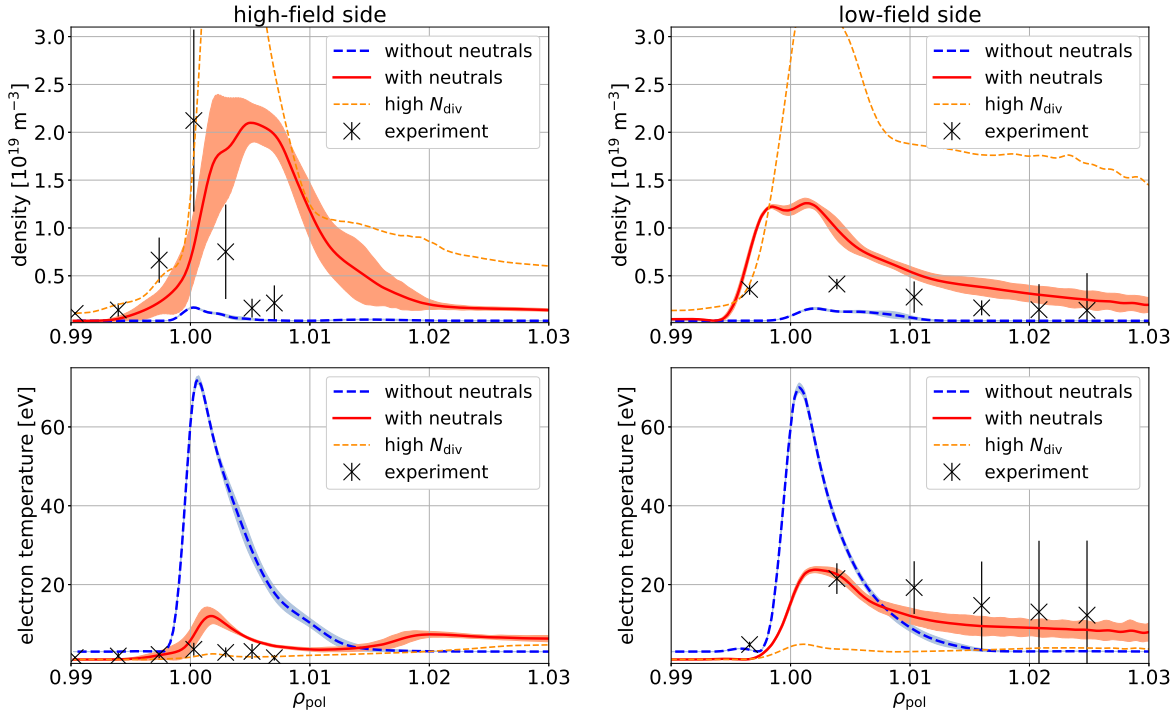

Figure 6.5: GRILLIX divertor profiles, comparing the reference simulation with $N_{div} = 5 \times 10^{17}$ m^{-3} (red curve) against core boundary density sourcing (i.e. without neutrals, blue dashed curve) from Ref. [3]. The dashed orange line shows results from a simulation with increased divertor neutrals density, $N_{div} = 3 \times 10^{18}$ m^{-3}. Simulation results are compared to Langmuir probe measurements [249] from ASDEX Upgrade discharge #36190 (3.3-3.4 s). HFS profiles are on the left, LFS profiles are on the right. The error bars on experimental data points indicate two standard deviations both due to turbulent fluctuations and diagnostic noise. The envelops around simulated profiles show two standard deviations of turbulent fluctuations.

6.5.4 Fluctuation amplitudes and turbulence characterisation

After having investigated the mean density and temperature profiles, we should also discuss their fluctuations. They are quantified by the standard deviation of an ensemble, here a time series and profiles in toroidal direction, normalised to the mean. The fluctuations at the divertor have been indicated in figure 6.5 in the previous section. Here we discuss fluctuation amplitudes at the outboard mid-plane, shown in figure 6.6. For turbulence characterisation, fluctuations of the electrostatic potential are important. They are commonly normalised to the mean electron temperature [88, 89], because the mean electrostatic potential becomes zero at some places.

The most remarkable observation is how different the fluctuation amplitudes are compared to simulations without neutrals [3, fig. 5c]. Electrostatic potential fluctuations are still the largest, indicating that interchange modes are dominant. However, without neutrals, they were followed by density fluctuations – while with neutrals, density fluctuations are the smallest in the confined region, compared to temperature fluctuations. The reason is the shift of the density source from the core boundary to the separatrix, which as we discussed in section 6.5.2 leads to a flat density gradient in the zonal average. Instead, turbulence is now rather driven by the temperature gradients, of which the ion temperature gradient is leading to the largest fluctuations due to the η_i mode [62, 130]. The mode is typically triggered at $\eta_i = L_n/L_{T_i} = \partial_r \ln T_i / \partial_r \ln n > 1$. Without neutrals, we had $\eta_i < 1$ for $\rho_{pol} < 0.997$ at the OMP (0.5 on average). With neutrals, we have $\eta_i > 1$ in the whole confined region, reaching 4 at $\rho_{pol} = 0.96$ at the OMP (2.2 on average). Therefore, together with the observation of the dominating T_i fluctuations, we conclude that the ITG instability is now dominant in the confined region[†] [65, 211]. In the SOL, $\eta_i \sim 1$ and the fluctuation amplitudes for density and temperatures are comparable, so here all of them

[†]In the plasma edge, electrons are generally not adiabatic, which can lead to comparable electron and ion heat fluxes even under ITG turbulence [149]. A difference in radial heat diffusivity of $\chi_e/\chi_i = 1/4 - 1$ is expected [213, table 1]. This fits with the heat fluxes observed in figure 6.2, but the dependence on the parallel conduction limiter $\alpha_{e,i}$ will require further studies.

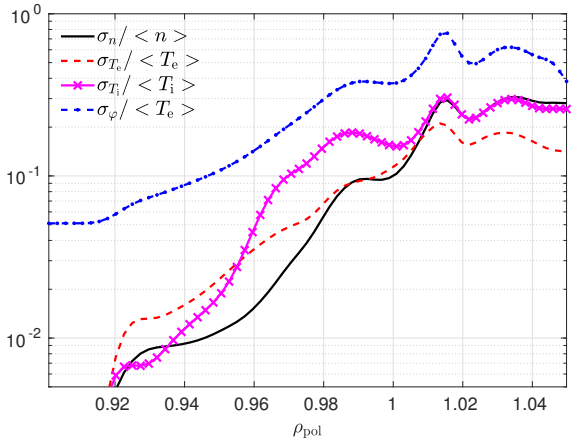

Figure 6.6: Outboard mid-plane fluctuation amplitudes. $\sigma_f^2 = \langle f^2 \rangle - \langle f \rangle^2$, the average is performed toroidally and in time over 200 μs.

participate in the turbulence drive.

6.5.5 Radial electric field

One of the key mechanisms regulating turbulent transport are sheared poloidal $E \times B$ flows. Previously, we have investigated theoretically which mechanisms contribute to the formation of a mean radial electric field [3]. With the recent implementation of a neutral gas model, satisfactory agreement in OMP density and temperature profiles with the experiment is obtained. Therefore, it is worthwhile to compare also the mean radial electric field in the experiment and in the simulation (again with and without neutral gas) – shown in figure 6.7. In the experiment, the edge $E_\mathrm{r} \propto \omega_\mathrm{D}$ was measured using Doppler reflectometry where the Doppler frequency shift ω_D is obtained from tracer density fluctuations under the assumption that the turbulence phase velocity (few hundred ms^{-1}) is small compared to the main $E_\mathrm{r} \times B$ velocity (few kms^{-1}): i.e. $v_{E\times B} \gg v_{ph}$ [190].

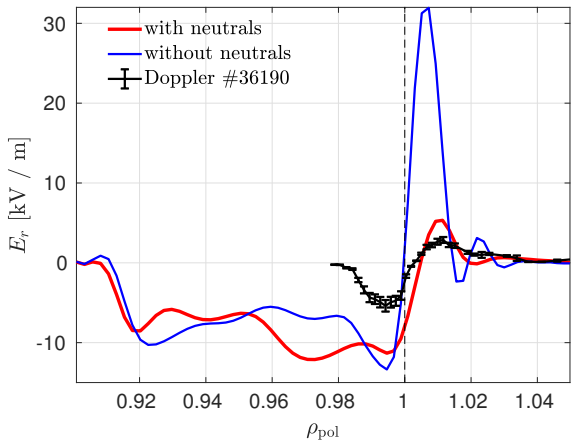

Figure 6.7: Outboard mid-plane radial electric field in simulations with and without neutrals, in comparison to Doppler reflectometry measurements at 2.235 to 2.635 s of the discharge.

Unlike for density and temperature profiles, the comparison of the electric field is not that satisfactory. In the SOL, the radial electric field is determined by sheath boundary conditions at the divertor, following $E_r|_{\mathrm{SOL}} \sim -3\partial_r T_\mathrm{e}|_{\mathrm{div}}$, and parallel current dynamics described by Ohm's law. With neutral gas, the temperature at the divertor is reduced and its gradient flattens. Additionally, the increased resistivity allows for the establishment of parallel gradients, including a parallel electric field [203]. As a result, a much more realistic mean radial electric field at the outboard mid-plane is obtained than without neutrals, but still a factor two larger than in the experiment. The remaining discrepancy is likely due to not yet

fully realistic boundary conditions at the divertor plates.

In the confined region, without neutrals, we have previously found the time averaged radial electric field to be determined by a combination of the ion pressure gradient, zonal flows and toroidal rotation [3]: $\langle E_r \rangle_t \approx \left\langle \frac{\partial_r p_i}{en} \right\rangle_t + \frac{m_i}{e} \langle \mathbf{u} \cdot \nabla \mathbf{u} \rangle_t \cdot \mathbf{e}_r + \langle u_\parallel B_\theta \rangle_t$. These terms did not change significantly with the neutrals, but the poloidally asymmetric density source from their ionization entering the ion continuity equation does sustain an additional mean poloidal rotation [94]. The mean radial electric field stabilizes the stationary plasma background, but leads to a poloidal $E \times B$ rotation of turbulent filaments in the anti-clockwise direction in the confined region, and in the clockwise direction in the SOL, with the flow shear peaking at the separatrix.

The discrepancy in the radial electric field between simulation and experiment suggests that a refinement of the fluid model is required. Previously, we have seen that fluid closure terms have a huge impact: the parallel ion viscosity by regulating poloidal rotation, and parallel ion and electron heat conductivities by regulating the zonal flow [3]. Future work will therefore be directed towards an ion viscosity consistent with neoclassical theory across all collisionality regimes [94, 138], and a more refined Landau fluid closure for the parallel heat flows [100].

6.6 Towards high-recycling and plasma detachment

One of the main challenges for fusion reactors is to maintain manageable heat loads on the divertor. In achieving this, it is unavoidable that a major part of the heat passing the separatrix has to be radiated away before reaching the targets, and the remainder shall be spread across the target area as evenly and widely as possible. As we see in figure 6.4, a fraction of the input power – 45 kW – is radiated away by deuterium even in attached conditions. Bolometry measurements suggest that additionally, 300 kW are radiated away by impurities (predominantly nitrogen), currently not contained in our simulation. However, the majority of the heat (roughly 500 kW) still reaches the targets.

The radiation capability of neutral gas is limited above a few eV plasma temperature, as particles are directly ionized away before emitting radiation. Nevertheless, ionization has a huge impact on the plasma: although total pressure is largely maintained, by raising the density while reducing the temperature the plasma collisionality is increased, as discussed in section 6.5.3. One of the consequences of increased collisionality is a reduced parallel heat conduction, which as we have seen in figure 6.3 leads to much more realistic (broader) OMP temperature profiles. Therefore, even in attached conditions, neutral gas recycling has a major role on the plasma state. Notably, as assumed in this work and confirmed in transport studies [245], main chamber recycling plays a negligible role compared to divertor recycling.

Is it possible to decrease the heat flux on the divertor targets further by increasing the divertor neutrals density N_{div}? Indeed, as we have shown in figure 6.5, for $N_{\text{div}} = 3 \times 10^{18}$ m^{-3} the target electron temperature can be decreased below 5 eV, with deuterium radiation increasing to 170 kW. However, figure 6.5 also shows that at the same time, plasma density is considerably increased. Not only does this not reduce the total target heat flux significantly, as even at low temperature we must also consider the energy released per ion recombining at the surface (13.6 eV). Increased density also has detrimental consequences for the main chamber wall. As we have seen in section 6.5.2, the ionization source is localised close to the separatrix, particularly at the HFS. At higher divertor neutrals density, not only the divertor plasma density increases, but the density increase spreads through the whole domain. The density profile at the outboard mid-plane is shown in figure 6.8. With increased neutrals recycling, the density gradient flattens in both the confined region and in the far SOL, while the density gradient in the near SOL remains similar. For the far SOL, this is known as density shoulder formation and is indeed found in detached plasmas [235, 236]. Increased far SOL density leads to higher fluxes to the main chamber wall, accelerating its erosion. Therefore, it is of interest to find exhaust solutions avoiding this.

An important constraint for turbulence simulations is that they are not unconditionally stable. In the near SOL, we observe large fluctuation amplitudes in both density and temperatures, characteristic of resistive-ballooning modes. With increasing separatrix density and collisionality, these modes can become strongly unstable, leading to a density limit [68, 247]. For this reason, our simulations with $N_{\text{div}} > 10^{18}$ m^{-3} were not able to reach a saturated state – unless the ionization rate coefficient is also decreased, as we found out incidentally. While the simulation with $N_{\text{div}} = 3 \times 10^{18}$ m^{-3} crashed after 1.5

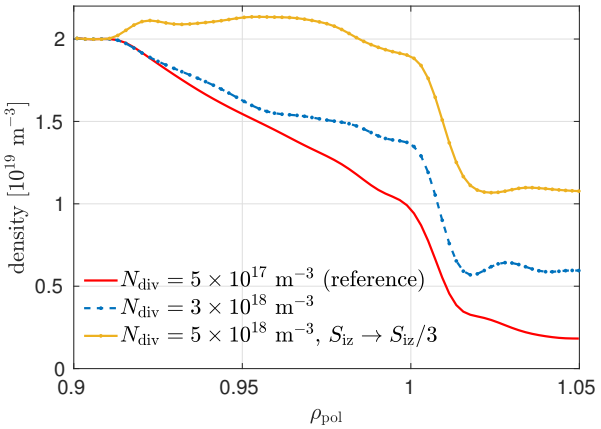

Figure 6.8: Outboard mid-plane plasma density as a function of divertor neutrals density. The reference simulation validated against AUG #36190 had $N_{\mathrm{div}} = 5 \times 10^{17}\ \mathrm{m}^{-3}$, the simulations with increased N_{div} only run stable if also the ionization rate is reduced.

ms, the simulation with $N_{\mathrm{div}} = 5 \times 10^{18}\ \mathrm{m}^{-3}$ and a three times lower ionization rate ran stable for more than 3 ms. The reason is not fully clear, as it is difficult to distinguish between physical and numerical stability in non-linear simulations. However, at lowered ionization rates the neutrals penetrate deeper into the plasma, moving the ionization front. At the HFS, it moves deeper into the confined region, flattening completely the density profile there (in fact, the core density source goes negative to hold the fixed density). In this regime, radial heat transport in the confined region becomes carried exclusively by the ions due to the ITG. At the LFS, the ionization front moves up and thereby more from the separatrix to the far SOL (but remains close to the divertor). Physically, a lowered ionization rate can be achieved by lowering the electron temperature in another way than by a density increase.

We conclude that further extensions are required for GRILLIX to be able to simulate detached conditions, most notably impurity radiation: to avoid an excessive increase of plasma density, leading to a density shoulder formation [235, 236] and the resistive-ballooning density limit [68, 247], the electron temperature must be lowered by other means. Additionally, we expect that parallel momentum losses due to ion-neutral friction/viscosity are required to allow plasma recombination to set in [145, 250], which would reduce the plasma density and hence total heat flux arriving at divertor targets.

6.7 Conclusions

The global Braginskii turbulence code GRILLIX was coupled to a diffusive neutral gas model, taking into account ionisation, recombination and charge exchange reactions. The neutrals become mainly ionised along the separatrix in the proximity of the X-point and strongly affect the plasma dynamics in various ways: The density profile in the confined region flattens while the temperature profile steepens, which alters the turbulence drive mechanism from ballooning modes to the ion temperature gradient mode. The ionization source distribution also leads to poloidal asymmetries. As the neutrals introduce a cooling mechanism via dilution and radiation, plasma collisionality increases in the edge and SOL, and parallel heat transport becomes less effective. In consequence, parallel temperature gradients arise in the SOL, while radial temperature profiles are broadened, yielding a realistic SOL fall-off length. The radial electric field in the SOL is significantly reduced due to a lowered electron temperature gradient at the divertor. At increasing divertor neutrals density, the plasma density rises over the whole domain, further flattening the density profile in the confined region and producing a density shoulder at the outboard mid-plane, but these simulations also tend to become resistive-ballooning unstable.

The simulations were validated against the attached L-mode ASDEX Upgrade discharge #36190. With the neutral gas model, a satisfactory match of outboard mid-plane density and electron temperature profiles is obtained. At the divertor targets, the profiles become much more realistic as well, but a discrepancy remains due to the use of a too simple neutrals boundary condition – a constant density across both divertor plates. The most significant discrepancy with the experiment currently seems to be in the radial electric field: its form matches very well – negative in the confined region, positive in the

SOL – but the amplitude is still a factor two too large.

For improving the agreement with the experiment, but most importantly for reliable and predictive reactor simulations, the primary goal is the elimination of the remaining free model parameters: the divertor neutrals density N_{div} and the free streaming limiters $\alpha_{\mathrm{e,i}}$ of the parallel heat conductivities. The former will be overcome in a straight forward way by implementing local recycling boundary conditions. For the latter, the implementation of a Landau-fluid closure could be a possible solution, as e.g. was done in the BOUT++ code [100]. Further important extensions might be neoclassical corrections to the ion viscosity [94, 138] as well as the consideration of ion orbit losses [227, 228], which can be expected to result in a more realistic radial electric field. However, since these are inherently kinetic effects, verification against gyrokinetic simulations will remain necessary [116]. Kinetic effects are important not just for the plasma, but also for the neutrals: they can be implemented by either a fully kinetic treatment [93, 108], or a hybrid fluid-kinetic model [251, 252]. Finally, for simulations in detached conditions, impurities and parallel momentum dissipation by the neutral gas [250] must be considered. Importantly, for reactor scale simulations, not only the physical model should be improved, but also the computational performance.

Overall, we conclude that a remarkable degree of agreement with the experiment can already be achieved, particularly in the outboard mid-plane profiles, and hence predictions for e.g. SOL fall-off lengths are becoming possible. In near future, the validation should be extended into regimes with improved confinement, such as the H- or I-mode – aiming to provide a better understanding of these regimes. But also, using the geometric flexibility of GRILLIX, advanced divertor [19] and negative triangularity [21] reactor concepts should be explored.

Acknowledgments

The authors thank Rainer Fischer for the integrated data analysis, and Dominik Brida for providing divertor target measurements. We also thank Marco Wischmeier for helpful discussions. This work has been carried out within the framework of the EUROfusion Consortium and has received funding from the Euratom research and training programme 2014–2018 and 2019–2020 under Grant Agreement No. 633053. The views and opinions expressed herein do not necessarily reflect those of the European Commission.

Chapter 7

Summary of contributions

This chapter summarises the published contributions of the author of this Phd thesis. Table 7.1 lists all peer-reviewed articles. The focus lies on the major publications [1], [3] and [4] that form the cumulative content of the dissertation. These articles are given in full length in chapters 3, 5 and 6, and in the journals style in appendix A. The major publications are summarized in sections 7.1.1, 7.1.2 and 7.1.3, respectively, indicating the contribution of the author of this dissertation. Note that a corrigendum [2] has been published to the paper [1] from chapter 3, which is referenced in the summary section 7.1.1 and given in full length in chapter 4. Further publications are discussed in section 7.2. Additionally, table 7.2 lists the author's conference contributions.

7.1 Major publications

The primary contributions to this cumulative dissertation constitute consecutive extensions of the GRILLIX code [106,107] towards predictive simulations of turbulent transport in the edge and SOL of tokamak fusion reactors. GRILLIX implements a unique numerical framework [160, 161] for efficient turbulence simulations in realistic diverted 3D tokamak geometry. The focus of this thesis lies on an increasingly realistic physical model that we ultimately were able to validate against the in-house experiment ASDEX Upgrade [254], which provides a large part of the physics base for ITER and DEMO. Among other things, it was anticipated and confirmed that ion temperature dynamics and the interaction with the neutral gas play an important role. Naturally, these state-of-the-art simulations provide unique insights into the physical mechanisms at play. But also, these simulations are always on the edge of computational feasibility, in particular as tokamaks become increasingly reactor relevant with size. Therefore, the contributions are accompanied by advanced numerical algorithms. While earlier contributions are more technical, the later ones move closer to the anticipated applications.

7.1.1 Thermal dynamics in the flux-coordinate independent turbulence code GRILLIX

Temperature plays a crucial role in tokamak experiments: varying from above 10 keV in the plasma core to essentially 0 keV at the walls, it is extremely inhomogeneous. Due to heat conduction, temperatures are also involved in qualitatively different (compared to density) and important dynamics [131]. Since thermonuclear ignition requires hot ions, not necessarily hot electrons, they are particularly important. The ion temperature gradient (ITG) mode [62,130] is one of the main drivers of turbulence, as it cannot be stabilized by drift waves. Further, the ions determine the background radial electric field (see also chapter 5 and Ref. [3]) and thus the turbulence suppression by $E \times B$ shearing in H-mode [40]. As discussed in sections 2.1.5 and 6.2, ions also determine the propagation of neutral gas by charge exchange reactions. Therefore, the first task in this PhD thesis was the extension of GRILLIX by ion temperature dynamics, including parallel heat conduction, whereas previously only electron temperature was considered [120].

The first contribution published during this thesis, in chapter 3, focused on this extension, and in particular on the solution of associated challenges. Special care in the numerical discretisation was required for the ion diamagnetic polarisation in the vorticity equation. Further, a 3D solver has been implemented for the solution of the stiff parallel ion and electron heat conductivities. This allowed

Table 7.1: Complete list of peer-reviewed articles in chronological order that were published during this PhD thesis. Three major publications that contribute to this cumulative dissertation are listed in black with references to the respective chapters. Other papers are marked in gray and are not included in this thesis.

Synthetic helium beam diagnostic and underlying atomic data. *Wladimir Zholobenko, Michael Rack, Detlev Reiter, Motoshi Goto, Yühe Feng, Bettina Küppers, and Petra Börner.* Published in: W. Zholobenko *et al.*, Nucl. Fusion **58**, 126006 (2018). [253]

Global turbulence simulations of the tokamak edge region with GRILLIX. *Andreas Stegmeir, Alexander Ross, Thomas Body, Manaure Francisquez, Wladimir Zholobenko, David Coster, Omar Maj, Peter Manz, Frank Jenko, Barrett N. Rogers, and Kab Seok Kang*. Published in: A. Stegmeir *et al.*, Phys. Plasmas **26**, 052517 (2019). [107].

On the nature of blob propagation and generation in the large plasma device: Global GRILLIX studies. *Alexander Ross, Andreas Stegmeir, Peter Manz, Daniel Groselj, Wladimir Zholobenko, David Coster and Frank Jenko.* Published in: A. Ross *et al.*, Phys. Plasmas **26**, 102308 (2019). [121].

Thermal dynamics in the flux-coordinate independent turbulence code GRILLIX. *Wladimir Zholobenko, Andreas Stegmeir, Thomas Body, Alexander Ross, Peter Manz, Omar Maj, David Coster, Frank Jenko, Manaure Francisquez, Ben Zhu, and Barrett N. Rogers.* Published in: W. Zholobenko *et al.*, Contributions to Plasma Physics **60**, e201900131 (2020). [1] (Chapter 3)

Corrigendum: Thermal dynamics in the flux-coordinate independent turbulence code GRILLIX. *Wladimir Zholobenko, Andreas Stegmeir, Thomas Body, Alexander Ross, Peter Manz, Omar Maj, David Coster, Frank Jenko, Manaure Francisquez, Ben Zhu, and Barrett N. Rogers.* Published in: W. Zholobenko *et al.*, Contributions to Plasma Physics **60**, e202000056 (2020). [2]

Treatment of advanced divertor configurations in the flux-coordinate independent turbulence code GRILLIX. *Thomas Body, Andreas Stegmeir, Wladimir Zholobenko, David Coster, and Frank Jenko.* Published in: T. Body *et al.*, Contributions to Plasma Physics **60**, e201900139 (2020). [118]

Electric field and turbulence in global Braginskii simulations across the ASDEX Upgrade edge and scrape-off layer. *Wladimir Zholobenko, Thomas Body, Peter Manz, Andreas Stegmeir, Ben Zhu, Michael Griener, Garrard Conway, David Coster, Frank Jenko, and the ASDEX Upgrade Team.* Published in: W. Zholobenko *et al.*, Plasma Phys. Control. Fusion **63**, 034001 (2021). [3] (Chapter 5)

The role of neutral gas in validated global edge turbulence simulations. *Wladimir Zholobenko, Andreas Stegmeir, Michael Griener, Garrard Conway, Thomas Body, David Coster, Frank Jenko, and the ASDEX Upgrade Team.* Published in: W. Zholobenko *et al.*, Nucl. Fusion, in press (2021). [4] (Chapter 6)

to use the Braginskii expressions in any parameter regime without time step limitations (previously, parallel electron heat conduction had to be reduced by more than an order of magnitude [107]). Besides the physical model for the interior plasma, also boundary conditions have been revisited: in particular sheath heat transmission boundary conditions for electrons and ions, and electrostatic potential boundary conditions both at the sheath and at the artificial core boundary.

These extensions have been guided by the pioneering work of the GDB group from the Dartmouth College in the USA [117]. They also motivated the test case chosen for simulations in this first contribution: an Alcator C-mod discharge in limited (circular) geometry. The relatively high density and low temperature, and correspondingly high collisionality, facilitate the application of a fluid model. Compar-

Table 7.2: List of conference contributions during this PhD thesis, in chronological order.

Development and evaluation of a synthetic helium beam diagnostic for Wendelstein 7-X. *Wladimir Zholobenko, Michael Rack, Detlev Reiter, Motoshi Goto, Bettina Küppers, Petra Börner.* DPG-Frühjahrstagung (DPG Spring Meeting) of the Atomic, Molecular, Plasma Physics and Quantum Optics Section (SAMOP), Erlangen, Germany, 4-9 March 2018 (talk).

Detachment with the 3D turbulent transport code GRILLIX. *Wladimir Zholobenko, Alexander Ross, Andreas Stegmeir, Thomas Body, David Coster, Omar Maj, Peter Manz, Frank Jenko.* DPG-Frühjahrstagung (DPG Spring Meeting) of the Matter and Cosmos Section (SMuK), Munich, Germany, 17-22 March 2019 (poster).

Thermal dynamics and neutrals in the SOL of diverted tokamaks with GRILLIX. *Wladimir Zholobenko, Andreas Stegmeir, Alexander Ross, Thomas Body, David Coster, Peter Manz, Frank Jenko.* 17th International Workshop on Plasma Edge Theory in Fusion Devices (PET2019), UCSD, La Jolla, California, USA, 19-21 August 2019 (talk).

Global electromagnetic simulations of turbulence and profile evolution across the tokamak edge and scrape-off layer. *Wladimir Zholobenko, Thomas Body, Andreas Stegmeir, Ben Zhu, David Coster, Peter Manz, Frank Jenko.* Joint Varenna-Lausanne international workshop on theory of fusion plasmas, Lausanne, Switzerland, 12-16 October 2020 (**invited talk**).

Global simulations of turbulence, transport and shear suppression across edge and SOL of diverted tokamaks. *Wladimir Zholobenko, Thomas Body, Peter Manz, Ben Zhu, Andreas Stegmeir, David Coster, Frank Jenko, ASDEX Upgrade Team.* 4th Asia Pacific Conference on Plasma Physics (AAPPS-DPP 2020), remote e-conference, 26-31 October 2020 (**invited talk**).

Simulations of turbulence, its suppression and profile evolution across the edge and scrape-off layer of the ASDEX Upgrade tokamak. *Wladimir Zholobenko, Thomas Body, Andreas Stegmeir, Michael Griener, Ben Zhu, Peter Manz, David Coster, Frank Jenko, Elisabeth Wolfrum, Manaure Francisquez, Barrett Roger, ASDEX Upgrade Team.* 28th IAEA Fusion Energy Conference (FEC 2020), remote e-conference, 10-15 May 2021 (**invited talk**).

ing to GDB, we were able to confirm that turbulence in this scenario is enhanced by increased collisionality, characteristic of resistive ballooning modes. Besides that, we could confirm that the background radial electric field in the confined region follows the ion pressure gradient, while it is anti-parallel to the electron temperature gradient in the SOL due to sheath boundary conditions, resulting in a sheared flow at the last closed flux surface.

A novel result was the investigation of the dynamics of the electric field: it was visible from movies of the simulations that besides small-scale turbulent fluctuations, there were also large scale oscillations. Temporal Fourier analysis of the flux-surface averaged electrostatic potential confirmed that in the confined region, the mean potential of the whole flux surface oscillates with a frequency spectrum in the acoustic range, characteristic of geodesic acoustic modes [255]. GAMs are driven by the compression of zonal flows, radially oscillating and stationary in time $E \times B$ flows sustained by the turbulence.

Further, it was emphasized that the electron and ion temperature profiles both in the confined region and in the SOL strongly depend on the parallel heat conduction, that could now be consistently incorporated thanks to the new solver. However, a mistake in the analysis was reported in a subsequent corrigendum contained in chapter 4: we have identified an error in the handling of input parameters due to which the parallel ion heat conductivity was equal to the electron conductivity in the original simulations, instead of 23 times smaller. The description of the numerical algorithm, physical model and

test case remain correct. Also most results remain true qualitatively. But some remarks had to be made regarding the heat conductivity.

The principal observation is that a larger parallel heat conduction reduces turbulent fluctuation amplitudes. This does not mean a reduction of the turbulent power flux though, as cross-phases can increase at the same time. Importantly, in a global code the background profiles can and do change significantly: a larger heat conductivity leads to smaller gradients in the confined region, suggesting a rather increased radial heat diffusivity. In the SOL, the sheath heat transmission plays an important role besides parallel heat conduction, cooling the electrons down. Both effects are likely even more effective in circular than in diverted geometry due to the immediate proximity of the confined region to the limiter.

As the first publication during this thesis, this work has relied on the guidance of the many co-authors. Nonetheless, the author of this dissertation carried out the vast majority of the research and writing up of the results, including problem definition, literature survey, code implementation, carrying out the simulations, their evaluation and the preparation of the manuscript. Andreas Stegmeir and Alexander Ross have implemented the diamagnetic polarization. Andreas Stegmeir has also supported the implementation of other terms, writing the article, and suggested the PIM library for solving the parallel diffusion problem. Thomas Body has helped with the implementation of parallel boundary conditions via penalisation. Peter Manz suggested how to analyse the GAMs. Omar Maj supported the solution of some intricate issues in the implementation of boundary conditions during the 3D solve, and critically reviewed the article. David Coster and Frank Jenko have guided the project, in particular with the problem definition, solution strategies and evaluation of results. Manaure Francisquez, Ben Zhu and Barrett Rogers advised with some special problems, and in particular the simulation setup and evaluation.

7.1.2 Electric field and turbulence in global Braginskii simulations across the ASDEX Upgrade edge and scrape-off layer

Motivated by the observations in the previous study as well as general interest, the second publication during this PhD thesis focused on the formation of a mean radial electric field and its interaction with turbulence. The general interest arises from the fact that sheared $E \times B$ flows are an important mechanism for the regulation and even suppression of turbulence [41, 67, 187, 192, 256]. Of particular interest is the turbulence suppression by $E \times B$ shear in the very edge of the confined region, the pedestal, in H-mode operation [40, 190, 257–259], which is facilitated in diverted geometry [111, 197, 198]. The mean radial electric field can be influenced by both mean background dynamics and turbulence [44, 186, 187], so their interaction is thought to be important.

A global turbulence code like GRILLIX is well suited to study the interaction between mean and turbulence driven flows. Further, owing to the newly implemented capability to treat numerically prescribed, arbitrary axisymmetric magnetic equilibria [118], simulations could be performed in the actual diverted equilibrium of ASDEX Upgrade. The goal was set to try to reproduce an actual AUG discharge. However, there are a few limiting factors that prevented us from exploring the whole AUG parameter space yet, as discussed in chapter 8. To establish the code and to study unsuppressed turbulence first, we decided to simulate the attached L-mode discharge #36190.

The literature on neoclassical transport [31, 44, 138] suggests that ion viscosity plays a major role in regulating the mean poloidal rotation, consisting of $E \times B$, diamagnetic and parallel rotation. This term becomes increasingly important with ion temperature and was still neglected in the previous contribution, but was implemented for this publication along with the collisional electron-ion heat exchange, completing the Braginskii equations.

One major achievement of this publication is the careful investigation of all the processes that determine the mean radial electric field. The dominant contribution on closed flux surfaces stems from the radial ion pressure gradient, which enters because the diamagnetic drift in a toroidal magnetic field leads to vertical motion. The charge imbalance caused by the opposite drift directions of electrons and ions is compensated by the Pfirsch-Schlüter current, mainly carried by the electrons. But the bulk plasma motion is determined by the drift of the heavier ions. Therefore, for a static plasma, the ion pressure gradient has to be balanced by a radial electric field such that the compression of the diamagnetic and $E \times B$ drifts balances. In principle, the electric field could also be smaller or larger than the ion pressure gradient: if the plasma is up-down symmetric, any poloidal rotation would even out the diamagnetic drift

over the flux surface. However, this is inhibited as the parallel Braginskii ion viscosity damps any net poloidal rotation. Toroidal momentum can enter from the SOL and saturate non-linearly at a finite value though. As it is mainly carried by the parallel velocity, it leads simultaneously to poloidal motion which is regulated by ion viscosity. Therefore, parallel velocity enters the balance for the radial electric field.

Additionally, at a sufficiently high grid resolution, we also find a contribution from zonal flows: stationary counter-propagating layers of $E_r \times B$ rotation with a mesoscale radial wavelength. These flows are sustained by sheared turbulent fluctuations, most efficiently by drift waves on small (sound Larmor radius) scales. They enter the radial force balance through the ion inertia, such that in total we obtain in a time average $\langle E_r \rangle_t = \langle \partial_r p_\mathrm{i} / en \rangle_t + \langle u_\parallel B_\theta \rangle_t + \frac{m_\mathrm{i}}{e} \langle \mathbf{u} \cdot \nabla \mathbf{u} \rangle_t \cdot \mathbf{e}_r$, with the poloidal magnetic field B_θ. Importantly, the inertia term not only modifies the electric field, but also the ion pressure gradient and the parallel velocity profiles. The zonal flows lead to an up-down pressure asymmetry, additionally to the inboard-outboard asymmetry due to ballooned turbulent transport. The flow was identified as stationary because it persists over multi-ms averages, but also the GAM sideband was observed in the 10 kHz range.

In the SOL, the electric field is determined by Ohm's law and sheath boundary conditions, leading to an $E \times B$ rotation opposite to the confined region. Therefore, the shearing rate peaks at the separatrix, surpassing the vortex-turn-over rate and leading to enhanced turbulence dissipation, but also enhancing the zonal flow drive. At the top of the device, vortex breaking is observed at the separatrix, feeding large intermittent filaments into the SOL.

We also point out the impact of fluid closure terms. In a rough comparison to AUG experiments, the results seemed reasonable – but as we show in the next contribution, a more detailed validation revealed that corrections to the fluid closure and the interaction with neutral gas can not be neglected.

The vast majority of the work has been carried out by the author of this dissertation, including problem definition, literature survey, code implementation, carrying out the simulations, their evaluation and the preparation of the manuscript. Yet we also want to acknowledge the contribution from the co-authors. Thomas Body has set up the AUG equilibrium, allowing simulations in that geometry. Peter Manz and Ben Zhu have motivated the study of the radial electric field and supported it significantly with valuable discussions. Michael Griener and Garrard Conway (and the ASDEX team) provided experimental data and guidance. Andreas Stegmeir, David Coster and Frank Jenko guided the project, discussed critical issues and advised on the manuscript preparation.

7.1.3 The role of neutral gas in validated global edge turbulence simulations

The final publication during this dissertation extends previous AUG simulations by the interaction with neutral gas. These simulations are validated quantitatively against measurements in the attached L-mode AUG discharge #36190, pointing out in particular the role of the neutral gas.

Due to the large fluctuation amplitudes in the plasma edge and scrape-off layer [87–92], turbulence cannot be separated from the evolution of the background. Background gradients therefore cannot be fixed, but must evolve (and fluctuate) self-consistently with the turbulence. The plasma transport is then determined by the turbulence, driven locally by instantaneous gradients, and globally by fluxes due to sources and sinks.

The major role of the neutrals is to provide a particle source and a heat sink for the plasma due to electron impact ionization. The particle source provides 99% of the plasma fuelling and has a non-trivial distribution peaking in the near-SOL, close to the target plates at the LFS, and close to the confined region at the HFS. Unlike in the previous simulations without neutrals, where plasma density was injected at the core boundary of the simulation at $\rho_\mathrm{pol} = 0.9$, a much more realistic flatter density gradient results in the confined region. At the outboard mid-plane, the density profile matches well the experimental measurements, including the SOL fall-off length. Poloidally, significant asymmetry is observed due to the density source asymmetry, caused by ballooned turbulent transport. The density asymmetry between the divertor plates is even larger in the experiment though, because a constant neutrals density was assumed across both divertor plates in the simulations.

In attached conditions of the investigated discharge, the overall heat sink is still small compared to the target heat flux. However, as density increases and electron temperature is dissipated by neutrals ionization in the divertor, the collisionality increases. This in turn reduces the parallel heat conduction, allowing parallel temperature gradients between the outboard mid-plane and divertor targets. As the par-

allel heat outflow reduces compared to the perpendicular turbulent flux, the temperature profile broadens radially, matching much better the experiment than without neutrals. We stress that in the (near) SOL, the Braginskii expressions for parallel heat conduction are reasonable, such that parallel heat flux limiters do not impact this result. They are rather important in the less collisional confined region.

The primary effect of the neutrals on turbulence in these simulations seems to be due to the modification of the sources and sinks distribution, and therefore different background gradients. As the density gradient flattens compared to the ion temperature gradient in the confined region, the turbulence drive changes from (resistive or kinetic) ballooning modes to ITG modes. This leads to larger ion temperature fluctuations and larger ion than electron heat transport. Further, the colder divertor strongly reduces the radial electric field in the SOL. The reduced $E \times B$ shear at the separatrix consequently has a lower impact on turbulence propagation and saturation.

Lastly, the transition to high-recycling conditions is explored by significantly increasing the divertor neutrals density. It is found that indeed, a far-SOL density shoulder is formed and the divertor temperature decreases. However, the increased density from ionization also drives the plasma unstable and still leads to a significant target heat flux. Therefore, it is concluded that for simulations of detached conditions, the effects of radiative cooling by impurities and momentum dissipation by the neutral gas still have to be incorporated.

The vast majority of the work has been carried out by the author of this dissertation, including problem definition, literature survey, code implementation, carrying out the simulations, their evaluation and the preparation of the manuscript. But it would not be possible without valuable contributions from the co-authors. Andreas Stegmeir has supported the code implementation and preparation of the manuscript. Michael Griener and Garrard Conway (and the ASDEX Upgrade team) provided experimental data and guidance. Thomas Body supported the evaluation of the simulations. David Coster supported the literature survey on the fluid neutrals model, its implementation and interpretation of the results. Frank Jenko guided the whole project.

7.2 Further publications

Other publications listed in table 7.1 are less crucial for this dissertation, but still noteworthy. W. Zholobenko *et al.*, Nucl. Fusion **58**, 126006 (2018) [253] is a paper based on the authors master thesis [143]. It investigates computationally the helium beam diagnostic [260], an important measurement technique for electron density and temperature in the plasma edge and SOL including their turbulent fluctuations [261, 262]. Among others, this diagnostic is part of the key experimental measurements against which our simulations in chapter 6 have been validated.

A. Stegmeir *et al.*, Phys. Plasmas **26**, 052517 (2019) [107] and A. Ross *et al.*, Phys. Plasmas **26**, 102308 (2019) [121] are the first applications of GRILLIX to experiments: the small COMPASS tokamak [263] and the linear LAPD device [264]. The author of this dissertation has contributed by reviewing the physical model, improving the boundary conditions and producing some simulations. The former publication set the basis for all consequent tokamak simulations. The major contribution of the latter is the discovery of the production mechanism of filaments in the linear device by analysing simulations with the wavelet technique – as the source of filaments in the tokamak SOL is still unknown, it is worthwhile to adapt this technique in near future also to out recent tokamak simulations.

T. Body *et al.*, Contributions to Plasma Physics **60**, e201900139 (2020) [118] extends and generalises the capability of GRILLIX to perform simulations in arbitrary (diverted) axisymmetric magnetic equilibria, primarily by allowing the prescription of the field by a discrete (numerical) representation and improving the treatment of boundary conditions via penalisation. Here, the author of this disseration (W. Zholobenko) has contributed by co-developing the code and the concepts, particularly the treatment of boundaries, and applying the new capabilities to relevant test cases, thereby verifying the implementation.

Part III

Discussion and Conclusions

Chapter 8

Discussion across dissertation topics

Being a cumulative dissertation, the results of this thesis primarily consist of independent publications. Each publication draws its conclusions. This chapter serves to tie them together by discussing the results across the topics. First, section 8.1 explains the motivation behind the specific setup selection for the simulations. Additionally to the published conclusions, section 8.2 discusses some selected physics results on the combined basis of all the contributions. Some plans for future model extensions are discussed in section 8.3, while section 8.4 stresses the need for the continuous optimisation of computational performance.

Our goal is predictive modelling of turbulent transport in future magnetic fusion devices as well as interpretative simulations of present machines, tokamaks in particular. Thereby, the plasma edge and SOL are of extraordinary interest. Among the key optimisation routes for magnetic confinement devices is the magnetic geometry [11,19,21,47], in particular of the divertor separating the main chamber plasma from the region of plasma-wall interaction. To allow flexible and efficient turbulence simulations in diverted geometry, GRILLIX is built on a novel numerical method, the flux-coordinate independent field-aligned approach [160, 161], which allows flexible and efficient turbulence simulations in arbitrary magnetic geometry [118].

The physical model also has to be chosen carefully. It is always a compromise between physical completeness and computational efficiency. In GRILLIX, a bottom up approach is taken: for the plasma, we started [119] from a Hasegawa-Wakatani model [59, 60], then built the cold ions Braginskii model [120] and finally, during this thesis, completed the Braginskii model with hot ions dynamics. The extensions of the physical model are supplemented by numerical advances, such as the implementation of a 3D solver for treating the Braginskii heat conductivities and ion viscosity (section 2.2.3), as well as computational optimisation. All this allowed first simulations of actual tokamaks at relevant parameters: C-mod in chapter 3, and ASDEX Upgrade (AUG) in chapter 5. First steps beyond the Braginskii model have been taken as well (chapter 6.3), and more will follow: likely in the direction of gyro-fluid models, investigating the effects of gyro-averaging, Landau damping and trapped particles (see section 8.3.1). Simultaneously, a top down approach is taken as well with GENE-X implementing a gyro-kinetic model with the FCI method [116].

Besides developing the plasma model, for plasma edge simulations – particularly global ones that include background evolution – it is crucial to respect the interaction of the plasma with the wall, neutral gas and impurities. To this end, the Debye sheath model has been revisited during this thesis (see chapter 2.1.6): as of now, a rather simple but robust set of boundary conditions is implemented (chapter 2.2.2), and investigations into improvements are ongoing [155]. Further, a first and yet rather simple fluid neutral gas model has been implemented and used in chapter 6, demonstrating clearly how essential it is for realistic global turbulence and transport simulations in the plasma edge. An impurity model is yet missing though, therefore simulations are preferably compared to pure deuterium discharges with a minimal impurity content. Realistic neutral gas and impurity models will become increasingly important in future work, because their control provides another crucial optimisation opportunity for magnetic fusion devices.

8.1 Selection of the simulation setup

The code development towards predictive capability is and must be supplemented by verification and validation. While verification merely confirms the correct solution of the model equations (see section 2.2.5), validation is required to assess the suitability of the model for the description of the experimental reality. This thesis documents the path towards validatable simulations, and this section discusses our choices of the simulation setups.

The path began with circular Alcator C-mod simulations in chapter 3. The goal was to reproduce some known and already quite challenging simulations from the GDB code from the Dartmouth College in the USA [117], improving and verifying some features of the GRILLIX code. Although this is neither a rigorous verification nor a validation scenario, some important insights could be gained and greatly helped to set the stage for diverted AUG simulations.

The natural choice for validation are simulations of the renowned and nearby ASDEX Upgrade (AUG) tokamak [254]. It provides a good diagnostics coverage and is highly relevant for ITER and DEMO. These simulations are computationally already quite challenging, as AUG is not a small but rather medium sized device. Nonetheless, first simulations have been successfully performed and show promising results, and more are to come.

A useful guide for the selection of a simulation scenario was the recent classification of AUG discharges in terms of the separatrix parameters, electron density and temperature, as shown in figure 8.1. This overview provides a clear separation between L- and H-mode discharges, as well as stationary discharges and those that ended with a disruption due to a density limit. In Ref. [247], this is explained by different drivers of instabilities – e.g. resistive-ballooning, ideal ballooning and ITG modes – and their stabilization or destabilization by electromagnetic effects, drift-waves, mean and zonal flows. In near future, it is of high interest to study how GRILLIX behaves in this parameter space. However, to begin with, we wanted to validate the code against one single discharge. We have selected the L-mode discharge #36190, with $n_{\text{sep}} \approx 10^{19}$ m^{-3} and $T_{\text{e,sep}} \approx 50 - 80$ eV, for a number of reasons: primarily, a relatively good coverage by diagnostics and low impurity content. Further, the plasma was attached so that one could expect a limited impact of the details of plasma-neutrals-wall interaction. The discharge is far enough from a density limit. The H-mode pedestal is an important but also controversially disputed topic [42], which we wanted to avoid in the very first simulations, including phenomena like microtearing turbulence [43] and edge localised modes [265, 266]. Also, H-modes are found at low collisionality and high beta. The former complicates the usage of fluid models, while the latter requires the consideration of magnetic flutter which was not yet explored in GRILLIX.

From the theory side, perhaps an even more interesting classification is in terms of dimensionless physics parameters. In particular, in Ref. [267] the discharges were grouped in terms of the collisionality and an MHD parameters at the separatrix, as shown in figure 8.2. The MHD parameter is defined as

$$\alpha_{\text{MHD}} = R q_{\text{cyl}}^2 \beta / \lambda_{\text{p}}, \tag{8.1}$$

with the machine major radius R, the local safety factor q_{cyl} at the OMP separatrix, the pressure gradient scale length λ_{p} and – most importantly – the plasma beta β, the ratio between plasma pressure and magnetic pressure. The collisionality is defined as

$$\nu_{\text{e}}^* = \frac{\pi q_{\text{cyl}} R}{1.03 \times 10^{16}} \frac{n_{\text{e}}}{T_{\text{e}}^2} Z_{\text{eff}}. \tag{8.2}$$

Again, we notice the separation of discharges between L- and H-modes, as well as the density limit. The discharge #36190 lies in the lower left of the diagram: this has the advantage that the risk of a density limit is minimized, but to the price of a relatively low collisionality, challenging for the fluid model. A more fluid friendly validation scenario has been developed at the TCV tokamak [155], in which GRILLIX has recently participated. However, as improved confinement regimes are the reactor relevant ones and are generally found at low edge collisionality, fluid model improvements have to be made either way. As the pressure gradient scale length is not a control parameter, the α_{MHD} dependence is basically a β dependence. The low beta justifies the neglect of electromagnetic flutter transport in present simulations, which as discussed in section 2.1.4 is either irrelevant or causes problems with the fluid closure terms.

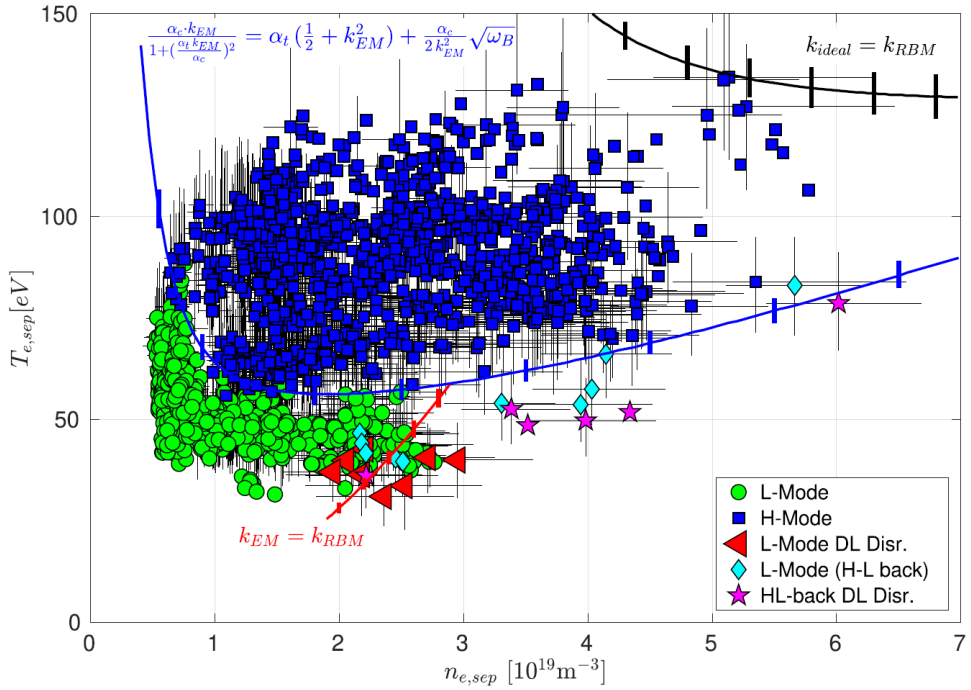

Figure 8.1: Separatrix operational space of ASDEX Upgrade in terms of electron density and temperature [247], indicating boundaries between L- and H-modes, and density limits (see text and the original publication).

The path towards reactor relevant H-mode simulations thus becomes clear: at higher plasma beta, the fluid closure terms must be corrected (see section 8.3.1) and magnetic flutter should be included. But also, further parameter dependencies hidden in this diagram shall be explored, such as the magnetic geometry shaping and plasma composition. Furthermore, the dependence on the machine size (compared to the gyro-radius) should be explored by simulations of other tokamaks at otherwise similar parameters.

8.2 Physics results

The principal result of this thesis is the further development of the GRILLIX code towards reactor relevant applications. For the first time, global simulations of turbulent transport across the edge and SOL of the ASDEX Upgrade tokamak could be validated quantitatively in chapter 6, showing among other things good agreement in outboard mid-plane density and temperature profiles. Although still further development is required, as discussed in section 8.3.1, these simulations build confidence that predictive turbulence simulations of the tokamak edge are feasible, for example for the SOL width. At the same time, the analysis of these cutting edge simulations provides intriguing physical insights into the processes in the plasma edge. The results from individual publications have been summarised in chapter 7. This section discusses some additional key physics insights across the topics of this thesis.

8.2.1 Difference between limited and diverted simulations

In a divertor, a set of coils carrying an additional toroidal current to the plasma current creates a magnetic separatrix, as shown in figure 1.2. This creates space between the confined plasma and the region of plasma-wall interaction by magnetically separating the main plasma from the divertor region. In a limiter configuration, the magnetic geometry is simpler, consisting only of a set of nested flux surfaces. The confined plasma impinges directly onto the wall, typically at a predetermined location, the limiter. Therefore, the confined and open flux surfaces are more strongly coupled.

Due to the geometrical complexity of a diverted tokamak, many turbulence studies of the plasma edge and SOL to date have been performed in a limiter configuration [101, 103, 105, 149, 265]. Indeed, many qualitative effects are similar in either configuration, for example there is a scrape-off layer in which the plasma flows out to the wall and is influenced by the Debye sheath. However, there are also

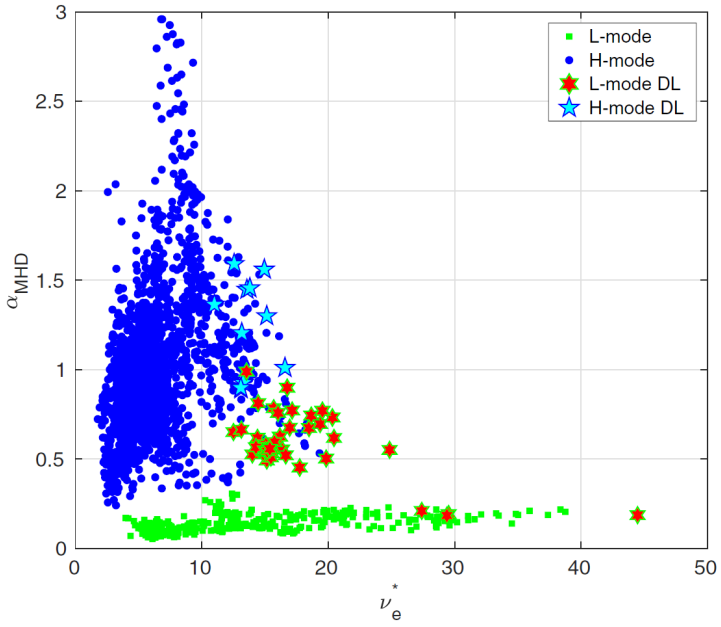

Figure 8.2: Separatrix operational space of ASDEX Upgrade in terms of collisionality and the MHD parameter α_{MHD} [267], indicating boundaries between L- and H-modes, and density limits (DL, see text and the original publication).

major differences, such as the much more severe shearing of structures [106, 107, 268] due to the divertor. Magnetic shear generally leads to turbulence suppression, and so performing simulations at parameters from chapter 5 but in circular geometry like in chapter 3 (instead of diverted AUG geometry) leads to a factor 20 larger radial power flux, far from the AUG experiment. With the safety factor becoming infinite at the separatrix, the divertor provides a much more abrupt radial transition (in ρ_{pol}) between confined and open flux surfaces, which we see when comparing our limited and diverted simulations. This abrupt transition and the resulting flow shear, together with magnetic shear, is thought among other things to facilitate the formation of a transport barrier in H-mode operation [197, 198, 256, 269]. At the same time, the divertor offers a significantly improved removal of particles and heat due to much better control of the neutral gas and impurities [11, 47]. In our simulations in chapter 6, we find for instance that the interaction between the confined plasma and neutral gas is localised around the X-point, a region of strong flux expansion. Due to the separation by the X-point, significant neutral gas density can be accumulated in the cold private flux region, facilitating its pumping without a major distortion of the confined plasma. Therefore, experimentally the advantage of diverted geometry is undisputed, and many groups besides GRILLIX have moved their simulations in this direction [99, 102].

Thus far, we have only began exploring the effects of diverted geometry on turbulence [107]. A significant milestone thereby is the validation of simulations in diverted geometry against the ASDEX Upgrade experiment in chapter 6, building confidence in the approach taken by GRILLIX. In future, this exploration shall be intensified. But also, more complex geometries shall be explored, such as advanced divertor concepts [18, 19, 26, 118].

8.2.2 The radial electric field

The radial electric field in a tokamak, leading to poloidal rotation of turbulent filaments by the $E \times B$ velocity, is of significant interest [41, 187]. In particular, a radial variation of E_r is thought to suppress turbulence by $E_r \times B$ shear [192, 256]. At the same time, turbulence influences the mean radial electric field through zonal flow formation [66, 67]. As mean field effects like viscous forces also influence E_r [44], a global code like GRILLIX is well suited to study this interaction. This was primarily the focus of chapter 5, as summarised in section 7.1.2, but it was also discussed in chapters 3 and 6.

The electric field enters through the Lorentz force in the momentum equation (2.2). The ion radial force balance, governing the mean E_r on closed flux surfaces, is its radial projection. The radial friction and viscous forces can be ignored. Since we are interested in mean fields, we average the equation in

time, dropping the ∂_t term. For ions, the result is

$$E_r = \frac{\partial_r p_\mathrm{i}}{en} + v_\phi B_\theta - v_\theta B_\phi + \frac{m_\mathrm{i}}{e} \langle \mathbf{v}_\mathrm{i} \cdot \nabla v_r \rangle_t \,. \tag{8.3}$$

The time average $\langle . \rangle_t$ is written explicitly only for the inertia term, because here it is important to note that it involves the whole quantity: even if there is no mean radial velocity, fluctuations can sustain a finite Reynolds stress, which is exactly what sustains the zonal flows.

In our simulations, we find indeed significant zonal flows if the grid resolution is sufficient to resolve the sound Larmor radius scale. In a flux surface average, the Reynolds stress oscillates around zero with a meso-scale radial wavelength $\lambda_\mathrm{ZF} \sim \sqrt{a\rho_s}$ [67], between the sound Larmor radius and the machine minor radius. Importantly, entering eq. (8.3) it sustains not only an additional oscillating (radially, not in time) radial electric field. Rather, all quantities in the radial force balance can be modified to different degrees, leading to staircase structures [215]. Besides the electric field, this is most visible in the radial (stationary) density profile, and also parallel velocity (toroidal rotation). In the ion temperature, the effect was less pronounced in chapter 5, but became stronger with a free-streaming parallel heat flux limiter in chapter 6. Also poloidal rotation can be modified beyond neoclassical estimates by the Reynolds stress [138, chapter 13.1], but in chapter 5 we found that the damping by the parallel Braginskii ion viscosity is too strong, as also discussed in section 8.3.1. We note that the radial modulation of background profiles also leads to a radial modulation of transport.

These staircase structures provide a way to experimentally observe the zonal flows [215]. Another important feature of zonal flows in a toroidal magnetic field is that they necessarily lead to an up-down pressure asymmetry [218]. This also leads to geodesic acoustic mode oscillations [255], as we have analysed in chapters 3 and 5.

Chapter 5 mostly focused on the interplay between mean and zonal flows, turbulence and mean profiles. Chapter 6 additionally introduced the effects of neutral gas. There is a number of ways how the neutral gas influences the radial electric field: firstly and most obviously, by modifying the background pressure profile. Secondly, by cooling the divertor, the sheath sustained radial electric field in the SOL is significantly reduced. However, the particle source from neutrals ionization also directly enters the particle conservation equation (5.8): therefore, in a stationary state the source must be balanced by a non-divergence-free flow. In practise, we have found that the ionization source on closed flux surfaces sustains a mean $E \times B$ poloidal rotation and a radial pinch that balance the poloidally asymmetric density source. In chapter 6, we have not focused on this effect because it was not yet substantial – but it may play an increasing role in detached regimes. Similarly, the direct vorticity damping by momentum exchange with the neutral gas was implemented, but did not play a significant role yet – however, tests suggest that with increasing neutrals density, this may be an effective mechanism for zonal flow suppression [244].

8.2.3 The turbulence drive

There is a number of possible turbulence driving instabilities. In chapter 3, we have performed limited C-mod simulations at rather high collisionality. The turbulence drive in the plasma edge was therefore clearly the resistive ballooning mode (RBM) [117]. However, this regime is far from the typical ones in ASDEX Upgrade. In chapter 5, the collisionality was much lower. Therefore, in the confined region the instability is rather driven by drift waves and/or kinetic ballooning modes [270]. A more detailed distinction could be made by implementing further diagnostics, e.g. for phase shifts between fluctuating quantities. In the SOL, both the η_i-mode [62,130] due to the steep ion temperature gradient (ITG) and the Kelvin-Helmholtz instability [212, table I] due to the large $E \times B$ shear are possible. Finally, in chapter 6 the plasma density source shifts from the core boundary to the separatrix due to the ionization of neutral gas. This results in a much flatter density gradient in the confined region, and turbulence being clearly driven by the ITG mode. In the SOL, on the other hand, neutrals lead to increased collisionality, such that resistive ballooning modes become relevant again [247].

8.2.4 The role of neutral gas

The primary effect of neutral gas is to provide the main plasma density source through its ionization, whereby electrons are cooled down. This is particularly important in a global code which evolves not

only turbulent fluxes but also the background profiles. Only with the neutral gas source, realistic density and temperature profiles could be obtained in chapter 6. The source was implemented self-consistently with a diffusive fluid neutrals model. Naturally, this influences the radial electric field and turbulence drive, as discussed above. Previous publications with a simple core boundary density source are therefore, in comparison, more academic and less realistic.

The effect of turbulent fluctuations on the plasma-neutrals interaction was so far found to be small [105]. For the mean field, in principle the density source and temperature sink for the neutral gas can be mimicked by prescribed constant source terms [155, 271], but as we show in section 6.5.2 their poloidal profiles in diverted geometry tend to be highly non-trivial, impossible to guess. Their choice can be guided by a coupling to mean-field transport codes [26, 27], but for a consistent and predictive solution this has to be iterated with the computation of transport coefficients by the turbulence code [246, 272], which is not obviously beneficial compared to a direct implementation of a neutral gas model in the global turbulence code. Nonetheless, pre-computing the sources from neutrals and impurities might simplify interpretative simulations. Further, the direct impact of turbulent fluctuations on the plasma-neutrals interaction can be expected to be more significant towards the reactor relevant detached divertor conditions [105], and vice versa the direct impact of neutrals on the turbulence (e.g. via flow damping) is expected to increase [243, 244]. Therefore, ultimately, a directly built-in neutral gas model will be preferable – perhaps a hybrid fluid-kinetic solution [251, 252].

Currently, the largest limitation of our neutrals model is the lack of self-consistent local recycling boundary conditions [145]. While this has to be improved in the near future, the constant divertor neutrals density boundary condition can be expected to perform better in the TCV than in the AUG tokamak, as the open geometry promotes neutral gas spreading around the plasma.

8.2.5 Parallel heat conduction and ion viscosity

A major technical achievement of this thesis is the efficient implementation of a solver for large parallel diffusion terms. Correspondingly, this allowed to study their physical effects.

The terms arise as dissipative corrections to the ideal fluid equations due to deviations of the underlying particle velocity distribution from a Maxwellian, which increases with lower collisionality. The heat conduction results from a larger fraction of fast particles in the distribution function, reacting faster than the bulk plasma to temperature gradients. The viscosity results from the deviation of the distribution function from spherical symmetry [56], an anisotropy between the pressure parallel and perpendicular to the magnetic field [138].

The implementation was described in chapters 2 and 3. In the latter, the effect of parallel electron and ion heat conductivities was studied, among other things. As a parallel diffusion term, the heat conduction transports heat along parallel temperature gradients. In the SOL, the heat enters from the confined region at the outboard mid-plane and flows towards the wall. If the heat flux across the LCFS is fixed, the parallel heat conduction determines the parallel temperature gradients in the SOL that support the outflow, and then the parallel outflow speed. The SOL width, the radial decay length of the temperature profile, is then determined by the competition between parallel conductive outflow and perpendicular turbulent transport.

The situation is complicated by the fact that the turbulent transport across the magnetic field also depends on the parallel heat conduction (although less strongly than the parallel heat flux in the SOL). The key finding is that temperature fluctuations are dissipated by an increasing parallel heat conductivity, resulting in lower average fluctuation amplitudes. However, the heat conductivity also leads to a larger phase shift between the temperature and the electrostatic potential, particularly for electrons as it competes with the adiabatic current response [131]. Therefore, the parallel heat conductivity can both reduce or increase turbulent heat transport, depending on the regime. In the RBM dominated regime in chapter 3, the perpendicular transport was rather slightly increased by parallel heat conduction, flattening the radial temperature profile in the confined region. In chapters 5 and 6, on the other hand, the parallel heat conduction suppressed the perpendicular turbulent heat flux – most significantly in the ITG dominated regime in chapter 6.

The ion viscosity was first used in chapter 5. It is comparable in magnitude to the ion heat conductivity and shares some similar features, but being a tensor it is also somewhat more complex. For the parallel

ion velocity, it also constitutes a diffusion term, damping parallel velocity fluctuations (sound waves). Unlike the heat conduction for thermal energy, parallel viscosity dissipates kinetic energy though, and even a constant parallel flow is damped by magnetic pumping. The reduced turbulent transport of parallel momentum may explain the reduced toroidal spin-up in the reference simulation, compared to chapter 5.5.1. Viscosity also contributes to the damping of zonal flows [208]. But most important is its damping of the mean poloidal rotation, familiar from neoclassical theory [31, 138]: as also perpendicular drifts enter the tensor expression, and being the dominant term in the flux surface average of the parallel momentum equation, the parallel velocity is forced to balance the drifts such that the mean poloidal rotation is damped, as we have shown in chapter 5.4.1. As discussed in section 8.2.2, this is important for the mean radial electric field and the resulting rotation of turbulent filaments.

It is important to remark that towards the experimentally relevant regimes in chapters 5 and 6, the Braginskii expressions for the electron and ion parallel heat conductivities had to be limited – otherwise they diverge at the low collisionality deeper in the confined plasma, suppressing the turbulent transport of heat too much. The ion viscosity has not been limited yet, but it is likely subject to similar issues. This is further discussed in section 8.3.1.

8.3 Possible model extensions

The contributions published during this dissertation document novel findings from state-of-the-art computer simulations. But as we aim to simulate tokamak reactors as realistically as possible, among the most important results are insights into the still required future developments. This section discusses some plasma model extensions that we believe to be important. The neutrals have been sufficiently discussed in chapter 6.

8.3.1 Beyond Braginskii

The drift-reduced Braginskii model is built on various approximations. Some are robust, others are not. The most obvious point at which the Braginskii model breaks down is the divergence of some fluid closure terms at high temperature (low collisionality): the parallel electron and ion heat conductivities and ion viscosity, as discussed in chapter 5. The basic role of collisionality in tokamaks is to inhibit the fast parallel transport [138], faster than bulk motion, which is described by diffusion terms in our fluid model. The induced perpendicular transport is mostly negligible compared to turbulent drift motion. However, contrary to what the Braginskii expressions suggest, other mechanisms exist that limit parallel flows even at vanishing collisionality.

The parallel heat flux is the highest fluid moment at which typically the closure is applied, and is the first to break down. As heat is mostly carried by the fast tail of the particles velocity distribution, the parallel heat flux is most sensitive to the distortion of the distribution function from a Maxwellian, which occurs without collisional inhibition of the parallel flow. However, a kinetic collisionless wave-particle resonance also limits this distortion – Landau damping [273]. The most simple approach to incorporate this effect into fluid models is to limit the parallel heat flux by a fraction of the free-streaming flux [205, 234], as we have done in chapter 6. However, this introduces free parameters, limiting the codes predictive capability. An extensive amount of literature exists on the more proper incorporation of Landau damping into fluid models [80, 81, 85, 274, 275]. In particular, recently a fast non-Fourier method was developed [276] that seems to work well also at higher collisionality [132] and in complex geometry [100], and shall be explored in GRILLIX in near future. In chapter 6 we have found that this is especially important in regimes where turbulence is driven by the temperature gradients (like ITG).

Unlike the parallel heat flux, the ion viscosity can not be well understood by one-dimensional models as it is due to the anisotropy of the distribution function [56]. In tokamaks, at sufficiently low collisionality, a particular anisotropy is of high interest: particles with large enough perpendicular to parallel velocity ratios are trapped in the magnetic mirror of the toroidal magnetic field, on so called banana orbits. These particles can not rotate poloidally, and they also slow down the passing particles via collisional friction, limiting the parallel ion viscosity. This process has been intensively studied by neoclassical theory [31, 138]. Improved formulae for the ion viscosity have been derived [139], valid approximatively

at arbitrary collisionality, and successfully incorporated in different fluid models [94, 226]. As discussed in section 2.1.4, reducing the ion viscosity at low collisionality is particularly important for simulations with magnetic flutter.

Particle trapping has also other consequences than the effect on parallel viscosity: for example, another important effect is the generation of the bootstrap current [277]. Of particular interest for plasma turbulence are also trapped electrons: one of the key mechanisms for linear instability drive (at lower collisionality) are the trapped electron modes (TEM) [71]. These modes are so prominent because particles are trapped on the unfavourable curvature side of the tokamak, and because trapped electrons can not participate in the adiabatic response to perturbations. Work exists for incorporating also TEMs into fluid models [81, 86]. However, a general model valid also at increased collisonality is unavailable yet [85], particularly for global ("full-f") simulations, requiring further research.

Finally, a subtle but important point is the proper incorporation of gyro-averaging. Recall the drift reduction in section 2.1.1: we remove the fast gyration of particles from the equations, allowing us to study turbulence due to the remaining drift motion of gyro-centres. However, what happens if the resulting turbulent fluctuations appear on the spatial scale of the ion Larmor radius? As we have seen in chapter 5, ions are typically somewhat hotter than the electrons, having therefore a Larmor radius somewhat larger than the sound Larmor radius – a scale on which drift-wave turbulence indeed occurs and is important, driving among other things the zonal flows. With a significant Larmor radius, ions do not experience the local electric field, but the average over the variation along the gyro-orbit – and an effectively reduced $E \times B$ velocity [278]. This stabilises the turbulence [279], and might reduce the zonal flow drive as discussed in chapter 5.4. This effect is incorporated in the reduced Braginskii equations to lowest order by the diamagnetic part of the polarisation velocity [37], see chapter 2.1.3. However, as discussed in Ref. [38, chapter 13.III], "*true* gyroaveraging in the sense of the ions and electrons having different drift velocities at small scales does not enter". The Braginskii equations can not yield gyro-averaging at a higher order in $k_\perp \rho_\mathrm{i}$, i.e. strictly they are valid only in the long-wavelength limit. The solution comes in the form of gyro-fluid equations: instead of forming the fluid closure over the kinetic equation and taking the drift approximation then, one forms the fluid closure over the gyro-kinetic equation. It was shown that in the local approximation, gyro-fluid equations constitute a superset of the Braginskii equations [72]. However, formulating a global gyro-fluid model is more challenging: the gyro-motion can no longer be averaged out if larger fluctuations occur on the gyro-radius scale. We have to at least postulate the smallness of $\varepsilon_\delta = k_\perp \rho_\mathrm{i} \frac{e\varphi_1}{T_\mathrm{i}} \ll 1$ [280], i.e. one requires either the fluctuation amplitude on the gyro-scale to be small, or the scale of larger fluctuations has to be bigger. Recently, progress on a full-f gyro-fluid model formulation has been made [110], paving the way for global fluid simulations with proper gyro-averaging.

8.3.2 Sheath boundary conditions

Sheath boundary conditions remain a significant topic of controversy [151–155] and therefore deserve a discussion. The most robust result regarding sheath physics is that there is a strong electric field between the main quasi-neutral plasma and the machine wall, $e(\varphi_\mathrm{se} - \varphi_\mathrm{wall}) \approx 3T_\mathrm{e}$ (2.71), on a rather small scale between few Debye lengths or ion Larmor radii [48, 147–150]: due to the fast thermal electron motion compared to the slow ions, a confining potential (for electrons) is necessary to keep the main plasma quasi-neutral, i.e. to prevent a continuous charge out-flow, see chapter 2.1.6. The electrostatic potential boundary condition is also the most important, because it is solved for via an elliptic boundary value problem, which is very susceptible to boundary conditions. This electric field is sustained by thermal energy loss of the electrons, cooling them via the respective boundary condition $\mp\chi_\parallel \nabla_\parallel T_\mathrm{e} = \gamma_\mathrm{e} T_\mathrm{e} n c_s$ (2.80), with $\gamma_\mathrm{e} \approx 2.5$. This is the set of boundary conditions used throughout this thesis, see chapter 2.2.2 and the appendix of chapter 5.

However, our own experience with simulations in this thesis, as well as recent literature [152–155], indicate that the reality is more complex and extensions are required. Firstly, as the plasma boundary is at the sheath entrance, the electric field in the sheath is in fact never seen by the main plasma. Its effect is rather that the electrostatic potential at the sheath entrance depends on the local temperatures and current. Therefore, φ_se is different across the main plasma boundary and creates an electric field along the boundary and a corresponding $E \times B$ drift through it. In simulations from chapter 5 we found that the

$E \times B$ velocity through the divertor boundary near the separatrix can be of the order of sound speed. This can create a total flux of particles and heat out of the wall, even if the parallel velocity is at sound speed (we have verified that this was not quite the case in chapter 5, though). A simple solution to this problem is a drift correction of the Bohm-Chodura boundary condition [148, 199]: $u_\parallel \mathbf{b}\cdot\mathbf{n} + \mathbf{v}_E\cdot\mathbf{n} \geq c_s|\mathbf{b}\cdot\mathbf{n}|$ instead of (2.81). It was indeed implemented in GRILLIX and successfully utilised in Ref. [155].

Secondly, non-zero parallel currents play an important role in the SOL [249]. Conducting sheath boundary conditions on the parallel current are also often applied in simulations with simple geometry [121, 150, 281]. However, in realistic tokamak geometry, this is difficult to implement consistently with the boundary condition on the electrostatic potential. The latter is very important as it enters the elliptic solver, while the parallel current in Ohm's law in fact does not strictly require any boundary condition at all. Therefore, in Ref. [155] the simple floating boundary condition $\nabla_\parallel j_\parallel|_{\text{se}} = 0$ was implemented and gave very good agreement with experimental measurements ($j_\parallel|_{\text{se}} = 0$ did not). The agreement of the plasma potential, set to the isolating sheath condition, was less ideal – but a better result can be expected by setting the conducting sheath boundary condition (2.75) on the potential,

$$e\varphi_{\text{se}} = T_{\text{e}}|_{\text{se}} \left[\Lambda - \ln\left(\frac{u_\parallel|_{\text{se}}}{c_s} - \frac{j_\parallel|_{\text{se}}}{e n_{\text{se}} c_s}\right)\right]. \tag{8.4}$$

A strong negative current would lead to a negative potential though, contradicting the sheath assumptions. This is not expected on average, but perhaps during fluctuations, requiring the implementation of electron sheath conditions [153].

Further, some work remains to be done on the numerics. Firstly, the implementation with the penalisation method (see chapter 2.2.2) – particularly with a finite width mask – is unsatisfactory because it converges with more poloidal planes, while FCI works best with fewer poloidal planes. Therefore, efforts must be undertaken in the near future to reduce the mask function width (ideally to zero). Secondly, the artificial boundary at an outer full flux surface must be relaxed to allow the actual physical plasma-wall interaction to take place also along the main chamber wall. Allowing outer flux surfaces to intersect wall elements will require to set parallel boundary conditions at intersection points, hence the issue with the finite penalisation width must be resolved first. However, it can be anticipated that field lines will exist that hit the wall at extremely shallow angles or are nearly parallel to the wall – in this case it is yet unclear what boundary conditions are to be used [49, chapter 25.2]. Finally, as pointed out above, local recycling boundary conditions for the neutrals are required.

8.4 Performance optimisation

Nature is complex, and so is turbulence, involving many spatial and temporal scales. A truly predictive computation must not only solve an appropriate physical model, but also resolve all the relevant scales. An appropriate numerical discretisation provides a good start, but the computational implementation is also crucial. In this regard, the main factor is optimal parallelisation. Consider the simulations in chapters 5 and 6: each running for 2-6 months, they were already quite challenging to perform. However, they were not really computationally expensive, running merely on 8 nodes of the Marconi A3 SKL supercomputer, consuming 0.4-1.5 MCPUh each. The supercomputer has 3188 nodes in total, meaning that if the computation could be scaled effectively to its full size, it would run in less than a day.

Of course, such an effective scaling is not trivial. Firstly, as of now GRILLIX is only MPI [177] parallelised over the sparse toroidal direction – many more compute nodes could be utilized if 3D domain decomposition was employed, but it is far less trivial to implement. But also, each Marconi A3 SKL compute node has 48 CPUs that can be utilized simultaneously with OpenMP [178], while MPI is required to communicate across nodes. As we have detailed in chapter 2.3, GRILLIX achieved barely a speed-up of 8 on 48 CPUs – meaning an additional speed-up of 6 was possible just by optimising the OpenMP performance. The performance seemed to be deteriorated by the intertwined usage of OpenMP and MPI, introducing many barriers and significant latencies. It was therefore unlikely that the 3D MPI decomposition would perform well. Therefore, the first step was a code refactoring, whereby OpenMP regions and MPI communication were largely separated, achieving much better OpenMP scalibility over the majority of the code.

While 2D and 3D solvers are still being optimised right now, these results encourage us that a factor 3-6 speed-up is possible in the very near future. Next, a 3D MPI decomposition should be implemented. This was done in circular geometry in the FCI code GDB [103], achieving good scaling up to more than 10^4 CPUs. But also, modern supercomputers increasingly utilize GPUs (graphics cards) rather than CPUs – offering simpler processing units, but in greatly increased numbers. Not only is the utilisation of GPUs, e.g. via OpenACC [182], unavoidable on modern supercomputers – it also provides a speed-up of 5-10 [282].

These computational advances are indeed required for ever more realistic tokamak simulations. Firstly, already our current simulations could run faster and at a better resolution. Faster run times would allow more parameters and regimes to be scanned, offering more insights and optimisation routes for the experiments. Secondly, even though ASDEX Upgrade is not a small tokamak, actual fusion reactors can be expected to be much larger, and have stronger magnetic fields and hence smaller Larmor radii – requiring more than 100 times larger poloidal grids compared to AUG. And lastly, our simulations are among the first ones resolving ion scale turbulent transport over the whole machine size (adding the plasma core to our domain does not significantly increase the simulated plasma volume) – but also turbulence on the electron Larmor radius scale must be considered [29]. Recently, by means of massive computational efforts, multi-scale simulations over electron and ion scales have been achieved [283,284], demonstrating that their interaction indeed affects the overall transport. However, it remains even more challenging to resolve the electron Larmor radius on the whole device scale. Therefore, we conclude that computational optimisation remains among the key development goals for plasma turbulence codes.

Chapter 9

Conclusions

During this thesis, the turbulence code GRILLIX has been significantly extended. The code is built on state-of-the-art numerical methods which allow self-consistent and efficient simulations of edge turbulence in diverted tokamaks. In particular, the now expanded physical model allowed first-of-their-kind simulations in actual ASDEX Upgrade geometry, at realistic parameters of an attached L-mode discharge, offering unique insights into turbulent transport across the edge and SOL of magnetic confinement fusion devices.

To this end, the principal achievement of this thesis is the fusion of insights and methods from local turbulence models and global mean-field transport models, together with cutting edge numerical and computational techniques. The plasma model has been extended to the fully global, drift-reduced Braginskii equations, including hot ions and electromagnetic effects. To enable the efficient solution of these equations, a 3D linear solver for the implicit treatment of parallel diffusion terms was implemented, such that the time step remains limited by shear Alfvén dynamics that we wish to resolve. The plasma-wall interaction strongly impacts turbulence and transport in the SOL, and in turn the determination of turbulent heat fluxes on machine walls is among the key objectives for predictive modelling. Therefore, the model of the interface between the plasma and the wall, the plasma sheath, has been reviewed. A major mechanism by which the wall influences the plasma is the release of neutral gas. Thus, a diffusive neutral gas model was added and shown to dramatically influence the plasma density and temperature profiles, allowing an adequate match to the experiment in chapter 6.

Our results emphasize the complexity of the plasma edge dynamics. Turbulent fluctuations range between 10% in the edge and 50% in the SOL, intertwining closely with the evolution of the background. This evolution is determined on one hand by sources and sinks: while the heat source stems from the plasma core, the density source is determined by neutral gas ionization in the X-point region and SOL, and the sink is mainly given by fluxes through the plasma sheath. On the other hand, the transport between sources and sinks is determined by turbulence. It is shown to be driven by various instabilities: drift waves, ballooning and ion temperature gradient modes. In the SOL, the neutral gas substantially increases the collisionality, triggering resistive instabilities. Generally, ballooning modes seem to dominate transport by large scale eddies, but small eddies driven by drift waves on the Larmor radius scale are also important because they fuse into a large scale zonal flow due to an inverse energy cascade. The $E \times B$ flow shear peaks at the separatrix, potentially breaking and decorrelating vortices, and increasing their dissipation there. But even where the shear is not strong enough to suppress the turbulence, the flow acts as an energy sink for vortices and modulates turbulent transport, leading to staircase structures.

The stationary radial electric field that determines $E \times B$ rotation is sustained by various mechanisms, investigated in chapter 5. Turbulence driven zonal flows appear on top of mean field effects, such as the balance between the ion diamagnetic and $E \times B$ compression on closed field lines. In the SOL, the sheath sets the electric field in dependence of the divertor temperature. Additionally, toroidal rotation enters the balance in the confined region, flowing in from the SOL.

This work demonstrates substantial progress towards predictive simulations of turbulent transport in the plasma edge and SOL, but it also exposes various opportunities for improvement. For the plasma, the fluid model has to be corrected for various kinetic effects such as Landau damping and trapped particles. The neutral gas model has to be extended for momentum exchange and thermal dynamics,

including also here low collisionality corrections. Impurities have to be considered. At the plasma-wall interface, drifts and currents must be included in sheath boundary conditions, and a local balance between plasma and neutrals fluxes due to recycling needs to be implemented. The numerical implementation could be improved, particularly for the boundary conditions. But also, we foresee significant prospects for the improvement of computational performance by better OpenMP parallelisation, 3D MPI domain decomposition and utilisation of GPU accelerators.

Our current simulations were able to reach a satisfying agreement with a selected ASDEX Upgrade experiment, yielding novel, intriguing and valuable discoveries about the physics at play. This was achieved by faithfully matching the magnetic geometry and utilizing an increasingly realistic physical model. Yet further extensions can be expected to improve the match and open up new and important possibilities. Firstly, the operational space of ASDEX Upgrade should be further explored, focusing in particular on regimes with improved confinement and exhaust. To make projections to reactors, the simulations must be extended to other machines: while smaller or comparable size machines like Alcator C-mod, COMPASS and TCV have already been simulated, larger machine simulations like JET or ITER will rely on increased computational performance. Finally, the shaping of magnetic geometry provides a key route for the optimisation of magnetic confinement fusion devices, while GRILLIX offers a unique capability for flexible and efficient turbulence simulations in complex magnetic fields – it is therefore of paramount interest to study advanced divertor, negative triangularity and stellarator reactor concepts.

Part IV

Appendix

Appendix A

Original publications

This chapter contains the original publications [1–4] that contribute to this cumulative dissertation in the respective journals format. In Chapters 3, 4, 5 and 6, these publications are included in a contiguous format with the rest of the dissertation. Additionally, we provide here for each paper a copyright notice, a publication summary and we indicate the individual contributions of the author of this thesis. The individual contributions are divided in problem definition, literature survey, code implementation, carrying out the simulations, their evaluation and manuscript preparation.

A.1 Thermal dynamics in the flux-coordinate independent turbulence code GRILLIX

COPYRIGHT

Reprinted with permission from
Wladimir Zholobenko, Andreas Stegmeir, Thomas Body, Alexander Ross, Peter Manz, Omar Maj, David Coster, Frank Jenko, Manaure Francisquez, Ben Zhu, Barrett Rogers
Thermal dynamics in the flux-coordinate independent turbulence code GRILLIX
Contributions to Plasma Physics. 2020; 60:e201900131.
DOI: https://doi.org/10.1002/ctpp.201900131

SUMMARY

GRILLIX employs the flux-coordinate independent approach (FCI), which allows us to study boundary plasma turbulence in realistic diverted configurations. Recently, the physical model in GRILLIX has been extended to a global drift reduced Braginskii model, without any separation between background and fluctuations. It includes electromagnetic and thermal dynamics with hot ions, relaxation of the Boussinesq approximation and non-linear parametric dependencies. This contribution presents solutions to associated issues, i.e. the ion diamagnetic polarisation and the stiff parallel heat conduction. Simulations based on parameters characteristic for the Alcator C-Mod tokamak were carried out. In circular geometry, the self-consistent electric field contains zonal flows and geodesic acoustic modes in the confined region. In the scrape-off layer the electron parallel heat conduction and its boundary condition determine the temperature and electric field, leading to sheared flows at the LCFS.

A corrigendum has been published to this article, see chapters 4 and A.2.

INDIVIDUAL CONTRIBUTIONS

Leading role in realizing the scientific project.

Problem definition	*significantly contributed*
Literature survey	*significantly contributed*
Code implementation	*significantly contributed*
Carrying out the simulations	*significantly contributed*
Evaluation of the simulations	*significantly contributed*
Manuscript preparation	*significantly contributed*

Received: 13 September 2019 | Accepted: 19 November 2019 | Published on: 22 December 2019

DOI: 10.1002/ctpp.201900131

ORIGINAL ARTICLE

Contributions to Plasma Physics

Thermal dynamics in the flux-coordinate independent turbulence code GRILLIX

W. Zholobenko[1] | A. Stegmeir[1] | T. Body[1] | A. Ross[1] | P. Manz[1] | O. Maj[1] | D. Coster[1] | F. Jenko[1] | M. Francisquez[2] | B. Zhu[3] | B.N. Rogers[4]

[1]Max Planck Institute for Plasma Physics, Garching, Germany

[2]MIT Plasma Science and Fusion Center, Cambridge, Massachusetts, USA

[3]Lawrence Livermore National Laboratory, Livermore, California, USA

[4]Department of Physics and Astronomy, 6127 Wilder Laboratory, Dartmouth College, Hanover, New Hampshire, USA

Correspondence
W. Zholobenko, Max-Planck-Institut für Plasmaphysik, D-85748 Garching, Germany.
Email: wladimir.zholobenko@ipp.mpg.de

Funding information
H2020 Euratom, 633053

Abstract

GRILLIX employs the flux-coordinate independent approach (FCI), which allows us to study boundary plasma turbulence in realistic diverted configurations. Recently, the physical model in GRILLIX has been extended to a global drift-reduced Braginskii model, without any separation between background and fluctuations. It includes electromagnetic and thermal dynamics with hot ions, relaxation of the Boussinesq approximation and non-linear parametric dependencies. This contribution presents solutions to associated issues, that is, the ion diamagnetic polarization and the stiff parallel heat conduction. Simulations based on parameters characteristic for the Alcator C-Mod tokamak were carried out. In circular geometry, the self-consistent electric field contains zonal flows and geodesic acoustic modes in the confined region. In the scrape-off layer, the electron parallel heat conduction and its boundary condition determine the temperature and electric field, leading to sheared flows at the last closed flux surface.

KEYWORDS

drifts, edge, flux-coordinate independent, heat conduction, SOL, turbulence

1 | INTRODUCTION

A fundamental issue investigated with turbulence codes like GRILLIX[1] is the competition between the turbulent perpendicular heat flux and the parallel one in the scrape-off layer (SOL), which determines the SOL width and the survival of the wall components of future fusion power plants. A comprehensive and self-consistent physical model is required that describes both effects in realistic and experimentally relevant magnetic geometries. The latter is discussed in a separate contribution to these proceedings,[2] while the physical model and its implementation is discussed herein.

The global drift-reduced Braginskii model, described in Section 2, does not separate between background and fluctuations, which is shown to be important for the edge plasma.[1,3–6] Alternatively, global gyrokinetic[7] or gyrofluid[8] models are being developed. In GRILLIX, we recently implemented the crucial ion temperature dynamics and an implicit

treatment of (electron) parallel heat conductivity. The consistent time discretization with the 3rd order Karniadakis[9] scheme is detailed in Section 3, as well as the matrix-free parallelized solution of the resulting system of equations by the PIM library.[10]

We demonstrate the importance of the newly implemented thermal effects by performing Alcator C-mod like L-mode simulations in circular geometry, illustrated in Section 4. Compared to previous work,[6] we confirm that the turbulence is stabilized by higher temperature and destabilized by higher density. The electric field in the confined region exceeds the ion pressure gradient and contains zonal flow as well as geodesic acoustic mode (GAM) components. In the SOL, it follows the electron temperature and its profile is strongly dependent on the electron parallel heat conductivity, while the ion conductivity plays a minor role. This results in a sheared electric field at the last closed flux surface (LCFS). This is also summarized in Section 5.

2 | PHYSICAL MODEL

The drift-reduced Braginskii model[11,12] describes edge and SOL turbulence in the low-frequency regime $\omega \ll \frac{eB}{M_i c}$. In the following, time scales are normalized to R_0/c_{s0}, with R_0 the major radius and $c_{s0} = \sqrt{T_{e0}/M_i}$ the sound speed at reference electron temperature T_{e0}. Perpendicular scales are normalized to the sound Larmor radius $\rho_{s0} = c\sqrt{T_{e0}M_i}/(eB_0)$ and parallel scales to R_0. The dynamical fields evolved in GRILLIX are the density n normalized to a reference density n_0, the electrostatic potential ϕ normalized to T_{e0}/e, the parallel ion velocity $u_\parallel$ normalized to c_{s0}, the electron and ion temperatures T_e and T_i normalized to reference values T_{e0}, respectively T_{i0}, the parallel current $j_\parallel$ normalized to en_0c_{s0} and the parallel component of the perturbed electromagnetic potential $A_\parallel$ normalized to $(\beta_0 B_0 \rho_{s0})^{-1}$ with $\beta_0 = 4\pi n_0 T_{e0}/B_0^2$:

$$\frac{d}{dt}n = nC(\phi) - C(p_e) + \nabla\cdot[(j_\parallel - nu_\parallel)\mathbf{b}], \tag{1}$$

$$\nabla\cdot\left[\frac{n}{B^2}\left(\frac{d}{dt}+u_\parallel\nabla_\parallel\right)\left(\nabla_\perp\phi+\tau\frac{\nabla_\perp p_i}{n}\right)\right] = -C(p_e+\tau p_i) + \nabla\cdot(\mathbf{b}j_\parallel), \tag{2}$$

$$\left(\frac{d}{dt}+u_\parallel\nabla_\parallel\right)u_\parallel = -\frac{\nabla_\parallel(p_e+\tau p_i)}{n}, \tag{3}$$

$$\frac{3}{2}\left(\frac{d}{dt}+v_\parallel\nabla_\parallel\right)T_e = T_eC(\phi) - \frac{T_e}{n}C(p_e) - \frac{5}{2}T_eC(T_e) + 0.71\frac{T_e}{n}\nabla\cdot(\mathbf{b}j_\parallel) + \left(\frac{\eta_{\parallel 0}}{T_e^{3/2}}\right)\frac{j_\parallel^2}{n} + \frac{1}{n}\nabla\cdot[(\chi_{\parallel e0}T_e^{5/2})\mathbf{b}\nabla_\parallel T_e], \tag{4}$$

$$\frac{3}{2}\left(\frac{d}{dt}+u_\parallel\nabla_\parallel\right)T_i = T_iC(\phi) - \frac{T_i}{n}C(p_e) + \frac{5}{2}\tau T_iC(T_i) - T_i\nabla\cdot(\mathbf{b}v_\parallel) + \frac{T_i}{n^2}j_\parallel\nabla_\parallel n + \frac{1}{n}\nabla\cdot[(\chi_{\parallel i0}T_i^{5/2})\mathbf{b}\nabla_\parallel T_i], \tag{5}$$

$$\beta_0\frac{\partial}{\partial t}A_\parallel + \mu\left(\frac{d}{dt}+v_\parallel\nabla_\parallel\right)\frac{j_\parallel}{n} = -\left(\frac{\eta_{\parallel 0}}{T_e^{3/2}}\right)j_\parallel - \nabla_\parallel\phi + \frac{\nabla_\parallel p_e}{n} + 0.71\nabla_\parallel T_e, \quad \nabla_\perp^2 A_\parallel = -j_\parallel, \tag{6}$$

where we have introduced as auxiliary variables the parallel electron velocity $v_\parallel = u_\parallel - j_\parallel/n$ and the electron and ion pressures $p_e = nT_e$, respectively, $p_i = nT_i$, The parallel gradient is defined as $\nabla_\parallel := \mathbf{b}\cdot\nabla$ with $\mathbf{b} = \mathbf{B}/B$ the unit vector of the static background magnetic field. The advective derivative is defined as $\frac{d}{dt} := \frac{\partial}{\partial t} + \delta_0\left(\frac{\mathbf{B}}{B^2}\times\nabla\phi\right)\cdot\nabla$ and the curvature operator as $C(f) := -\delta_0\left(\nabla\times\frac{\mathbf{B}}{B^2}\right)\cdot\nabla f$. The dimensionless parameters of the system are the drift scale $\delta_0 := R_0/\rho_{s0}$, the dynamical plasma beta β_0 defined above, the electron to ion mass and temperature ratios $\mu := m_e/M_i$ respectively $\tau := T_{i0}/T_{e0}$, the normalized parallel resistivity $\eta_{\parallel 0} := 0.51\frac{R_0}{\tau_{e0}c_{s0}}\frac{m_e}{M_i}$, and normalized parallel electron and ion heat conductivities $\chi_{\parallel e0} := 3.15\frac{\tau_{e0}c_{s0}}{R_0}\frac{M_i}{m_e}$ and $\chi_{\parallel i0} := 3.9\frac{\tau_{i0}c_{s0}}{R_0}\frac{T_{i0}}{T_{e0}}$, respectively, where τ_{e0} and τ_{i0} are the electron ion collision times evaluated at reference. The equations are supplemented by sources for density, electron and ion temperature, and by numerical dissipation terms.

Insulating Bohm sheath boundary conditions[13] are applied at the limiter/divertor target plates:

$$u_\parallel \gtrless \sqrt{T_e}, \quad j_\parallel = 0, \quad \phi = \Lambda T_e, \quad \nabla_\parallel T_e = -\frac{\gamma_e}{(\chi_{\parallel e0}T_e^{5/2})}T_e n u_\parallel, \quad \nabla_\parallel T_i = 0, \quad \nabla_\parallel n = 0, \tag{7}$$

where $\Lambda \approx 0.5 \ln \frac{M_i}{2\pi m_e}$ is the sheath floating potential and $\gamma_e \approx 2.5$ is the electron sheath transmission coefficient. Additionally, the simulation domain is bounded by inner and outer limiting flux surfaces, where homogeneous Neumann boundary conditions are applied to $n, T_e, T_i, u_\parallel$ and homogeneous Dirichlet boundary conditions to $A_\parallel$. At the outer radial boundary, ϕ is set to ΛT_e, and in order to allow the potential to float at the inner boundary a zonal homogeneous Neumann boundary condition is applied, that is, $\partial_\rho \langle \phi \rangle_\theta = 0$ and $\phi - \langle \phi \rangle_\theta = 0$, with $\langle \rangle_\theta$ denoting the flux surface average and ρ a coordinate perpendicular to flux surfaces.

We note that the model is global, which is reflected in the fact that all parametric dependencies are kept and the routinely employed Boussinesq approximation is not applied. In comparison to the previous version,[1] GRILLIX was extended by ion thermal dynamics. However, magnetic flutter terms, as well as terms arising from the viscous part of the ion stress tensor, for example, magnetic pumping terms, are not yet implemented in the GRILLIX model.

3 | NUMERICAL IMPLEMENTATION

GRILLIX is based on the flux-coordinate independent approach[14,15] (FCI), which avoids the common singularities of flux-coordinates[16] at the separatrix and X-point(s). A cylindrical grid is used, where parallel operators are discretised via a field line map between adjacent poloidal planes. For a comprehensive description of GRILLIX and the FCI implementation, we refer to Stegmeir et al.,[1] and we discuss here numerical techniques of the most recent extensions, that is, ion thermal dynamics and the implicit treatment of the parallel heat conduction.

3.1 | Ion diamagnetic polarization

The main difficulty in the implementation of ion thermal dynamics is the calculation of the electrostatic potential in the presence of the ion diamagnetic polarization term in Equation (2), where one has to take into account the time derivatives correctly. The time-stepping scheme in GRILLIX is based on a 3rd order backward differentiation formula (BDF3), where a quantity f, subject to $\partial_t f = F(f)$, is evolved in time according to

$$f^{t+1} - \frac{6}{11}\Delta t F^{t+1} = \frac{18}{11} f^t - \frac{9}{11} f^{t-1} + \frac{2}{11} f^{t-2}, \tag{8}$$

with time step Δt and $F^{t+1} = F(f^{t+1})$. BDF3 is an implicit scheme that modifies to an explicit scheme (Karniadakis[9]) via approximating $F^{t+1} \approx 3F^t - 3F^{t-1} + F^{t-2}$. For the temporal discretisation of the vorticity equation, we define the generalized vorticity at time step t

$$\Omega_j^t := \nabla \cdot \left[\frac{n^{t+1}}{B^2} \left(\nabla_\perp \phi^{t+j} + \tau \frac{\nabla_\perp p^{i+j}}{n^{t+j}} \right) \right], \tag{9}$$

where the index j is only attached to quantities that the time derivative acts on. Integrator (8) applied to (2) yields

$$\Omega_{+1}^t = \frac{18}{11}\Omega_0^t - \frac{9}{11}\Omega_{-1}^t + \frac{2}{11}\Omega_{-2}^t + \frac{6}{11}\Delta t (3F^t - 3F^{t-1} + F^{t-2}), \tag{10}$$

where the F terms contain advection and the right hand side terms of Equation (2), which can be computed explicitly. We note that before this step, the continuity Equation (1) has already been advanced and therefore $\Omega^t_{0,-1,-2}$ can be computed directly as n^{t+1} is available. The electrostatic potential at time $t+1$ is finally obtained by solving

$$\Omega_{+1}^t - \tau \nabla \cdot \left(\frac{1}{B^2} \nabla_\perp p_i^{t+1} \right) = \nabla \cdot \left(\frac{n^{t+1}}{B^2} \nabla_\perp \phi^{t+1} \right), \tag{11}$$

where p_i^{t+1} is also available due to the prior advancement of the ion thermal Equation (5). Therefore, Equation (11) is a two-dimensional elliptic equation for ϕ^{t+1} and is solved in GRILLIX via an efficient geometric multigrid solver within each poloidal plane separately.[1] We note that the final implementation of the model with ion thermal dynamics was verified successfully with the Method of Manufactured Solutions,[17] which is continuously integrated in GRILLIX.

3.2 | Semi-implicit nonlinear parallel heat conduction

With the Braginskii closure for the 3-moment fluid equations,[11] the resulting parabolic heat conduction term leads to a severe restriction on the allowed time step if treated with the same high-order explicit scheme as the hyperbolic rest of the system. In a global model, this constraint depends on temperature and density and therefore on space and time, so that either the time step or the heat conductivity has to be significantly reduced.[1] However, due to its crucial role in setting the SOL temperature profile[1] and symmetrizing the temperature profile on closed flux surfaces,[6] a remedy had to be found.

A natural solution is to treat this term implicitly. This can be performed consistently within the Karniadakis time stepping scheme by splitting the equations into an explicit and an implicit part, $F(f) = F_{\mathrm{ex}}(f) + F_{\mathrm{im}}(f)$, and approximating only the explicit part by $F_{\mathrm{ex}}^{t+1} \approx 3F_{ex}^{t} - 3F_{\mathrm{ex}}^{t-1} + F_{\mathrm{ex}}^{t-2}$. The implicit part contains only the parabolic heat conduction terms for electrons and ions (as well as penalization terms[1,18] for parallel boundary conditions, omitted here for brevity), while the rest of the system of equations is treated explicitly. This results in two nonlinear 3D elliptic problems (for T_{e} and T_{i}) that have to be solved at every time step,

$$\left[1 - \frac{6}{11}\Delta t \frac{\chi_{\parallel 0}}{n^t}\nabla\cdot(T^*)^{5/2}\mathbf{b}\nabla_\parallel\right] T^{t+1} = \frac{18}{11}T^t - \frac{9}{11}T^{t-1} + \frac{2}{11}T^{t-2} + \frac{6}{11}\Delta t\left[3F_{\mathrm{ex}}^{t} - 3F_{\mathrm{ex}}^{t-1} + F_{\mathrm{ex}}^{t-2}\right]. \tag{12}$$

T^* in the brackets has to be T^{t+1} according to the Karniadakis scheme, requiring Newton iterations for the solution of the nonlinear system of equations. However, the $O(\Delta t)$ linearization $T^* = T^t$ (or higher order approximations) can be used without impact on the stability of the scheme.

In FCI, the grid can be toroidally sparse, keeping the condition number of the linear system low. The Karniadakis scheme (BDF3), however, is not A-stable, and therefore large enough imaginary eigenvalues would make it unstable. The continuous diffusion operator is self-adjoint and has only real eigenvalues, but this is not generally given on the discrete level in FCI - in GRILLIX, these properties are preserved by the support operator method.[15,19]

To solve the linear system, we use the Parallel Iterative Methods (PIM 2.3) library[10]; particularly, the well scalable restarted GMRES algorithm,[20] with a matrix-free implementation. This is useful because the matrix for parallel operators is somewhat complex in FCI, and has to be distributed among MPI processes and recomputed every time step due to the nonlinearity. With PIM, no matrix is ever built and (12) is simply defined by existing operators, saving memory space, computational cost, and effort.

4 | C-MOD L-MODE IN CIRCULAR GEOMETRY

The setup is based on,[6] although we use a very different implementation, most notably a fully non-field-aligned grid. The normalization parameters are major radius $R_0 = 68\,\mathrm{cm}$, minor radius $a = 22\,\mathrm{cm}$, equilibrium toroidal magnetic field $B_0 = 4.1$ T, deuterium ion mass $M_i = 2m_p$, density $n_0 = 8\times10^{13}$ cm^{-3} and temperature $T_0 = 30\,\mathrm{eV}$. For electron collisions, we use the effective charge state $Z = 1.5$. This results in dimensionless parameters: $\delta = 3{,}520$, $\beta_0 = 2.88\times10^{-5}$, $\mu = 2.72\times10^{-4}$, $\tau = 1$, $\eta_{\parallel 0} = 6.03\times10^{-2}$, $\chi_{\parallel \mathrm{e}0} = 26.6$, $\chi_{\parallel \mathrm{i}0} = 1.15$. We define the normalized radial coordinate $\rho = \sqrt{(R-R_0)^2 + Z^2}$, then the safety factor $q(\rho) = 4/(1 - 3.71(\rho - 0.305))$ defines the poloidal magnetic field profile.

The grid consists of 16 poloidal planes and a uniform poloidal resolution of $3\times\rho_{s0} \approx 0.58$ mm. The time step is $\Delta t = 5\times10^{-5}\frac{R_0}{c_{s0}} \approx 0.9$ ns. The simulation domain is $\rho \in (0.2412, 0.3685)$, with LCFS at $\rho = 0.3235$. In total, the grid consists of circa 5.4×10^6 points. In order to test the resolution, a simulation with 16×10^6 points was run until $t = 0.6$ ms and showed no significant difference in the profiles. A sixth-order hyperviscosity $4{,}000\nabla_\perp^6$ was applied in perpendicular direction on all fields to cut off turbulent spectra on grid scale, as well as regular diffusion $0.05\,\nabla\cdot(\mathbf{b}\nabla_\parallel)$ on n,Ω and $u_\parallel$ in parallel direction.

The reference simulation has as initial condition $(n,T_{\mathrm{e}},T_{\mathrm{i}}) = (2,3,3)$ at the core boundary and $n = T_{\mathrm{e}} = T_{\mathrm{i}} = 0.2$ in the SOL, with a smooth transition in the edge region. The initial temperature profile is shown in Figure 2. An adaptive source keeps the profiles fixed at the core boundary and $n > 0.03$, $T_{\mathrm{e}} > 0.07$ and $T_{\mathrm{i}} > 0.03$. Otherwise, they are free to evolve in the rest of the domain, with a sink given by sheath boundary conditions at the limiter boundary. Other fields are set to stabilize the initial profile, that is, an electric field balances the ion diamagnetic polarization, and Pfirsch-Schlüter currents balance the pressure gradient. Additionally, one simulation with $n = 4$ at the core (double density) and one with $T_{\mathrm{e}} = T_{\mathrm{i}} = 6$ (double temperature) were carried out, as well as scans with parallel heat conductivity $\chi_{\parallel 0}$ at reference core parameters.

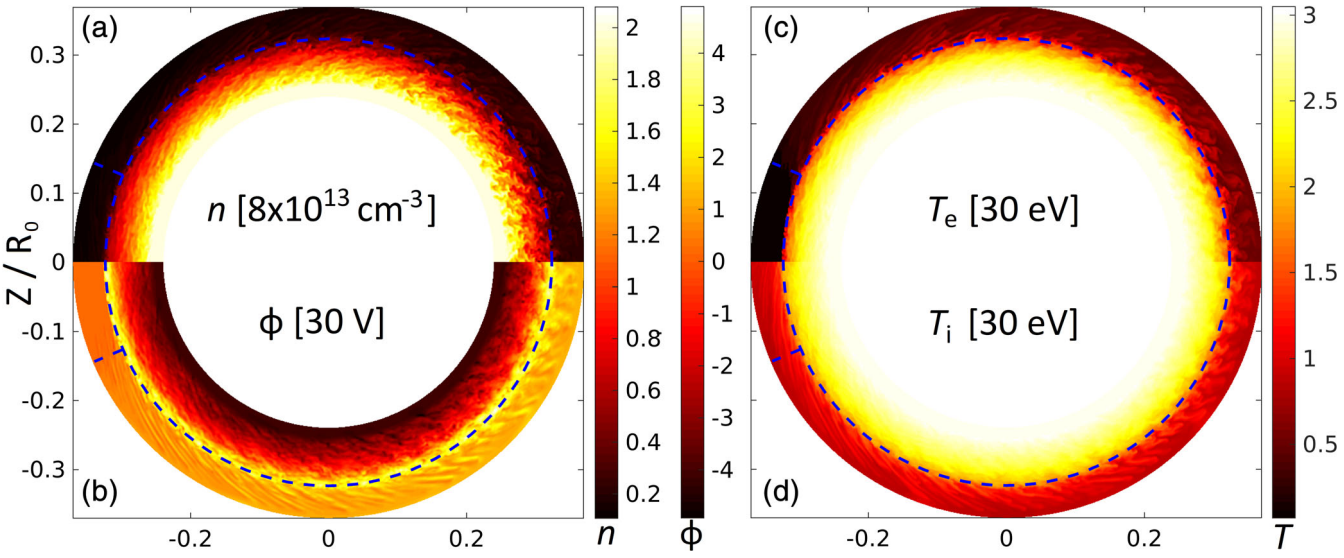

FIGURE 1 Poloidal snapshot of (a) density, (b) potential, (c) electron, and (d) ion temperature at $t = 1.44$ ms. The horizontal coordinate is $(R - R_0)/R_0$. The average profiles are (nearly) up-down symmetric, hence only half the plane is shown. The blue dashed line indicates the limiter location on the inboard midplane (parallel sheath boundary region) and the last closed flux surface (LCFS)

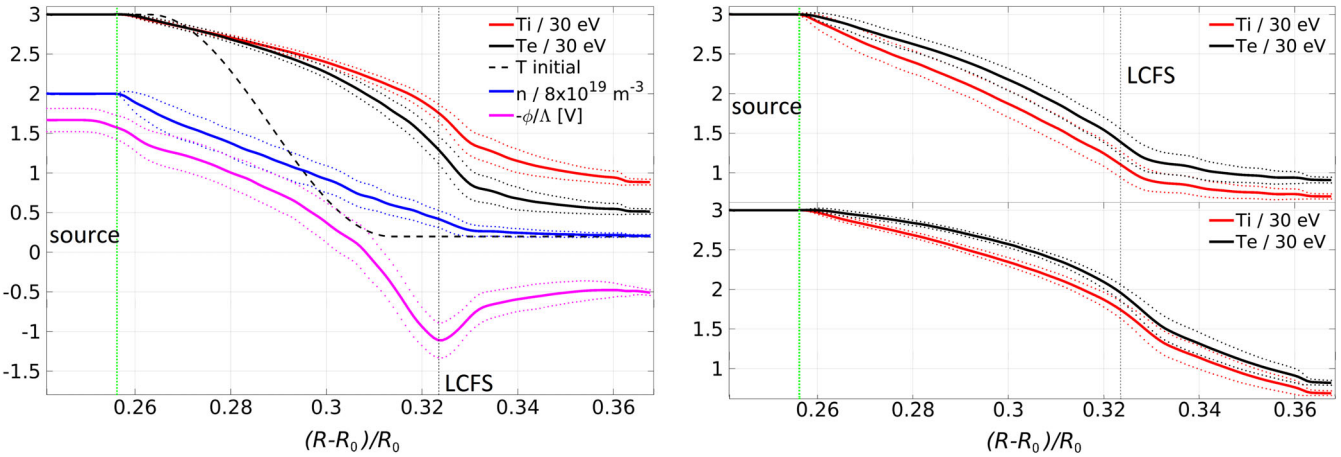

FIGURE 2 Mean radial profiles (T_i, T_e, T initial, n,$-\phi/\Lambda$ from top to bottom) at the outboard midplane at $t \approx 1.4$ ms. Dotted lines indicate the $\pm\sigma_f$ fluctuation level. The negative potential $-\phi$ and its fluctuation level are divided by $\Lambda = 2.69$. Last closed flux surface (LCFS) and source region are marked. *Left*: reference simulation with $\chi_{\parallel e0} = 26.6$, $\chi_{\parallel i0} = 1.15$, $\gamma_e = 2.5$. *Top right*: $\chi_{\parallel e0} = \chi_{\parallel i0} = 1.15$ and $\gamma_e = 0.1$ (case 2); *bottom right*: $\chi_{\parallel e0} = 26.6$, $\chi_{\parallel i0} = 1.15$, $\gamma_e = 0$ (case 1, see Section 4.1)

Simulations were run until $t = 80\frac{R_0}{c_{s0}} \approx 1.5$ ms (for circa 9 days on the Marconi-A3 SKL partition, on eight nodes with 2 MPI processes per node times 24 cores). The resulting poloidal profiles of n,ϕ,T_e, and T_i at $t = 1.44$ ms are displayed in Figure 1. All profiles except T_i are saturated, with T_i still rising at $t > 3$ ms.[6] Averaged toroidally and in time over $10\frac{R_0}{c_{s0}} \approx 0.2$ ms (40 snapshots), profiles and fluctuation amplitudes $\sigma_f^2 = \langle f^2 \rangle - \langle f \rangle^2$ at the outboard midplane are shown in Figure 2.

With the updated voriticity equation, the electric field in the confined region is proportional to the ion pressure gradient, exceeding it by circa 50%. On the other hand, due to sheath boundary conditions the potential in the SOL is following $\phi = \Lambda T_e$. A potential maximum results at the separatrix, leading to a jump in the electric field and consequently sheared $E \times B$ flows. The potential oscillations in the confined region contain a strong poloidally and toroidally symmetric part at acoustic frequencies, indicating the presence of GAMs.[21] Figure 3 shows the frequency spectrum. The radial profile of the acoustic frequency $\widehat{f} \approx \frac{\sqrt{2}}{2\pi}\sqrt{T_e + T_i}$ is shown as a reference, $f = \frac{c_{s0}}{R_0}\widehat{f} = 56\text{kHz} \times \widehat{f}$ in physical units.

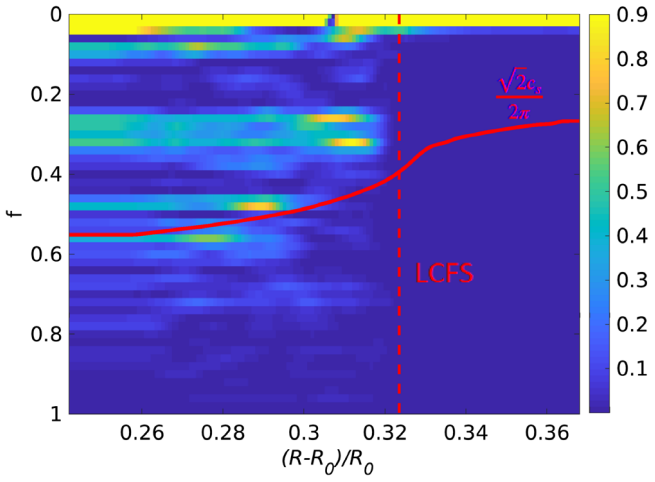

FIGURE 3 Frequency spectrum of poloidally and toroidally averaged electrostatic potential fluctuations

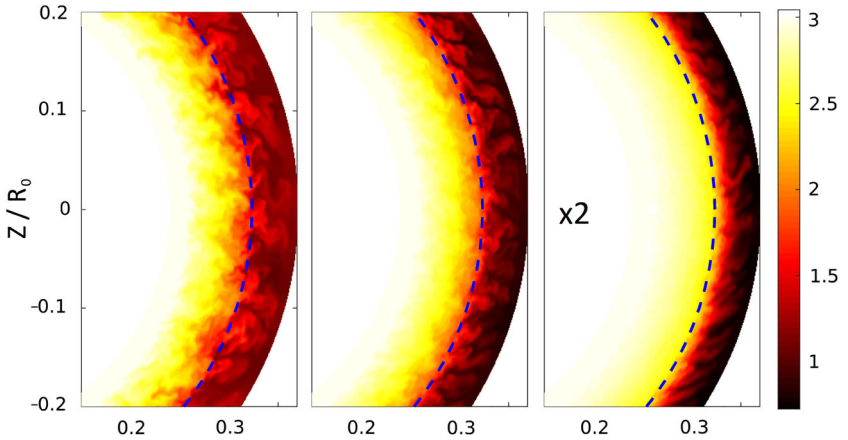

FIGURE 4 Outboard midplane ion temperature snapshot at 1.44 ms in: double density, reference, and double temperature (left to right). Horizontal axis is $(R-R_0)/R_0$. last closed flux surface (LCFS) marked by blue dashed line

We confirm the results by Zhu et al.[6] in that the turbulence is enhanced with increasing density and suppressed with increasing temperature, most visible in T_i, which is shown in Figure 4. However, investigating the different behaviour of electron and ion temperature, we find a surprising dependence on parallel heat conductivity, discussed in the following section.

4.1 | Parallel heat conduction

To test the relevance and effect of the parallel heat conduction, four additional simulations were carried out. Comparing to the reference ($n|_\mathrm{core} = 2$, $T|_\mathrm{core} = 3$) with $\chi_{\parallel \mathrm{e}0} = 26.6$, $\chi_{\parallel \mathrm{i}0} = 1.15$ and $\gamma_\mathrm{e} = 2.5$ these have

1. $\chi_{\parallel \mathrm{e}0} = 26.6$, $\chi_{\parallel \mathrm{i}0} = 1.15$, $\gamma_\mathrm{e} = 0$
2. $\chi_{\parallel \mathrm{e}0} = \chi_{\parallel \mathrm{i}0} = 1.15$ and $\gamma_\mathrm{e} = 0.1$
3. $\chi_{\parallel \mathrm{e}0} = \chi_{\parallel \mathrm{i}0} = 0.1$ and $\gamma_\mathrm{e} = 0.01$
4. $\chi_{\parallel \mathrm{e}0} = 26.6$, $\chi_{\parallel \mathrm{i}0} = 30$, $\gamma_\mathrm{e} = 2.5$

T_e and T_i for cases 1 and 2 are shown in Figure 2 on the right. In the reference run, and also double n and double T, ions are hotter in the SOL than electrons, as expected from experiments. This is due to the electron heat sheath transmission. Without this boundary condition (case 1), electrons are hotter. This trend extends into the confined region. A lowered electron heat conductivity (case 2) also requires a reduced γ_e to avoid unphysical gradients at the sheath, and hence also has the same effect. Additionally, a reduced electron heat conductivity increases the T_e and T_i fluctuation level and flattens profiles, likely due to the lowered flux surface symmetrization and fluctuation damping.

Further reducing both heat conductivities (case 3) has no effect on neither the profiles nor fluctuation levels at the outboard midplane. However, the up-down asymmetry becomes more visible, as in the results of Zhu et al.[6]

The difference in heat conductivity between electrons and ions *does not* explain the different saturation time of T_e and T_i. In fact, setting $\chi_{\parallel \mathrm{i}0} = 30$ (case 4) or lowering it to 0.1 has barely any influence on the profiles at all. The electron

heat conductivity has a much higher impact on both electron and ion transport –only T_e enters Ohm's law and sheath boundary conditions, thereby setting the SOL potential and currents.

5 | CONCLUSION

The thermal model in GRILLIX was extended by ion temperature dynamics, including the ion diamagnetic polarization drift, leading to a self-consistent electric field with zonal flows and GAMs. In circular geometry simulations, the electric field on closed field lines balances the ion pressure gradient, somewhat exceeding it. In the SOL, the electric potential follows the electron temperature due to sheath boundary conditions and Ohm's law. This leads to a maximum in the electrostatic potential at the LCFS and a jump of the electric field. Turbulence is destabilized by higher density, while higher temperature is somewhat stabilizing.

A 3D iterative implicit solver now allows for a realistically large parallel heat conductivity without affecting the time step and hence simulation time. The electron-parallel heat conductivity, together with sheath heat transmission boundary conditions, largely determines the SOL temperature profile – for both electrons and ions. In the confined region, it leads to flux surface symmetrization and fluctuation reduction. The ion heat conductivity, on the other hand, plays a much smaller role.

ACKNOWLEDGMENTS

This work has been the framework of the EUROfusion Consortium and has received funding from the Euratom research and training program 2014–2018 and 2019–2020 under Grant Agreement No. 633053. The views and opinions expressed herein do not necessarily reflect those of the European Commission.

REFERENCES

[1] A. Stegmeir, A. Ross, T. Body, M. Francisquez, W. Zholobenko, D. Coster, O. Maj, P. Manz, F. Jenko, B. Rogers, K. S. Kang, *Phys. Plasmas* **2019**, *26*, 052517.
[2] T. Body, A. Stegmeir, W. Zholobenko, D. Coster, F. Jenko, accepted to *Contrib. Plasma Phys.* **2019**.
[3] F. D. Halpern, P. Ricci, S. Jolliet, J. Loizu, J. Morales, A. Mosetto, F. Musil, F. Riva, T. M. Tran, C. Wersal, *J. Comput. Phys.* **2016**, *315*, 388.
[4] B. D. Dudson, J. Leddy, *Plasma Phys. Controlled Fusion* **2017**, *59*, 054010.
[5] P. Tamain, H. Bufferand, G. Ciraolo, C. Colin, D. Galassi, P. Ghendrih, F. Schwander, E. Serre, *J. Comput. Phys.* **2016**, *321*, 606.
[6] B. Zhu, M. Francisquez, B. N. Rogers, *Phys. Plasmas* **2017**, *24*, 055903.
[7] N.R. Mandell, A. Hakim, G.W. Hammett, M. Francisquez, *arXiv:1908.05653 [physics.plasm-ph]*, **2019**.
[8] T. T. Ribeiro, B. Scott, *Plasma Phys. Controlled Fusion* **2008**, *50*, 055007.
[9] G. E. Karniadakis, M. Israeli, S. A. Orszag, *J. Comput. Phys.* **1991**, *97*, 414.
[10] R. D. da Cunha, T. Hopkins, *Appl. Num. Math.* **1995**, *19*, 33.
[11] S. I. Braginskii, in *Reviews of Plasma Physics*, Vol. *1* (Ed: M. A. Leontovich), Consultants Bureau, New York, **1965**.
[12] A. Zeiler, J. F. Drake, B. Rogers, *Phys. Plasmas* **1997**, *4*, 2134.
[13] P. C. Stangeby, The Plasma Boundary of Magnetic Fusion Devices. Series in Plasma Physics, CRC Press, Boca Raton, **2000**.
[14] F. Hariri, M. Ottaviani, *Comput. Phys. Commun.* **2013**, *184*, 2419.
[15] A. Stegmeir, D. Coster, O. Maj, K. Hallatschek, K. Lackner, *Comput. Phys. Commun.* **2016**, *198*, 139.
[16] W. D. D'haeseleer, W. N. G. Hitchon, J. D. Callen, J. L. Sohet, *Flux Coordinates and Magnetic Field Structure: A Guide to a Fundamental Tool of Plasma Theory*. *Springer Series in Computational Physics*, Springer, Berlin Heidelberg, **1991**.
[17] K. Salari, P. Knupp, *Code Verification by the Method of Manufactured Solutions*, Sandia National Laboratories, **2000**, Sandia Report SAND2000-1444.
[18] B. Zhu, M. Francisquez, B. N. Rogers, *Comp. Phys. Commun.* **2018**, *232*, 46.
[19] A. Stegmeir, D. Coster, A. Ross, O. Maj, K. Lackner, E. Poli, *Plasma Phys. Controlled Fusion* **2018**, *60*, 035005.
[20] R. D. da Cunha, T. Hopkins, *Adv. Comput. Math.* **1994**, *2*, 261.
[21] G. D. Conway, B. Scott, J. Schirmer, M. Reich, A. Kendl, The ASDEX Upgrade Team, *Plasma Phys. Controlled Fusion* **2005**, *47*, 1165.

How to cite this article: Zholobenko W, Stegmeir A, Body T, et al. Thermal dynamics in the flux-coordinate independent turbulence code GRILLIX. *Contributions to Plasma Physics*. 2020;60:e201900131. https://doi.org/10.1002/ctpp.201900131

A.2 Corrigendum: Thermal dynamics in the flux-coordinate independent turbulence code GRILLIX

COPYRIGHT

Wladimir Zholobenko, Andreas Stegmeir, Thomas Body, Alexander Ross, Peter Manz, Omar Maj, David Coster, Frank Jenko, Manaure Francisquez, Ben Zhu, Barrett Rogers
Corrigendum: Thermal dynamics in the flux-coordinate independent turbulence code GRILLIX
Contributions to Plasma Physics. 2020; 60:e202000056.
DOI: https://doi.org/10.1002/ctpp.202000056

INDIVIDUAL CONTRIBUTIONS

Leading role in realizing the scientific project.

Problem definition	*significantly contributed*
Literature survey	*significantly contributed*
Code implementation	*significantly contributed*
Carrying out the simulations	*significantly contributed*
Evaluation of the simulations	*significantly contributed*
Manuscript preparation	*significantly contributed*

Received: 8 April 2020 | Revised: 24 April 2020 | Accepted: 24 April 2020 | Published on: 15 June 2020

DOI: 10.1002/ctpp.202000056

CORRIGENDUM

Contributions to Plasma Physics

Corrigendum: Thermal dynamics in the flux-coordinate independent turbulence code GRILLIX

W. Zholobenko[1] | A. Stegmeir[1] | T. Body[1] | A. Ross[1] | P. Manz[1] | O. Maj[1] | D. Coster[1] | F. Jenko[1] | M. Francisquez[2] | B. Zhu[3] | B.N. Rogers[4]

[1]Max Planck Institute for Plasma Physics, Garching, Germany

[2]MIT Plasma Science and Fusion Center, Cambridge, Massachusetts,

[3]Lawrence Livermore National Laboratory, 7000 East Avenue, Livermore, California,

[4]Department of Physics and Astronomy, 6127 Wilder Laboratory, Dartmouth College, Hanover, New Hampshire,

Correspondence
Email: wladimir.zholobenko@ipp.mpg.de

Funding information
Euratom, Grant/Award Number: 633053

We have discovered that one of the original articles [1] findings, that the actual choice of the dimensionless parameter $\chi_{\parallel i0}$ for the ion heat conductivity* seemed to play no role for the simulation results, was not physical. Instead, due to a mistake in the handling of input parameters, $\chi_{\parallel i0}$ was actually not used in the code - the dimensionless electron heat conductivity $\chi_{\parallel e0}$ was used instead. Hence, the results in chapter 4 and the conclusions are correct only if $\chi_{\parallel i0} = \chi_{\parallel e0}$. For the reference case, this means $\chi_{\parallel i0} = \chi_{\parallel e0} = 26.6$ was used,† instead of what we thought was $\chi_{\parallel i0} = 1.15$ and $\chi_{\parallel e0} = 26.6$. The rest of the code and model is correct.

We have fixed the error, verified the code and rerun all the simulations. The main conclusion is that the dimensionless ion heat conductivity $\chi_{\parallel i0}$ plays as much of a role for the equilibrium ion temperature profile T_i as the electron heat conductivity $\chi_{\parallel e0}$ for the electron profile T_e. Further, with the correct heat conductivity $\chi_{\parallel i0} = 1.15$, T_i saturates faster - after $t \gtrsim 50\frac{R_0}{c_{s0}} \approx 0.9$ ms - while it was still not saturated at 1.5 ms with the wrong $\chi_{\parallel i0} = \chi_{\parallel e0} = 26.6$. The saturation time for the plasma density n and electron temperature T_e remain the same - $t \gtrsim 30\frac{R_0}{c_{s0}} \approx 0.5$ ms.

Figure 1, left, shows the saturated radial profiles for the reference simulation. We find that in comparison to the mistakenly used $\chi_{\parallel i0} = 26.6$, the proper, lower ion heat conductivity $\chi_{\parallel i0} = 1.15$ increases the stationary ion temperature gradient $\partial_r T_i$ in the confined region, leading to $T_i < T_e$ at the separatrix. The T_i profile and fluctuation level are now similar to those of the plasma density n. The T_e and n profiles remain unaffected. The stationary profile of the electrostatic potential ϕ flattens in the confined region due to the lower T_i, while it remains the same in the SOL following T_e. In the far SOL, $T_i > T_e$ is found due to electron sheath heat transmission - unlike in the case without this boundary condition ($\gamma_e = 0$). We note that the previously observed result, $T_i > T_e$ also at the separatrix, is recovered again at higher temperature, see double temperature case in Figure 1, right.

Other results of the original article [1] hold true, at least qualitatively. The GAM frequency spectrum, shown in Figure 2, is somewhat different quantitatively. With the lower ion heat conductivity $\chi_{\parallel i0}$, the ion temperature fluctuates more, but overall the turbulence is nonetheless enhanced with increasing density and suppressed with increasing temperature, see Figure 3. In cases 2 and 3 from chapter 4.1, we already had $\chi_{\parallel i0} = \chi_{\parallel e0}$ (and case 4 was actually nearly the same as the reference scenario), so the result holds that reducing $\chi_{\parallel i0}$ and $\chi_{\parallel e0}$ below 0.1 has no impact on outboard midplane profiles.

*$\chi_{\parallel i0}$ is obtained by normalizing the Braginskii ion parallel heat conductivity to $\chi_{\parallel}^{i} = \chi_{\parallel i0} n_0 c_{s0} R_0 \widehat{T}_i^{5/2}$, with $\widehat{T}_i = T_i / T_{i0}$.
†We have for deuterium $\chi_{\parallel i0}/\chi_{\parallel e0} = 23 \neq 35$ because the electron collision frequency was calculated with $Z_{\text{eff}} = 1.5$.

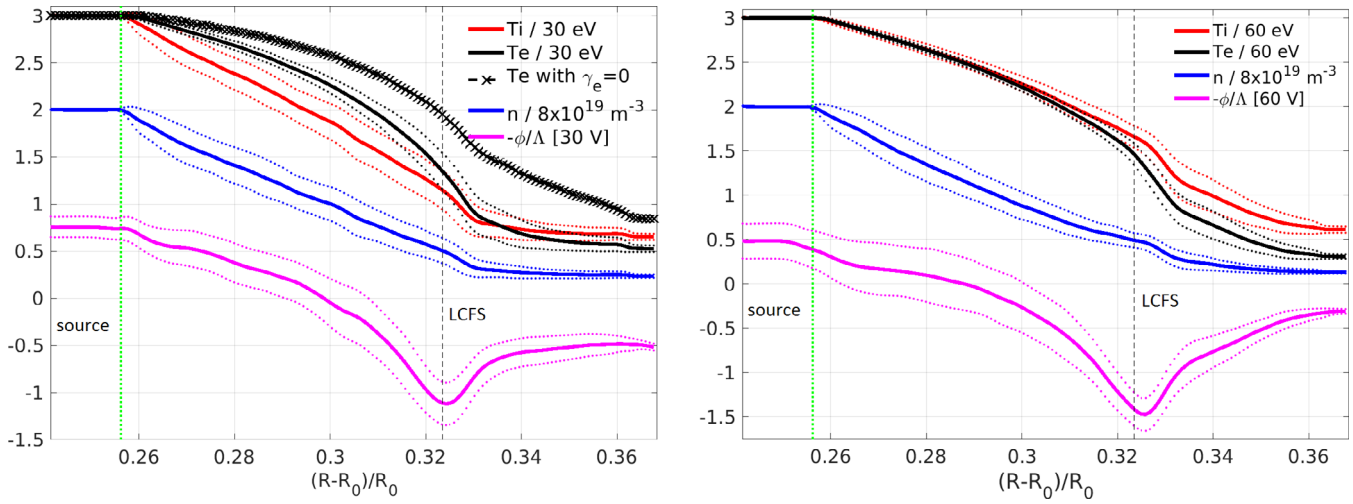

FIGURE 1 Mean radial profiles (T_i, T_e, n, $-\phi/\Lambda$) at the outboard mid-plane in saturated state. Dotted lines indicate the $\pm\sigma_f$ fluctuation level. The negative potential $-\phi$ and its fluctuation level are divided by $\Lambda = 2.69$. LCFS and source region are marked. Left: reference case with $T_e = T_i = 90$ eV at the core boundary, with additionally the T_e profile from the simulation with no sheath heat conduction (case 1 from chapter 4.1, $\gamma_e = 0$). Right: simulation with double the temperature

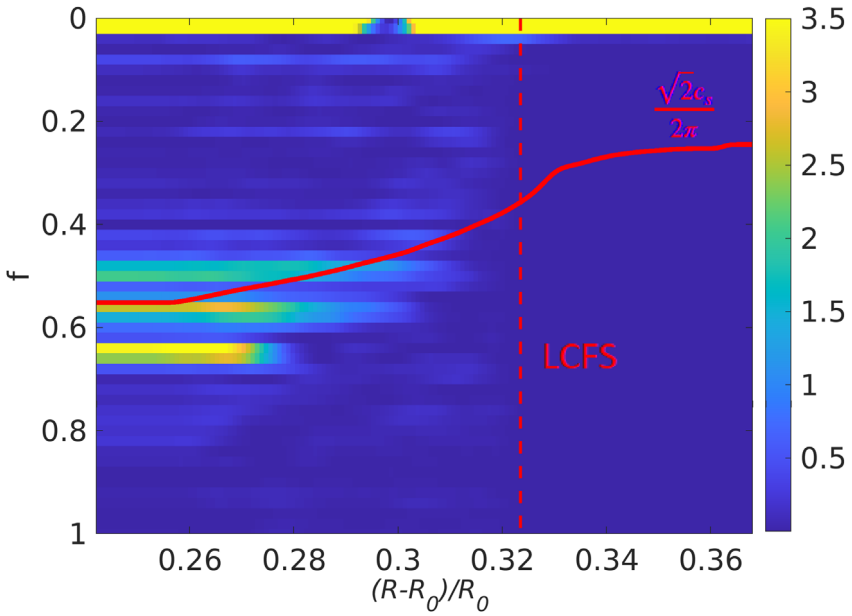

FIGURE 2 Frequency spectrum of poloidally and toroidally averaged electrostatic potential fluctuations

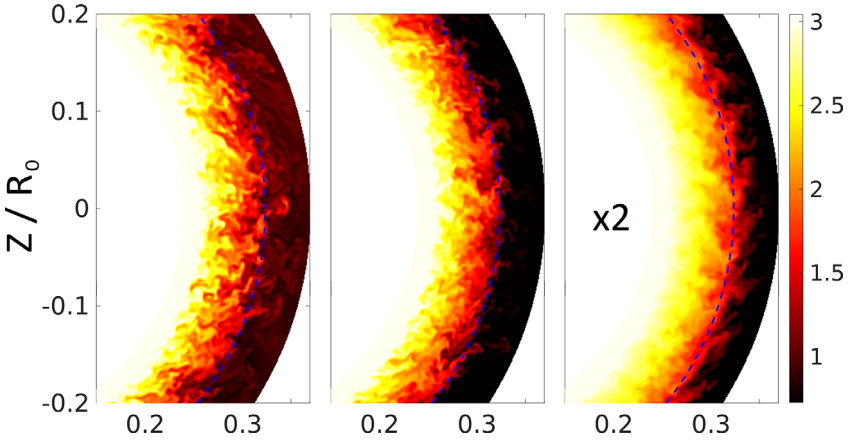

FIGURE 3 Outboard mid-plane ion temperature snapshot at 1.44 ms in: double density, reference, double temperature (left to right). Horizontal axis is $(R - R_0)/R_0$. LCFS marked by blue dashed line

We additionally remark that the Bohm sheath boundary conditions (7) for parallel velocity should contain T_i, $u_\parallel \gtrless \sqrt{T_e + T_i}$. Also, there is a mistake in the indexes in Equation (9): instead of $\nabla_\perp p^{i+j}$, it should read $\nabla_\perp p_i^{t+j}$.

ACKNOWLEDGMENTS

This work has been carried out within the framework of the EUROfusion Consortium and has received funding from the Euratom research and training programme 2014-2018 and 2019-2020 under grant agreement No 633053. The views and opinions expressed herein do not necessarily reflect those of the European Commission.

REFERENCE

[1] W. Zholobenko, A. Stegmeir, T. Body, A. Ross, P. Manz, O. Maj, D. Coster, F. Jenko, M. Francisquez, B. Zhu, B. N. Rogers, *Contributions to Plasma Physics* **2019**, e201900131. https://doi.org/10.1002/ctpp.201900131.

How to cite this article: Zholobenko W, Stegmeir A, Body T, et al. Corrigendum: Thermal dynamics in the flux-coordinate independent turbulence code **GRILLIX**. *Contributions to Plasma Physics*. 2020;60:e202000056. https://doi.org/10.1002/ctpp.202000056

A.3 Electric field and turbulence in global Braginskii simulations across the ASDEX Upgrade edge and scrape-off layer

COPYRIGHT

Wladimir Zholobenko, Thomas Body, Peter Manz, Andreas Stegmeir, Ben Zhu, Michael Griener, Garrard Conway, David Coster, Frank Jenko, the ASDEX Upgrade Team
Electric field and turbulence in global Braginskii simulations across the ASDEX Upgrade edge and scrape-off layer
2021 *Plasma Physics and Controlled Fusion* **63** 034001
DOI: https://doi.org/10.1088/1361-6587/abd97e

SUMMARY

Turbulence simulations in diverted geometry across the edge and scrape-off layer (SOL) of ASDEX Upgrade are performed with the GRILLIX code [107]. The underlying global (full-f) drift-reduced Braginskii model allows to concurrently study the self-consistent dynamics of the turbulence and the background as well as the evolution of toroidal and zonal flows. Different contributions to the radial electric field are identified. The dominant contribution on closed flux surfaces comes from the ion pressure gradient, due to the diamagnetic drift in the curved magnetic field. Large deviations can be induced, in particular, by the polarization particle flux, leading to zonal flows. The latter are driven by small-scale eddies, but do not exhibit much impact on the overall transport which is driven by ballooning modes at larger scales. Ion viscosity is found to be important in damping poloidal rotation through adjusting of the parallel velocity profile, but not via direct vorticity damping. The zonal flow drive peaks at the separatrix, where a strong shear layer forms due to the sheath-induced counter-propagating SOL flow, allowing for the formation of a transport barrier. The temperature profile across the separatrix is determined by the competition between cross-field transport and outflow in the SOL, the latter being largely controlled by the parallel heat conductivity.

INDIVIDUAL CONTRIBUTIONS

Leading role in realizing the scientific project.

Problem definition	*significantly contributed*
Literature survey	*significantly contributed*
Code implementation	*significantly contributed*
Carrying out the simulations	*significantly contributed*
Evaluation of the simulations	*significantly contributed*
Manuscript preparation	*significantly contributed*

Plasma Physics and Controlled Fusion

PAPER • **OPEN ACCESS**

Electric field and turbulence in global Braginskii simulations across the ASDEX Upgrade edge and scrape-off layer

To cite this article: W Zholobenko *et al* 2021 *Plasma Phys. Control. Fusion* **63** 034001

OPEN ACCESS
IOP Publishing
Plasma Physics and Controlled Fusion
Plasma Phys. Control. Fusion **63** (2021) 034001 (19pp)
https://doi.org/10.1088/1361-6587/abd97e

Electric field and turbulence in global Braginskii simulations across the ASDEX Upgrade edge and scrape-off layer

W Zholobenko[1], T Body[1], P Manz[1], A Stegmeir[1], B Zhu[2], M Griener[1], G D Conway[1], D Coster[1], F Jenko[1] and the ASDEX Upgrade Team[3]

[1] Max-Planck-Institut für Plasmaphysik, D-85748 Garching, Germany
[2] Lawrence Livermore National Laboratory, 7000 East Avenue, Livermore, CA 94550, United States of America

E-mail: Wladimir.Zholobenko@ipp.mpg.de

Received 30 September 2020, revised 3 December 2020
Accepted for publication 7 January 2021
Published 12 February 2021

Abstract

Turbulence simulations in diverted geometry across the edge and scrape-off layer (SOL) of ASDEX Upgrade are performed with the GRILLIX code (Stegmeir *et al* 2019 *Phys. Plasmas* **26** 052517). The underlying global (full-*f*) drift-reduced Braginskii model allows to concurrently study the self-consistent dynamics of the turbulence and the background as well as the evolution of toroidal and zonal flows. Different contributions to the radial electric field are identified. The dominant contribution on closed flux surfaces comes from the ion pressure gradient, due to the diamagnetic drift in the curved magnetic field. Large deviations can be induced, in particular, by the polarization particle flux, leading to zonal flows. The latter are driven by small-scale eddies, but do not exhibit much impact on the overall transport which is driven by ballooning modes at larger scales. Ion viscosity is found to be important in damping poloidal rotation through adjusting of the parallel velocity profile, but not via direct vorticity damping. The zonal flow drive peaks at the separatrix, where a strong shear layer forms due to the sheath-induced counter-propagating SOL flow, allowing for the formation of a transport barrier. The temperature profile across the separatrix is determined by the competition between cross-field transport and outflow in the SOL, the latter being largely controlled by the parallel heat conductivity.

Supplementary material for this article is available online

Keywords: turbulence simulations, electric field, zonal flows, Braginskii, ASDEX Upgrade, edge and scrape-off layer

(Some figures may appear in colour only in the online journal)

[3] See author list of Meyer H *et al* 2019 *Nucl. Fusion* **59** 112014

1. Introduction

The radial electric field and the resulting $E \times B$ flows are of central importance in determining magnetic confinement properties of tokamaks [1–3]. In the confined region, the electric field consists of mean-field (neoclassical) contributions as well as of zonal flows generated by the turbulence [4]. The latter result from the interaction of poloidal and radial fluctuations through the Reynolds stress [5], but can also be amplified by the anomalous Stringer drive [6, 7]. A review of zonal flow experiments can be found in [8]. In the scrape-off layer (SOL), on the other hand, in the absence of closed flux surfaces, the electric field is primarily determined by dynamics parallel to the magnetic field, and particularly by the sheath boundary conditions [9, 10]. The interface between closed and open field lines is of central interest. Different mechanisms act on the two sides of the separatrix, leading to electric fields of different signs. Therefore, the electric field changes abruptly across a narrow region and produces strongly sheared $E \times B$ flows [11]. This shearing is thought to act as a turbulence suppression mechanism [12, 13], playing a key role in the transition to improved confinement regimes.

To study the formation of the electric field and its back-reaction on turbulent transport, involving both mean and zonal flows, a global (full-f) turbulence model is required. While gyrokinetic models [14, 15] can be more realistic if collisions and electromagnetic effects are taken into account, fluid models are attractive due to their significantly lower computational cost. In the present work, we present theoretical and computational results based on the global version of the drift-reduced Braginskii two-fluid model [16, 17], which is widely used for both direct turbulence simulations [18–21] and simplified transport studies [22, 23]. Although restricted (strictly speaking) in its validity to sufficiently collisional regimes, important insights can be gained. More refined studies may become possible in the future with the help of gyrofluid models employing appropriate closure schemes [24, 25], with full-f formulations currently still under development [26]. The study of the tokamak edge is further complicated by the relatively complex magnetic geometry. As diverted geometry is beneficial for confinement [27–29] and impurity exhaust [30], theoretical and computational studies must adapt to that geometry. A computationally feasible implementation is achieved through the flux-coordinate independent (FCI) approach [31, 32], implemented in the code GRILLIX [33].

In the present study, we report on the first global turbulence simulations in diverted geometry across the edge and SOL of ASDEX Upgrade (AUG), based on the L-mode discharge #36190. The results illuminate many aspects of tokamak edge physics, such as high and intermittent fluctuation levels, up to 10% at the separatrix and of order unity in the SOL. Turbulent vortices in the confined region develop a mean poloidal rotation in the electron diamagnetic drift direction, as the radial electric field balances the ion pressure gradient. Due to the sheath at the divertor, the flow is in the ion diamagnetic drift direction in the SOL. A shear layer develops at the separatrix in which vortices are strained out and decorrelated. Zonal flows are driven by drift waves and damped by the geodesic acoustic mode (GAM). However, this barely affects the ballooning driven transport. Ion viscosity is found to be important for damping poloidal rotation. The competition between perpendicular and parallel transport leads to the formation of a temperature pedestal due to the high parallel heat conduction. Nevertheless, we note that the validity of our fluid model might be yet restricted due to the low collisionality in the plasma edge, and lack of neutral gas recycling and impurities in the SOL.

The remainder of the manuscript is organized as follows. In section 2 we illustrate the key components of the model that lead to the formation of the multi-scale electric field (the full set of equations is detailed in appendix A). Section 3 describes the performed AUG simulations: the setup, saturation, input power, equilibrium profiles, and fluctuation levels. The electric field is presented and analysed in section 4, with its determining contributions and its impact on the turbulence. A separate discussion on the role of fluid closure terms – ion viscosity and heat conductivities – is presented in section 5. Finally, conclusions and an outlook are given in section 6.

2. The electric field in drift-reduced Braginskii models

The radial electric field E_r in a tokamak is commonly explained by the radial force balance. It is derived from the Braginskii ion momentum conservation equation [16] by neglecting inertia, viscosity and friction (electron momentum is assumed to be small in this regard). This yields in the SI unit system

$$E_r = \frac{\partial_r p_\mathrm{i}}{en} - (\mathbf{v} \times \mathbf{B}) \cdot \mathbf{e}_r = \frac{\partial_r p_\mathrm{i}}{en} + v_\phi B_\theta - v_\theta B_\phi, \qquad (1)$$

where $\partial_r p_\mathrm{i}$ is the radial component of the ion pressure gradient, n the plasma density, e the elementary charge and $\mathbf{B}$ the magnetic field. The fluid velocity $\mathbf{v}$ with its poloidal (v_θ) and toroidal (v_ϕ) component is in this expression yet undetermined, but depends implicitly on the electric field and other parameters in a non-trivial way. Therefore, this force balance equation is illustrative, but insufficient to actually determine the electric field. To do that we require additionally at least the ion particle balance equation, and further charge and momentum balance equations.

Following the drift reduction procedure we assume that the dynamics of interest is slow compared to the gyromotion, $\omega \ll \Omega_\mathrm{i} = eB/(M_\mathrm{i} c)$. Applying an ordering expansion to the perpendicular momentum balance, plasma motion can be expressed via perpendicular drift velocities and parallel streaming $u_\parallel$ along magnetic field lines. For ions, this reads

$$\mathbf{v}^\mathrm{i} = \mathbf{v}_E + \mathbf{v}^\mathrm{i}_* + \mathbf{u}_\mathrm{pol} + u_\parallel \mathbf{b}, \qquad (2)$$

where $\mathbf{b} = \mathbf{B}/B$ is the unit vector of the magnetic field. The perpendicular drifts are to leading order the $E \times B$ velocity $\mathbf{v}_E = \mathbf{E} \times \mathbf{B}/B^2$ and the diamagnetic velocity $\mathbf{v}^\mathrm{i}_* = \mathbf{B} \times \nabla p_i/(enB^2)$, i.e. the inverse of (1) in terms of $\mathbf{v}$. The

polarisation velocity $\mathbf{u}_{\text{pol}}$ includes the first order correction effects in the radial force balance which have been neglected in equation (1), namely inertia and viscosity. It is responsible for the emergence of turbulence in our model, as detailed in section 2.2. The obtained expression for the ion velocity (2) is inserted into the ion continuity equation yielding

$$\frac{\partial n}{\partial t} + \nabla \cdot n\left(\mathbf{v}_E + \mathbf{v}_*^{\text{i}} + \mathbf{u}_{\text{pol}} + u_\parallel \mathbf{b}\right) = S_n, \tag{3}$$

with S_n a source term.

The diamagnetic particle flux can be rewritten as

$$\begin{aligned} n\mathbf{v}_*^{\text{i}} &= -\nabla \times \left(\frac{p_{\text{i}}}{eB^2}\mathbf{B}\right) + \frac{p_{\text{i}}}{e}\nabla \times \frac{\mathbf{B}}{B^2} \\ &\approx -\nabla \times \left(\frac{p_{\text{i}}}{eB^2}\mathbf{B}\right) + \frac{2p_{\text{i}}}{eB^3}\mathbf{B} \times \nabla B, \end{aligned} \tag{4}$$

which due to $\nabla \cdot \nabla \times \mathbf{A} = 0$ shows that it is 'nearly divergence-free' [9, chapter 18.7], in the sense that its divergence is non-zero only in a curved magnetic field. The last equality requires $\nabla \times \mathbf{B} \ll \mathbf{b} \times \nabla B$.

It is convenient to introduce here the curvature operator

$$C(f) = -\nabla \cdot \left(\frac{\mathbf{B}}{B^2} \times \nabla f\right) = -\left(\nabla \times \frac{\mathbf{B}}{B^2}\right) \cdot \nabla f, \tag{5}$$

which represents advection of a field f along the magnetic field curvature[4]. It allows us to write

$$\nabla \cdot (n\mathbf{v}_E) = \mathbf{v}_E \cdot \nabla n - nC(\varphi), \tag{6}$$

$$\nabla \cdot (n\mathbf{v}_*^{\text{i}}) = -\frac{1}{e}C(p_{\text{i}}), \tag{7}$$

where we express the electric field component orthogonal to the magnetic field via the electrostatic potential $\mathbf{E}_\perp = -\nabla_\perp \varphi$, neglecting electromagnetic effects in the drift plane. We notice that due to the diamagnetic particle flux being 'nearly divergence-free', it does not cause any advection, an effect known as 'diamagnetic cancellation'. The pressure gradient enters only through magnetic curvature.

In quasi-steady state $\left\langle \frac{\partial n}{\partial t} \right\rangle = 0$, the ion particle balance equation (3) for the background profiles becomes

$$\left\langle \mathbf{v}_E \cdot \nabla n - nC(\varphi) - \frac{1}{e}C(p_{\text{i}}) + \nabla \cdot (n\mathbf{u}_{\text{pol}}) + \nabla \cdot (nu_\parallel \mathbf{b}) - S_n \right\rangle = 0, \tag{8}$$

where the brackets $\langle \ldots \rangle$ denote a suitable ensemble average, either in time, in space, or both. This equilibrium particle balance is central in determining the electric field on closed field lines.

It is sufficient to consider only the ion continuity equation as the electron particle balance is tied to it by the quasi-neutrality condition $e\partial_t(n_{\text{e}} - n_{\text{i}}) = \nabla \cdot \mathbf{j} = 0$. We illustrate results using the ion particle balance, but it is equivalent and in fact numerically advantageous to solve the electron continuity (A1) and the quasi-neutrality (A2) equations instead, see also section 2.2 and appendix A. However, this approach constrains our model to a single ion species – for a drift-reduced multi-species model see e.g. [35].

2.1. The equilibrium (static) electric field on closed flux surfaces

In the confined region, to lowest order, we can assume $\langle \mathbf{v}_E \cdot \nabla n \rangle = 0$ since for the background we have only a radial density gradient and no radial $E \times B$ advection. For now, let us also neglect any flows, i.e. $\left\langle \nabla \cdot n(\mathbf{u}_{\text{pol}} + u_\parallel \mathbf{b}) \right\rangle = 0$. In absence of stationary sources S_n, the balance for the stationary fields becomes

$$n\nabla \cdot (\mathbf{v}_E) + \nabla \cdot (n\mathbf{v}_*^{\text{i}}) = -nC(\varphi) - C(p_{\text{i}})/e = 0. \tag{9}$$

As there are no background poloidal gradients along closed flux surfaces, $\partial_\theta f \approx 0$, the balance is fulfilled by the static equilibrium radial electric field

$$E_r = \frac{\partial_r p_{\text{i}}}{en}. \tag{10}$$

We expect the dominant contribution to the radial electric field on closed flux surfaces to be this balance between $E \times B$ and diamagnetic compression of ion density along the curved magnetic field [1, 2]. Corrections, especially in L-mode, can be significant though – see section 4.1. It is worth pointing out that under this equilibrium electric field, the background plasma is at rest (i.e. static), but fluctuations are $E \times B$ advected. Deviations from equation (9), on the other hand, also impact the background.

2.2. Anomalous electric field

Besides the lowest order equilibrium electric field (10), additional contributions arise from polarisation and parallel particle fluxes contained in equation (8). Obtaining closed form analytical expressions for their stationary contributions is not possible. In this section we discuss the form and role of the ion polarisation velocity and viscosity, while numerical simulation results will be presented in section 4.

As noted at equation (2), the polarisation velocity is the correction to the perpendicular ion velocity which contains inertia and viscosity. However, the latter depend themselves on

[4] Alternatively, one could replace the diamagnetic velocity by $\tilde{\mathbf{v}}_*^{\text{i}} = \frac{2T_{\text{i}}}{eB^3}\mathbf{B} \times \nabla B$ for a flux conservative formulation [18, 34].

the perpendicular ion velocity in a non-trivial way. Therefore, in reduced fluid models, the polarisation velocity is approximated to first order by inserting the zero order approximation $\mathbf{v}^{\mathrm{i}}_{\perp 0} = \mathbf{v}_E + \mathbf{v}^{\mathrm{i}}_*$ into inertia and viscous stress. Since the divergence of the zeroth order velocities is of the same order as the divergence of the polarisation velocity, $\nabla\cdot(n\mathbf{u}_{\mathrm{pol}}) \sim \nabla\cdot\left(n\mathbf{v}^{\mathrm{i}}_{\perp 0}\right)$, it has to be retained for divergence terms [36, 37]. Explicitly, the expression reads

$$\nabla\cdot(n\mathbf{u}_{\mathrm{pol}}) = \nabla\cdot\left[-\frac{nM_{\mathrm{i}}}{eB^2}\left(\frac{\partial}{\partial t} + \mathbf{v}_E\cdot\nabla + u_{\parallel}\nabla_{\parallel}\right) \times \left(\nabla_{\perp}\varphi + \frac{\nabla_{\perp}p_{\mathrm{i}}}{en}\right)\right] - \frac{1}{6e}C(G), \tag{11}$$

where the first term on the right hand side represents inertia, and the second viscosity. We can also write

$$\nabla\cdot(n\mathbf{u}_{\mathrm{pol}}) = \nabla\cdot\left(n\mathbf{u}^{\mathrm{in}}_{\mathrm{pol}}\right) - \frac{1}{6e}C(G). \tag{12}$$

The viscous stress function [38] is

$$G = -\eta^{\mathrm{i}}_0\left[\frac{2}{B^{3/2}}\nabla\cdot\left(u_{\parallel}B^{3/2}\mathbf{b}\right) - \frac{1}{2}\left(C(\varphi) + \frac{1}{en}C(p_{\mathrm{i}})\right)\right], \tag{13}$$

with the dominant Braginskii viscosity coefficient $\eta^{\mathrm{i}}_0 = 0.96 p_{\mathrm{i}}\tau_{\mathrm{i}}$ and ion collision time τ_{i}.

Due to the time derivative in the inertial part, the direct implementation of the ion continuity equation is cumbersome. Instead, in drift-reduced Braginskii codes like GRILLIX, the electron continuity equation is used – where the polarisation velocity can be neglected due to the small electron mass – together with the quasi-neutrality, or vorticity, equation $e\partial_t(n_{\mathrm{e}} - n_{\mathrm{i}}) = \nabla\cdot\mathbf{j} = 0$. The latter reads

$$e\nabla\cdot(n\mathbf{u}_{\mathrm{pol}}) = C(p_{\mathrm{e}} + p_{\mathrm{i}}) - \nabla\cdot(j_{\parallel}\mathbf{b}), \tag{14}$$

with the parallel current $j_{\parallel} = en(u_{\parallel} - v_{\parallel})$ and parallel electron velocity $v_{\parallel}$. If the right hand side of (14) balances, i.e. the diamagnetic charge separation is balanced by a parallel current, we obtain the Pfirsch–Schlüter current [39, chapter 8.4]. However, we will see in section 4 that the divergence of the polarisation flux is not necessarily small.

Equation (14) is typically called vorticity equation because under some (too) strong approximations, regarding the size of density fluctuations and homogeneity of the magnetic field, one can rewrite

$$\nabla\cdot\left[\frac{n}{B^2}\frac{\mathrm{d}}{\mathrm{d}t}\left(\nabla_{\perp}\varphi + \frac{\nabla_{\perp}p_{\mathrm{i}}}{en}\right)\right] \sim \frac{n_0}{B}\frac{\mathrm{d}}{\mathrm{d}t}\mathbf{b}\cdot\nabla\times\left(\mathbf{v}_E + \mathbf{v}^{\mathrm{i}}_*\right). \tag{15}$$

The quantity on the right hand side is the 2D fluid vorticity $\Omega_{\mathrm{F}} = \mathbf{b}\cdot\nabla\times\left(\mathbf{v}_E + \mathbf{v}^{\mathrm{i}}_*\right)$, not to be confused with the generalised vorticity defined in appendix A. Note that while the diamagnetic velocity is 'nearly divergence-free', it is not rotation-free.

The inertial part of the vorticity equation is central to fluid plasma turbulence models, particularly the non-linearity $\mathbf{v}_E\cdot\nabla\mathbf{E}_{\perp}$, as it is ultimately responsible for the turbulent inverse energy cascade [40]. This term also contains the Reynolds stress, responsible for zonal flow drive [5]. We note that a rigorous decomposition into mean field and fluctuating flows in a global model is quite complex, e.g. one requires the Favre instead of the Reynolds average [41]. Further, a second Reynolds stress term contained in $u_{\parallel}\nabla_{\parallel}\nabla_{\perp}\varphi$ couples 2D turbulence to parallel dynamics [42]. This decomposition will not be further detailed here. In the steady-state, we must have $\left\langle\partial_t\left(\nabla_{\perp}\varphi + \frac{\nabla_{\perp}p_{\mathrm{i}}}{en}\right)\right\rangle = 0$. Therefore, we will use $\left\langle\nabla\cdot\left(n\mathbf{u}^{\mathrm{in}}_{\mathrm{pol}}\right)\right\rangle$ as a measure of the stationary Reynolds stress.

2.3. The role of ion viscosity and poloidal rotation

In this section we summarize some key insights from neoclassical theory [39] for the confined plasma. The main difference to our model is that inertia, and hence the polarisation velocity $\mathbf{u}_{\mathrm{pol}}$ from the previous chapter, is neglected. In this case it is then a good assumption that pressure and electrostatic potential are constant along closed flux surfaces ψ. With $\partial_r f = RB_p\partial_{\psi}f$, one obtains the relation [39, chapter 8.5]

$$E_r = \frac{1}{en}\frac{\partial p_{\mathrm{i}}}{\partial r} + u_{\parallel}B_{\theta}\frac{B}{B_{\phi}} - v_{\theta}\frac{B^2}{B_{\phi}}. \tag{16}$$

v_{θ} is the flux surface averaged poloidal rotation. An important result is then that according to the Braginskii fluid closure, poloidal rotation is damped to zero due to the ion viscosity [39, chapter 12.3]. The reason is that in a flux surface average over the parallel momentum equation (A3), one finds the condition

$$\langle\mathbf{B}\cdot\nabla\cdot\Pi_{\mathrm{i}}\rangle_S = 3\eta^{\mathrm{i}}_0\left\langle\left(\nabla_{\parallel}B\right)^2\right\rangle_S v_{\theta} = 0. \tag{17}$$

Π_{i} is thereby the Braginskii ion viscous stress tensor. We will write this with the viscous stress function G defined above in equation (13),

$$\mathbf{B}\cdot\nabla\cdot\Pi_{\mathrm{i}} = \frac{2}{3}B^{5/2}\nabla_{\parallel}\frac{G}{B^{3/2}}. \tag{18}$$

The situation is more complicated, however, when turbulent transport is considered (i.e. $\mathbf{u}_{\mathrm{pol}}$) – see also [39, chapter 13.1] – as will be detailed in section 4.1 on the basis of numerical simulations. Note, as the viscous stress function G appears in Braginskii's ion temperature equation (A6), this flow damping acts as a heating mechanism for ions known as 'magnetic pumping'.

2.4. The (simple) SOL electric field

In the SOL, due to the absence of closed flux surfaces, parallel dynamics and boundary conditions take a more important role [9, 10]. The electrostatic Ohm's law – used here for simplicity, although our full model is electromagnetic, see appendix A – reads

$$\eta_{\parallel}j_{\parallel} = -\nabla_{\parallel}\varphi + \frac{\nabla_{\parallel}p_{\mathrm{e}}}{en} + \frac{0.71}{e}\nabla_{\parallel}T_{\mathrm{e}}, \tag{19}$$

with resistivity $\eta_\parallel$. We have insulating sheath boundary conditions $j_\parallel = 0$ at the divertor. And in present simulations, without any neutral particles or impurities, there are no significant sources or sinks for any terms in the above equation. This results in flat parallel gradients (in an average over turbulent fluctuations). Therefore, T_e is roughly equal at the outboard mid-plane and at the divertor, and resistivity is negligibly small. At the divertor, the insulating sheath boundary condition

$$\varphi = \Lambda T_\mathrm{e} \tag{20}$$

for the potential applies, with $\Lambda = -\frac{1}{2}\ln\left[\left(2\pi\frac{m_\mathrm{e}}{M_\mathrm{i}}\right)\left(1+\frac{T_\mathrm{i}}{T_\mathrm{e}}\right)\right] \approx 2.69$. Hence, due to $\nabla_\parallel\varphi \approx 0$, we expect $\varphi = \Lambda T_\mathrm{e}$ to also hold at the outboard mid-plane. Having $E_r \sim \partial_r p_\mathrm{i}/en$ in the confined region (10) and $E_r \sim -\Lambda\partial_r T_\mathrm{e}$ in the SOL, we expect a jump of the electric field across the separatrix, and contra-rotating poloidal flows inside and outside of it [11].

It should be noted that in reality, contrary to our yet simplified model, the presence of neutral gas and impurities in the SOL leads to more complex parallel gradients, even in attached conditions. Furthermore, the sheath can conduct significant currents. Therefore, the SOL dynamics itself can be much more involved, particularly in detached plasmas [43].

3. AUG simulations

It is not possible to solve analytically the full set of equations detailed in appendix A, and particularly the non-linear polarisation discussed in section 2.2. Therefore, we employ the code GRILLIX [33]. For the first time, global numerical simulations are performed in a diverted magnetic equilibrium and at experimental parameters based on an AUG discharge (#36190), without any down-scaling. The setup is presented in section 3.1 and results are summarized in subsequent sections. The reference simulation can be seen in supplementary movie 1 (available online at (stacks.iop.org/PPCF/63/034001/mmedia)). It shows the initial evolution of plasma density within the poloidal plane, as well as outboard mid-plane pressure and radial electric field profiles. Further, supplementary movie 2 shows the dynamics of density fluctuations relative to the background, in the saturated state of the simulation with increased poloidal resolution (see text below).

We note that these simulations are very computationally demanding, consuming each between 0.4–2 MCPUh and 2–5 months of run time, as described in the next section.

3.1. The simulation setup

This section details the setup of the simulations – namely geometry, parameters, initial state, resolution and computational cost – guided by the AUG discharge #36190 at time $t = 2$–4 s. In this discharge the toroidal magnetic field was $B_\mathrm{tor} = -2.5$ T, i.e. in favourable configuration with $\mathbf{B}\times\nabla B \sim -\hat{\mathbf{e}}_Z$ towards

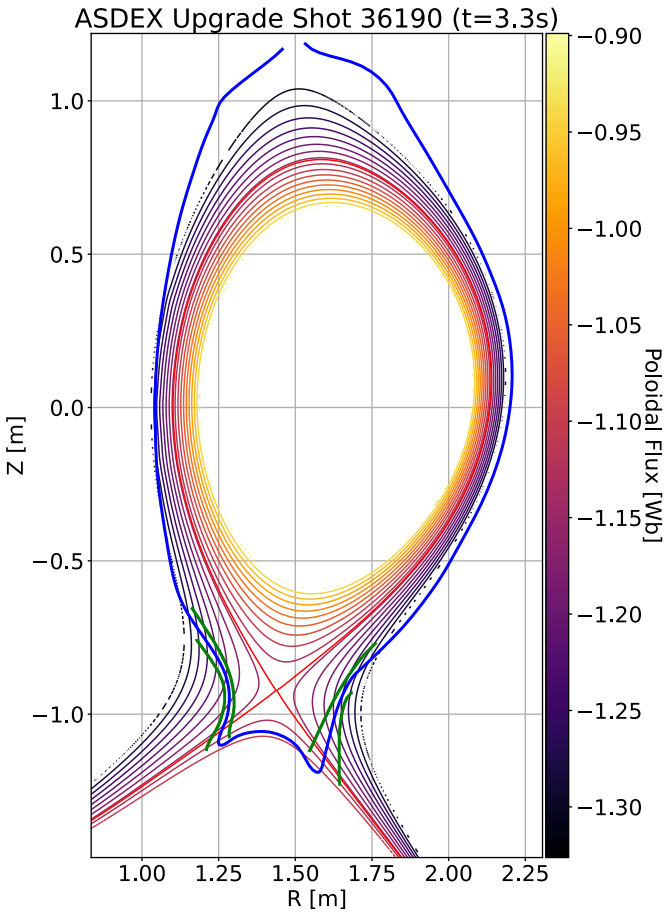

Figure 1. Flux surfaces of the equilibrium used for the simulation. The red line marks the separatrix. The blue line gives the first wall and divertor. The simulation domain extends beyond the divertor legs due to the implementation of parallel boundary conditions via penalisation [33], with the penalisation transition area bounded by the two green lines.

the X-point. The plasma current was $I_p = 0.8$ MA[5] resulting in $q_{95} = 4.4$, and the average triangularity was $\delta = 0.21$. Further important inputs are the measured $T_\mathrm{e} \approx 350$ eV and $n_\mathrm{e} \approx 2\times10^{19}$ m^{-3} at $\rho_\mathrm{pol} = 0.9$, and $T_\mathrm{e} \approx 50$–80 eV and $n_\mathrm{e} \approx 1\times10^{19}$ m^{-3} at the separatrix. The total heating power in the discharge was roughly 800 kW: 550 kW neutral beam injection, 500 kW ohmic heating and subtracting 250 kW radiation losses.

The geometry is illustrated in figure 1 by the poloidal flux function Ψ. The separatrix and machine walls are highlighted. The simulation domain extends beyond the divertor legs due to the implementation of parallel boundary conditions via penalisation [33]. We define the normalized poloidal flux radius as

[5] One difference between experiment and simulation is the choice of the helicity of the poloidal magnetic field: in the experiment, the plasma current flows in the opposite direction to the toroidal magnetic field, while we chose them to be parallel in most of our simulations, i.e. the poloidal magnetic field rotates in the opposite direction. However, we have repeated the reference simulation (defined below) with the correct helicity and found no physical difference except the direction of toroidal rotation – within a poloidal plane, nothing changes at all.

$\rho_{\text{pol}} = \sqrt{\frac{\Psi-\Psi_0}{\Psi_X-\Psi_0}}$, with Ψ_0 and Ψ_X the poloidal magnetic flux at magnetic axis and separatrix, respectively. Simulations are performed for $\rho_{\text{pol}} > 0.9$, since our fluid model is not valid in the plasma core, and the reduced domain saves computational cost. The outer most flux surface is chosen at the location where the HFS main chamber wall acts as a plasma limiter, at $\rho_{\text{pol}} = 1.05$.

Our choice of reference values is guided by parameters and measurements in AUG discharge #36190: major radius $R_0 = 1.65$ m, magnetic field on axis $B_0 = 2.5$ T, density $n_0 = 10^{19}$ m^{-3}, electron and ion temperatures $T_{\text{e}0} = T_{\text{i}0} = 100$ eV, $Z_{\text{eff}} = 1.3$ and deuterium ion mass $M_{\text{i}} = 2m_{\text{p}}$. We note that in a global model, reference density and temperature are only required for the normalization of the equations, to write them in dimensionless form as in appendix A, and have no physical relevance. They are chosen only on the order of measured separatrix values, since their exact choice does not matter. Z_{eff} is considered only in the calculation of the electron collision frequency. The resulting dimensionless collisionless parameters of the system – see appendix A for their definition – are $\delta = 2854.2$, $\beta_0 = 3.227 \times 10^{-5}$, $\mu = 2.723 \times 10^{-4}$ and $\zeta = 1$. The collisional parameters are $\nu_{\text{e}0} = 12.30$, $\eta_{\|0} = 0.0017$, $\chi_{\|\text{e}0} = 940$, $\chi_{\|\text{i}0} = 35.35$ and $\eta_{\text{i}0} = 8.70$. The Braginskii heat conductivity is known to be inappropriate at low collisionality [22, 44, 45]. For instance, it becomes arbitrarily large as $\sim T^{5/2}$ due to the lack of kinetic flux limiting effects, such as Landau damping. In this work, we use a simple flux limiter which reduces the stiffness and therefore computational expense of the parallel heat conduction: $\chi_{\|\text{e,i}0} T_{\text{e,i}}^{5/2} \leqslant 940$. For the chosen reference values, we obtain as reference drift scale and ion Larmor radius

$$\rho_{s0} = \frac{\sqrt{M_{\text{i}} T_{\text{e}0}}}{eB_0} = \rho_{\text{i}0} = \frac{\sqrt{M_{\text{i}} T_{\text{i}0}}}{eB_0} = 0.578\,\text{mm}. \tag{21}$$

Note that the local Larmor radius varies with magnetic field and temperature. E.g. at reference temperature, it is larger by 25% at the outboard mid-plane due to the reduced local magnetic field of $B \approx 2$ T.

In diverted geometry and in absence of neutral gas ionization, we find that density can drop arbitrarily low in the far SOL and private flux region. This contradicts the experimental observation that density can even rise in the far SOL [46], i.e. the simulations are missing the necessary mechanism, e.g. neutral gas ionization. It also makes the solution of the equations unnecessarily expensive, since in particular the parabolic part becomes very stiff at low collisionality. As a simple solution we apply an adaptive source to keep the density above 3×10^{17} m^{-3}, and temperatures above 3 eV. This source does not hinder cross-field inflow but limits parallel outflow in the far SOL, starting to act above $\rho_{\text{pol}} = 1.02$ in the reference simulation, but e.g. only above $\rho_{\text{pol}} = 1.04$ in the simulation in section 5.2. For simplicity, respectively, due to the unphysical core boundary at $\rho_{\text{pol}} = 0.9$, simulations are adaptively flux driven: the heat and particle sources at the core boundary are adapted in time such as to hold density and temperature fixed there – while in the rest of the domain they evolve freely.

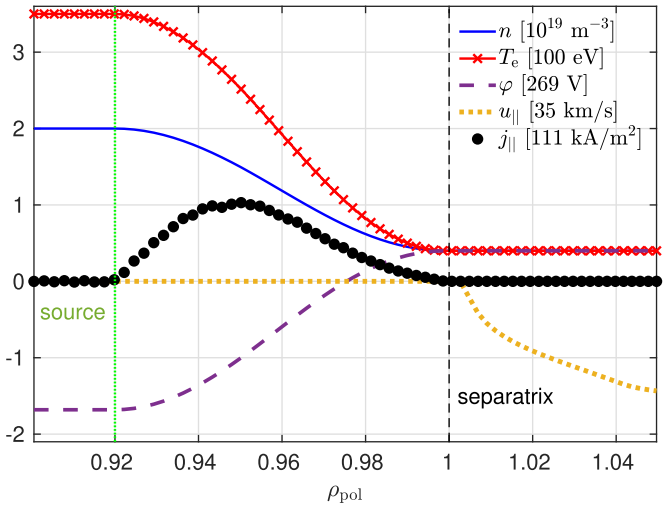

Figure 2. Initial normalized outboard mid-plane ($Z = 0$) profiles in the reference simulation.

In a global code, background profiles are not chosen but rather evolve freely in accordance with turbulent fluxes. Nonetheless, an initial state must be chosen for the simulation. The most trivial choice would be a flat, or even zero, background profile – which then evolves due to sources at the core boundary. However, in our experience the saturated state is reached faster the closer the initial state is to the final. We choose as initial state for density and temperatures the simple profile as function of ρ_{pol}

$$f(\rho) = \begin{cases} f_{\text{ped}} & \text{for: } \rho < \rho_{\text{ped}}, \\ -A\sin(a\cdot\rho + b) + B & \text{for: } \rho_{\text{ped}} \leqslant \rho \leqslant \rho_{\text{sep}}, \\ f_{\text{sep}} & \text{for: } \rho_{\text{sep}} < \rho, \end{cases} \tag{22}$$

with

$$A = \frac{f_{\text{ped}} - f_{\text{sep}}}{2}, \qquad B = f_{\text{ped}} - A,$$
$$a = \frac{\pi}{\rho_{\text{sep}} - \rho_{\text{ped}}}, \qquad b = -\frac{\pi}{2}\frac{\rho_{\text{sep}} + \rho_{\text{ped}}}{\rho_{\text{sep}} - \rho_{\text{ped}}}.$$

In present simulations, we chose $\rho_{\text{ped}} = 0.92$ and $\rho_{\text{sep}} = 0.999$. The value f_{ped} is held constant between $\rho = 0.9$ and $\rho = 0.92$ by an adaptive source. In the SOL, the initial profile is flat and equal to f_{sep}.

The core boundary, respectively, pedestal top values are chosen in accordance to the experiment as $n_{\text{ped}} = 2 \times 10^{19}$ m^{-3} and $T_{\text{ped}}^{\text{e,i}} = 350$ eV. The separatrix and SOL initial values are less relevant because they adapt in the course of the simulation. An important restriction comes from the choice of flat SOL profiles: simulations saturate faster with f_{sep} as low as possible, since it also initialises lower far SOL values. On the other hand, ideal ballooning stability of the initial profiles prohibits large radial gradients in the confined region, which is correlated with the Greenwald density limit [47]. Our choice for the reference case is $n_{\text{sep}} = 4 \times 10^{18}$ m^{-3}, $T_{\text{sep}}^{\text{e}} = 40$ eV and $T_{\text{sep}}^{\text{i}} = 50$ eV. In the confined region, electrostatic potential and current are chosen such that the

initial pressure profile is stable: $\partial_r\varphi = -\partial_r p_\mathrm{i}/(en)$ according to (10), resulting in $\mathbf{u}_\mathrm{pol} = G = \Omega = 0$ (no vorticity and polarisation velocity), and $\nabla\cdot(j_\parallel\mathbf{b}) = eC(p_\mathrm{e}+p_\mathrm{i})$ according to (14). The parallel velocity is chosen as zero. In the SOL, the initial state is chosen such that it fulfils the Bohm boundary conditions (A10). Particularly, the parallel velocity is $u_\parallel = \pm\sqrt{(T_\mathrm{e}+T_\mathrm{i})/M_\mathrm{i}}$ at each divertor plate, with a linear dependence on distance between the plates. The initial outboard mid-plane profiles are illustrated in figure 2. To trigger an instability and consequent turbulence, random noise of magnitude 10^{-5} is added to the density and temperature profiles.

For the reference simulation, we choose as poloidal resolution $h_f = 2.5\rho_{s0} = 1.45$ mm. Toroidally, we resolve 16 planes. The time step is chosen slightly below the stability limit as $\Delta t = 5\times10^{-5}R_0/c_{s0} = 1.2$ ns. Due to the limited resolution, the turbulent spectrum must be cut at the poloidal grid scale. To this end, third order hyperviscosity is applied as detailed in appendix A, with $\nu_\perp = 3350$ for all fields. Being able to resolve even smaller scales is highly desirable, particularly in a global code. Eventually, our choice of resolution is a compromise, restricted by the allowable computational expense. Nevertheless, we also performed convergence tests with $h_f = 1.67\rho_{s0}$, and a separate test with 24 planes at $2.5\rho_{s0}$. For the $1.67\rho_{s0}$ simulation, hyperviscosity was reduced to 300. For the 24 planes simulation, the timestep had to be reduced to 0.7 ns.

It is worth mentioning the computational cost of these simulations, and how it scales. The reference case with $2.5\rho_{s0}$ poloidal resolution and 16 toroidal planes ($\sim$7 million points) required for simulating 1 ms of the discharge 9 days on 384 processor cores (8 nodes) of the Marconi-A3 SKL partition. As we find saturation only after $t \gtrsim 5$ ms, at least roughly 0.4 MCPUh and 2 months of patience were required per simulation. Increasing poloidal resolution to $1.67\rho_{s0}$ raised both the number of grid points and the cost and duration of the simulation by a factor of 2. Increasing toroidal resolution raises the cost quadratically with the number of planes as the maximum allowed timestep is inversly proportional to toroidal resolution, i.e. 24 instead of 16 poloidal planes roughly doubles the cost.

We find no large differences in heat transport with increasing resolution, suggesting that it is mostly captured by the reference case. In detail, however, ion heat transport slightly increases with toroidal resolution, and zonal flows increase with poloidal resolution, as detailed in sections 3.2 and 4, respectively.

3.2. *Input power and saturation*

In current simulations, fixed density and temperature are prescribed at an artificial core boundary at $\rho_\mathrm{pol} = 0.9$ – held constant by an adaptive heat and particle source. In figure 3 we show how the input power $\langle P_\mathrm{e,i}\rangle_V = 3/2\left\langle T_\mathrm{e,i}S_n + nS_{T_\mathrm{e,i}}\right\rangle_V$ for the reference simulation varies in time – with particle and temperature sources S_n and $S_{T_\mathrm{e,i}}$ averaged over the whole volume. In the same plot, we show the globally averaged electrostatic potential oscillations (in units of 25 V) – this is due to the GAM, which is always present in global edge

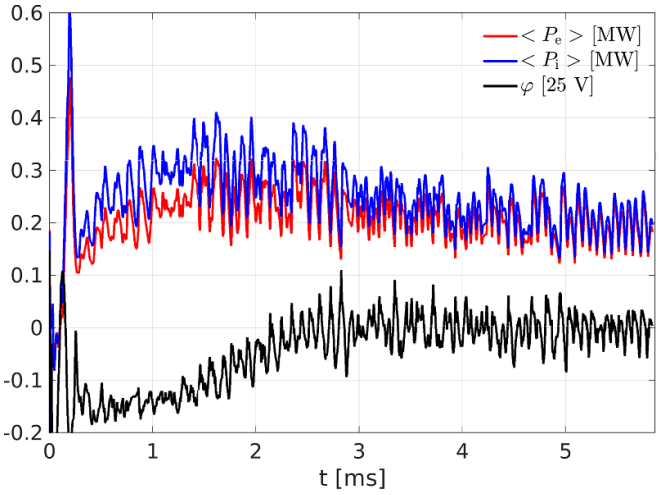

Figure 3. Total electron and ion heating power input in the simulation as a function of time. The globally averaged potential in units of 25 V is also shown. The input power oscillates following the GAM. At later times, it saturates at 196 kW for electrons and 236 kW for ions.

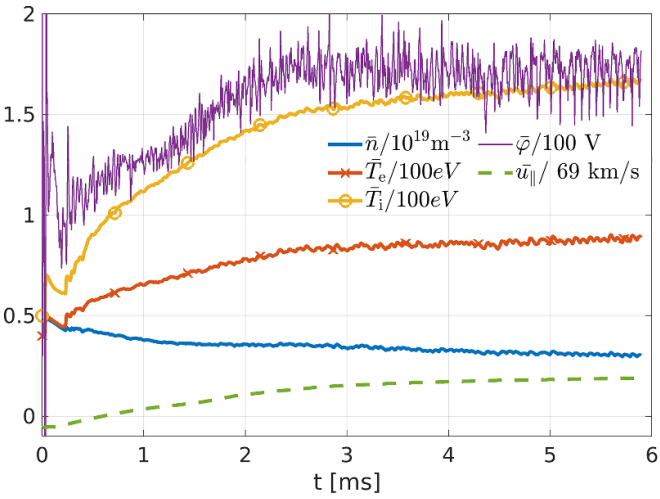

Figure 4. Zonally averaged separatrix density, electron and ion temperatures, and electrostatic potential in normalized units. The parallel velocity shown, averaged over the whole domain, is a measure of toroidal rotation.

simulations [27]. It is important that flux-surface-symmetric potential oscillations like the GAM are permitted up to the core boundary through the implementation of the zonal Neumann boundary condition (see appendix A). But the GAM also leads to an up-down asymmetric pressure oscillation [48], while the adaptive source acts to hold pressure constant – and therefore follows the GAM with the same frequency, damping the pressure oscillation at the core boundary. While the oscillation of the source is a numerical artifact, on average $\langle P_\mathrm{e,i}\rangle_V$ saturates at $t \gtrsim 5$ ms on a reasonable level: 192 ± 29 kW for electrons and 224 ± 36 kW for ions, with one standard deviation quantifying the oscillations. This is roughly half the input power in AUG discharge #36190.

In figure 4, we show zonally averaged separatrix values for density, electron and ion temperatures and electrostatic

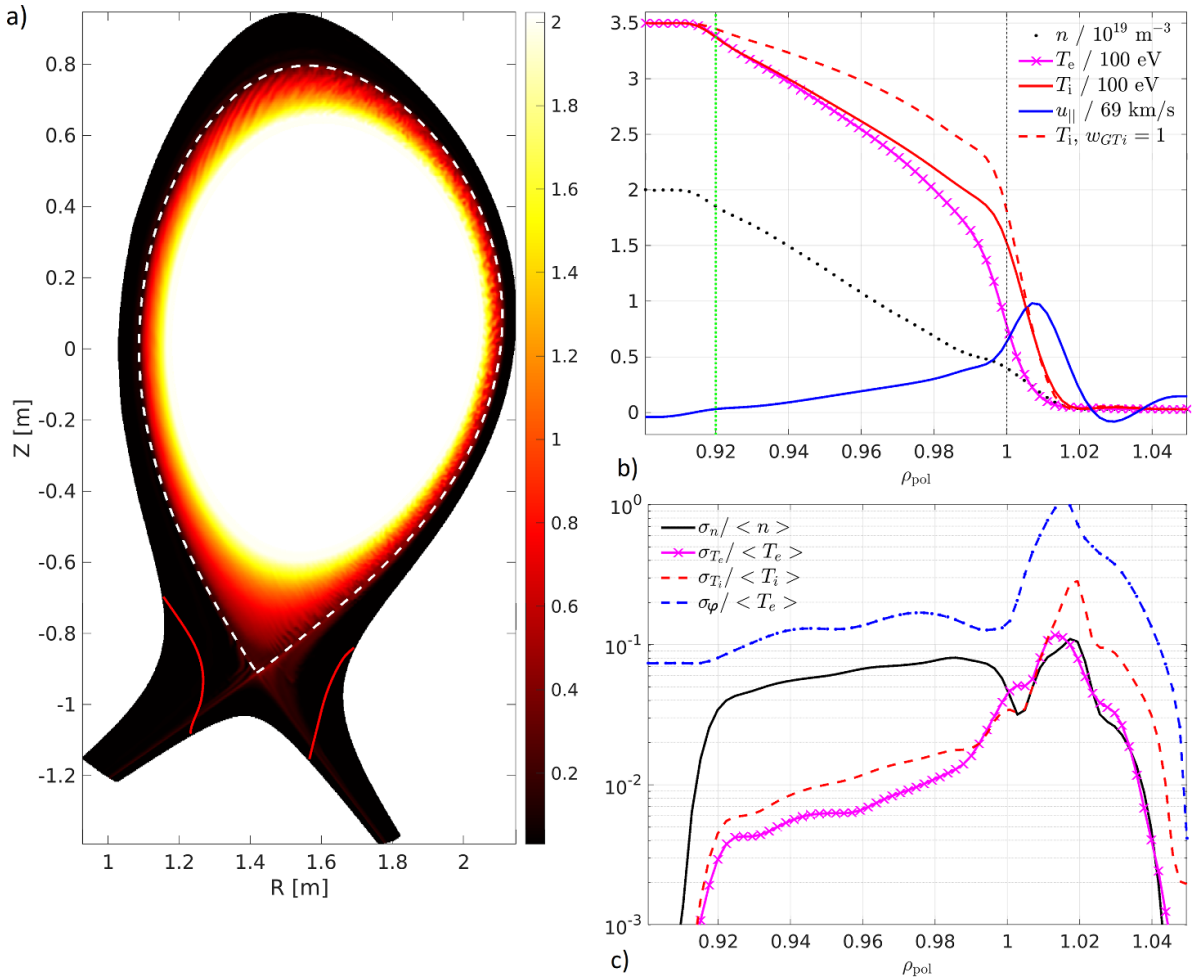

Figure 5. (a) 2D density profile in the poloidal cross section for the quasi-steady state at 7347 μs simulation time for the reference case. The separatrix is shown with a dashed white line, the divertor boundary with a red line. (b) Outboard mid-plane ($Z = 0$) background profiles, averaged in time over 1 ms and toroidally over 16 planes. '$w_{GTi} = 1$' means with viscous ion heating in the confined region, see also text. (c) OMP fluctuation level, with mean $\bar{f} = \langle f \rangle_t$ and variance $\sigma_f^2 = \langle f^2 \rangle_t - \langle f \rangle_t^2$.

potential. As indicated by the input power, in the confined region turbulence, and largely also profiles, saturate within 3 ms of simulation time. Further outside, however, time scales are longer due to lower temperatures – particularly in the SOL, where the transit time is of the order 1 ms (as can be estimated from ~ 50 m connection length and 60 km s^{-1} flow velocity from figure 5). Turbulence at this time is locally saturated, but globally profiles vary predominantly due to the outflow in the SOL, as we started from flat profiles there. Therefore, for the confined region, the separatrix values are a good criterion for saturation. In the following, we will use the data from $t > 4$ ms for our statistical analysis, although temperatures are still very slowly evolving. Additionally, the globally averaged parallel velocity is shown which is a measure of toroidal rotation. It saturates at 13 km s^{-1} in the direction of the plasma current – a reasonable value for AUG [49].

In unfavourable configuration, i.e. with $\mathbf{B} \times \nabla B \sim +\hat{\mathbf{e}}_Z$ away from the X-point, the input power is slightly lower: 187 ± 29 and 204 ± 33 kW for electrons and ions, respectively. The simulation with 24 toroidal planes (higher toroidal resolution) has 176 ± 26 kW for electrons and 221 ± 32 kW for ions, respectively. For the $1.67\rho_{s0}$ simulation (higher poloidal resolution), we get 187 ± 13 kW for electrons and 221 ± 17 kW for ions – i.e. no significant difference to the reference case with $2.5\rho_{s0}$. This is remarkable as zonal flows (a radial modulation of the electric field, pressure and parallel velocity) are much more pronounced in the $1.67\rho_{s0}$ simulation, as discussed in section 4, suggesting that overall thermal transport seems to be barely affected by zonal flows. The reduced oscillation amplitude also indicates a less pronounced GAM. There are no other qualitative differences between the reference simulation and the simulations with higher poloidal or toroidal resolution, as profiles and fluctuation levels remain very similar. Therefore, we conclude that thermal transport is largely resolved in the reference simulation. Increasing resolution further is desirable, but requires a significant speed-up of the code.

3.3. Quasi-steady state profiles, fluctuation levels and transport

Figure 5(a) shows a snapshot of the plasma density in a poloidal plane, in quasi-steady state at $t = 308 R_0/c_{s0} \approx 7$ ms for the reference simulation. Figure 5(b) displays profiles at

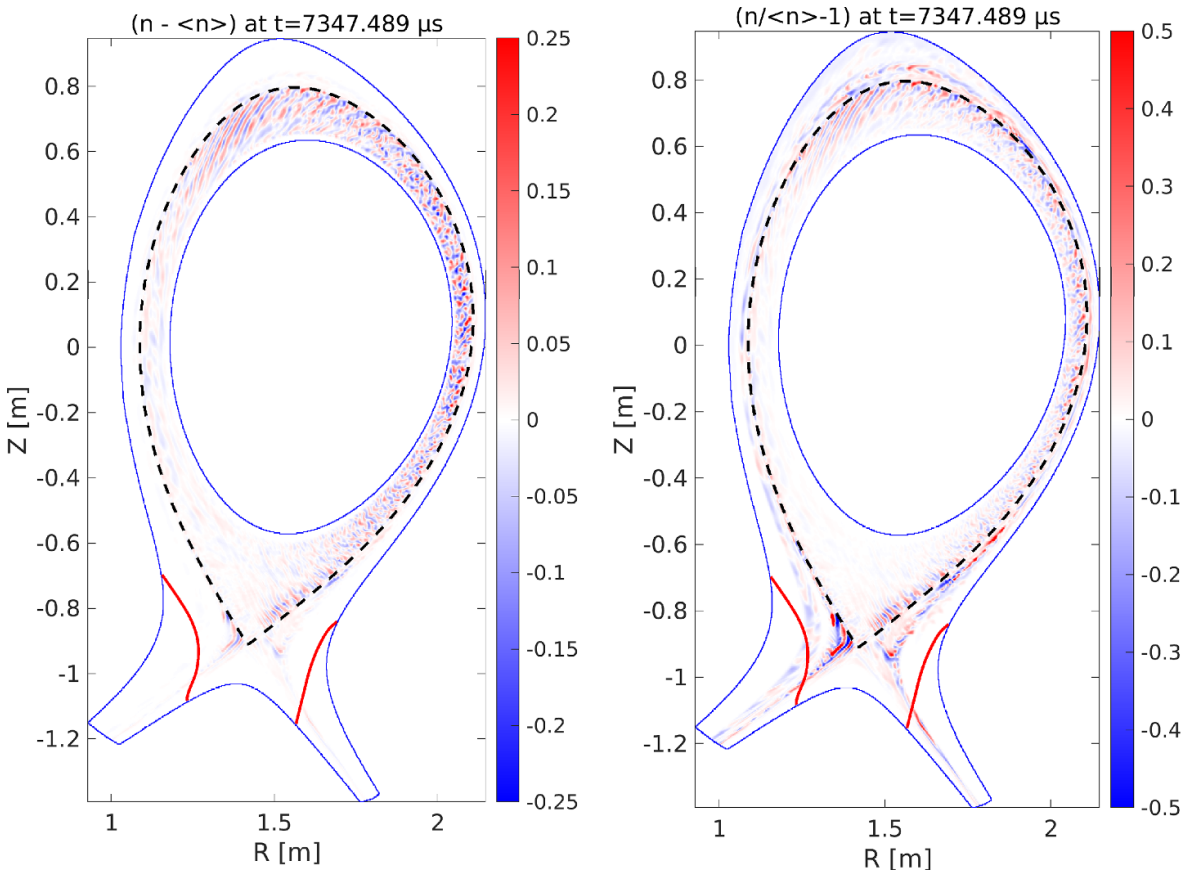

Figure 6. Density fluctuations at a snapshot in quasi-steady state state, at circa 7.3 ms simulation time. Left: $n - \langle n \rangle$ in units of 10^{19} m^{-3}, right: normalized to the local mean density $(n - \langle n \rangle)/\langle n \rangle$. The separatrix is marked with a dashed black line, the divertor with a red line and poloidal domain boundaries with a blue line. See supplementary movie 2 for the dynamics.

the outboard mid-plane ($Z = 0$), averaged toroidally and in time over 1 ms, for density, temperature and parallel velocity. While the density profile is rather flat, we see steep pedestals in temperatures around the separatrix – the reason is high heat conductivity, as discussed in section 5.2. Experimentally, pedestals are observed in L-mode at low density, particularly for T_e [50].

We see some penetration of parallel velocity into the confined region, much less than without ion viscosity in figure 11 though. '$w_{GTi} = 1$' stands for active viscous ion heating (in equation (A6)) in the confined region – ions are significantly hotter in that case. It was not possible to run stable simulations with this effect active also in the SOL, hence why the reference simulation is without viscous ion heating – this is further discussed in section 5.1. If active also in the SOL, the heating is even stronger there, leading to non-monotonous T_i profiles peaking in the SOL and unstable simulations.

Figure 5(c) shows fluctuation levels at the outboard mid-plane. The potential fluctuations are normalised to background (mean) electron temperature, and are the largest in the system. As we have $\sigma_\varphi/\bar{T}_e \gtrsim 2\sigma_n/\bar{n}$ in the confined region, with T_e and T_i fluctuations an order of magnitude smaller, this indicates that turbulence in the confined region is ballooning driven [51, 52]. Around the separatrix, there is a local minimum in $\sigma_n/\bar{n}$ and $\sigma_\varphi/\bar{\varphi}$, indicating some level of turbulence suppression due to the sheared $E \times B$ flow. In the SOL, fluctuation amplitudes peak around $\rho_{pol} \approx 1.01$–1.02, at the bottom of the steep gradients. We have here $\sigma_\varphi/\bar{T}_e \gg \sigma_n/\bar{n}$, roughly an order of magnitude, but also rather high $\sigma_{T_i}/\bar{T}_i$ and a steep ion temperature gradient. This suggests a combination of the Kelvin–Helmholtz instability [53, table I] and ITG drive.

The induction of a perturbed magnetic field, $\beta_0 \partial_t A_\parallel$, is crucial for the dynamics of the parallel electric field and current, and therefore electrostatic turbulent transport. The perturbation $\tilde{\mathbf{B}} = \nabla \times A_\parallel \mathbf{b}$ does not necessarily lead to significant additional electromagnetic transport, though: in current simulations, we have $|\tilde{\mathbf{B}}|/B < 0.1\%$. In principle, the additional electromagnetic transport can be nonetheless large, depending on the efficiency of parallel (heat) transport along the perturbed magnetic field [54]. However, we have verified that the effect is small in present low-β simulations by additional tests that included electromagnetic flutter (that is therefore otherwise disabled to save a factor 2 in computational time).

Figure 6 shows the difference between one snapshot's density and mean background density – in absolute units of 10^{19} m^{-3} (left), as well as normalized to the local mean density (right). Fluctuations are much more prominent on the LFS than on the HFS, which is typical for ballooning modes. In

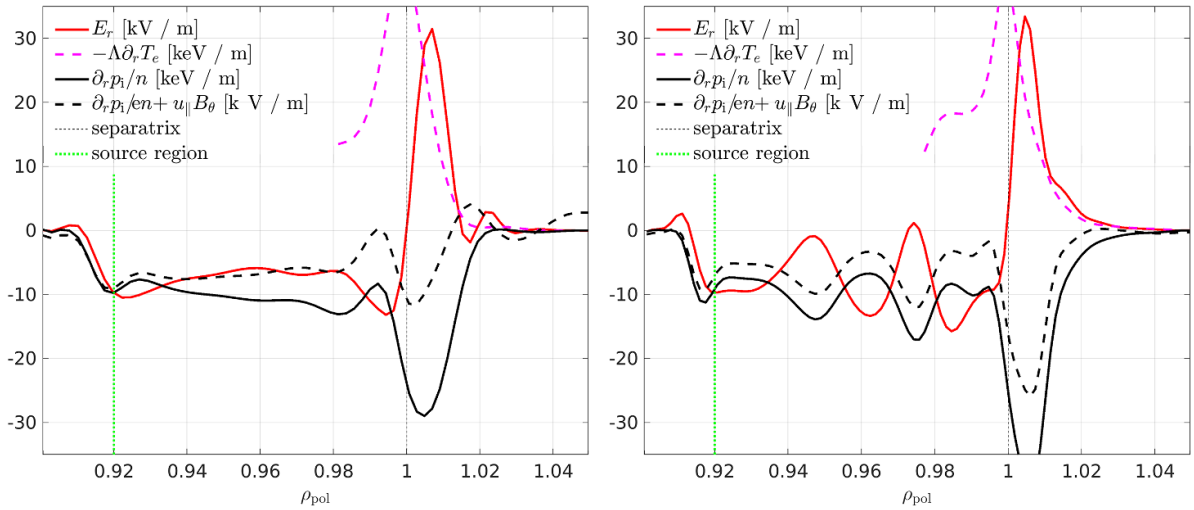

Figure 7. Radial electric field profile vs. ion pressure gradient at the outboard mid-plane, in quasi-stationary phase ($t \gtrsim 4$ ms), averaged in time over 1 ms and toroidally over 16 planes. The $2.5\rho_{s0}$ reference simulation is shown on the left and the $1.67\rho_{s0}$ simulation on the right.

absolute units, fluctuations are negligible in the SOL compared to the confined region – relative to the small local background density, however, SOL fluctuations are much larger, reaching up to 100%, particularly in the region around the X-point where the poloidal magnetic field is weak.

While figure 6 clearly demonstrates poloidal asymmetries in the transport, we can still compute average radial diffusivities in quasi-steady state. For $E \times B$ particle and heat fluxes

$$\Gamma_r = \langle \mathbf{v}_E \cdot \mathbf{e}_r n \rangle \,, \quad Q_r^{\mathrm{e,i}} = \left\langle \frac{3}{2} \mathbf{v}_E \cdot \mathbf{e}_r T_{\mathrm{e,i}} n \right\rangle \tag{23}$$

we define diffusivities as suggested by [55] via

$$D_\perp = \frac{\Gamma_r}{|\langle \partial_r n \rangle|}, \quad \chi_\perp^{\mathrm{e,i}} = \frac{Q_r^{\mathrm{e,i}} - 1.5 T_{\mathrm{e,i}} \Gamma_r}{\langle n \rangle |\langle \partial_r T_{\mathrm{e,i}} \rangle|}. \tag{24}$$

In the global average $\langle \rangle_{r,\theta,\phi,t}$ we obtain for the confined region $D_\perp = 0.18\ \mathrm{m^2\ s^{-1}}$, $\chi_\perp^{\mathrm{e}} = 0.27\ \mathrm{m^2\ s^{-1}}$ and $\chi_\perp^{\mathrm{i}} = 0.46\ \mathrm{m^2\ s^{-1}}$ – reasonable values for AUG experiments [22]. $\chi_\perp^{\mathrm{i}} > \chi_\perp^{\mathrm{e}}$ might imply the presence of the ITG mode – scans of the parallel electron heat conductivity in section 5.2, however, show that this is an effect from diffusive heat flux damping rather than linear instability drive. $\chi_\perp^{\mathrm{e}} = 2/3 D_\perp$ corroborates the finding that turbulence is driven by ballooning modes [55, 56]. Further evidence could be gained by Fourier analysis in field aligned coordinates, particularly from the parallel envelope and the relative phase shifts between the potential, density and temperatures [51, 52] – but this analysis is complicated for us due to the non-field-aligned grid, and will be deferred to future work.

The presented results also hold in the 1.5 times higher resolution simulations (even higher was not yet computationally feasible, as explained in section 3.1). But it should be remarked, as detailed in the next section, that at higher poloidal resolution the increased zonal flow leads to a radial modulation of profiles and fluctuation levels – a staircase structure [57]. However, in present simulations, this has no impact on overall transport (and profiles, disregarding the modulation) as described in section 3.2.

4. The radial electric field

According to our theory developed in section 2, in collisional drift-reduced Braginskii models the equilibrium electric field is determined by the ion particle balance (8) in the confined region and by the sheath boundary conditions (20) in the SOL. We begin by showing in figure 7 the simulated radial electric field in comparison to the ion pressure gradient (and parallel rotation) at the outboard mid-plane ($Z = 0$) in quasi-steady state. In the SOL, the electrostatic potential follows the electron temperature profile, $E_r \sim -\Lambda \partial_r T_\mathrm{e}$, producing a positive electric field. In the confined region, the electric field is negative, which produces counter-propagating flows at the separatrix.

The deviation from $E_r = \frac{\partial_r p_\mathrm{i}}{en}$ indicates that the equilibrium balance from the diamagnetic compression (9) is accompanied by a contribution from toroidal or turbulence driven zonal flows. In the next section we will show that poloidal rotation is small. If zonal flows are small, too, one can use equation (16), $E_r = \partial_r p_\mathrm{i}/en + u_\parallel B_\theta$, to understand the electric field. In a large aspect ratio tokamak, $B \approx B_\phi \gg B_\theta$, and so toroidal rotation is mostly given by the parallel velocity. In the left figure 7, in the domain $\rho_\mathrm{pol} \in (0.94, 0.98)$, this equality is indeed quite well fulfilled. The deviation, however, is caused by the zonal flow, which becomes even more pronounced with increased poloidal resolution in the right figure.

Zonal flows [5, 48] are typically static in time, but can be overlaid by the GAM oscillation (discussed in section 3.2) and, naturally, turbulent oscillations. They are constant over flux surfaces and have a typical mesoscale radial wavelength [8]. Importantly, we find that high poloidal resolution is necessary to properly resolve the zonal flow production at ρ_s scale [48, 58] – which is why results throughout this section are compared between the reference simulation at $2.5\rho_{s0}$ and

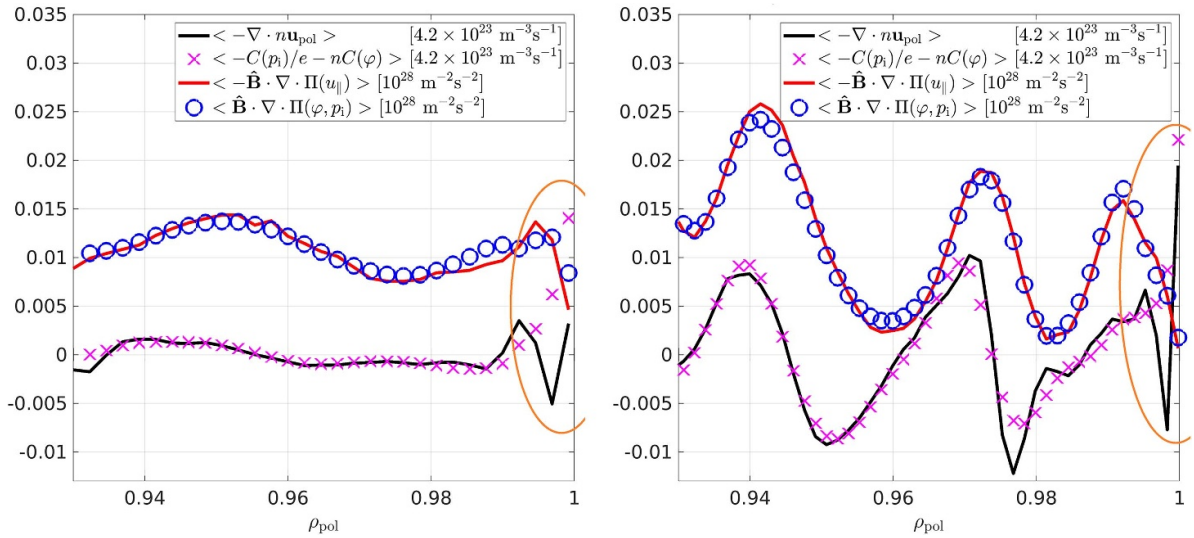

Figure 8. Flux surface averaged dominant terms in the ion particle balance equation (black line and magenta crosses) and in the parallel momentum balance equation (red line and blue circles), also averaged in time over 1 ms, in the $2.5\rho_{s0}$ reference simulation on the left and $1.67\rho_{s0}$ simulation on the right. Dominant terms in the ion momentum balance are the parts of the stress tensor $\Pi_{\rm i}$, whereby $\hat{\mathbf{B}} = \mathbf{B}/B_0$.

$1.67\rho_{s0}$ resolution[6]. On the other hand, equilibrium profiles and input power are nearly identical at both resolutions – see section 3.2. Thus the turbulent transport is barely affected by these zonal flows.

The zonal flow drive is very sensitive to adiabaticity. Only at high adiabaticity the zonal flow drive is efficient [59]. The low wavenumber region responsible for the transport and driving the turbulence is characterized by interchange turbulence, which is less adiabatic. Therefore, this region is less susceptible to the zonal flow. The more drift-wave dominated region around $k_\perp \rho_s = 1$ is responsible for the zonal flow drive, but due to its higher adiabaticity it is not the main driver of the transport. In AUG, low-frequency zonal flows have been not observed so far, not even around the L-H transition [2]. With respect to typical AUG L-mode parameters the present simulations are at particularly low densities and high electron temperatures. Under these conditions the plasma is highly adiabatic, which is beneficial for the generation of zonal flows. However, as we have $T_{\rm i} > T_{\rm e}$, finite Larmor radius effects should stabilize the region around $k_\perp \rho_s = 1$, which in drift-reduced Braginskii models is taken into account only to lowest order. This might lead to an over-prediction of the zonal flow activity.

4.1. Particle, charge and momentum balance on closed field lines

In this section we want to investigate the composition of the mean radial electric field on closed flux surfaces. Zonal flows will be explained by the dominant contributions to the ion particle balance equation (8), averaged in time and over the flux surface. Additionally, the dominant term in the parallel momentum balance – the ion viscous stress (17) – will reveal a non-trivial contribution from the parallel flow. It is important to note that at any single point in time and space, without averaging, $\partial_t n$ and $\mathbf{v}_E \cdot \nabla n$ are by far the dominant terms in the continuity equation (and similarly for $u_\parallel$ in the parallel momentum equation), but become less important in a large enough ensemble average, consistent with the neoclassical ordering.

As pointed out in the previous section, the electric field is mostly negative in the confined region, as it mainly follows the ion pressure gradient according to $E_r \sim \partial_r p_{\rm i}/en$ due to the static equilibrium balance $nC(\varphi) \sim -C(p_{\rm i})/e$ (see equation (9)). We are interested in deviations from this balance, and so we show the residue $-C(p_{\rm i})/e - nC(\varphi)$ by magenta crosses in figure 8. This residue has to be balanced by other terms in the ion particle balance (8). In the flux surface average, parallel derivatives are annihilated, i.e. $\left\langle \nabla \cdot (nu_\parallel \mathbf{b}) \right\rangle_S = 0$, and the $E \times B$ advection $\mathbf{v}_E \cdot \nabla n$ is mostly small. Therefore, the residue is mostly balanced by the black curve, which is the divergence of the polarisation particle flux $\nabla \cdot n\mathbf{u}_{\rm pol}$ defined in equation (11). In the average, it is a measure of the Reynolds stress. We therefore conclude that the zonal flow can be understood as the residue between $E \times B$ and diamagnetic compression which is sustained by the ion polarisation flux (or equivalently the Reynolds stress),

$$\langle enC(\varphi) + C(p_{\rm i}) \rangle_{S,t} \approx \langle \nabla \cdot (en\mathbf{u}_{\rm pol}) \rangle_{S,t}\,.$$

As explained in the previous section, the zonal flow is driven by near-adiabatic drift waves on Larmor radius scale, and is therefore more pronounced in the higher resolved simulation (but does not necessarily impact overall transport).

The remaining deviation between the two curves is explained by hyperviscosity $\mathcal{D}_\Omega$, which is the grid scale numerical dissipation defined in appendix A. It is, however, not just a numerical artifact. As hyperviscosity only acts on grid scale (the value of $\nu_\perp$ is reduced from 3350 to 300

[6] Note that in a global computation the local Larmor radius ρ_s changes strongly throughout the domain – refer to section 3.1 for a detailed description of the simulation setup for both cases.

between the $2.5\rho_{s0}$ and the $1.67\rho_{s0}$ resolution simulations), it dissipates the energy arriving there due to the turbulent cascade. This process is enhanced by shear layers, and so dissipation is even stronger in the higher resolution simulation. The separatrix deserves particular attention in this regard, since the $E\times B$ shear peaks there, as discussed in the next section. Close to to the separatrix, as marked by the yellow ellipse, this results in a peak of $\nabla\cdot(n\mathbf{u}_{\rm pol})$ as well as $\mathcal{D}_\Omega$, and also $\mathbf{v}_E\cdot\nabla n$ largely balanced by $\mathcal{D}_n$.

It is interesting that the divergence of the polarisation particle flux can in fact be conveniently computed from the quasi-neutrality equation (14). In the flux surface average, $\langle\nabla\cdot j_\parallel\mathbf{b}\rangle_S=0$, hence $\langle\nabla\cdot(n\mathbf{u}_{\rm pol})\rangle_{S,t}=\langle C(p_{\rm e}+p_{\rm i})/e-\mathcal{D}_\Omega\rangle_{S,t}$. This means that the zonal flow results in $<C(p)>_S\neq 0$, i.e. a (predominantly up-down) pressure asymmetry [60]. Additionally, ballooned transport leads to an inboard-outboard asymmetry [60, 61]. Therefore, neither pressure nor the electrostatic potential can be assumed to be constant along a flux surface ψ (thereby $C(p_{\rm e})\approx C(p_{\rm i})$).

Let us now discuss the role of ion viscosity. Strictly speaking, the Reynolds stress is only contained in the inertial part of the polarisation particle flux $\nabla\cdot(n\mathbf{u}^{\rm in}_{\rm pol})$ (see section 2.2). However, we find that the viscous part $C(G)$ is always more than two orders of magnitude smaller than the other contributions in the particle balance, i.e. negligible. This means that in present simulations, viscosity does not directly damp the zonal flow. It does, however, efficiently damp poloidal rotation. To see this, we multiply the parallel momentum balance equation (A3) by density n and the magnetic field strength B and average it in time and over flux surfaces. By this, the parallel pressure gradient is annihilated, $\langle B\nabla_\parallel p\rangle_S=0$. The remaining dominant contribution is from the viscous stress function G, or more precisely from its constituents. We have defined the ion viscous stress tensor $\Pi_{\rm i}$ in terms of G in section 2.3. We now compare the part of it containing the parallel velocity, plotted in red in figure 8, with the remaining part containing the static equilibrium balance $C(\varphi)+C(p_{\rm i})/en$, plotted in blue. As the two parts mostly balance, we conclude that poloidal rotation is near zero according to equation (17),

$$\langle\mathbf{B}\cdot\nabla\cdot\Pi_{\rm i}\rangle_{S,t}=3\eta_0^{\rm i}\left\langle\left(\nabla_\parallel B\right)^2\right\rangle_{S,t}v_\theta\approx 0.$$

A small deviation is sustained by $n\mathbf{v}_E\cdot\nabla u_\parallel$ and $p_{\rm i}C(u_\parallel)$. Importantly, this condition is fulfilled also in spite of pronounced zonal flows in the high resolution simulation – both parts of the viscous stress tensor are modulated, but cancel each other. This means that while viscosity does not directly damp the zonal flow via $C(G)$, it does damp the resulting mean poloidal rotation by adjusting the parallel velocity $u_\parallel$!

An important observation is that in the lower resolution simulation ($2.5\rho_{s0}$), the zonal flow is small, but on average over the radial domain constituents of the stress tensor in the parallel momentum balance are the same. In fact, both simulations develop the same mean toroidal rotation (which is roughly the same as parallel rotation in a large aspect ratio tokamak). Although not strictly valid due to the above mentioned necessary asymmetries along a flux surface, equation (16) suggests that parallel velocity also modifies the electric field locally, which seems to be more important than zonal flows in the low resolution case, figure 7 left, at $\rho_{\rm pol}\in(0.94,0.98)$. The generation, transport and saturation of toroidal rotation are outside the scope of the present study, but a review can be found in [62]. Importantly, in absence of momentum sources in the confined region, as in our present simulations, net toroidal rotation can be only generated in the SOL (see [63]) and transported inward. This is indeed suggested by the parallel velocity profile in figure 5. We point out that ion viscosity seems to be important also for the saturation of this process, as discussed in section 5.1.

The same analysis as above can be performed in a different ensemble average, e.g. toroidal and time (poloidally resolved), as was done in [61] – but more data are required, and results are less concise (2D). A more detailed examination of the generation of mean flows can be found in [41, 64]. We find, consistent with [61], that $C(G)$ is negligible in the vorticity equation. Instead, zonal flows are damped by the GAM oscillation which in turn loses energy through the coupling to Alfvén waves and finally resistivity [48J]. However, we find that this damping is not complete, perhaps because unlike electron pressure, ion pressure does not enter Ohm's law.

4.2. Transition to the SOL: vortex breaking and straining-out at the separatrix

We have shown that the electric field is governed by the ion particle balance in the confined region, and by sheath boundary conditions in the SOL – at least in present simulations. The separatrix has its own specific dynamics as it acts as a boundary between closed and open field lines. We can see this by examining what happens to the turbulent eddies. Figure 9 shows the average shearing rate vs. vortex-turn-over rate at the outboard mid-plane. The former is roughly given by $\omega_s=|\partial_R\bar{v}_\theta|\approx\left|B^{-1}\partial_R^2\langle\varphi\rangle_{t,\phi}\right|$. The latter is estimated by one standard deviation of vorticity $\Omega_{\rm std}=\sqrt{\langle\Omega_F^2\rangle-\langle\Omega_F\rangle^2}$, whereby the fluid vorticity is calculated from the generalised vorticity in GRILLIX via $\Omega_F=\omega_{\rm ci0}\hat{B}\hat{\Omega}/\hat{n}$, with $\omega_{\rm ci0}=eB_0/M_{\rm i}$.

Small vortices are elongated, thinned and finally absorbed by the shear flow [4, 58, 65] – driving the zonal flow. Stronger vorticies survive. Importantly, as stated in the last section and visible in figure 8, this process extends up to and peaks at the separatrix. Even though larger zonal flows do lead to somewhat higher shearing, we find that the average vortex-turn-over rate is larger than the shearing rate in the confined region at both $2.5\rho_{s0}$ and $1.67\rho_{s0}$ resolution – explaining why they have barely any effect on overall transport. At the separatrix additional shearing is provided externally due to sheath boundary conditions and the fast SOL outflow, such that the shearing rate exceeds the vortex-turn-over rate and

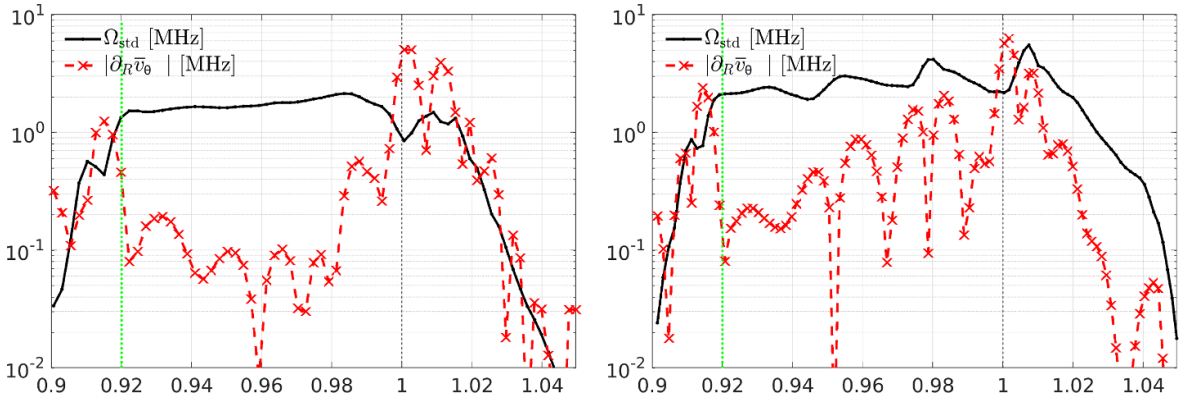

Figure 9. Vortex turn-over rate Ω_{std} compared to the shearing rate ω_s, see text for their definition, in the $2.5\rho_{s0}$ reference simulation on the left and $1.67\rho_{s0}$ simulation on the right.

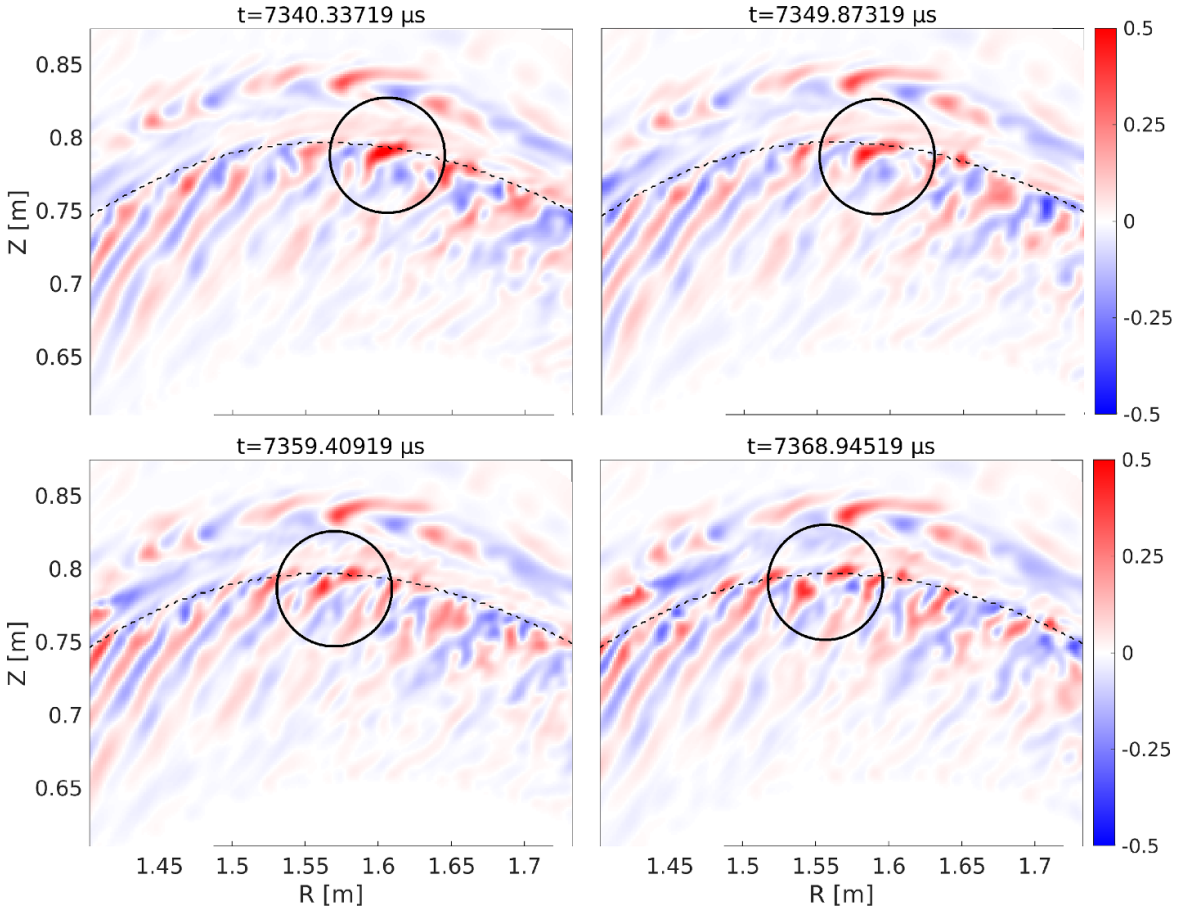

Figure 10. Eddy tilting, straining-out, decorrelation and a single breaking event in the $2.5\rho_{s0}$ reference simulation, at the separatrix on top of the device (compare with figure 6). Colour scale shows density fluctuation amplitudes relative to the background, $(n - \langle n \rangle)/\langle n \rangle$.

the eddies can be torn apart. In figure 10, at the top of the device, the tilting of eddies is particularly visible. We highlighted one exemplary vortex breaking event (see [66] for a similar experimental finding). Ultimately, vortices are strained out by the shear flow, and dissipated at grid scale. In the particle balance this manifests as a peaked $E \times B$ advection rate balanced by dissipation. Supplementary movie 2 shows the dynamics of density fluctuations.

Note also how the far SOL structures appear to be nearly frozen in time in contrast – as temperature in hitting $\sim$3 eV there, time scales are an order of magnitude slower. These structures, pronounced on the scale relative to the background, are in fact tiny due to the very low background $\bar{n} \approx 3 \times 10^{17}$ m^{-3}. Nevertheless, as transport has to saturate globally including the far SOL, its slow dynamics restricts the overall saturation of the simulations.

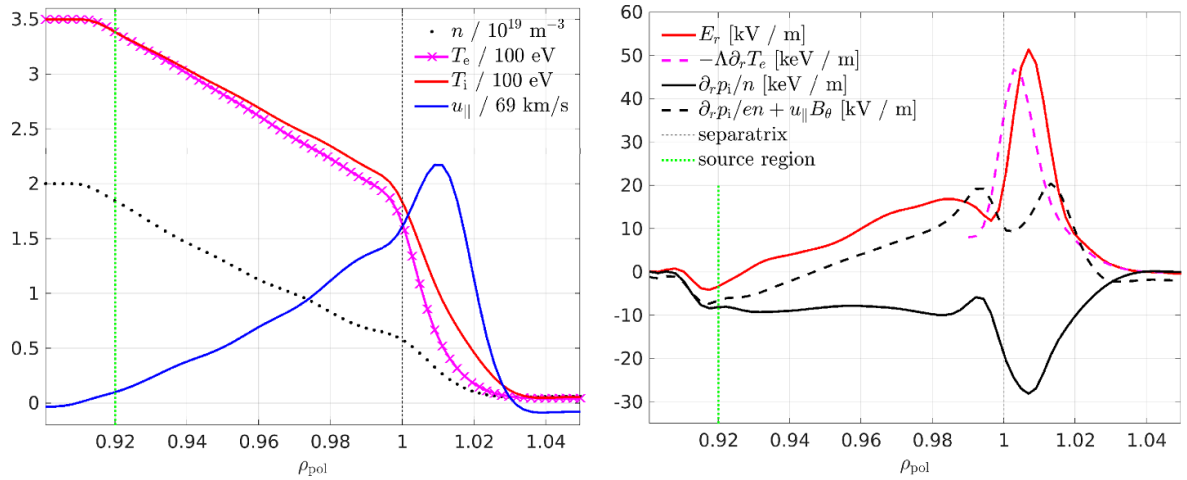

Figure 11. Outboard mid-plane state variables profiles (left) and radial electric field (right) without ion viscosity ($G=0$) at $t=2$ ms simulation time (saturated turbulence, but flows still evolving). Compare to figures 5(b) and 7 (left).

5. The role of fluid closure terms

Due to the low collisionality in fusion plasmas, the greatest limitation of our model is the collisional fluid closure. In this section we show explicitly its role. This is particularly important as towards lower collisionality, the discussed closure terms – ion viscosity and electron/ion heat conductivity – diverge as $\sim T^{5/2}$. For the current simulations, a 3D iterative solver [67] allowed us to treat these terms without constraints on the allowed time step – consuming, however, already up to 50% of the computation time. Towards less collisional, hotter regimes (H-mode) additional improvements will be therefore necessary.

5.1. The impact of ion viscosity

The viscosity of ions, represented by the viscous stress function G – see sections 2.2–2.3, is an important dissipation mechanism. In section 4.1 we found that $C(G)$, which enters the perpendicular drifts as a higher order correction, is negligible in the polarisation velocity. On the other hand, $\nabla_\parallel G$, which enters the parallel momentum balance at leading order, is crucial for damping poloidal rotation. We have also seen in section 3.3 that this damping leads to significant ion heating.

To closer investigate this, we have conducted a simulation without ion viscosity at all ($G=0$). The results at $t=2$ ms simulation time are shown in figure 11: outboard mid-plane profiles of density, temperature, parallel velocity and electric field. The density profile is very similar to the reference case in figure 5. The electric field is much larger and almost throughout positive, though. The temperature profiles are broader, fluctuations are larger (up to 15% in density in the confined region) and input power is much larger in this simulation – 482 $\pm$ 118 kW for electrons and 525 $\pm$ 127 kW for ions, respectively – suggesting increased turbulent transport. The larger fluctuation in input power also suggests stronger GAM oscillations.

The electric field is larger in the SOL due to the increased electron temperature gradient. In the confined region, we have performed the same analysis as in section 4.1, finding only a very small contribution from the zonal flow. Although viscosity was disabled in the simulation, we can still compute what the contribution from viscous stress in the parallel momentum balance would have been. Naturally, we find that the viscosity balance (17) is not fulfilled: in the reference simulation, figure 8 left, in an average also over the radial domain, we had $\left\langle \hat{\mathbf{B}}\cdot\nabla\cdot\Pi(u_\parallel)\right\rangle_{S,t,r} = -1.07\times10^{26}\,\mathrm{m^{-2}\,s^{-2}}$ and $\left\langle \hat{\mathbf{B}}\cdot\nabla\cdot\Pi(\varphi,p_i)\right\rangle_{S,t,r} = 1.10\times10^{26}\ \mathrm{m^{-2}\,s^{-2}}$. In the simulation in this section, without viscosity, one would get $\left\langle \hat{\mathbf{B}}\cdot\nabla\cdot\Pi(u_\parallel)\right\rangle_{S,t,r} = -16.38\times10^{26}\ \mathrm{m^{-2}s^{-2}}$ and $\left\langle \hat{\mathbf{B}}\cdot\nabla\cdot\Pi(\varphi,p_i)\right\rangle_{S,t,r} = 5.23\times10^{26}\,\mathrm{m^{-2}\,s^{-2}}$. This means that without viscosity, the plasma obtains a significant poloidal rotation.

At this point, $t=2$ ms, the simulation crashes as the electric field starts having large (machine scale) oscillations. A possible reason is the Stringer instability [7, 68], which is expected at low – or absent – viscosity. As the instability is also connected to parallel [60] and toroidal [68] rotation, it is not surprising that we get $\left\langle -\hat{\mathbf{B}}\cdot\nabla\cdot\Pi(u_\parallel)\right\rangle_{S,t,r} > \left\langle \hat{\mathbf{B}}\cdot\nabla\cdot\Pi(\varphi,p_i)\right\rangle_{S,t,r}$. In fact, mean toroidal rotation reaches 26 km s^{-1} already at $t=2$ ms, compared to 13 km s^{-1} in the saturated reference simulation. However, the inflow of momentum from the SOL [62, 63] and the non-linear Reynolds stress [42] could also be important. At this point, we will not go more into details. But we can conclude that ion viscosity is a crucial mechanism – particularly for damping of poloidal rotation, but also ion heating – and has to be included in realistic tokamak simulations.

5.2. The impact of heat conductivity

The parallel heat conductivity largely determines the parallel heat flux in Braginskii models. Besides obvious consequences for the SOL heat exhaust, circular C-mod simulations [67, 69]

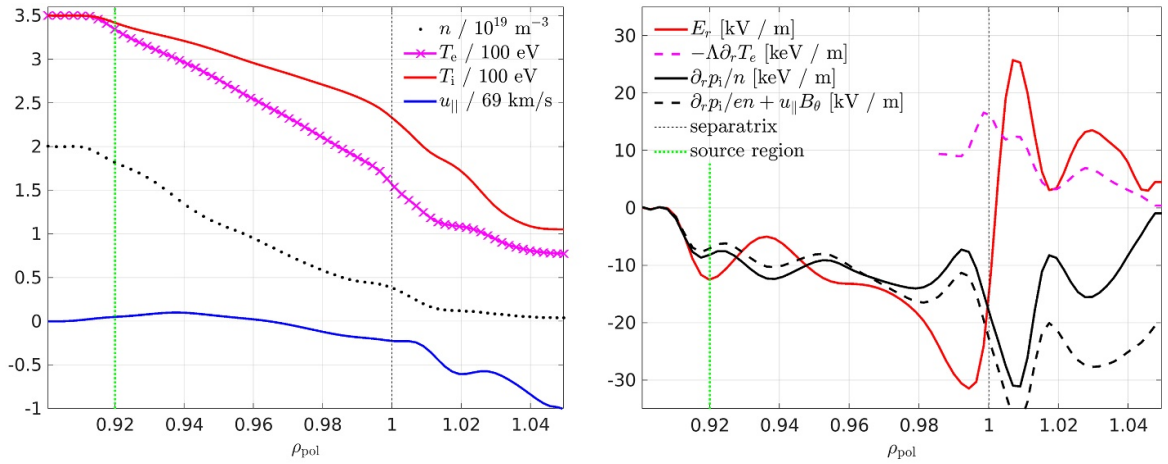

Figure 12. Saturated outboard mid-plane state variables profiles (left) and radial electric field (right) for $\chi_{\|e0} = \chi_{\|i0} = 35.35$ and $\gamma_e = 0$.

have previously shown that flattening of the parallel electron and ion temperature profiles in the confined region can also reduce cross-field transport. To illustrate their impact in current computations, we have repeated the reference simulation with the electron heat conduction lowered to the level of ions, i.e. $\chi_{\|e0} = 35.35$ instead of 940, and sheath heat transmission factor $\gamma_e = 0$ instead of 2.5. The resulting saturated profiles are displayed in figure 12 (unlike with zero ion viscosity, these simulations were running stably).

The most prominent feature is that electron and ion temperature profiles become much broader, including in the SOL, i.e. the pedestal disappears. This is because the profile around the separatrix is determined by the competition of perpendicular transport and parallel outflow, and reducing the heat conductivity and sheath heat transmission significantly hinders the latter. As a secondary effect, due to the increased temperature the ion viscosity increases, damping the parallel flow more strongly. Further, the electric field well deepens. Again, a similar analysis as in section 4.1 reveals that, in this case, this is due to the increased polarisation flux, i.e. zonal flow. This can be either due to a change in the linear instability drive [56], or due to an increased effective resolution: even though the nominal resolution is still $2.5\rho_{s0}$, the separatrix temperature has increased by roughly a factor 2, such that the effective resolution in terms of the local Larmor radius has increased by $\sqrt{2}$. Similarly as with reduced ion viscosity, the density fluctuation level increases up to $\sim$15% in the confined region, and input power increases to 535 $\pm$ 232 kW for electrons and 463 $\pm$ 202 kW for ions, respectively. Noticeably, not only the fluctuations increase, but also electrons are now transporting more heat than ions. This corroborates the hypothesis that transport is driven by ballooning rather than ITG modes, except that for the reference case (with high electron heat conduction) the electron heat flux is more suppressed than the ion heat flux by parallel conductivity.

6. Conclusions

For the first time, global turbulence simulations (using the drift-reduced Braginskii model) have been performed across the edge and SOL of AUG, in diverted geometry and at realistic parameters. Away from the inner boundary of the simulation in the core region of the plasma, the background profiles evolve freely, together with the turbulence. A quasi-steady state is reached asymptotically after about 3–4 ms. The saturated input power of about 400 kW is typical for low density AUG L-mode discharges. At the separatrix, the plasma profiles are determined by a competition between perpendicular transport and parallel outflow. A pedestal develops in the electron temperature due to high parallel heat conductivity.

Particular attention was given to the electric field. On closed flux surfaces, the radial electric field is predominantly determined by equilibrium compression, leading to $E_r = \frac{\partial_r p_i}{en}$. Additionally, we find contributions from toroidal rotation and (in particular) zonal flows. The latter absorb smaller eddies, leading to an inverse energy cascade to larger scales. In the SOL, sheath boundary conditions dominate, forcing the electric field to change sign across the separatrix. The resulting shear flow reinforces straining-out and decorrelation of vortices, leading to intermittent outbursts of up to twice the magnitude compared to the laminar background outflow in the SOL.

The stationary zonal flow, a perturbation between the electric field and pressure with a mesoscale radial wavelength, is driven by the Reynolds stress within the polarisation particle flux. A poloidal resolution scan shows that the drive happens on Larmor radius scale by near-adiabatic drift waves which do not significantly contribute to transport. On the other hand, fluctuation levels and average diffusivities suggest that transport is driven by larger scale interchange modes, i.e. coarse simulations are able to mostly capture the transport.

The role of the fluid closure terms – ion viscosity and heat conductivities – was explicitly examined. We find that ion viscosity is negligible in damping vorticity, but highly effective in damping poloidal rotation by adjusting of the parallel velocity profile, while also generating considerable ion heating through magnetic pumping. The electron and ion heat conductivities, on the other hand, are important for parallel heat fluxes,

and they largely determine the pedestal and SOL temperature profiles. Both damping mechanisms, viscosity and heat conduction, affect the electric field and reduce the perpendicular transport.

A limiting factor for the simulations is their computational cost. MPI communication and OpenMP performance are currently being optimized, which should allow for faster medium-sized tokamak simulations, also including magnetic flutter (important at higher beta [70]). For larger devices like ITER and DEMO, a larger speed-up or scalability is required, by means of GPU accelaration or 3D MPI domain decomposition.

Further work is needed to extend the applicability of our model to H-mode conditions. Most pressing, as the Braginskii fluid closure loses validity towards lower collisionality regimes, Knudsen corrections [71] (modelling Landau damping [72]) will have to be introduced for heat conductivities. The ion viscosity will have to be adapted to properly model the neoclassical electric field [22, 73]. In this regard, generation and damping of poloidal and toroidal rotation should be studied in more detail. Ways to include the ion orbit loss effect [74, 75] should be explored, as this might explain why so far we found no significant difference between the favourable and unfavourable direction of the toroidal magnetic field. Furthermore, even in attached L-mode regimes, the applicability of our model in the SOL is yet limited. In our current simulations, the SOL electric field is determined by an isolating sheath, and the pressure profile by the competition between turbulent cross-field transport and parallel outflow. In a real SOL, the sheath can conduct significant currents, and neutral gas recycling and impurities lead to complex density and temperature profiles and flows. The resulting strong gradients between the outboard mid-plane and the divertor, and particularly plasma detachment, are of great interest for fusion reactors. Correspondingly, the incorporation of the aforementioned effects is being urgently pursued.

Acknowledgments

The authors thank E Wolfrum, A Bergmann, E Poli, M Francisquez, B N Rogers, E Fable, T Görler, A Chankin, J Loizu, V Rozhansky, A Cathey Cevallos, M Faitsch, R W Brzozowski III and S Makarov for helpful discussions. This work has been carried out within the framework of the EUROfusion Consortium and has received funding from the Euratom research and training programme 2014–2018 and 2019–2020 under Grant Agreement No. 633053. The views and opinions expressed herein do not necessarily reflect those of the European Commission. B Zhu is supported by the U.S. Department of Energy Contract DE-AC52-07NA27344 through the Lawrence Livermore National Laboratory.

Appendix A. Global drift-reduced Braginskii equations in GRILLIX

The current physical model in GRILLIX builds on its recent extension by hot ions [67]. The most important newly added terms arise from the ion stress tensor [36], particularly its viscous part. Additionally, collisional electron-ion heat exchange was added.

In the following, time scales are normalised to R_0/c_{s0}, with R_0 the major radius and $c_{s0} = \sqrt{T_{e0}/M_i}$ the sound speed at reference electron temperature T_{e0}. Perpendicular scales are normalised to the sound Larmor radius $\rho_{s0} = c\sqrt{T_{e0}M_i}/(eB_0)$ (in CGS units) and parallel scales to R_0. The dynamical fields evolved in GRILLIX are the density n normalised to a reference density n_0, the electrostatic potential φ normalised to T_{e0}/e, the parallel ion velocity $u_\parallel$ normalised to c_{s0}, the electron and ion temperatures T_e and T_i normalised to reference values T_{e0}, respectively, T_{i0}, the parallel current $j_\parallel$ normalised to en_0c_{s0} and the parallel component of the perturbed electromagnetic potential $A_\parallel$ normalised to $(\beta_0 B_0 \rho_{s0})^{-1}$ with $\beta_0 = 4\pi n_0 T_{e0}/B_0^2$.

The normalized equations (A1)–(A7) represent electron continuity equation, vorticity equation, parallel momentum balance, Ohm's law, electron and ion temperature equations and Ampere's law. The advective derivative is defined as $\frac{\mathrm{d}}{\mathrm{d}t} = \frac{\partial}{\partial t} + \delta_0 \left(\frac{\mathbf{B}}{B^2} \times \nabla\varphi\right) \cdot \nabla$ and the curvature operator as $C(f) = -\delta_0 \left(\nabla \times \frac{\mathbf{B}}{B^2}\right) \cdot \nabla f$. The equation set requires a number of auxiliary quantities: The parallel electron velocity $v_\parallel = u_\parallel - j_\parallel/n$, the electron and ion pressures $p_e = nT_e$, respectively, $p_i = nT_i$, generalized vorticity $\Omega = \nabla \cdot \left[\frac{n}{B^2}\left(\nabla_\perp \varphi + \zeta \frac{\nabla_\perp p_i}{n}\right)\right]$ and generalised electromagnetic potential $\Psi_m = \beta_0 A_\parallel + \mu \frac{j_\parallel}{n}$. The ion viscous stress function G was defined in equation (13) and is normalized as $G = n_0 T_{i0} \hat{G}$. The parallel gradient is defined as $\nabla_\parallel = \mathbf{b} \cdot \nabla$, with $\mathbf{b} = \mathbf{B}/B$ the unit vector of the background magnetic field. While electromagnetic induction is taken into account in equation (A4), transport by electromagnetic fluctuations (flutter) is implemented, but currently disabled due to significant additional computational cost.

The four dimensionless, collisionless parameters of the system are the drift scale $\delta_0 = R_0/\rho_{s0}$, dynamical plasma beta β_0 defined above, and electron to ion mass and temperature ratios $\mu = m_e/M_i$, respectively, $\zeta = T_{i0}/T_{e0}$. For the collisional parameters, we require τ_{e0} and τ_{i0} – the electron, respectively, ion collision times evaluated at reference temperature and density and normalised to R_0/c_{s0}. Then, the remaining five dimensionless collisional parameters of the system are the electron collisionality $\nu_{e0} = 1/\tau_{e0}$, normalised parallel resistivity $\eta_{\parallel 0} = 0.51\mu\nu_{e0}$, normalised parallel electron and ion heat conductivities $\chi_{\parallel e0} = 3.15\tau_{e0}/\mu$, respectively, $\chi_{\parallel i0} = 3.9\tau_{i0}\zeta$, and normalized ion viscosity $\eta_{i0} = 0.96\tau_{i0}$. Additionally, via the parameter w_{GTi}, ion viscous heating which is usually dropped in literature [36] can be switched on and off.

$$\frac{\mathrm{d}}{\mathrm{d}t}n = nC(\varphi) - C(p_\mathrm{e}) + \nabla\cdot\left[\left(j_\parallel - nu_\parallel\right)\mathbf{b}\right] + \mathcal{D}_n(n) + S_n, \tag{A1}$$

$$\nabla\cdot\left[\frac{n}{B^2}\left(\frac{\mathrm{d}}{\mathrm{d}t} + u_\parallel\nabla_\parallel\right)\left(\nabla_\perp\varphi + \zeta\frac{\nabla_\perp p_\mathrm{i}}{n}\right)\right] = -C(p_\mathrm{e} + \zeta p_\mathrm{i}) + \nabla\cdot\left(j_\parallel\mathbf{b}\right) - \frac{\zeta}{6}C(G) + \mathcal{D}_\Omega(\Omega), \tag{A2}$$

$$\left(\frac{\mathrm{d}}{\mathrm{d}t} + u_\parallel\nabla_\parallel\right)u_\parallel = -\frac{\nabla_\parallel\left(p_\mathrm{e} + \zeta p_\mathrm{i}\right)}{n} + \zeta T_\mathrm{i}C(u_\parallel) - \frac{2}{3}\zeta\frac{B^{3/2}}{n}\nabla_\parallel\frac{G}{B^{3/2}} + \mathcal{D}_u(u_\parallel), \tag{A3}$$

$$\beta_0\frac{\partial}{\partial t}A_\parallel + \mu\left(\frac{\mathrm{d}}{\mathrm{d}t} + v_\parallel\nabla_\parallel\right)\frac{j_\parallel}{n} = -\left(\frac{\eta_{\parallel 0}}{T_\mathrm{e}^{3/2}}\right)j_\parallel - \nabla_\parallel\varphi + \frac{\nabla_\parallel p_\mathrm{e}}{n} + 0.71\nabla_\parallel T_\mathrm{e} + \mathcal{D}_\Psi(\Psi_m), \tag{A4}$$

$$\begin{aligned}\frac{3}{2}\left(\frac{\mathrm{d}}{\mathrm{d}t} + v_\parallel\nabla_\parallel\right)T_\mathrm{e} = {}& T_\mathrm{e}C(\varphi) - \frac{T_\mathrm{e}}{n}C(p_e) - \frac{5}{2}T_\mathrm{e}C(T_\mathrm{e}) - T_\mathrm{e}\nabla\cdot\left(v_\parallel\mathbf{b}\right) + 0.71\frac{T_\mathrm{e}}{n}\nabla\cdot\left(j_\parallel\mathbf{b}\right)\\ &+ \frac{1}{n}\nabla\cdot\left[\left(\chi_{\parallel\mathrm{e}0}T_\mathrm{e}^{5/2}\right)\mathbf{b}\nabla_\parallel T_\mathrm{e}\right] - 2\nu_{\mathrm{e}0}\mu\left(\frac{n}{T_\mathrm{e}^{3/2}}\right)\left(T_\mathrm{e} - \zeta T_\mathrm{i}\right) + \left(\frac{\eta_{\parallel 0}}{T_\mathrm{e}^{3/2}}\right)\frac{j_\parallel^2}{n} + \frac{3}{2}\left(\mathcal{D}_{T_\mathrm{e}}(T_\mathrm{e}) + S_{T_\mathrm{e}}\right),\end{aligned} \tag{A5}$$

$$\begin{aligned}\frac{3}{2}\left(\frac{\mathrm{d}}{\mathrm{d}t} + u_\parallel\nabla_\parallel\right)T_\mathrm{i} = {}& T_\mathrm{i}C(\varphi) - \frac{T_\mathrm{i}}{n}C(p_e) + \frac{5}{2}\zeta T_\mathrm{i}C(T_\mathrm{i}) - T_\mathrm{i}\nabla\cdot\left(u_\parallel\mathbf{b}\right) + \frac{T_\mathrm{i}}{n}\nabla\cdot\left(j_\parallel\mathbf{b}\right)\\ &+ \frac{1}{n}\nabla\cdot\left[\left(\chi_{\parallel\mathrm{i}0}T_\mathrm{i}^{5/2}\right)\mathbf{b}\nabla_\parallel T_\mathrm{i}\right] + 2\nu_{\mathrm{e}0}\mu\left(\frac{n}{T_\mathrm{e}^{3/2}}\right)\left(\frac{1}{\zeta}T_\mathrm{e} - T_\mathrm{i}\right) + \frac{2w_{GTi}}{9\eta_{\mathrm{i}0}}\frac{G^2}{nT_\mathrm{i}^{5/2}} + \frac{3}{2}\left(\mathcal{D}_{T_\mathrm{i}}(T_\mathrm{i}) + S_{T_\mathrm{i}}\right),\end{aligned} \tag{A6}$$

$$\nabla_\perp^2 A_\parallel = -j_\parallel. \tag{A7}$$

S_n, S_{T_e} and S_{T_i} are source functions driving the system with particles and energy. For numerical reasons, respectively, in order to cut the turbulent spectrum, a dissipation is added to all equations of the form

$$\mathcal{D}_f = \nu_{f\perp}\nabla_\perp^{2N}f + \nu_{f\parallel}\nabla\cdot\left(\mathbf{b}\nabla_\parallel f\right) + \nabla\cdot\left(\nu_{f,\mathrm{buffer}}\nabla_\perp f\right), \tag{A8}$$

with constants $\nu_{f\perp}$, $\nu_{f\parallel}$ for every field. $\nu_{f,\mathrm{buffer}}$ is zero in most of the domain, but is high in the last few grid points towards the radial boundaries. For hyperviscosity, $N = 3$ is chosen.

The system is energy conserving, with the exception of numerical dissipation, neglect of polarisation velocity in perpendicular advection and boundary conditions. We note that parallel viscosity in equation (A3) is treated implicitly, similarly to electron and ion heat conduction [67], while all other terms are advanced explicitly in time.

At the inner and outer limiting flux surfaces, the following homogeneous boundary conditions are applied

$$\partial_\rho n = 0,\ \partial_\rho T_{\mathrm{e,i}} = 0,\ \partial_\rho u_\parallel = 0,\ \Omega = 0, A_\parallel = 0,\ \partial_\rho j_\parallel = 0, \tag{A9}$$

to prevent particles and energy fluxes through the boundary. For the potential, the sheath boundary condition $\phi|_{\rho_\mathrm{max}} = \Lambda T_\mathrm{e}$ is applied at the outer wall boundary. At the inner (core) boundary ρ_min, the zonal homogeneous Neumann boundary condition $\partial_\rho\langle\varphi\rangle_\theta = 0$ and $\varphi - \langle\varphi\rangle_\theta = 0$ is applied, which allows the potential to float but prevents net $E\times B$ flux through that boundary.

At the divertor, insulating Bohm sheath boundary conditions are applied

$$u_\parallel \gtrless \sqrt{T_\mathrm{e} + T_\mathrm{i}},\quad j_\parallel = 0,\quad \phi = \Lambda T_\mathrm{e},\quad \nabla_\parallel T_\mathrm{e} = -\frac{\gamma_\mathrm{e}}{\left(\chi_{\parallel\mathrm{e}0}T_\mathrm{e}^{5/2}\right)}T_\mathrm{e}nu_\parallel,\quad \nabla_\parallel T_\mathrm{i} = 0,\quad \nabla_\parallel n = 0,\quad \nabla_\parallel\Omega = 0, \tag{A10}$$

where $\Lambda = 2.69$ and $\gamma_e = 2.5$.

For further numerical details on the implementation of the model in GRILLIX, e.g. the FCI approach and the immersed boundary technique, we refer to previous publications [33, 67, 76, 77].

ORCID iDs

W Zholobenko https://orcid.org/0000-0002-2624-0251
T Body https://orcid.org/0000-0003-1904-6300
P Manz https://orcid.org/0000-0002-5724-0174
A Stegmeir https://orcid.org/0000-0001-8629-5062
B Zhu https://orcid.org/0000-0003-2225-045X
M Griener https://orcid.org/0000-0003-2953-536X
D Coster https://orcid.org/0000-0002-2470-9706
F Jenko https://orcid.org/0000-0001-6686-1469

References

[1] Burrell K H *et al* 1994 Role of the radial electric field in the transition from L (low) mode to H (high) mode to VH (very high) mode in the DIII-D tokamak* *Phys. Plasmas* **1** 1536
[2] Cavedon M *et al* 2016 Interplay between turbulence, neoclassical and zonal flows during the transition from low to high confinement mode at ASDEX Upgrade *Nucl. Fusion* **57** 014002
[3] Itoh K and Itoh S-I 1996 The role of the electric field in confinement *Plasma Phys. Control. Fusion* **38** 1
[4] Stroth U, Manz P and Ramisch M 2011 On the interaction of turbulence and flows in toroidal plasmas *Plasma Phys. Control. Fusion* **53** 024006
[5] Diamond P H *et al* 2005 Zonal flows in plasma—a review *Plasma Phys. Control. Fusion* **47** R35
[6] Drake J F *et al* 1993 Tokamak edge transport, L-H transition and generation of velocity shear layers *Plasma Physics and Controlled Nuclear Fusion Research 1992* vol 2 (Vienna: IAEA)
[7] Hassam A B *et al* 1991 Spontaneous poloidal spin-up of tokamaks and the transition to the H mode *Phys. Rev. Lett.* **66** 309
[8] Fujisawa A 2008 A review of zonal flow experiments *Nucl. Fusion* **49** 013001
[9] Stangeby P 2000 *The Plasma Boundary of Magnetic Fusion Devices (Series in Plasma Physics)* (Boca Raton, FL: CRC Press)
[10] Loizu J *et al* 2012 Boundary conditions for plasma fluid models at the magnetic presheath entrance *Phys. Plasmas* **19** 122307
[11] Conway G D *et al* 2010 Interaction of mean and oscillating plasma flows across confinement mode transitions *Plasma Fusion Res.* **5** S2005
[12] Biglari H, Diamond P H and Terry P W 1990 Influence of sheared poloidal rotation on edge turbulence *Phys. Fluids B* **2** 1
[13] Hahm T S and Burrell K H 1995 Flow shear induced fluctuation suppression in finite aspect ratio shaped tokamak plasma *Phys. Plasmas* **2** 1648
[14] Dif-Pradalier G *et al* 2009 Interplay between gyrokinetic turbulence, flows and collisions: perspectives on transport and poloidal rotation *Phys. Rev. Lett.* **103** 065002
[15] Charidakos I K *et al* 2018 Analysis of equilibrium and turbulent fluxes across the separatrix in a gyrokinetic simulation *Phys. Plasmas* **25** 072306
[16] Braginskii S I 1965 Transport processes in a plasma *Reviews of Plasma Physics* vol 1, ed A M A Leontovich (New York: Consultants Bureau) pp 205–311
[17] Zeiler A, Drake J F and Rogers B 1997 Nonlinear reduced Braginskii equations with ion thermal dynamics in toroidal plasma *Phys. Plasmas* **4** 2134
[18] Tamain P *et al* 2016 The TOKAM3X code for edge turbulence fluid simulations of tokamak plasmas in versatile magnetic geometries *J. Comput. Phys.* **321** 606
[19] Dudson B D and Leddy J 2017 Hermes: global plasma edge fluid turbulence simulations *Plasma Phys. Control. Fusion* **59** 054010
[20] Zhu B, Francisquez M and Rogers B N 2018 Up–down symmetry breaking in global tokamak edge simulations *Nucl. Fusion* **58** 106039
[21] Paruta P *et al* 2018 Simulation of plasma turbulence in the periphery of diverted tokamak by using the GBS code *Phys. Plasmas* **25** 112301
[22] Rozhansky V *et al* 2009 New B2SOLPS5.2 transport code for H-mode regimes in tokamaks *Nucl. Fusion* **49** 025007
[23] Bufferand H *et al* 2017 Implementation of drift velocities and currents in SOLEDGE2D–EIRENE *Nucl. Mater. Energy* **12** 852
[24] Ribeiro T T and Scott B 2005 Tokamak turbulence computations on closed and open magnetic flux surfaces *Plasma Phys. Control. Fusion* **47** 1657
[25] Scott B D 2007 Nonlinear polarization and dissipative correspondence between low-frequency fluid and gyrofluid equations *Phys. Plasmas* **14** 102318
[26] Held M, Wiesenberger M and Kendl A 2020 Padé-based arbitrary wavelength polarization closures for full-F gyro-kinetic and -fluid models *Nucl. Fusion* **60** 066014
[27] Chang C *et al* 2017 Fast low-to-high confinement mode bifurcation dynamics in a tokamak edge plasma gyrokinetic simulation *Phys. Rev. Lett.* **118** 175001
[28] Manz P *et al* 2018 Magnetic configuration effects on the Reynolds stress in the plasma edge *Phys. Plasmas* **25** 072508
[29] Galassi D *et al* 2019 Tokamak edge plasma turbulence interaction with magnetic X-Point in 3D global simulations *Fluids* **4** 50
[30] Pitcher C S and Stangeby P C 1997 Experimental divertor physics *Plasma Phys. Control. Fusion* **39** 779
[31] Hariri F and Ottaviani M 2013 A flux-coordinate independent field-aligned approach to plasma turbulence simulations *Comput. Phys. Commun.* **184** 2419
[32] Stegmeir A *et al* 2016 The field line map approach for simulations of magnetically confined plasmas *Comput. Phys. Commun.* **198** 139
[33] Stegmeir A *et al* 2019 Global turbulence simulations of the tokamak edge region with GRILLIX *Phys. Plasmas* **26** 052517
[34] Rozhansky V *et al* 2001 Simulation of tokamak edge plasma including self-consistent electric fields *Nucl. Fusion* **41** 387
[35] Poulsen A *et al* 2020 Collisional multispecies drift fluid model *Phys. Plasmas* **27** 032305
[36] Zeiler A 1999 Tokamak edge turbulence *IPP Report* 5/88 (Garching: Max-Planck-Institut für Plasmaphysik)
[37] Scott B 2001 Low frequency fluid drift turbulence in magnetised plasmas *IPP Report* 5/92 (Garching: Max-Planck-Institut für Plasmaphysik)
[38] McCarthy D R *et al* 1993 Formation of the shear layer in toroidal edge plasma *Phys. Fluids* B **5** 1188

[39] Helander P and Sigmar D J 2002 *Collisional Transport in Magnetized Plasmas* (Cambridge: Cambridge University Press)

[40] Manz P, Ramisch M and Stroth U 2009 Experimental estimation of the dual cascade in two-dimensional drift-wave turbulence *Plasma Phys. Control. Fusion* **51** 035008

[41] Held M *et al* 2018 Non-Oberbeck–Boussinesq zonal flow generation *Nucl. Fusion* **58** 104001

[42] Gürcan O D *et al* 2007 Intrinsic rotation and electric field shear *Phys. Plasmas* **14** 042306

[43] Wensing M *et al* 2020 X-point potential well formation in diverted tokamaks with unfavorable magnetic field direction *Nucl. Fusion* **60** 054005

[44] Tskhakaya D *et al* 2008 On kinetic effects during parallel transport in the SOL *Contrib. Plasma Phys.* **48** 89

[45] Xia T Y and Xu X Q 2015 Nonlinear fluid simulation of particle and heat fluxes during burst of ELMs on DIII-D with BOUT++ code *Nucl. Fusion* **55** 113030

[46] Meyer H *et al* 2017 Overview of progress in European medium sized tokamaks towards an integrated plasma-edge/wall solution *Nucl. Fusion* **57** 102014

[47] Eich T *et al* 2018 Correlation of the tokamak H-mode density limit with ballooning stability at the separatrix *Nucl. Fusion* **58** 034001

[48] Scott B D 2005 Energetics of the interaction between electromagnetic ExB turbulence and zonal flows *New J. Phys.* **7** 92

[49] Plank U *et al* 2020 H-mode power threshold studies in mixed ion species plasmas at ASDEX Upgrade *Nucl. Fusion* **60** 074001

[50] Sauter P *et al* 2011 L- to H-mode transitions at low density in ASDEX Upgrade *Nucl. Fusion* **52** 012001

[51] Scott B D 2002 The nonlinear drift wave instability and its role in tokamak edge turbulence *New J. Phys.* **4** 52

[52] Scott B D 2003 Computation of electromagnetic turbulence and anomalous transport mechanisms in tokamak plasmas *Plasma Phys. Control. Fusion* **45** A385

[53] Jassby D L 1972 Transverse velocity shear instabilities within a magnetically confined plasma *Phys. Fluids* **15** 1590

[54] Pueschel M J, Kammerer M and Jenko F 2008 Gyrokinetic turbulence simulations at high plasma beta *Phys. Plasmas* **15** 102310

[55] Kotschenreuther M *et al* 2019 Gyrokinetic analysis and simulation of pedestals to identify the culprits for energy losses using 'fingerprints' *Nucl. Fusion* **59** 096001

[56] Hallatschek K and Zeiler A 2000 Nonlocal simulation of the transition from ballooning to ion temperature gradient mode turbulence in the tokamak edge *Phys. Plasmas* **7** 2554

[57] Dif-Pradalier G *et al* 2015 Finding the elusive E × B staircase in magnetized plasmas *Phys. Rev. Lett.* **114** 085004

[58] Manz P, Ramisch M and Stroth U 2009 Physical mechanism behind zonal-flow generation in drift-wave turbulence *Phys. Rev. Lett.* **103** 165004

[59] Schmid B *et al* 2017 Collisional scaling of the energy transfer in drift-wave zonal flow turbulence *Phys. Rev. Lett.* **118** 055001

[60] Manz P *et al* 2016 Poloidal asymmetric flow and current relaxation of ballooned transport during I-phase in ASDEX Upgrade *Phys. Plasmas* **23** 052302

[61] Zhu B, Francisquez M and Rogers B N 2017 Global 3D two-fluid simulations of the tokamak edge region: turbulence, transport, profile evolution and spontaneous E × B rotation *Phys. Plasmas* **24** 055903

[62] Stoltzfus-Dueck T 2019 Intrinsic rotation in axisymmetric devices *Plasma Phys. Control. Fusion* **61** 124003

[63] Loizu J *et al* 2014 Intrinsic toroidal rotation in the scrape-off layer of tokamaks *Phys. Plasmas* **21** 062309

[64] Wiesenberger M and Held M 2020 Angular momentum and rotational energy of mean flows in toroidal magnetic fields (arXiv:2003.02707)

[65] Xu M *et al* 2011 Generation of a sheared plasma rotation by emission, propagation and absorption of drift wave packets *Phys. Rev. Lett.* **107** 055003

[66] Shesterikov I *et al* 2012 Direct evidence of eddy breaking and tilting by edge sheared flows observed in the TEXTOR tokamak *Nucl. Fusion* **52** 042004

[67] Zholobenko W *et al* 2020 Thermal dynamics in the flux-coordinate independent turbulence code GRILLIX *Contrib. Plasma Phys.* **60** e201900131

[68] Peeters A G 1998 Stringer spin up due to anomalous transport *Phys. Plasmas* **5** 2399

[69] Zholobenko W *et al* 2020 Corrigendum: thermal dynamics in the flux-coordinate independent turbulence code GRILLIX *Contrib. Plasma Phys.* **60** e202000056

[70] Hatch D *et al* 2016 Microtearing turbulence limiting the JET-ILW pedestal *Nucl. Fusion* **56** 104003

[71] Thyagaraja A, Haas F and Cook I 1980 Temperature fluctuations and heat transfer in tokamaks *Nucl. Fusion* **20** 611

[72] Scott B 1997 Three-dimensional computation of drift Alfvén turbulence *Plasma Phys. Control. Fusion* **39** 1635

[73] De Dominici G *et al* 2019 Flux driven pedestal formation in tokamaks: turbulence simulations validated against the isotope effect (arXiv:1912.09792)

[74] Chang C S, Kue S and Weitzner H 2002 X-transport: a baseline nonambipolar transport in a diverted tokamak plasma edge *Phys. Plasmas* **9** 3884

[75] Brzozowski R W *et al* 2019 A geometric model of ion orbit loss under the influence of a radial electric field *Phys. Plasmas* **26** 042511

[76] Stegmeir A *et al* 2018 GRILLIX: a 3D turbulence code based on the flux-coordinate independent approach *Plasma Phys. Control. Fusion* **16** 035005

[77] Body T *et al* 2020 Treatment of advanced divertor configurations in the flux-coordinate independent turbulence code GRILLIX *Contrib. Plasma Phys.* **60** e201900139

A.4 The role of neutral gas in validated global edge turbulence simulations

COPYRIGHT

Wladimir Zholobenko, Andreas Stegmeir, Michael Griener, Garrard Conway, Thomas Body, David Coster, Frank Jenko, the ASDEX Upgrade Team
The role of neutral gas in validated global edge turbulence simulations
2021 *Nuclear Fusion* **61** 116015
DOI: https://doi.org/10.1088/1741-4326/ac1e61

SUMMARY

To make predictions for and design fusion reactors, a multitude of physical processes must be considered. In the edge and scrape-off layer (SOL), turbulent fluctuations intertwine with the plasma background, which is largely determined by neutral gas, and magnetic geometry plays an important role. A diffusive neutrals model has now been implemented in the global Braginskii edge turbulence code GRILLIX. The code is based on the flux-coordinate independent (FCI) approach, which allows efficient turbulence simulations in diverted equilibria. We validate simulations across the ASDEX Upgrade edge and SOL against measurements in discharge #36190, and find much better agreement thanks to the neutrals. Disentangling the effects of the neutral gas, we find that it affects the plasma in several ways. Firstly, the ionization of neutrals modifies the radial profiles of plasma density and temperature, leading to a transition of the turbulence drive from general ballooning type to ion temperature gradient (ITG) type. Secondly, strong poloidal asymmetries can be induced due to divertor recycling, depending on the ionization pattern. As ballooned perpendicular plasma transport is stronger at the low-field side, neutrals penetrate deeper into the plasma at the high-field side, leading to significant ionization and radiation there. With increasing divertor neutrals density, the targets cool down while plasma density increases, more strongly at the high-field side. Much of the dynamics takes place directly around the X-point and along the separatrix, which can be resolved by the FCI approach. Potential remains in extending the model and the code, but our results build confidence that predictive capability is within reach for major design questions for fusion reactors, such as the near SOL fall-off length.

INDIVIDUAL CONTRIBUTIONS

Leading role in realizing the scientific project.

Problem definition	*significantly contributed*
Literature survey	*significantly contributed*
Code implementation	*significantly contributed*
Carrying out the simulations	*significantly contributed*
Evaluation of the simulations	*significantly contributed*
Manuscript preparation	*significantly contributed*

PAPER • OPEN ACCESS

The role of neutral gas in validated global edge turbulence simulations

To cite this article: W. Zholobenko *et al* 2021 *Nucl. Fusion* **61** 116015

OPEN ACCESS
IOP Publishing | International Atomic Energy Agency Nuclear Fusion

Nucl. Fusion **61** (2021) 116015 (13pp) https://doi.org/10.1088/1741-4326/ac1e61

The role of neutral gas in validated global edge turbulence simulations

W. Zholobenko*, A. Stegmeir, M. Griener, G.D. Conway, T. Body, D. Coster, F. Jenko and the ASDEX Upgrade Team[a]

Max-Planck-Institut für Plasmaphysik, Boltzmannstraße 2, 85748 Garching, Germany

E-mail: Wladimir.Zholobenko@ipp.mpg.de

Received 27 May 2021, revised 22 July 2021
Accepted for publication 17 August 2021
Published 7 October 2021

Abstract

To make predictions for and design fusion reactors, a multitude of physical processes must be considered. In the edge and scrape-off layer (SOL), turbulent fluctuations intertwine with the plasma background, which is largely determined by neutral gas, and magnetic geometry plays an important role. A diffusive neutrals model has now been implemented in the global Braginskii edge turbulence code GRILLIX. The code is based on the flux-coordinate independent (FCI) approach, which allows efficient turbulence simulations in diverted equilibria. We validate simulations across the ASDEX Upgrade edge and SOL against measurements in discharge #36190, and find much better agreement thanks to the neutrals. Disentangling the effects of the neutral gas, we find that it affects the plasma in several ways. Firstly, the ionization of neutrals modifies the radial profiles of plasma density and temperature, leading to a transition of the turbulence drive from the general ballooning type to the ion temperature gradient type. Secondly, strong poloidal asymmetries can be induced due to divertor recycling, depending on the ionization pattern. As ballooned perpendicular plasma transport is stronger at the low-field side, neutrals penetrate deeper into the plasma at the high-field side, leading to significant ionization and radiation there. With increasing divertor neutrals density, the targets cool down while plasma density increases, more strongly at the high-field side. Much of the dynamics take place directly around the X-point and along the separatrix, which can be resolved by the FCI approach. Potential remains in extending the model and the code, but our results build confidence that predictive capability is within reach for major design questions for fusion reactors, such as the near SOL fall-off length.

Keywords: neutrals–plasma interaction, turbulence simulations, ASDEX Upgrade tokamak, edge and scrape-off layer, validation, Braginskii

S Supplementary material for this article is available online

(Some figures may appear in colour only in the online journal)

* Author to whom any correspondence should be addressed.

[a] See Meyer *et al* 2019 (https://doi.org/10.1088/1741-4326/ab18b8) for the ASDEX Upgrade Team.

1. Introduction

Among the key design goals for fusion reactors are manageable heat and particle exhaust at optimal core confinement, which is only possible in divertor geometry [1]. Extrapolations from today's experiments to reactors unfortunately suggest that current solutions might not suffice [2], and advanced divertor [3, 4], detachment [5, 6] and confinement [7, 8] concepts are required. Yet, in designing them, it is challenging to predict the complex nonlinear plasma response, and particularly the turbulent transport. The most reliable way is direct numerical simulations [9], and recently various methods have been developed in order to handle complex diverted geometries [10–13] in edge turbulence codes. Among them, GRILLIX [14–16] is able to perform turbulence simulations in any axisymmetric magnetic equilibrium [17] at moderate computational cost, thanks to the flux-coordinate independent (FCI), locally field-aligned discretisation [18, 19]. However, before reliable predictions can be made, the code should be validated against present experiments. GRILLIX was previously validated against the linear large plasma device (LAPD) [20] and was recently validated against diverted TCV experiments [21]. With the latest advances in the GRILLIX model, detailed below, we now perform a validation against an attached L-mode discharge in the ASDEX Upgrade (AUG) diverted tokamak.

It has long been recognised that at the plasma edge, recycling, i.e. neutralisation of the plasma at the wall and re-ionization of the neutral gas, plays a major role in establishing the density and temperature profiles [22]. Transport codes in 2D [23–25] and 3D [26] with sophisticated wall, neutral gas and impurity models [27–29] are routinely used to interpret and design experiments. However, the results substantially depend on heuristic turbulent transport models. Due to large fluctuation amplitudes in the scrape-off layer (SOL) [9, 30, 31], background evolution and turbulent fluctuations cannot be well separated, prohibiting a straightforward implementation of local turbulence models in those transport codes. Global turbulence codes that solve for turbulence and transport simultaneously, on the other hand, are complex and computationally expensive, and only recently began implementing neutral gas models [32–34].

In this contribution, we report on the implementation of a neutral gas model in the global turbulence code GRILLIX. Starting simple, the model defines source terms for plasma density, vorticity and electron temperature due to charge exchange (CX), ionization and recombination reactions between the plasma and one atomic neutrals species. The neutrals diffuse homogeneously, with their temperature assumed to be equal to the ions, modelling their microscopically ballistic motion inhibited only by CX collisions with the plasma. The plasma model consists of two-fluid drift-reduced [35] global Braginskii equations, as was lastly summarized in [16]. The only advancement from the Braginskii equations so far is the implementation of a limiter for the parallel heat conduction [36–42], the crudest possible model for Landau damping of the parallel heat flux at low collisionality, where the original Braginskii closure would break down.

With these extensions, GRILLIX is validated against AUG discharge #36190: we compare electron density and temperature profiles at the outboard mid-plane (OMP) and at the divertor, as well as the radial electric field at the OMP. Along with the comparison to the experiment, we stress the role of the neutral gas in these simulations. The primary effect is the plasma density source given by neutrals ionization, which has a non-trivial profile in the SOL and reaching to the separatrix around the X-point, particularly at the high-field side (HFS). The non-trivial source distribution leads to poloidal density asymmetries in the plasma edge. Compared to simulations without neutrals, a much flatter density profile results in the confined region. Consequently, the turbulence is driven not by general ballooning modes, but predominantly by ion temperature gradient (ITG) modes—characterised by large ion temperature fluctuations and larger ion than electron heat transport. Further, due to the dilution of the plasma by cold electrons from neutrals ionization and the accompanying radiation, the electron fluid is cooled down significantly towards the divertor plates. As plasma collisionality increases, its heat conduction is reduced and parallel temperature gradients establish. With reduced parallel heat outflow, the perpendicular turbulent transport flattens radial temperature profiles in the near SOL at the OMP, resulting in much more realistic fall-off lengths. With increasing divertor neutral density, the far SOL plasma density also rises, ultimately building a 'density shoulder' [43, 44].

The remainder of the manuscript is organized as follows. The neutral gas model is described in section 2. The implementation of the parallel heat flux limiter is documented in section 3. The simulation setup is summarised in section 4, recapitulating the basics from our previous work [16] and focusing on novel aspects concerning the neutrals and the heat flux limiter. The central results of this work—the validation of the simulations against AUG and the role of neutral gas therein—are detailed in section 5. Section 6 discusses the high-recycling regime reached at higher divertor neutrals density, and the necessary model extensions for turbulence simulations in detached conditions. Finally, conclusions and an outlook are given in section 7.

2. Neutral gas model

We consider a single ion species plasma and the corresponding neutral atoms. Molecules are currently ignored, as they are not as important in the attached tokamak conditions, due to the low dissociation energy of 4.5 eV[1]. The plasma and neutral fluids interact via the electron impact ionization and recombination reactions,

$$\mathrm{e}^- + \mathrm{D} \leftrightarrow 2\mathrm{e}^- + \mathrm{D}^+, \tag{1}$$

[1] Molecular assisted dissociation and ionization are the dominant processes [45] and should be considered as an electron cooling effect [23], but are yet negligible compared to atomic ionization and dilution. They will become important for reaching detached conditions however [22, 45, 46]: molecular assisted dissociation and ionization reduce the ionization length of particles and can lead to an up to 100% higher upstream density required to reach detachment [45], while molecular assisted recombination contributes only 10%–20% to the total recombination rate, dominated by atoms [45, 46].

and the CX process

$$\mathrm{D}^+ + \mathrm{D} \leftrightarrow \mathrm{D} + \mathrm{D}^+. \tag{2}$$

Electron impact ionization and recombination result in density exchange between the neutral (N) and ionized (n) fluids according to

$$S_n = k_{\mathrm{iz}} nN - k_{\mathrm{rec}} n^2 = -S_{\mathrm{N}}. \tag{3}$$

This source term is added to the right-hand side of the plasma continuity equation (A1) in [16]. The rate coefficients are obtained from the publicly accessible Amjuel database [47]. Note that the recombination rate is virtually irrelevant for $T_{\mathrm{e}} > 2$ eV.

Additionally, electron impact reactions affect the thermal energy of the electron fluid. For the pressure, we can write

$$\frac{3}{2}\frac{\mathrm{d}p_{\mathrm{e}}}{\mathrm{d}t} \sim -W_{\mathrm{iz}} nN - W_{\mathrm{rec}} n^2 \tag{4}$$

with electron cooling rates due to ionization W_{iz} and recombination W_{rec}. These contain both the thermal energy dissipation through radiation, due to electron impact excitation and radiative de-excitation, as well as the energy transfer of 13.6 eV between bound and free electrons. Note that the latter process cools the plasma during ionization and radiative recombination, but heats it up during three-body recombination, such that W_{rec} becomes negative at $T_{\mathrm{e}} < 1$ eV. For the electron temperature, we then obtain the source

$$S_{T_{\mathrm{e}}} = -\frac{2}{3}\left(W_{\mathrm{iz}} N + W_{\mathrm{rec}} n\right) - \left(k_{\mathrm{iz}} N - k_{\mathrm{rec}} n\right) T_{\mathrm{e}}. \tag{5}$$

The second bracket results from $\partial_t T_{\mathrm{e}} = \left(\partial_t p_{\mathrm{e}} - T_{\mathrm{e}} \partial_t n\right)/n$ and inserting S_n. $k_{\mathrm{iz}} N T_{\mathrm{e}}$ is in fact the dominant term at $T_{\mathrm{e}} > 20$ eV. It can be understood as a dilution of the hot plasma by cold, newly ionized electrons.

Charge exchange involves no transfer of internal energy and is therefore elastic, very efficiently mixing the momentum and thermal energy of the neutral and ion fluids, while conserving density. Therefore, and for simplicity, we will assume that ions and neutral atoms share the same temperature $T_{\mathrm{i}} = T_{\mathrm{N}}$ (which is strictly valid only if the CX mean free path is smaller than the T_{i} gradient length [48]). The only exception to this is right at the divertor targets: the neutrals do not thermalise instantaneously, rather having the temperature of the wall there, $T_{\mathrm{N}} \approx 0$ compared to the attached plasma conditions $T_{\mathrm{i}} \gtrsim 10$ eV. Modelling of the neutral gas temperature in more detail is complex, as the rich chemistry (including the interaction with the wall) and the relatively large mean free path prohibit the representation of the neutrals velocity space distribution by a simple local Maxwellian; usually either kinetic [28, 32] or multi-group fluid [49] treatments are required.

The primary importance of CX in our model is that this scattering process is the only one that efficiently inhibits the ballistic motion of the dilute neutrals. Similarly to [23, 49, 50], we describe the motion of the neutral gas as diffusion, with the diffusion coefficient

$$D_{\mathrm{N}} = \frac{c_{\mathrm{s,N}}^2}{\nu_{\mathrm{cx}}} = \frac{T_{\mathrm{i}}/m_{\mathrm{i}}}{k_{\mathrm{cx}} n}. \tag{6}$$

Here, $c_{\mathrm{s,N}} = \sqrt{T_{\mathrm{i}}/m_{\mathrm{i}}}$ is the neutral gas sound velocity, $m_{\mathrm{N}} \approx m_{\mathrm{i}}$ the neutrals mass, ν_{cx} the CX frequency and k_{cx} the CX rate coefficient. The latter is estimated according to equation (24) in [51] via $k_{\mathrm{cx}} = 2.93 \sigma_{\mathrm{cx}} c_{\mathrm{s,N}}$, with the hydrogen CX cross section being roughly 7×10^{-19} m^2. Additionally, as suggested by [50, 52], the diffusion coefficient is limited to keep the neutrals flux below the sound limit (in low collisionality regions of the domain), i.e. $\tilde{D}_{\mathrm{N}} = \min\left(D_{\mathrm{N}}, N T_{\mathrm{i}} c_{\mathrm{s,N}} / \left|\nabla N T_{\mathrm{i}}\right|\right)$.

The neutral particles conservation equation then becomes

$$\frac{\partial N}{\partial t} = \nabla \cdot \frac{\tilde{D}_{\mathrm{N}}}{T_{\mathrm{i}}} \nabla N T_{\mathrm{i}} - k_{\mathrm{iz}} nN + k_{\mathrm{rec}} n^2. \tag{7}$$

It is important that neutrals also diffuse along the ion temperature gradient [23, 50], as they otherwise penetrate too deep into the confined plasma. An exception to this is right at the divertor, where $T_{\mathrm{N}} \approx 0$—effectively $\nabla T_{\mathrm{i}}|_{\mathrm{div}} = 0$ in equation (7)—prevents local trapping of neutral gas between the neutrals density and ion temperature gradients.

Note that the motion of the neutral gas is isotropic, contrary to the strongly anisotropic plasma motion. The plasma flows very quickly parallel to the magnetic field, but its motion in the perpendicular direction is strongly inhibited and described by micro turbulence. To resolve this, GRILLIX uses the FCI approach with a strongly anisotropic grid, very sparse toroidally but dense in the poloidal plane. As the neutrals also move fast within the poloidal plane, this results in a stiff 2D diffusion problem. It is solved by means of the same multigrid algorithm used for the electromagnetic fields [15], taking 5%–10% of the total computing time.

We remark that the current model has little influence on the plasma parallel velocity. Due to the small electron mass, we ignore the impact of electron–neutral collisions on the momentum of the electron fluid. For the ion and neutral fluids, we assume that CX collisions are frequent enough that their parallel velocities are approximately equal and are determined by the plasma, like for the temperature. In effect, this disregards transport of parallel velocity and temperature by the neutrals. Further, the dissipation of the parallel momentum by neutrals viscosity [23], due to CX and neutral–neutral collisions, is assumed to be negligible. We expect these assumptions to be reasonable in present simulations of an attached AUG discharge, where N/n in the near-SOL does not exceed 5%. But this will need to be re-examined at higher neutrals densities, towards detachment conditions. The only effect on parallel velocity currently considered is indirect: as the temperature at the divertor drops due to the neutrals, the plasma parallel velocity at the boundaries lowers due to the Bohm sheath boundary condition.

However, we do consider the dissipation of vorticity due to the transfer of perpendicular momentum. Assuming that momentum is simply exchanged between ions and neutrals

during ionization and recombination, we find the local momentum density exchange rate

$$\frac{\mathrm{d}}{\mathrm{d}t} m_\mathrm{i} n \mathbf{v}_\mathrm{i} \sim k_\mathrm{iz} N n m_\mathrm{i} \mathbf{v}_\mathrm{N} - k_\mathrm{rec} n^2 m_\mathrm{i} \mathbf{v}_\mathrm{i} + k_\mathrm{cx} N n m_\mathrm{i} (\mathbf{v}_\mathrm{N} - \mathbf{v}_\mathrm{i}). \quad (8)$$

Rewriting this in terms of $m_\mathrm{i} n \frac{\mathrm{d}}{\mathrm{d}t}\mathbf{v}_\mathrm{i}$, adding it to the Braginskii ion equation of motion [53] and crossing it with $\times\mathbf{B}$, we obtain for the perpendicular ion velocity (in cgs units)

$$B^2 \frac{en}{c} \mathbf{v}^\mathbf{i}_\perp = -\nabla p_\mathrm{i} \times \mathbf{B} + en\mathbf{E} \times \mathbf{B} - m_\mathrm{i} n \frac{\mathrm{d}\mathbf{v}_\mathrm{i}}{\mathrm{d}t} \times \mathbf{B} - (\nabla \cdot \Pi_\mathrm{i}) \times \mathbf{B} + (k_\mathrm{iz} + k_\mathrm{cx}) N n m_\mathrm{i} (\mathbf{v}_\mathrm{N} - \mathbf{v}_\mathrm{i}) \times \mathbf{B}. \quad (9)$$

We readily identify the first two terms on the right-hand side of the equation as diamagnetic $\mathbf{v}^\mathrm{i}_*$ and $E \times B$ velocity $\mathbf{v}_E$. The remaining terms themselves depend on $\mathbf{v}^\mathbf{i}_\perp$ and are approximated in terms of diamagnetic and $E \times B$ velocities following the drift-reduction procedure [35]. The third term then becomes the polarisation velocity, crucial for turbulence, together with the fourth term, the ion stress-tensor Π_i [16]. The last term on the right-hand side is perpendicular velocity exchange between ions and neutrals. Here, we note that the neutrals mean free path $\lambda_\mathrm{N} = c_\mathrm{s,N}/\nu_\mathrm{cx}$ is much larger than the relevant perpendicular scale for the plasma, the Larmor radius. Therefore, we have $\nabla \cdot \mathbf{v}_\mathrm{N} \ll \nabla \cdot \mathbf{v}_\mathrm{i}$ and can ignore the neutrals velocity here, i.e. the vorticity source due to momentum gain from neutrals [32, 54]. Finally, we obtain the vorticity sink due to momentum loss to neutrals as

$$S_\Omega = -\nabla \cdot \left[\frac{m_\mathrm{i} c^2 n N}{eB^2} (k_\mathrm{iz} + k_\mathrm{cx}) \left(\nabla_\perp \varphi + \frac{\nabla_\perp p_\mathrm{i}}{en} \right) \right]. \quad (10)$$

This sink is added to the right-hand side of the vorticity equation (A2); see the appendix in [16]. Under a Boussinesq type approximation, which we do not apply, this is roughly $S_\Omega \approx -\frac{\nu_\mathrm{iz}+\nu_\mathrm{cx}}{\omega_\mathrm{ci}} N \Omega_\mathrm{F}$, with $\omega_\mathrm{ci} = eB/m_\mathrm{i}c$, $\nu_\mathrm{iz} = nk_\mathrm{iz}$ and the fluid vorticity $\Omega_\mathrm{F} = \mathbf{b} \cdot \nabla \times \left(\mathbf{v}_E + \mathbf{v}^\mathrm{i}_* \right)$. This vorticity sink has been found to be important in situations with high neutrals densities, e.g. in linear devices [55] and in detached tokamak conditions [56]. But in our simulations so far, we have not observed a significant effect yet.

As a last point, the biggest limitations of the model are the boundary conditions. We currently only implement Dirichlet and homogeneous Neumann boundary conditions: zero flux at the main chamber wall, zero neutrals density at the core boundary and a fixed neutrals density N_div at the divertor. With this, N_div must be scanned to obtain global recycling, i.e. plasma density sourced to $\sim 99\%$ by neutral gas ionization, as detailed in section 4 (main chamber recycling is neglected, as suggested by transport studies [57]). Local recycling boundary conditions [23] will be implemented in the near future, demanding adaptations to the code structure: the challenge here is that neutrals are much more mobile across flux surfaces than the plasma, requiring boundary conditions on the perpendicular rather than on the parallel fluxes. We note that the divertor neutrals density as a free parameter is likely to mask the general simplicity of the current neutrals model, ignoring the effects of neutrals viscosity, details of their velocity distribution, molecules and details of the plasma–wall–neutrals interaction (including gas puffing, pumping, outgassing, etc). On one hand, this avoids the problem of possibly long saturation times due to local recycling [58] and allows a relatively good match to the experiment with a very simple neutrals model, such that qualitative effects can already be studied in relevant conditions. On the other hand, predictive simulations will require a more complete model without free parameters.

3. Plasma model improvements

For the plasma, the global drift reduced Braginskii model is employed in GRILLIX. It can handle arbitrary fluctuation levels (no δf splitting), features electromagnetic effects and electron/ion thermal dynamics. The model has been comprehensively summarised in the appendix of [16]. Here, some additional improvements are outlined.

The Braginskii heat conductivities $\chi^\mathrm{e}_\parallel = 3.16 n T_\mathrm{e} \tau_\mathrm{e}/m_\mathrm{e} \sim T_\mathrm{e}^{5/2}$ and $\chi^\mathrm{i}_\parallel = 3.9 n T_\mathrm{i} \tau_\mathrm{i}/m_\mathrm{i} \sim T_\mathrm{i}^{5/2}$ [53] are known to be inappropriate at low collisionality [24, 40, 41]. In this work, we will limit them by a harmonic average between the Braginskii and the free streaming heat flux, $\tilde{q} = \left(\frac{1}{|q_\mathrm{Braginskii}|} + \frac{1}{q_\mathrm{FS}} \right)^{-1}$, with $q_\mathrm{FS} = \alpha n \sqrt{T/m} T$ (see chapter 26.2 in [38]). For the heat conduction, this can be rewritten as

$$\begin{aligned} \tilde{\chi}^{\mathrm{e,\,i}}_\parallel &= \chi^{\mathrm{e,\,i}}_\parallel \left(1 + \frac{|q_\mathrm{Braginskii}|}{q_\mathrm{FS}} \right)^{-1} \\ &= \chi^{\mathrm{e,\,i}}_\parallel \left(1 + \frac{\chi^{\mathrm{e,\,i}}_\parallel |\nabla_\parallel T|}{\alpha n \sqrt{T/m} T} \right)^{-1} \\ &\approx \chi^{\mathrm{e,\,i}}_\parallel \left(1 + \frac{\chi^{\mathrm{e,\,i}}_\parallel}{\alpha_{\mathrm{e,\,i}} n \sqrt{T_{\mathrm{e,\,i}}/m_{\mathrm{e,\,i}}} R_0 q} \right)^{-1}. \end{aligned} \quad (11)$$

In the last expression, we have approximated $\left| \nabla_\parallel T_{\mathrm{e,\,i}} \right| / T_{\mathrm{e,\,i}} \approx 1/qR_0$ with the machine major radius R_0 and the safety factor q, to avoid the non-linearity in $\nabla_\parallel T$ in the temperature equation. To avoid issues with the diverging safety factor at the separatrix, it is set to constantly $q = 4$. Note that due to the mass factor, the limiter is more severe for ions than for electrons. This Knudsen correction [36] is frequently used in literature [37, 39, 41] and constitutes a first step towards a Landau fluid close [42, 59], but similarly to previous work [41], we will find a significant dependence of simulation results on the free parameter $\alpha_\mathrm{e,i}$.

Besides changing the expression for the parallel heat flux according to (11), we also modify the electron temperature boundary condition $\nabla_\parallel \log(T_\mathrm{e}) = -\gamma_\mathrm{e} n u_\parallel / \chi^\mathrm{e}_\parallel$ at the divertor: taking into account a finite secondary electron emission coefficient [38] of roughly 0.75, we set $\gamma_\mathrm{e} = 1$ (instead of 2.5). For the ions, we keep $\nabla_\parallel \log(T_\mathrm{i}) = 0$.

Finally, we note that unlike in our previous work, viscous ion heating is less pronounced and poses no stability issues any more because of increased collisionality due to neutrals. Due to previous concerns [16], the reference simulation in the present work has also been run without viscous ion heating.

But we have repeated the simulation with viscous ion heating on and found only a small effect, 7% higher ion temperature at the OMP separatrix with an otherwise identical profile.

4. Simulation setup

We briefly recapitulate the simulation setup, detailed in section 3.1 of [16], and then describe the additional challenges in the present work due to the extensions discussed above. The simulations are based on and compared to AUG discharge #36190 (at 2–4 s), an attached L-mode with 800 kA plasma current, $q_{95} = 4.4$ and average triangularity of $\delta = 0.21$. The toroidal magnetic field is $B_{\mathrm{tor}} = -2.5$ T on the axis, i.e. in the favourable configuration with $\mathbf{B} \times \nabla B \sim -\hat{\mathbf{e}}_Z$ towards the divertor X-point. The plasma is heated by 550 kW neutral beam injection and 500 kW ohmic heating, whereby 300 kW are radiated away by impurities.

The magnetic geometry is a lower single null diverted equilibrium, reconstructed from the AUG discharge #36190 at 3.3 s. The simulated domain extends from the core boundary at $\rho_{\mathrm{pol}} = 0.9$ and across the separatrix to $\rho_{\mathrm{pol}} = 1.05$. The outer radial boundary is at the last flux surface intersected by the machine main chamber wall. The artificial core boundary is chosen to be far enough away from the separatrix to not pollute the dynamics there, but not too far into the collisionless plasma core where the fluid model loses its validity. At the core boundary, an adaptive source keeps fixed density and temperature values based on the experiment ($n_{\mathrm{ped}} = 2 \times 10^{19}$ m^{-3} and $T^{\mathrm{e,\,i}}_{\mathrm{ped}} = 350$ eV), but a zonal Neumann boundary condition allows the potential to float [60]—in the rest of the domain, plasma profiles are free to evolve self-consistently.

The difference to the previous setup is that the plasma model shown in the appendix of [16] has been extended by the diffusive neutral gas model described in section 2. Additionally, we have improved the limiter for the parallel conductive Braginskii heat flux, as explained in section 3. Both additions introduce free parameters: the divertor neutrals density N_{div}, and the free streaming parallel heat conduction limiters $\alpha_{\mathrm{e,i}}$. The computational cost of 83 kCPUh per 1 ms simulation allows us to roughly adjust these parameters, and investigate their role. However, the simulations must run for at least 3–4 ms, which takes a few months due to the as yet limited parallelizability of the code (in practice, 384 Intel SkyLake CPU cores were used simultaneously per simulation). Therefore, fine tuning was not possible, and we have limited ourselves to a relatively coarse resolution of 16 poloidal planes and a grid distance of 1.45 mm within each plane, totalling 7 million grid points. We have previously found this to be sufficient to resolve the overall transport and profile evolution [16].

The neutral gas model has a major impact on the simulations. Most importantly, the dominant plasma density source is now shifted from the core boundary at $\rho_{\mathrm{pol}} = 0.9$ to the separatrix and SOL, where neutrals are ionized. The ionization source depends on the local neutrals density, which is not obtained in a fully self-consistent way, as local recycling boundary conditions are not yet implemented: a fixed neutrals density N_{div} must be prescribed via a Dirichlet boundary

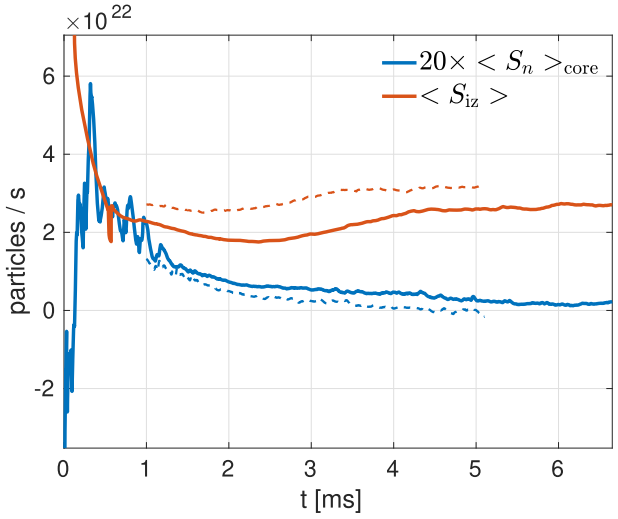

Figure 1. Time evolution of the volume integrated core particles source S_n magnified by 20 to be compared with the ionization particle source S_{iz}. Solid line: reference simulation with $N_{\mathrm{div}} = 5 \times 10^{17}$ m^{-3}, dashed line: $N_{\mathrm{div}} = 8 \times 10^{17}$ m^{-3}.

condition at the divertor, the neutrals then expand into the interior domain according to the diffusion model described in section 2 and are ionized according to Amjuel [47] reaction rate coefficients. Recycling is then obtained in a global sense by scanning and adjusting the N_{div} parameter. Note that the adaptive source at the core boundary still holds the plasma density fixed there at 2×10^{19} m^{-3}, but the goal is that the required source strength saturates between 0%–1% of the ionization source. Figure 1 shows the time evolution of the volume integrated core particle source S_n compared to the integrated ionization source S_{iz} in our reference simulation with $N_{\mathrm{div}} = 5 \times 10^{17}$ m^{-3}. The initial spike in S_{iz} is due to the initial condition on the neutrals density N, which is constant in the whole domain and equal to N_{div}. After the initial transient phase, S_{iz} increases and S_n decreases as more heat is arriving at the divertor. After saturation at $t \approx 4$ ms, we have $S_n/S_{\mathrm{iz}} \approx 0.5\%$, i.e. 99.5% recycling. For comparison, the dashed line shows the evolution of the density sources for $N_{\mathrm{div}} = 8 \times 10^{17}$ m^{-3}. Once S_n gets too close to zero, the separatrix density becomes too high and simulations become unstable due to resistive ballooning modes [61, 62].

Figure 2 shows the input power at the core boundary of the simulation evolving in time, which is required to maintain the fixed pressure there due to turbulent radial heat outflow. After 4 ms in the reference simulation, it is at about 100 kW for electrons and 430 kW for ions, which is in reasonable agreement with the 750 kW net heating in the experiment (after the subtraction of the 300 kW radiated by impurities, as those are not present in the simulation). With varying divertor neutrals density, we were able to change the input power by at most 5%. However, the input power is sensitive to the free streaming limiter $\alpha_{\mathrm{e,i}}$ for the parallel conductive heat flux, introduced in section 3. In the reference simulation, $\alpha_{\mathrm{e,i}} = 1$ as suggested by [37, 59]. But choosing $\alpha_{\mathrm{e,i}} = 0.1$ increases the total heat transport to about 2 MW, as shown by the dashed lines in figure 2. On the other hand, only limiting the electron and ion heat

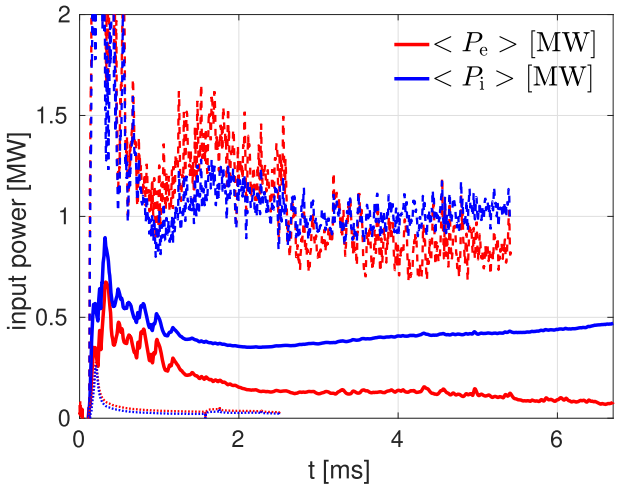

Figure 2. Input power at the core boundary of the simulation as a function of time. Solid lines show the reference simulation ($\alpha_{e,i} = 1$), and dashed lines show the input power at $\alpha_{e,i} = 0.1$. The dotted lines show the input power without a free-streaming flux limit, but with $\chi_{\parallel}^{e,i} \leqslant 10^{27} \mathrm{m}^{-1}\ \mathrm{s}^{-1}$ (see text).

conductivities to $\chi_{\parallel}^{e,i} \leqslant 10^{27}\ \mathrm{m}^{-1}\ \mathrm{s}^{-1}$ as was done in simulations without neutrals [16] leads to barely 34 kW electron and 26 kW ion heat transport: as noted in section 3, the free streaming limiter is much stronger for ions than for electrons—therefore, the simple limiter allows a particularly large parallel ion heat flux (still smaller than for electrons, though), which suppresses ITG turbulence [63]. Hence, we conclude that better agreement in net heat transport to the experiment—and potentially OMP temperature profiles shown in figure 3—might be achieved by fine tuned $\alpha_{e,i}$, but reasonable results have already been obtained with $\alpha_{e,i} = 1$. Rather, in future, we will consider further extending the fluid closure to better approximate Landau damping, e.g. as in [64].

5. Validation of attached L-mode AUG simulations

After discussing the recent model extensions and the simulation setup, we can now present simulation results. As in our previous work without neutrals [16], the simulations saturate after 4 ms in the sense that mean profiles do not visibly change any more, at least over the next few ms (they might change on time scales > 10 ms, but such long simulations are currently out of scope). At this stage, we can separate the mean and the fluctuating parts of the fields by time and toroidal averaging and analyse them. In the following sections, we will compare mean density, temperature and electric field profiles in the reference simulation with $N_{div} = 5 \times 10^{17}\ \mathrm{m}^{-3}$ to experimental measurements, as well as to simulations without neutrals and with higher divertor neutrals density. Besides analysing OMP and divertor pressure profiles, we discuss the 2D density profile in a poloidal plane, its asymmetry due to the ionization source distribution and the consequences of the density profile on fluctuation amplitudes. Additionally, for the reference simulation, supplementary movie 1 https://stacks.iop.org/NF/61/116015/mmedia shows the evolution of plasma density in a poloidal cross section, as well as the radial electric field at the OMP. Supplementary movie 2 shows the dynamics in high-recycling conditions, as discussed in section 6.

5.1. Outboard mid-plane profiles

Figure 3 shows the comparison between the simulated and experimentally measured density and electron temperature at the OMP. The measured data result from integrated data analysis [65] of electron cyclotron emission, interferometry, Thomson scattering, lithium and helium beam spectroscopy at 3.25–3.35 s of AUG discharge #36190. For the simulation, we average the profiles toroidally and in time over 200 μs. We show both the simulation profiles from [16] without neutrals (blue dashed lines), as well as the new results with neutral gas ionization (in red). Although no reliable ion temperature measurements are available for this discharge, we show the simulated T_i together with T_e, as the ion heat channel is important for the L–H transition [66].

The main observation is that both the density and electron temperature profiles become much more realistic with the neutral gas model. Without neutrals, with plasma density being sourced to 100% at the core boundary, a steep density gradient builds up as plasma is flowing out in the SOL at the divertor. With neutrals, the density source is localised around the separatrix, and a much more realistic profile results. The radial oscillation on top of the profile—observed both experimentally and in simulations—is stationary over many ms but slowly varying over hundreds of ms and explained in simulations by a zonal flow [16].

For electron temperature, it turned out in the aftermath that we chose a slightly too high core boundary temperature, 350 eV instead of 300 eV as measured experimentally. While this does result in a somewhat steeper gradient in the confined region, the profile at the separatrix is actually close to the experiment—and very different from the profile without neutrals. The reason is partly the different density profile, leading to a different turbulence drive as explained in section 5.4. But the neutral gas also directly influences the temperature according to equation (5): while recombination is virtually absent as T_e does not fall below 1 eV, ionization is effectively cooling the plasma in regions of significant neutrals density (see section 5.2). The colder divertor, as detailed in section 5.3, reduces the parallel heat conductivity, allowing for significant parallel gradients in the SOL and reducing the direct parallel heat outflow at the OMP separatrix. As the OMP temperature profile is determined by the competition between perpendicular turbulent transport and parallel conductive outflow, reducing the latter flattens the radial T_e profile and results in much more realistic SOL fall-off lengths.

5.2. Ionisation pattern and poloidal asymmetry

While the density profile agrees well with experimental measurements at the OMP, it exhibits a surprising amount of poloidal asymmetry, even in the confined region. The 2D density profile in the poloidal cross section at 4 ms simulation time is displayed in figure 4. We see that density is higher at the

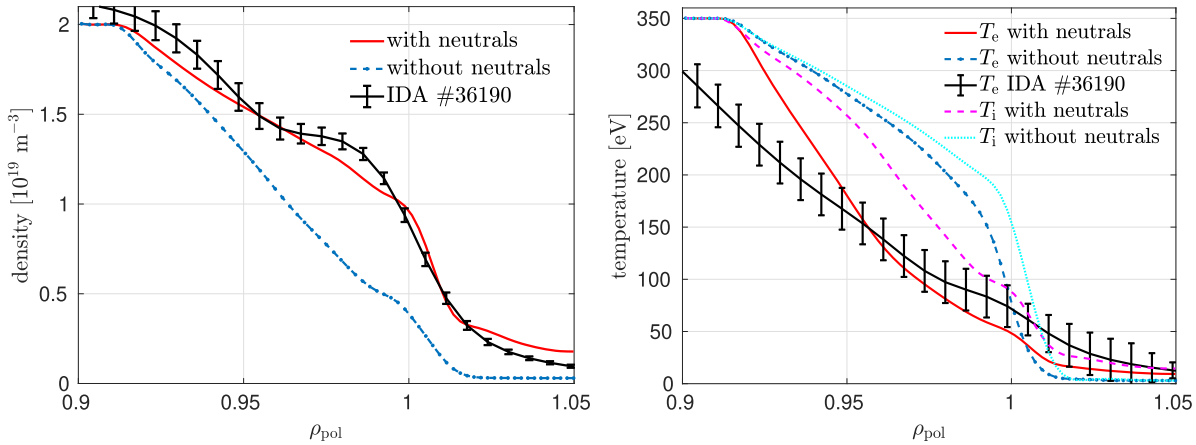

Figure 3. Validation of GRILLIX simulations against integrated data analysis from ASDEX Upgrade discharge #36190 (3.25–3.35 s), at the outboard mid-plane, comparing the model with neutral gas ionization ($N_{\mathrm{div}} = 5 \times 10^{17}$ m^{-3}) against core boundary density sourcing (i.e. without neutrals) from [16]. Reliable measurement are available only for T_e, but we also show the simulated T_i.

HFS and lower at the low-field side (LFS), peaking near the *X*-point at the HFS. The reason for this is partly the density source distribution due to ionization: on the right of figure 4, we show the mean deuterium radiation density around the *X*-point, which has the same spacial distribution as the ionization rate. On the LFS, it peaks near the divertor target where the neutrals density is highest, and otherwise has a broad distribution around the heat channel close to the separatrix. On the HFS, ionization peaks further upstream, very close to the separatrix.

The difference in radiation and ionization patterns between LFS and HFS is due to the ballooned perpendicular turbulent transport being much stronger at the LFS, broadening the SOL profile there and leading to significant fluxes to the LFS divertor. On the HFS, much less power crosses the separatrix at the inboard mid-plane, allowing the neutrals to penetrate deeper into the plasma. They are then ionized slightly below the separatrix as the confined plasma is slightly shifted downwards due to the $\mathbf{B} \times \nabla B$ drift. This becomes particularly clear from a comparable simulation in unfavourable configurations, where the plasma is shifted upward and barely any heat at all reaches the HFS divertor and the neutrals front extends into the confined region.

The density profile is determined not only by the HFS–LFS and up-down asymmetric source distribution, but also by transport between sources and sinks. Around the *X*-point, the density gradient in the confined region is reversed, i.e. ascending towards the separatrix, and a mean radial $E \times B$ flow brings density from the source region into the confined plasma. Plasma density peaks at the *X*-point, accumulating there due to the long parallel connection length. As we will discuss in section 5.5, the mean poloidal $E \times B$ rotation in the anticlockwise direction (enhanced by the poloidally asymmetric density source from ionization) brings the density from the *X*-point to the OMP. Along the way, ITG driven turbulent transport (see section 5.4) tends to eject density together with the heat again, resulting in a descending density slope at the OMP as shown in figure 3. In a zonal average, however, the outward transport is only as strong as to keep the zonal average density gradient flat, hence the overall ITG transport. Overall, this results in a somewhat higher density at the HFS OMP than on the LFS. This asymmetry might be overestimated though, as the parallel ion flow might be too strongly damped by the Braginskii ion viscosity [67]. Also, these results are not fully self-consistent yet, as equal neutrals density is prescribed at both divertor plates. Therefore, while current simulations show that poloidal asymmetries can arise from the ionization source distribution, the details must be more closely investigated in future work. Nevertheless, the relatively good agreement between measured and simulated density profiles at the OMP is encouraging.

5.3. Divertor target profiles

In section 5.1, we have seen relatively good agreement with the experiment at the OMP thanks to our neutrals model. However, recycling is implemented only in a global sense, with a constant divertor neutrals density N_{div} across both divertor plates. Therefore, less good agreement is expected at the target plates. Nevertheless, figure 5 generally shows a significant improvement with the neutrals model.

Without neutrals the density is below 2×10^{18} m^{-3}, and the parallel temperature profile in the SOL is flat resulting in nearly identical radial profiles at HFS, LFS and OMP with a peak temperature of 70 eV. With neutrals, due to dilution of the plasma and radiation, the divertor temperature decreases. At the same time, the plasma density increases, sourced by neutrals ionization. The increased collisionality and therefore decreased parallel heat conduction reduce the parallel heat flux and allow turbulence to spread the heat further radially, broadening the temperature profile at both the divertor targets and OMP. Remarkably, even at identical neutrals density of $N_{\mathrm{div}} = 5 \times 10^{17}$ m^{-3} at both divertor plates, we find an in-out asymmetry: as neutrals are ionized deeper in the plasma at the HFS, the plasma density increases more strongly there, while electron temperature falls lower than at the LFS.

Experimentally, an even larger in-out asymmetry is observed, suggesting that neutrals should have a higher density at the HFS than at the LFS divertor. The mismatch

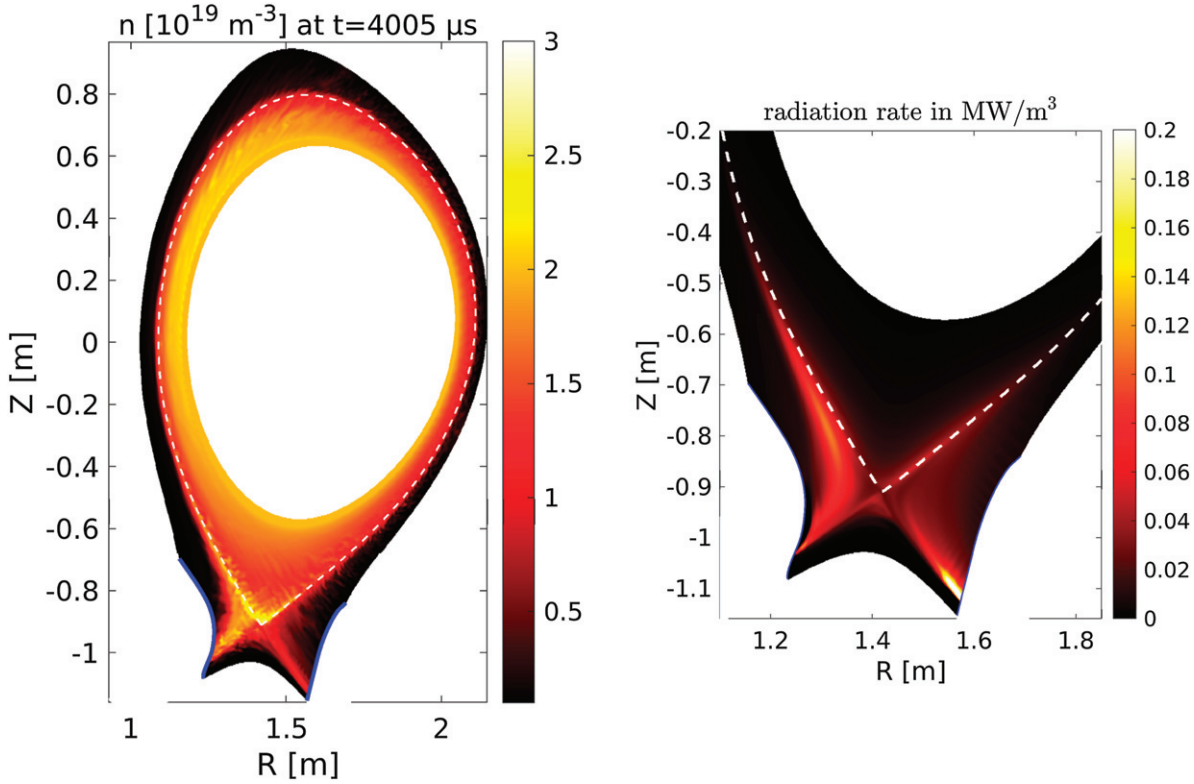

Figure 4. (Left) 2D density snapshot in the poloidal cross section for the quasi-steady state at 4 ms of the reference simulation. See supplementary movie 1 for the dynamics. (Right) Mean deuterium radiation density.

in the plasma density profiles also indicates that the neutrals density might be inhomogeneous across the target plates, motivating the implementation of local recycling boundary conditions. However, the profiles are closer to experimental ones than without neutrals at all, most remarkably the peak density at the HFS and the temperature at the LFS. Turbulent fluctuations of up to 40% in the simulations also partly explain the fluctuations in experimental measurements, particularly close to the separatrix, while experimental uncertainties in the far SOL might still be affected by noise.

A simulation with higher $N_{\mathrm{div}} = 3 \times 10^{18}$ m^{-3} improves the match in the HFS temperature profile, corroborating that HFS divertor neutrals density should be higher than at the LFS, but it impairs the LFS temperature comparison and produces too high a plasma density. As discussed above, N_{div} had to be scanned to achieve global recycling, but high neutrals density simulations were also an attempt to reach detached conditions, though they did not run stable to saturation as will be discussed in section 6.

5.4. Fluctuation amplitudes and turbulence characterisation

After having investigated the mean density and temperature profiles, we should also discuss their fluctuations. They are quantified by the standard deviation of an ensemble, here a time series and profiles in toroidal direction, normalised to the mean. The fluctuations at the divertor have been indicated in figure 5 in the previous section. Here, we discuss fluctuation amplitudes at the OMP, shown in figure 6. For turbulence characterisation, fluctuations of the electrostatic potential are important. They are commonly normalised to the mean electron temperature [30, 31], because the mean electrostatic potential becomes zero in some places.

The most remarkable observation is how different the fluctuation amplitudes are compared to simulations without neutrals (see figure 5(c) in [16]). Electrostatic potential fluctuations are still the largest, indicating that interchange modes are dominant. However, without neutrals, they were followed by density fluctuations, while with neutrals, density fluctuations are the smallest in the confined region, compared to temperature fluctuations. The reason is the shift of the density source from the core boundary to the separatrix, which, as we discussed in section 5.2, leads to a flat density gradient in the zonal average. Instead, turbulence is now rather driven by the temperature gradients, of which the ion temperature gradient leads to the largest fluctuations due to the η_{i} mode [69, 70]. The mode is typically triggered at $\eta_{\mathrm{i}} = L_n/L_{T_{\mathrm{i}}} = \partial_{\mathrm{r}} \ln T_{\mathrm{i}}/\partial_{\mathrm{r}} \ln n > 1$. Without neutrals, we had $\eta_{\mathrm{i}} < 1$ for $\rho_{\mathrm{pol}} < 0.997$ at the OMP (0.5 on average). With neutrals, we have $\eta_{\mathrm{i}} > 1$ in the whole confined region, reaching 4 at $\rho_{\mathrm{pol}} = 0.96$ at the OMP (2.2 on average). Therefore, together with the observation of the dominating T_{i} fluctuations, we conclude that the ITG instability is now dominant in the confined region[2] [73, 74]. In the SOL,

[2] In the plasma edge, electrons are generally not adiabatic, which can lead to comparable electron and ion heat fluxes even under ITG turbulence [71]. A difference in radial heat diffusivity of $\chi_{\mathrm{e}}/\chi_{\mathrm{i}} = 1/4 - 1$ is expected [72, table 1]. This fits with the heat fluxes observed in figure 2, but the dependence on the parallel conduction limiter $\alpha_{\mathrm{e,i}}$ will require further studies.

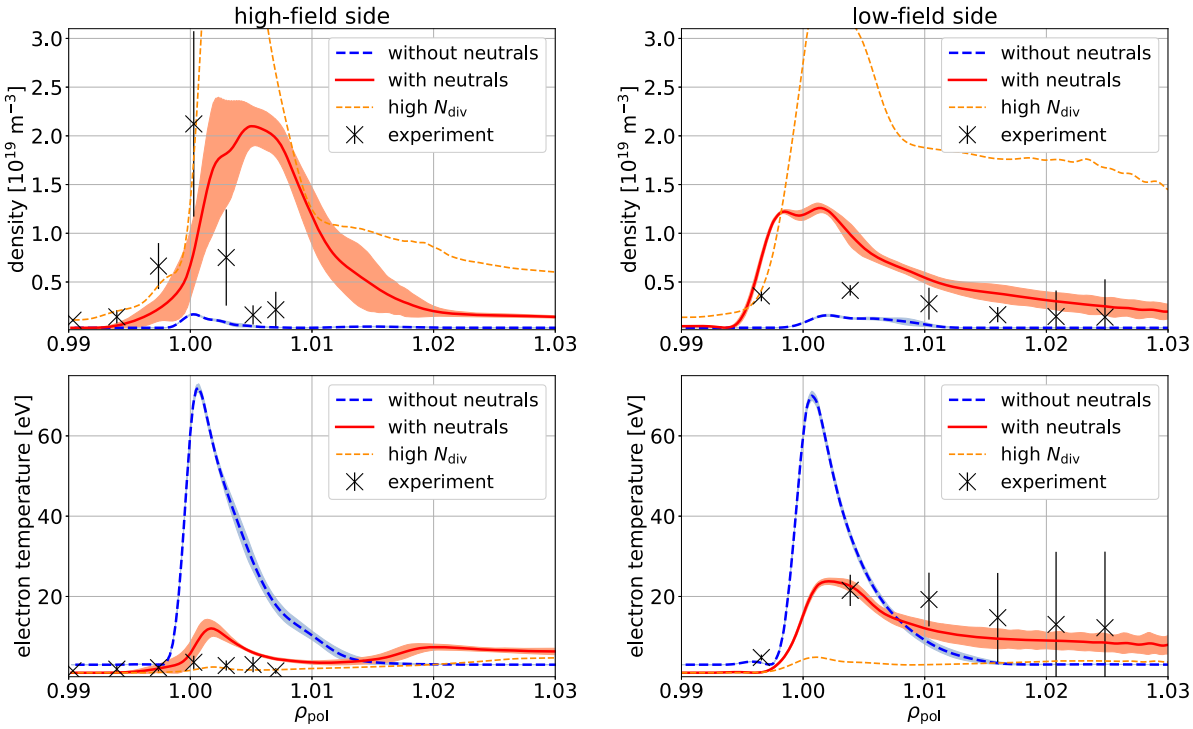

Figure 5. GRILLIX divertor profiles, comparing the reference simulation with $N_{div} = 5 \times 10^{17}$ m^{-3} (red curve) against core boundary density sourcing (i.e. without neutrals, blue dashed curve) from [16]. The dashed orange line shows results from a simulation with increased divertor neutrals density, $N_{div} = 3 \times 10^{18}$ m^{-3}. Simulation results are compared to Langmuir probe measurements [68] from ASDEX Upgrade discharge #36190 (3.3–3.4 s). HFS profiles are on the left, LFS profiles are on the right. The error bars on experimental data points indicate two standard deviations both due to turbulent fluctuations and diagnostic noise. The envelops around simulated profiles show two standard deviations of turbulent fluctuations.

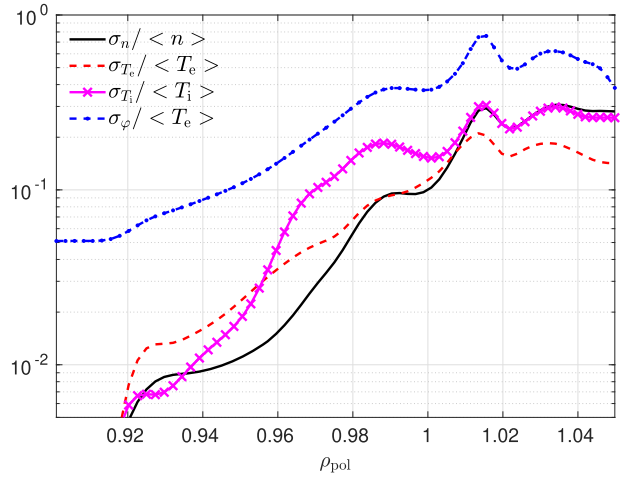

Figure 6. Outboard mid-plane fluctuation amplitudes. $\sigma_f^2 = \langle f^2 \rangle - \langle f \rangle^2$, the average is performed toroidally and in time over 200 μs.

$\eta_i \sim 1$ and the fluctuation amplitudes for density and temperatures are comparable, so here all of them participate in the turbulence drive.

5.5. Radial electric field

One of the key mechanisms regulating turbulent transport are sheared poloidal $E \times B$ flows. Previously, we have investigated theoretically which mechanisms contribute to the formation of a mean radial electric field [16]. With the recent implementation of a neutral gas model, satisfactory agreement in OMP density and temperature profiles with the experiment is obtained. Therefore, it is worthwhile to also compare the mean radial electric field in the experiment and in the simulation (again with and without neutral gas), as shown in figure 7. In the experiment, the edge $E_r \propto \omega_D$ was measured using Doppler reflectometry where the Doppler frequency shift ω_D is obtained from tracer density fluctuations under the assumption that the turbulence phase velocity (few hundred ms^{-1}) is small compared to the main $E_r \times B$ velocity (few kms^{-1}), i.e. $v_{E\times B} \gg v_{ph}$ [75].

Unlike for density and temperature profiles, the comparison of the electric field is not that satisfactory. In the SOL, the radial electric field is determined by sheath boundary conditions at the divertor, following $E_r|_{SOL} \sim -3\partial_r T_e|_{div}$, and parallel current dynamics described by Ohm's law. With neutral gas, the temperature at the divertor is reduced and its gradient flattens. Additionally, the increased resistivity allows for the establishment of parallel gradients, including a parallel electric field [76]. As a result, a much more realistic mean radial electric field at the OMP is obtained than without neutrals, but still a factor of two larger than in the experiment. The remaining discrepancy is likely due to not yet fully realistic boundary conditions at the divertor plates.

In the confined region, without neutrals, we have previously found the time averaged radial electric field to be determined by a combination of the ion pressure gradient, zonal flows

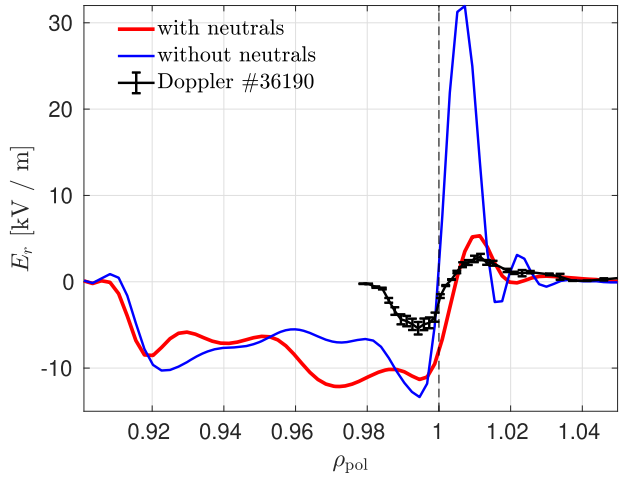

Figure 7. Outboard mid-plane radial electric field in simulations with and without neutrals, in comparison to Doppler reflectometry measurements at 2.235 to 2.635 s of the discharge.

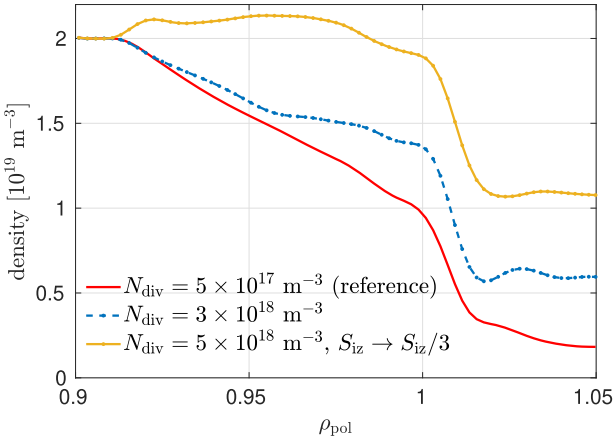

Figure 8. Outboard mid-plane plasma density as a function of divertor neutrals density. The reference simulation validated against AUG #36190 had $N_{\rm div} = 5 \times 10^{17}$ m^{-3}, the simulations with increased $N_{\rm div}$ only run stable if the ionization rate is also reduced.

and toroidal rotation [16]: $\langle E_{\rm r} \rangle_t \approx \left\langle \frac{\partial_{\rm r} p_i}{en} \right\rangle_t + \frac{m_{\rm e}}{e} \langle \mathbf{u} \cdot \nabla \mathbf{u} \rangle_t \cdot \mathbf{e}_{\rm r} + \left\langle u_{\parallel} B_\theta \right\rangle_t$. These terms did not change significantly with the neutrals, but the poloidally asymmetric density source from their ionization entering the ion continuity equation does sustain an additional mean poloidal rotation [24]. The mean radial electric field stabilizes the stationary plasma background, but leads to a poloidal $E \times B$ rotation of turbulent filaments in the anti-clockwise direction in the confined region, and in the clockwise direction in the SOL, with the flow shear peaking at the separatrix.

The discrepancy in the radial electric field between simulation and experiment suggests that a refinement of the fluid model is required. Previously, we have seen that fluid closure terms have a huge impact: the parallel ion viscosity by regulating poloidal rotation, and parallel ion and electron heat conductivities by regulating the zonal flow [16]. Future work will therefore be directed towards an ion viscosity consistent with neoclassical theory across all collisionality regimes [24, 77], and a more refined Landau fluid closure for the parallel heat flows [64].

6. Towards high-recycling and plasma detachment

One of the main challenges for fusion reactors is to maintain manageable heat loads on the divertors. In achieving this, it is unavoidable that a major part of the heat passing the separatrix has to be radiated away before reaching the targets, and the remainder shall be spread across the target area as evenly and widely as possible. As we see in figure 4, a fraction of the input power—45 kW—is radiated away by deuterium, even in attached conditions. Bolometry measurements suggest that, additionally, 300 kW are radiated away by impurities (predominantly nitrogen), currently not contained in our simulation. However, the majority of the heat (roughly 500 kW) still reaches the targets.

The radiation capability of neutral gas is limited above a few eV plasma temperature, as particles are directly ionized away before emitting radiation. Nevertheless, ionization has a huge impact on the plasma: although total pressure is largely maintained, by raising the density while reducing the temperature the plasma collisionality is increased, as discussed in section 5.3. One of the consequences of increased collisionality is a reduced parallel heat conduction, which, as we have seen in figure 3, leads to much more realistic (broader) OMP temperature profiles. Therefore, even in attached conditions, neutral gas recycling has a major role on the plasma state. Notably, as assumed in this work and confirmed in transport studies [57], main chamber recycling plays a negligible role compared to divertor recycling.

Is it possible to decrease the heat flux on the divertor targets further by increasing the divertor neutrals density $N_{\rm div}$? Indeed, as we have shown in figure 5, for $N_{\rm div} = 3 \times 10^{18}$ m^{-3} the target electron temperature can be decreased below 5 eV, with deuterium radiation increasing to 170 kW. However, figure 5 also shows that at the same time, plasma density is considerably increased. Not only does this not reduce the total target heat flux significantly, as even at low temperatures we must also consider the energy released per ion recombining at the surface (13.6 eV). Increased density also has detrimental consequences for the main chamber wall. As we have seen in section 5.2, the ionization source is localised close to the separatrix, particularly at the HFS. At higher divertor neutrals density, not only does the divertor plasma density increase, but the density increase spreads through the whole domain. The density profile at the OMP is shown in figure 8. With increased neutrals recycling, the density gradient flattens in both the confined region and in the far SOL, while the density gradient in the near SOL remains similar. For the far SOL, this is known as density shoulder formation and is indeed found in detached plasmas [43, 44]. Increased far SOL density leads to higher fluxes to the main chamber wall, accelerating its erosion. Therefore, it is of interest to find exhaust solutions avoiding this.

An important constraint for turbulence simulations is that they are not unconditionally stable. In the near SOL, we

observe large fluctuation amplitudes in both density and temperatures, characteristic of resistive-ballooning modes. With increasing separatrix density and collisionality, these modes can become strongly unstable, leading to a density limit [61, 62]. For this reason, our simulations with $N_{\mathrm{div}} > 10^{18}$ m^{-3} were not able to reach a saturated state, unless the ionization rate coefficient is also decreased, as we found out incidentally. While the simulation with $N_{\mathrm{div}} = 3 \times 10^{18}$ m^{-3} crashed after 1.5 ms, the simulation with $N_{\mathrm{div}} = 5 \times 10^{18}$ m^{-3} and a three times lower ionization rate ran stable for more than 3 ms. The reason is not fully clear, as it is difficult to distinguish between physical and numerical stability in nonlinear simulations. However, at lowered ionization rates the neutrals penetrate deeper into the plasma, moving the ionization front. At the HFS, it moves deeper into the confined region, flattening completely the density profile there (in fact, the core density source goes negative to hold the fixed density). In this regime, radial heat transport in the confined region becomes carried exclusively by the ions due to the ITG. At the LFS, the ionization front moves up and thereby more from the separatrix to the far SOL (but remains close to the divertor). Physically, a lowered ionization rate can be achieved by lowering the electron temperature in another way than by a density increase. The remarkably violent dynamics in this simulation can be observed in supplementary movie 2.

We conclude that further extensions are required for GRILLIX to be able to simulate detached conditions, most notably impurity radiation: to avoid an excessive increase of plasma density, leading to a density shoulder formation [43, 44] and the resistive-ballooning density limit [61, 62], the electron temperature must be lowered by other means. Additionally, we expect that parallel momentum losses due to ion–neutral friction/viscosity are required to allow plasma recombination to set in [23, 78], which would reduce the plasma density and hence the total heat flux arriving at divertor targets.

7. Conclusions

The global Braginskii turbulence code GRILLIX was coupled to a diffusive neutral gas model, taking into account ionisation, recombination and CX reactions. The neutrals become mainly ionised along the separatrix in the proximity of the *X*-point and strongly affect the plasma dynamics in various ways: the density profile in the confined region flattens, while the temperature profile steepens, which alters the turbulence drive mechanism from ballooning modes to the ITG mode. The ionization source distribution also leads to poloidal asymmetries. As the neutrals introduce a cooling mechanism via dilution and radiation, plasma collisionality increases in the edge and SOL, and parallel heat transport becomes less effective. In consequence, parallel temperature gradients arise in the SOL, while radial temperature profiles are broadened, yielding a realistic SOL fall-off length. The radial electric field in the SOL is significantly reduced due to a lowered electron temperature gradient at the divertor. At increasing divertor neutrals density, the plasma density rises over the whole domain, further flattening the density profile in the confined region and producing a density shoulder at the OMP, but these simulations also tend to become resistive-ballooning unstable.

The simulations were validated against the attached L-mode AUG discharge #36190. With the neutral gas model, a satisfactory match of OMP density and electron temperature profiles is obtained. At the divertor targets, the profiles become much more realistic as well, but a discrepancy remains due to the use of a too simple neutral boundary condition—a constant density across both divertor plates. The most significant discrepancy with the experiment currently seems to be in the radial electric field: its form matches very well—negative in the confined region, positive in the SOL—but the amplitude is still a factor of two too large.

For improving the agreement with the experiment, but most importantly for reliable and predictive reactor simulations, the primary goal is the elimination of the remaining free model parameters: the divertor neutrals density N_{div} and the free streaming limiters $\alpha_{\mathrm{e,i}}$ of the parallel heat conductivities. The former will be overcome in a straight forward way by implementing local recycling boundary conditions. For the latter, the implementation of a Landau-fluid closure could be a possible solution, e.g. as was done in the BOUT++ code [64]. Further important extensions might be neoclassical corrections to the ion viscosity [24, 77] as well as the consideration of ion orbit losses [79, 80], which can be expected to result in a more realistic radial electric field. However, since these are inherently kinetic effects, verification against gyrokinetic simulations will remain necessary [81]. Kinetic effects are important not just for the plasma, but also for the neutrals: they can be implemented by either a fully kinetic treatment [28, 32], or a hybrid fluid-kinetic model [82, 83]. Finally, for simulations in detached conditions, impurities and parallel momentum dissipation by the neutral gas [78] must be considered. Importantly, for reactor scale simulations, not only should the physical model be improved, but also the computational performance.

Overall, we conclude that a remarkable degree of agreement with the experiment can already be achieved, particularly in the OMP profiles. Hence, predictions for important observables such as the SOL fall-off lengths are becoming possible. In near future, the validation should be extended into regimes with improved confinement, such as the H- or I-mode, aiming to provide a better understanding of these regimes. But also, using the geometric flexibility of GRILLIX, advanced divertor [3] and negative triangularity [7] reactor concepts should be explored.

Acknowledgments

The authors thank Rainer Fischer for the integrated data analysis, and Dominik Brida for providing divertor target measurements. We also thank Marco Wischmeier for helpful discussions. This work has been carried out within the framework of the EUROfusion Consortium and has received funding from the Euratom research and training programme 2014–2018 and 2019–2020 under Grant Agreement No. 633053. The views

and opinions expressed herein do not necessarily reflect those of the European Commission.

ORCID iDs

W. Zholobenko https://orcid.org/0000-0002-2624-0251
A. Stegmeir https://orcid.org/0000-0001-8629-5062
M. Griener https://orcid.org/0000-0003-2953-536X
T. Body https://orcid.org/0000-0003-1904-6300
D. Coster https://orcid.org/0000-0002-2470-9706
F. Jenko https://orcid.org/0000-0001-6686-1469

References

[1] Pitcher C.S. and Stangeby P.C. 1997 Experimental divertor physics *Plasma Phys. Control. Fusion* **39** 779
[2] Eich T. *et al* 2013 Scaling of the tokamak near the scrape-off layer H-mode power width and implications for ITER *Nucl. Fusion* **53** 093031
[3] Militello F. *et al* 2021 Preliminary analysis of alternative divertors for DEMO *Nucl. Mater. Energy* **26** 100908
[4] Zohm H., Militello F., Morgan T.W., Morris W., Reimerdes H. and Siccinio M. 2021 The EU strategy for solving the DEMO exhaust problem *Fusion Eng. Des.* **166** 112307
[5] Reimold F., Wischmeier M., Bernert M., Potzel S., Kallenbach A., Müller H.W., Sieglin B. and Stroth U. 2015 Divertor studies in nitrogen induced completely detached H-modes in full tungsten ASDEX Upgrade *Nucl. Fusion* **55** 033004
[6] Kallenbach A. *et al* 2015 Partial detachment of high power discharges in ASDEX Upgrade *Nucl. Fusion* **55** 053026
[7] Austin M.E. *et al* 2019 Achievement of reactor-relevant performance in negative triangularity shape in the DIII-D tokamak *Phys. Rev. Lett.* **122** 115001
[8] Wang L. *et al* 2021 Integration of full divertor detachment with improved core confinement for tokamak fusion plasmas *Nat. Commun.* **12** 1365
[9] Fasoli A., Brunner S., Cooper W.A., Graves J.P., Ricci P., Sauter O. and Villard L. 2016 Computational challenges in magnetic-confinement fusion physics *Nat. Phys.* **12** 411
[10] Chang C.S. *et al* 2017 Gyrokinetic projection of the divertor heat-flux width from present tokamaks to ITER *Nucl. Fusion* **57** 116023
[11] Dorf M. and Dorr M. 2021 Continuum gyrokinetic simulations of edge plasmas in single-null geometries *Phys. Plasmas* **28** 032508
[12] Tamain P., Bufferand H., Ciraolo G., Colin C., Galassi D., Ghendrih P., Schwander F. and Serre E. 2016 The TOKAM3X code for edge turbulence fluid simulations of tokamak plasmas in versatile magnetic geometries *J. Comput. Phys.* **321** 606
[13] Paruta P., Ricci P., Riva F., Wersal C., Beadle C. and Frei B. 2018 Simulation of plasma turbulence in the periphery of diverted tokamak by using the GBS code *Phys. Plasmas* **25** 112301
[14] Stegmeir A., Coster D., Ross A., Maj O., Lackner K. and Poli E. 2018 GRILLIX: a 3D turbulence code based on the flux-coordinate independent approach *Plasma Phys. Control. Fusion* **60** 035005
[15] Stegmeir A. *et al* 2019 Global turbulence simulations of the tokamak edge region with GRILLIX *Phys. Plasmas* **26** 052517
[16] Zholobenko W., Body T., Manz P., Stegmeir A., Zhu B., Griener M., Conway G.D., Coster D. and Jenko F. 2021 Electric field and turbulence in global Braginskii simulations across the ASDEX Upgrade edge and scrape-off layer *Plasma Phys. Control. Fusion* **63** 034001
[17] Body T. *et al* 2020 Treatment of advanced divertor configurations in the flux-coordinate independent turbulence code GRILLIX *Contrib. Plasma Phys.* **60** e201900139
[18] Hariri F. and Ottaviani M. 2013 A flux-coordinate independent field-aligned approach to plasma turbulence simulations *Comput. Phys. Commun.* **184** 2419
[19] Stegmeir A., Coster D., Maj O., Hallatschek K. and Lackner K. 2016 The field line map approach for simulations of magnetically confined plasmas *Comput. Phys. Commun.* **198** 139
[20] Ross A., Stegmeir A., Manz P., Groselj D., Zholobenko W., Coster D. and Jenko F. 2019 On the nature of blob propagation and generation in the large plasma device: global GRILLIX studies *Phys. Plasmas* **26** 102308
[21] Oliveira D.S. *et al* 2021 Validation of edge turbulence codes against the TCV-X21 diverted L-mode reference case *Nucl. Fusion* (Submitted)
[22] Krasheninnikov S.I. and Kukushkin A.S. 2017 Physics of ultimate detachment of a tokamak divertor plasma *J. Plasma Phys.* **83** 155830501
[23] Rensink M.E. *et al* 1998 A comparison of neutral gas models for divertor plasmas *Contrib. Plasma Phys.* **38** 325
[24] Rozhansky V., Kaveeva E., Molchanov P., Veselova I., Voskoboynikov S., Coster D., Counsell G., Kirk A. and Lisgo S. 2009 New B2SOLPS5.2 transport code for H-mode regimes in tokamaks *Nucl. Fusion* **49** 025007
[25] Bufferand H. *et al* 2017 Implementation of drift velocities and currents in SOLEDGE2D-EIRENE *Nucl. Mater. Energy* **12** 852
[26] Feng Y. *et al* 2014 Recent improvements in the EMC3-EIRENE code *Contrib. Plasma Phys.* **54** 426
[27] Stotler D. and Karney C. 1994 Neutral gas transport modeling with DEGAS 2 *Contrib. Plasma Phys.* **34** 392
[28] Reiter D., Baelmans M. and Börner P. 2005 The EIRENE and B2-EIRENE codes *Fusion Sci. Technol.* **47** 172
[29] Romazanov J. *et al* 2017 First ERO2.0 modeling of Be erosion and non-local transport in JET ITER-like wall *Phys. Scr.* **T170** 014018
[30] Ritz C.P. *et al* 1989 Fluctuation-induced energy flux in the tokamak edge *Phys. Rev. Lett.* **62** 1844
[31] Zweben S.J., Boedo J.A., Grulke O., Hidalgo C., LaBombard B., Maqueda R.J., Scarin P. and Terry J.L. 2007 Edge turbulence measurements in toroidal fusion devices *Plasma Phys. Control. Fusion* **49** S1
[32] Wersal C. and Ricci P. 2015 A first-principles self-consistent model of plasma turbulence and kinetic neutral dynamics in the tokamak scrape-off layer *Nucl. Fusion* **55** 123014
[33] Stotler D.P., Lang J., Chang C.S., Churchill R.M. and Ku S. 2017 Neutral recycling effects on ITG turbulence *Nucl. Fusion* **57** 086028
[34] Fan D.M., Marandet Y., Tamain P., Bufferand H., Ciraolo G., Ghendrih P. and Serre E. 2019 Effect of turbulent fluctuations on neutral particles transport with the TOKAM3X-EIRENE turbulence code *Nucl. Mater. Energy* **18** 105
[35] Zeiler A., Drake J.F. and Rogers B. 1997 Nonlinear reduced Braginskii equations with ion thermal dynamics in toroidal plasma *Phys. Plasmas* **4** 2134
[36] Thyagaraja A., Haas F.A. and Cook I. 1980 Temperature fluctuations and heat transfer in tokamaks *Nucl. Fusion* **20** 611
[37] Scott B. 1997 Three-dimensional computation of drift Alfvén turbulence *Plasma Phys. Control. Fusion* **39** 1635
[38] Stangeby P. 2000 *The Plasma Boundary of Magnetic Fusion Devices* (*Series in Plasma Physics*) (Boca Raton, FL: CRC Press)
[39] Fundamenski W. 2005 Parallel heat flux limits in the tokamak scrape-off layer *Plasma Phys. Control. Fusion* **47** R163

[40] Tskhakaya D. *et al* 2008 On kinetic effects during parallel transport in the SOL *Contrib. Plasma Phys.* **48** 89

[41] Xia T.Y. and Xu X.Q. 2015 Nonlinear fluid simulation of particle and heat fluxes during burst of ELMs on DIII-D with BOUT++ code *Nucl. Fusion* **55** 113030

[42] Umansky M.V., Dimits A.M., Joseph I., Omotani J.T. and Rognlien T.D. 2015 Modeling of tokamak divertor plasma for weakly collisional parallel electron transport *J. Nucl. Mater.* **463** 506

[43] Carralero D. *et al* 2014 An experimental investigation of the high density transition of the scrape-off layer transport in ASDEX Upgrade *Nucl. Fusion* **54** 123005

[44] Wynn A. *et al* 2018 Investigation into the formation of the scrape-off layer density shoulder in JET ITER-like wall L-mode and H-mode plasmas *Nucl. Fusion* **58** 056001

[45] Fantz U., Reiter D., Heger B. and Coster D. 2001 Hydrogen molecules in the divertor of ASDEX Upgrade *J. Nucl. Mater.* **290–293** 367

[46] Kukushkin A.S., Krasheninnikov S.I., Pshenov A.A. and Reiter D. 2017 Role of molecular effects in divertor plasma recombination *Nucl. Mater. Energy* **12** 984

[47] Reiter D. 2020 EIRENE https://eirene.de/ Last visited on 15 January 2021

[48] Vold E.L., Prinja A.K., Najmabadi F. and Conn R.W. 1990 The neutral diffusion approximation in a consistent tokamak edge plasma–neutral computation *J. Nucl. Mater.* **176–177** 570

[49] Thrysøe A.S. *et al* 2018 Plasma particle sources due to interactions with neutrals in a turbulent scrape-off layer of a toroidally confined plasma *Phys. Plasmas* **25** 032307

[50] Umansky M.V., Rognlien T.D., Fenstermacher M.E., Borchardt M., Mutzke A., Riemann J., Schneider R. and Owen L.W. 2003 Modeling of localized neutral particle sources in 3D edge plasmas *J. Nucl. Mater.* **313–316** 559

[51] Helander P., Krasheninnikov S.I. and Catto P.J. 1994 Fluid equations for a partially ionized plasma *Phys. Plasmas* **1** 3174

[52] Coster D.P., Bonnin X., Braams B., Reiter D. and Schneider R. 2004 Simulation of the edge plasma in tokamaks *Phys. Scr.* **7**

[53] Braginskii S.I. 1965 Transport processes in a plasma *Reviews of Plasma Physics* ed A.M.A. Leontovich vol 1 (New York: Consultants Bureau) pp 205–311

[54] Zhang Y. and Krasheninnikov S.I. 2020 Effect of neutrals on the anomalous edge plasma transport *Plasma Phys. Control. Fusion* **62** 115018

[55] Fisher D.M., Rogers B.N., Rossi G.D., Guice D.S. and Carter T.A. 2015 Three-dimensional two-fluid Braginskii simulations of the large plasma device *Phys. Plasmas* **22** 092121

[56] Zhang Y., Krasheninnikov S.I., Masline R. and Smirnov R.D. 2020 Neutral impact on anomalous edge plasma transport and its correlation with divertor plasma detachment *Nucl. Fusion* **60** 106023

[57] Zito A. *et al* 2021 Numerical modelling of an enhanced perpendicular transport regime in the scrape-off layer of ASDEX Upgrade *Plasma Phys. Control. Fusion*

[58] Rognlien T.D., Umansky M.V., Xu X.Q. and Cohen R.H. 2004 Self-consistent simulation of turbulence and transport in tokamak edge plasmas *Contrib. Plasma Phys.* **44** 188

[59] Scott B.D. 2005 Free-energy conservation in local gyrofluid models *Phys. Plasmas* **12** 102307

[60] Zholobenko W. *et al* 2020 Thermal dynamics in the flux-coordinate independent turbulence code GRILLIX *Contrib. Plasma Phys.* **60** e201900131

[61] Rogers B.N., Drake J.F. and Zeiler A. 1998 Phase space of tokamak edge turbulence, the $L-H$ transition, and the formation of the edge pedestal *Phys. Rev. Lett.* **81** 4396

[62] Eich T. and Manz P. 2021 The separatrix operational space of ASDEX Upgrade due to interchange-drift-Alfvén turbulence *Nucl. Fusion* **61** 086017

[63] Hallatschek K. and Zeiler A. 2000 Nonlocal simulation of the transition from ballooning to ion temperature gradient mode turbulence in the tokamak edge *Phys. Plasmas* **7** 2554

[64] Zhu B. *et al* 2021 Drift reduced Landau fluid model for magnetized plasma turbulence simulations in BOUT++ framework (arXiv:2102.04976)

[65] Fischer R., Fuchs C.J., Kurzan B., Suttrop W. and Wolfrum E. 2010 Integrated data analysis of profile diagnostics at ASDEX Upgrade *Fusion Sci. Technol.* **58** 675

[66] Ryter F., Barrera Orte L., Kurzan B., McDermott R.M., Tardini G., Viezzer E., Bernert M. and Fischer R. 2014 Experimental evidence for the key role of the ion heat channel in the physics of the L–H transition *Nucl. Fusion* **54** 083003

[67] Scott B.D. 2007 Nonlinear polarization and dissipative correspondence between low-frequency fluid and gyrofluid equations *Phys. Plasmas* **14** 102318

[68] Brida D., Silvagni D., Eich T., Faitsch M. and McCarthy P. 2020 Role of electric currents for the SOL and divertor target heat fluxes in ASDEX Upgrade *Plasma Phys. Control. Fusion* **62** 105014

[69] Guzdar P.N. 1983 Ion-temperature-gradient instability in toroidal plasmas *Phys. Fluids* **26** 673

[70] Mosetto A., Halpern F.D., Jolliet S., Loizu J. and Ricci P. 2015 Finite ion temperature effects on scrape-off layer turbulence *Phys. Plasmas* **22** 012308

[71] Ribeiro T.T. and Scott B. 2008 Gyrofluid turbulence studies of the effect of the poloidal position of an axisymmetric Debye sheath *Plasma Phys. Control. Fusion* **50** 055007

[72] Kotschenreuther M. *et al* 2019 Gyrokinetic analysis and simulation of pedestals to identify the culprits for energy losses using fingerprints *Nucl. Fusion* **59** 096001

[73] Scott B.D. 2002 The nonlinear drift wave instability and its role in tokamak edge turbulence *New J. Phys.* **4** 52

[74] Scott B.D. 2003 Computation of electromagnetic turbulence and anomalous transport mechanisms in tokamak plasmas *Plasma Phys. Control. Fusion* **45** A385

[75] Conway G.D., Poli E. and Happel T. (the ASDEX Upgrade Team) 2010 Interaction of mean and oscillating plasma flows across confinement mode transitions *Plasma Fusion Res.* **5** S2005

[76] Wensing M., Loizu J., Reimerdes H., Duval B.P. and Wischmeier M. (the TCV team) 2020 *X*-point potential well formation in diverted tokamaks with unfavorable magnetic field direction *Nucl. Fusion* **60** 054005

[77] Helander P. and Sigmar D.J. 2002 *Collisional Transport in Magnetized Plasmas* (Cambridge: Cambridge University Press)

[78] Pshenov A.A., Kukushkin A.S. and Krasheninnikov S.I. 2017 Energy balance in plasma detachment *Nucl. Mater. Energy* **12** 948

[79] Chang C.S., Kue S. and Weitzner H. 2002 X-transport: a baseline nonambipolar transport in a diverted tokamak plasma edge *Phys. Plasmas* **9** 3884

[80] Brzozowski R.W., Jenko F., Bilato R. and Cavedon M. 2019 A geometric model of ion orbit loss under the influence of a radial electric field *Phys. Plasmas* **26** 042511

[81] Michels D., Stegmeir A., Ulbl P., Jarema D. and Jenko F. 2021 GENE-X: a full-f gyrokinetic turbulence code based on the flux-coordinate independent approach *Comput. Phys. Commun.* **264** 107986

[82] Valentinuzzi M. 2018 Modélisation numérique des flux de puissances sur les composants face au plasma de Tokamak à l'aide de techniques de couplage avancées entre codes fluides et cinétiques *PhD Thesis* Plasma Aix-Marseille Thèse de doctorat dirigée par Marandet, Yannick et Ciraolo, Guido Energie, rayonnement

[83] Horsten N., Samaey G. and Baelmans M. 2020 A hybrid fluid-kinetic model for hydrogenic atoms in the plasma edge of tokamaks based on a micro-macro decomposition of the kinetic equation *J. Comput. Phys.* **409** 109308

Bibliography

[1] W. Zholobenko, A. Stegmeir, T. Body *et al.* Thermal dynamics in the flux-coordinate independent turbulence code GRILLIX. *Contributions to Plasma Physics*, **60** (5-6), e201900131 (2020).

[2] W. Zholobenko, A. Stegmeir, T. Body *et al.* Corrigendum: Thermal dynamics in the flux-coordinate independent turbulence code GRILLIX. *Contributions to Plasma Physics*, **60** (5-6), e202000056 (2020).

[3] W. Zholobenko, T. Body, P. Manz *et al.* Electric field and turbulence in global Braginskii simulations across the ASDEX Upgrade edge and scrape-off layer. *Plasma Physics and Controlled Fusion*, **63** (3), 034001 (2021).

[4] W. Zholobenko, A. Stegmeir, M. Griener *et al.* The role of neutral gas in validated global edge turbulence simulations. *Nuclear Fusion* (2021).

[5] Paris Agreement to the United Nations Framework Convention on Climate Change (2015).

[6] S. C. Cowley. The quest for fusion power. *Nature Physics*, **12** (5), 384 (2016).

[7] J. Ongena, R. Koch, R. Wolf *et al.* Magnetic-confinement fusion. *Nature Physics*, **12** (5), 398 (2016).

[8] ITER. https://www.iter.org/sci/Fusion (2021).

[9] IEA. *Key World Energy Statistics 2020*. OECD Publishing, Paris (2020).

[10] V. Smirnov. Tokamak foundation in USSR/Russia 1950–1990. *Nuclear Fusion*, **50** (1), 014003 (2009).

[11] C. S. Pitcher and P. C. Stangeby. Experimental divertor physics. *Plasma Physics and Controlled Fusion*, **39** (6), 779 (1997).

[12] S. I. Krasheninnikov and A. S. Kukushkin. Physics of ultimate detachment of a tokamak divertor plasma. *Journal of Plasma Physics*, **83** (5) (2017).

[13] IPP. https://www.ipp.mpg.de/15144/zuendbedingungen (2021).

[14] J. D. Lawson. Some Criteria for a Power Producing Thermonuclear Reactor. *Proceedings of the Physical Society. Section B*, **70** (1), 6 (1957).

[15] JET Team. Fusion energy production from a deuterium-tritium plasma in the JET tokamak. *Nuclear Fusion*, **32** (2), 187 (1992).

[16] G. Federici, W. Biel, M. Gilbert *et al.* European DEMO design strategy and consequences for materials. *Nuclear Fusion*, **57** (9), 092002 (2017).

[17] G. Federici, C. Bachmann, L. Barucca *et al.* Overview of the DEMO staged design approach in Europe. *Nuclear Fusion*, **59** (6), 066013 (2019).

[18] H. Zohm, F. Militello, T. Morgan *et al.* The EU strategy for solving the DEMO exhaust problem. *Fusion Engineering and Design*, **166**, 112307 (2021).

[19] F. Militello, L. Aho-Mantila, R. Ambrosino *et al.* Preliminary analysis of alternative divertors for DEMO. *Nuclear Materials and Energy*, **26**, 100908 (2021).

[20] M. Kikuchi. Steady state tokamak reactor based on the bootstrap current. *Nuclear Fusion*, **30** (2), 265 (1990).

[21] M. E. Austin, A. Marinoni, M. L. Walker *et al.* Achievement of Reactor-Relevant Performance in Negative Triangularity Shape in the DIII-D Tokamak. *Phys. Rev. Lett.*, **122**, 115001 (2019).

[22] A. H. Boozer. Stellarators and the path from ITER to DEMO. *Plasma Physics and Controlled Fusion*, **50** (12), 124005 (2008).

[23] J. Knaster, A. Moeslang and T. Muroga. Materials research for fusion. *Nature Physics*, **12** (5), 424 (2016).

[24] R. Ambrosino. DTT - Divertor Tokamak Test facility: A testbed for DEMO. *Fusion Engineering and Design*, **167**, 112330 (2021).
[25] A. J. Creely, M. J. Greenwald, S. B. Ballinger *et al.* Overview of the SPARC tokamak. *Journal of Plasma Physics*, **86** (5) (2020).
[26] T. Lunt, H. Zohm, A. Herrmann *et al.* Proposal of an alternative upper divertor in ASDEX Upgrade supported by EMC3-EIRENE simulations. *Nuclear Materials and Energy*, **12**, 1037 (2017).
[27] S. Wiesen, D. Reiter, V. Kotov *et al.* The new SOLPS-ITER code package. *Journal of Nuclear Materials*, **463**, 480 (2015).
[28] F. Orain, M. Bécoulet, G. Dif-Pradalier *et al.* Non-linear magnetohydrodynamic modeling of plasma response to resonant magnetic perturbations. *Physics of Plasmas*, **20** (10), 102510 (2013).
[29] F. Jenko, W. Dorland, M. Kotschenreuther *et al.* Electron temperature gradient driven turbulence. *Physics of Plasmas*, **7** (5), 1904 (2000).
[30] T. Görler, X. Lapillonne, S. Brunner *et al.* The global version of the gyrokinetic turbulence code GENE. *Journal of Computational Physics*, **230** (18), 7053 (2011).
[31] F. L. Hinton and R. D. Hazeltine. Theory of plasma transport in toroidal confinement systems. *Reviews of Modern Physics*, **48** (2), 239 (1976).
[32] T. Hender, J. Wesley, J. Bialek *et al.* Chapter 3: MHD stability, operational limits and disruptions. *Nuclear Fusion*, **47** (6), S128 (2007).
[33] A. M. Dimits, G. Bateman, M. A. Beer *et al.* Comparisons and physics basis of tokamak transport models and turbulence simulations. *Physics of Plasmas*, **7** (3), 969 (2000).
[34] The Millennium Prize Problems. Clay Mathematics Institute (2000). https://www.claymath.org/millennium-problems/navier%E2%80%93stokes-equation.
[35] A. Kolmogorov. The local structure of isotropic turbulence in an incompressible viscous fluid. In *Dokl. Akad. Nauk SSSR*, volume 30, pages 301–305 (1941).
[36] M. Shavit and G. Falkovich. Singular Measures and Information Capacity of Turbulent Cascades. *Physical Review Letters*, **125** (10), 104501 (2020).
[37] A. Zeiler. Tokamak Edge Turbulence. Habilitation treatise, IPP Report 5/88 (1999).
[38] B. Scott. Low Frequency Fluid Drift Turbulence in Magnetised Plasmas. Habilitation treatise, IPP Report 5/92 (2001).
[39] F. Wagner, G. Becker, K. Behringer *et al.* Regime of Improved Confinement and High Beta in Neutral-Beam-Heated Divertor Discharges of the ASDEX Tokamak. *Physical Review Letters*, **49** (19), 1408 (1982).
[40] F. Ryter, L. B. Orte, B. Kurzan *et al.* Experimental evidence for the key role of the ion heat channel in the physics of the L–H transition. *Nuclear Fusion*, **54** (8), 083003 (2014).
[41] K. H. Burrell, E. J. Doyle, P. Gohil *et al.* Role of the radial electric field in the transition from L (low) mode to H (high) mode to VH (very high) mode in the DIII-D tokamak*. *Physics of Plasmas*, **1** (5), 1536 (1994).
[42] E. J. Doyle, W. A. Houlberg, Y. Kamada *et al.* Chapter 2: Plasma confinement and transport. *Nuclear Fusion*, **47** (6), S18 (2007).
[43] D. Hatch, M. Kotschenreuther, S. Mahajan *et al.* Microtearing turbulence limiting the JET-ILW pedestal. *Nuclear Fusion*, **56** (10), 104003 (2016).
[44] U. Stroth, P. Manz and M. Ramisch. On the interaction of turbulence and flows in toroidal plasmas. *Plasma Physics and Controlled Fusion*, **53** (2), 024006 (2011).
[45] T. Eich, A. W. Leonard, R. A. Pitts *et al.* Scaling of the tokamak near the scrape-off layer H-mode power width and implications for ITER. *Nuclear Fusion*, **53** (9), 093031 (2013).
[46] A. Loarte, B. Lipschultz, A. S. Kukushkin *et al.* Chapter 4: Power and particle control. *Nuclear Fusion*, **47** (6), S203 (2007).
[47] A. Loarte. Effects of divertor geometry on tokamak plasmas. *Plasma Physics and Controlled Fusion*, **43** (6), R183 (2001).
[48] R. Chodura. *Plasma Flow in the Sheath and the Presheath of a Scrape-Off Layer*, pages 99–134. Springer US, Boston, MA (1986). ISBN 978-1-4757-0067-1.
[49] P. Stangeby. *The Plasma Boundary of Magnetic Fusion Devices (Series in Plasma Physics)*. CRC Press (2000). ISBN 0750305592.

[50] A. Fasoli, S. Brunner, W. A. Cooper *et al.* Computational challenges in magnetic-confinement fusion physics. *Nature Physics*, **12** (5), 411 (2016).

[51] J. XIAO and H. QIN. Explicit structure-preserving geometric particle-in-cell algorithm in curvilinear orthogonal coordinate systems and its applications to whole-device 6D kinetic simulations of tokamak physics. *Plasma Science and Technology*, **23** (5), 055102 (2021).

[52] A. J. Brizard and T. S. Hahm. Foundations of nonlinear gyrokinetic theory. *Rev. Mod. Phys.*, **79**, 421 (2007).

[53] J. A. Krommes. Nonlinear gyrokinetics: a powerful tool for the description of microturbulence in magnetized plasmas. *Physica Scripta*, **T142**, 014035 (2010).

[54] S. Maeyama, T.-H. Watanabe, Y. Idomura *et al.* Implementation of a gyrokinetic collision operator with an implicit time integration scheme and its computational performance. *Computer Physics Communications*, **235**, 9 (2019).

[55] M. A. Miller, R. M. Churchill, A. Dener *et al.* Encoder–decoder neural network for solving the nonlinear Fokker–Planck–Landau collision operator in XGC. *Journal of Plasma Physics*, **87** (2) (2021).

[56] S. I. Braginskii. Transport Processes in a Plasma. In A. M. A. Leontovich, editor, *Reviews of Plasma Physics*, volume 1. Consultants Bureau, New York (1965).

[57] A. Zeiler, J. F. Drake and B. Rogers. Nonlinear reduced Braginskii equations with ion thermal dynamics in toroidal plasma. *Physics of Plasmas*, **4** (6), 2134 (1997).

[58] A. N. Simakov and P. J. Catto. Drift-ordered fluid equations for field-aligned modes in low-β collisional plasma with equilibrium pressure pedestals. *Physics of Plasmas*, **10** (12), 4744 (2003).

[59] A. Hasegawa, C. G. Maclennan and Y. Kodama. Nonlinear behavior and turbulence spectra of drift waves and Rossby waves. *The Physics of Fluids*, **22** (11), 2122 (1979).

[60] A. Hasegawa and M. Wakatani. Plasma Edge Turbulence. *Phys. Rev. Lett.*, **50**, 682 (1983).

[61] D. Dobrott, D. B. Nelson, J. M. Greene *et al.* Theory of Ballooning Modes in Tokamaks with Finite Shear. *Physical Review Letters*, **39** (15), 943 (1977).

[62] A. Mosetto, F. D. Halpern, S. Jolliet *et al.* Finite ion temperature effects on scrape-off layer turbulence. *Physics of Plasmas*, **22** (1), 012308 (2015).

[63] B. D. Scott. The mechanism of self-sustainment in collisional drift wave turbulence. *Physics of Fluids B: Plasma Physics*, **4** (8), 2468 (1992).

[64] J. F. Drake, A. Zeiler and D. Biskamp. Nonlinear Self-Sustained Drift-Wave Turbulence. *Physical Review Letters*, **75** (23), 4222 (1995).

[65] B. D. Scott. The nonlinear drift wave instability and its role in tokamak edge turbulence. *New Journal of Physics*, **4**, 52 (2002).

[66] P. H. Diamond, S.-I. Itoh, K. Itoh *et al.* Zonal flows in plasma—a review. *Plasma Physics and Controlled Fusion*, **47** (5), R35 (2005).

[67] A. Fujisawa. A review of zonal flow experiments. *Nuclear Fusion*, **49** (1), 013001 (2008).

[68] B. N. Rogers, J. F. Drake and A. Zeiler. Phase Space of Tokamak Edge Turbulence, the $L-H$ Transition, and the Formation of the Edge Pedestal. *Phys. Rev. Lett.*, **81**, 4396 (1998).

[69] M. N. Rosenbluth and F. L. Hinton. Poloidal Flow Driven by Ion-Temperature-Gradient Turbulence in Tokamaks. *Physical Review Letters*, **80** (4), 724 (1998).

[70] F. Jenko and B. D. Scott. Effect of Nonlinear Electron Landau Damping in Collisionless Drift-Wave Turbulence. *Physical Review Letters*, **80** (22), 4883 (1998).

[71] T. Dannert and F. Jenko. Gyrokinetic simulation of collisionless trapped-electron mode turbulence. *Physics of Plasmas*, **12** (7), 072309 (2005).

[72] B. D. Scott. Nonlinear polarization and dissipative correspondence between low-frequency fluid and gyrofluid equations. *Physics of Plasmas*, **14** (10), 102318 (2007).

[73] W. W. Lee. Gyrokinetic approach in particle simulation. *Physics of Fluids*, **26** (2), 556 (1983).

[74] A. Bottino, B. Scott, S. Brunner *et al.* Global Nonlinear Electromagnetic Simulations of Tokamak Turbulence. *IEEE Transactions on Plasma Science*, **38** (9), 2129 (2010).

[75] V. Grandgirard, M. Brunetti, P. Bertrand *et al.* A drift-kinetic Semi-Lagrangian 4D code for ion turbulence simulation. *Journal of Computational Physics*, **217** (2), 395 (2006).

[76] R. Hager, E. Yoon, S. Ku *et al.* A fully non-linear multi-species Fokker–Planck–Landau collision operator for simulation of fusion plasma. *Journal of Computational Physics*, **315**, 644 (2016).
[77] G. Dif-Pradalier, V. Grandgirard, Y. Sarazin *et al.* Interplay between Gyrokinetic Turbulence, Flows, and Collisions: Perspectives on Transport and Poloidal Rotation. *Physical Review Letters*, **103** (6), 065002 (2009).
[78] A. D. Siena, R. Bilato, T. Görler *et al.* New High-Confinement Regime with Fast Ions in the Core of Fusion Plasmas. *Physical Review Letters*, **127** (2) (2021).
[79] A. D. Siena, A. B. Navarro and F. Jenko. Turbulence Suppression by Energetic Particle Effects in Modern Optimized Stellarators. *Physical Review Letters*, **125** (10), 105002 (2020).
[80] G. W. Hammett and F. W. Perkins. Fluid moment models for Landau damping with application to the ion-temperature-gradient instability. *Physical Review Letters*, **64** (25), 3019 (1990).
[81] M. A. Beer and G. W. Hammett. Toroidal gyrofluid equations for simulations of tokamak turbulence. *Physics of Plasmas*, **3** (11), 4046 (1996).
[82] P. B. Snyder and G. W. Hammett. Electromagnetic effects on plasma microturbulence and transport. *Physics of Plasmas*, **8** (3), 744 (2001).
[83] N. Mattor. Collisionless fluid closure theory and the phase velocity transform. *Physics of Plasmas*, **5** (5), 1822 (1998).
[84] B. Scott. E×B shear flows and electromagnetic gyrofluid turbulence. *Physics of Plasmas*, **7** (5), 1845 (2000).
[85] B. D. Scott. Free-energy conservation in local gyrofluid models. *Physics of Plasmas*, **12** (10), 102307 (2005).
[86] F. L. Hinton, M. N. Rosenbluth and R. E. Waltz. Reduced equations for electromagnetic turbulence in tokamaks. *Physics of Plasmas*, **10** (1), 168 (2003).
[87] G. A. Hallock, A. J. Wootton and R. L. Hickok. Space-potential and density fluctuations in the ISX-B tokamak. *Physical Review Letters*, **59** (12), 1301 (1987).
[88] C. P. Ritz, R. V. Bravenec, P. M. Schoch *et al.* Fluctuation-Induced Energy Flux in the Tokamak Edge. *Physical Review Letters*, **62** (16), 1844 (1989).
[89] S. J. Zweben, J. A. Boedo, O. Grulke *et al.* Edge turbulence measurements in toroidal fusion devices. *Plasma Physics and Controlled Fusion*, **49** (7), S1 (2007).
[90] J. A. Boedo, D. Rudakov, R. Moyer *et al.* Transport by intermittent convection in the boundary of the DIII-D tokamak. *Physics of Plasmas*, **8** (11), 4826 (2001).
[91] O. Grulke, J. L. Terry, B. LaBombard *et al.* Radially propagating fluctuation structures in the scrape-off layer of Alcator C-Mod. *Physics of Plasmas*, **13** (1), 012306 (2006).
[92] N. B. Ayed, A. Kirk, B. Dudson *et al.* Inter-ELM filaments and turbulent transport in the Mega-Amp Spherical Tokamak. *Plasma Physics and Controlled Fusion*, **51** (3), 035016 (2009).
[93] D. Reiter, M. Baelmans and P. Börner. The EIRENE and B2-EIRENE Codes. *Fusion Science and Technology*, **47** (2), 172 (2005).
[94] V. Rozhansky, E. Kaveeva, P. Molchanov *et al.* New B2SOLPS5.2 transport code for H-mode regimes in tokamaks. *Nuclear Fusion*, **49** (2), 025007 (2009).
[95] D. Stotler, C. Karney, M. Rensink *et al.* Coupling of Parallelized DEGAS 2 and UEDGE Codes. *Contributions to Plasma Physics*, **40** (3-4), 221 (2000).
[96] A. Kallenbach, Y. Andrew, M. Beurskens *et al.* EDGE2D modelling of edge profiles obtained in JET diagnostic optimized configuration. *Plasma Physics and Controlled Fusion*, **46** (3), 431 (2004).
[97] Y. Feng, H. Frerichs, M. Kobayashi *et al.* Recent Improvements in the EMC3-Eirene Code. *Contributions to Plasma Physics*, **54** (4-6), 426 (2014).
[98] H. Bufferand, P. Tamain, S. Baschetti *et al.* Three-dimensional modelling of edge multi-component plasma taking into account realistic wall geometry. *Nuclear Materials and Energy*, **18**, 82 (2019).
[99] B. D. Dudson and J. Leddy. Hermes: global plasma edge fluid turbulence simulations. *Plasma Physics and Controlled Fusion*, **59** (5), 054010 (2017).
[100] B. Zhu, H. Seto, X. qiao Xu *et al.* Drift reduced Landau fluid model for magnetized plasma turbulence simulations in BOUT++ framework. *arXiv:2102.04976* (2021).

[101] F. Halpern, P. Ricci, S. Jolliet *et al.* The GBS code for tokamak scrape-off layer simulations. *Journal of Computational Physics*, **315**, 388 (2016).

[102] P. Paruta, P. Ricci, F. Riva *et al.* Simulation of plasma turbulence in the periphery of diverted tokamak by using the GBS code. *Physics of Plasmas*, **25** (11), 112301 (2018).

[103] B. Zhu, M. Francisquez and B. N. Rogers. GDB: A global 3D two-fluid model of plasma turbulence and transport in the tokamak edge. *Computer Physics Communications*, **232**, 46 (2018).

[104] P. Tamain, H. Bufferand, G. Ciraolo *et al.* The TOKAM3X code for edge turbulence fluid simulations of tokamak plasmas in versatile magnetic geometries. *Journal of Computational Physics*, **321**, 606 (2016).

[105] D. Fan, Y. Marandet, P. Tamain *et al.* Effect of turbulent fluctuations on neutral particles transport with the TOKAM3X-EIRENE turbulence code. *Nuclear Materials and Energy*, **18**, 105 (2019).

[106] A. Stegmeir, D. Coster, A. Ross *et al.* GRILLIX: a 3D turbulence code based on the flux-coordinate independent approach. *Plasma Physics and Controlled Fusion*, **16** (3), 035005 (2018).

[107] A. Stegmeir, A. Ross, T. Body *et al.* Global turbulence simulations of the tokamak edge region with GRILLIX. *Physics of Plasmas*, **26** (5), 052517 (2019).

[108] C. Wersal and P. Ricci. A first-principles self-consistent model of plasma turbulence and kinetic neutral dynamics in the tokamak scrape-off layer. *Nuclear Fusion*, **55** (12), 123014 (2015).

[109] J. Leddy, B. Dudson and H. Willett. Simulation of the interaction between plasma turbulence and neutrals in linear devices. *Nuclear Materials and Energy*, **12**, 994 (2017).

[110] M. Held, M. Wiesenberger and A. Kendl. Padé-based arbitrary wavelength polarization closures for full-F gyro-kinetic and -fluid models. *Nuclear Fusion*, **60** (6), 066014 (2020).

[111] C. Chang, S. Ku, G. Tynan *et al.* Fast Low-to-High Confinement Mode Bifurcation Dynamics in a Tokamak Edge Plasma Gyrokinetic Simulation. *Physical Review Letters*, **118** (17), 175001 (2017).

[112] C. Chang, S. Ku, A. Loarte *et al.* Gyrokinetic projection of the divertor heat-flux width from present tokamaks to ITER. *Nuclear Fusion*, **57** (11), 116023 (2017).

[113] D. Stotler, J. Lang, C. Chang *et al.* Neutral recycling effects on ITG turbulence. *Nuclear Fusion*, **57** (8), 086028 (2017).

[114] M. Dorf and M. Dorr. Continuum gyrokinetic simulations of edge plasmas in single-null geometries. *Physics of Plasmas*, **28** (3), 032508 (2021).

[115] M. Francisquez, T. N. Bernard, B. Zhu *et al.* Fluid and gyrokinetic turbulence in open field-line, helical plasmas. *Physics of Plasmas*, **27** (8), 082301 (2020).

[116] D. Michels, A. Stegmeir, P. Ulbl *et al.* GENE-X: A full-f gyrokinetic turbulence code based on the flux-coordinate independent approach. *Computer Physics Communications*, **264**, 107986 (2021).

[117] B. Zhu, M. Francisquez and B. N. Rogers. Global 3D two-fluid simulations of the tokamak edge region: Turbulence, transport, profile evolution, and spontaneous E×B rotation. *Physics of Plasmas*, **24** (5), 055903 (2017).

[118] T. Body, A. Stegmeir, W. Zholobenko *et al.* Treatment of advanced divertor configurations in the flux-coordinate independent turbulence code GRILLIX. *Contributions to Plasma Physics*, **60** (5-6), e201900139 (2020).

[119] A. K. Stegmeir. *GRILLIX: A 3D turbulence code for magnetic fusion devices based on a field line map*. Dissertation, Technische Universität München, München (2015).

[120] A. Ross. *Extension of GRILLIX: Towards a global fluid turbulence code for realistic magnetic geometries*. Dissertation, Technische Universität München, München (2018).

[121] A. Ross, A. Stegmeir, P. Manz *et al.* On the nature of blob propagation and generation in the large plasma device: Global GRILLIX studies. *Physics of Plasmas*, **26** (10), 102308 (2019).

[122] S. Chapman, T. Cowling, D. Burnett *et al. The Mathematical Theory of Non-uniform Gases: An Account of the Kinetic Theory of Viscosity, Thermal Conduction and Diffusion in Gases*. Cambridge Mathematical Library. Cambridge University Press (1953). ISBN 9780521408448.

[123] B. A. Trubnikov. Particle Interactions in a Fully Ionized Plasma. In A. M. A. Leontovich, editor, *Reviews of Plasma Physics*, volume 1. Consultants Bureau, New York (1965).

[124] V. M. Zhdanov. Transport Processes in Multicomponent Plasma. *Plasma Physics and Controlled Fusion*, **44** (10), 2283 (2002).

[125] A. Poulsen, J. J. Rasmussen, M. Wiesenberger *et al.* Collisional multispecies drift fluid model. *Physics of Plasmas*, **27** (3), 032305 (2020).
[126] L. Spitzer and R. Härm. Transport Phenomena in a Completely Ionized Gas. *Physical Review*, **89** (5), 977 (1953).
[127] W. Horton. Nonlinear drift waves and transport in magnetized plasma. *Physics Reports*, **192** (1-3), 1 (1990).
[128] D. R. McCarthy, J. F. Drake, P. N. Guzdar *et al.* Formation of the shear layer in toroidal edge plasma. *Physics of Fluids B: Plasma Physics*, **5** (4), 1188 (1993).
[129] B. D. Dudson, S. L. Newton, J. T. Omotani *et al.* On Ohm's law in reduced plasma fluid models. *arXiv:2105.05329* (2021).
[130] P. N. Guzdar. Ion-temperature-gradient instability in toroidal plasmas. *Physics of Fluids*, **26** (3), 673 (1983).
[131] P. Manz, T. Happel, U. Stroth *et al.* Physical mechanism behind and access to the I-mode confinement regime in tokamaks. *Nuclear Fusion*, **60** (9), 096011 (2020).
[132] M. Umansky, A. Dimits, I. Joseph *et al.* Modeling of tokamak divertor plasma for weakly collisional parallel electron transport. *Journal of Nuclear Materials*, **463**, 506 (2015).
[133] U. Stroth. *Plasmaphysik*. Springer Berlin Heidelberg (2018).
[134] F. Riva, F. Militello, S. Elmore *et al.* Three-dimensional plasma edge turbulence simulations of the Mega Ampere Spherical Tokamak and comparison with experimental measurements. *Plasma Physics and Controlled Fusion*, **61** (9), 095013 (2019).
[135] B. Scott. Three-dimensional computation of drift Alfvén turbulence. *Plasma Physics and Controlled Fusion*, **39** (10), 1635 (1997).
[136] T. Dannert and F. Jenko. Vlasov simulation of kinetic shear Alfvén waves. *Computer Physics Communications*, **163** (2), 67 (2004).
[137] M. J. Pueschel, M. Kammerer and F. Jenko. Gyrokinetic turbulence simulations at high plasma beta. *Physics of Plasmas*, **15** (10), 102310 (2008).
[138] P. Helander and D. J. Sigmar. *Collisional Transport in Magnetized Plasmas*. Cambridge University Press (2002). ISBN 0521807980.
[139] S. Hirshman and D. Sigmar. Neoclassical transport of impurities in tokamak plasmas. *Nuclear Fusion*, **21** (9), 1079 (1981).
[140] C. Wersal and P. Ricci. Impact of neutral density fluctuations on gas puff imaging diagnostics. *Nuclear Fusion*, **57** (11), 116018 (2017).
[141] EIRENE. `http://www.eirene.de/`. Last visited on January 15, 2021.
[142] OPEN-ADAS. `http://open.adas.ac.uk/`. Last visited on January 15, 2021.
[143] W. Zholobenko, M. Rack and D. Reiter. Development and evaluation of a synthetic helium beam diagnostic for Wendelstein 7-X. Technical Report Juel-4407, Jülich (2018).
[144] P. Helander, S. I. Krasheninnikov and P. J. Catto. Fluid equations for a partially ionized plasma. *Physics of Plasmas*, **1** (10), 3174 (1994).
[145] M. E. Rensink, L. Lodestro, G. D. Porter *et al.* A Comparison of Neutral Gas Models for Divertor Plasmas. *Contributions to Plasma Physics*, **38** (1/2), 325 (1998).
[146] M. Umansky, T. Rognlien, M. Fenstermacher *et al.* Modeling of localized neutral particle sources in 3D edge plasmas. *Journal of Nuclear Materials*, **313-316**, 559 (2003).
[147] S. Parker, R. Procassini, C. Birdsall *et al.* A Suitable Boundary Condition for Bounded Plasma Simulation without Sheath Resolution. *Journal of Computational Physics*, **104** (1), 41 (1993).
[148] P. C. Stangeby and A. V. Chankin. The ion velocity (Bohm–Chodura) boundary condition at the entrance to the magnetic presheath in the presence of diamagnetic and E×B drifts in the scrape-off layer. *Physics of Plasmas*, **2** (3), 707 (1995).
[149] T. Ribeiro and B. Scott. Gyrofluid turbulence studies of the effect of the poloidal position of an axisymmetric Debye sheath. *Plasma Physics and Controlled Fusion*, **50** (5), 055007 (2008).
[150] J. Loizu, P. Ricci, F. D. Halpern *et al.* Boundary conditions for plasma fluid models at the magnetic presheath entrance. *Physics of Plasmas*, **19** (12), 122307 (2012).
[151] T. Lunt, G. Fussmann and O. Waldmann. Experimental Investigation of the Plasma-Wall Transition. *Physical Review Letters*, **100** (17), 175004 (2008).

[152] J. Loizu, P. Ricci and C. Theiler. Existence of subsonic plasma sheaths. *Physical Review E*, **83** (1), 016406 (2011).

[153] J. Loizu, J. Dominski, P. Ricci *et al.* Potential of a plasma bound between two biased walls. *Physics of Plasmas*, **19** (8), 083507 (2012).

[154] D. Tskhakaya. One-dimensional plasma sheath model in front of the divertor plates. *Plasma Physics and Controlled Fusion*, **59** (11), 114001 (2017).

[155] D. S. Oliveira, T. Body, D. Galassi *et al.* Validation of edge turbulence codes against the TCV-X21 diverted L-mode reference case. *Nuclear Fusion* (2021). Submitted.

[156] M. Ottaviani. An alternative approach to field-aligned coordinates for plasma turbulence simulations. *Physics Letters A*, **375** (15), 1677 (2011).

[157] G. W. Hammett, M. A. Beer, W. Dorland *et al.* Developments in the gyrofluid approach to Tokamak turbulence simulations. *Plasma Physics and Controlled Fusion*, **35** (8), 973 (1993).

[158] A. M. Dimits. Fluid simulations of tokamak turbulence in quasiballooning coordinates. *Physical Review E*, **48** (5), 4070 (1993).

[159] B. Scott. Shifted metric procedure for flux tube treatments of toroidal geometry: Avoiding grid deformation. *Physics of Plasmas*, **8** (2), 447 (2001).

[160] F. Hariri and M. Ottaviani. A flux-coordinate independent field-aligned approach to plasma turbulence simulations. *Computer Physics Communications*, **184** (11), 2419 (2013).

[161] A. Stegmeir, D. Coster, O. Maj *et al.* The field line map approach for simulations of magnetically confined plasmas. *Computer Physics Communications*, **198**, 139 (2016).

[162] A. Stegmeir, O. Maj, D. Coster *et al.* Advances in the flux-coordinate independent approach. *Computer Physics Communications*, **213**, 111 (2017).

[163] M. Held, M. Wiesenberger and A. Stegmeir. Three discontinuous Galerkin schemes for the anisotropic heat conduction equation on non-aligned grids. *Computer Physics Communications*, **199**, 29 (2016).

[164] M. Held, M. Wiesenberger, J. Madsen *et al.* The influence of temperature dynamics and dynamic finite ion Larmor radius effects on seeded high amplitude plasma blobs. *Nuclear Fusion*, **56** (12), 126005 (2016).

[165] B. Shanahan, B. Dudson and P. Hill. Fluid simulations of plasma filaments in stellarator geometries with BSTING. *Plasma Physics and Controlled Fusion*, **61** (2), 025007 (2018).

[166] G. Latu, M. Mehrenberger, Y. Güçlü *et al.* Field-Aligned Interpolation for Semi-Lagrangian Gyrokinetic Simulations. *Journal of Scientific Computing*, **74** (3), 1601 (2017).

[167] W. Dekeyser, X. Bonnin, S. Lisgo *et al.* SOLPS-ITER Study of neutral leakage and drift effects on the alcator C-Mod divertor plasma. *Nuclear Materials and Energy*, **12**, 899 (2017).

[168] K. Schneider. Immersed boundary methods for numerical simulation of confined fluid and plasma turbulence in complex geometries: a review. *Journal of Plasma Physics*, **81** (6) (2015).

[169] G. E. Karniadakis, M. Israeli and S. A. Orszag. High-Order Splitting Methods for the Incompressible Navier-Stokes Equations. *Journal of Computational Physics*, **97**, 414 (1991).

[170] V. Naulin. Electromagnetic transport components and sheared flows in drift-Alfvén turbulence. *Physics of Plasmas*, **10** (10), 4016 (2003).

[171] B. D. Scott. Tokamak edge turbulence: background theory and computation. *Plasma Physics and Controlled Fusion*, **49** (7), S25 (2007).

[172] A. Arakawa. Computational Design for Long-Term Numerical Integration of the Equations of Fluid Motion: Two-Dimensional Incompressible Flow. Part I. *Journal of Computational Physics*, **135** (2), 103 (1997).

[173] W. Hackbusch. *Multi-Grid Methods and Applications*. Springer Berlin Heidelberg (1985).

[174] K. Salari and P. Knupp. *Code verification by the method of manufactured solutions*. Sandia National Laboratories (2000). Sandia Report SAND2000-1444.

[175] W. R. Inc. Mathematica, Version 12.1. Champaign, IL, 2021.

[176] J. Shin, M. Hall and J. Chame. Superword-Level Parallelism in the Presence of Control Flow. In *International Symposium on Code Generation and Optimization*. IEEE (2005).

[177] Message Passing Interface Forum. MPI: A Message-Passing Interface Standard. Technical report, University of Tennessee, Knoxville, TN, USA (1994).

[178] OpenMP Architecture Review Board. OpenMP Application Program Interface Version 5.0 (2018).
[179] A. Meister. *Numerik linearer Gleichungssysteme*. Springer Fachmedien Wiesbaden (2015).
[180] R. da Cunha and T. Hopkins. The Parallel Iterative Methods (PIM) package for the solution of systems of linear equations on parallel computers. *Applied Numerical Mathematics*, **19** (1-2), 33 (1995).
[181] R. da Cunha and T. Hopkins. A parallel implementation of the restarted GMRES iterative algorithm for nonsymmetric systems of linear equations. *Advances in Computational Mathematics*, **2** (3), 261 (1994).
[182] OpenACC-Standard.org. The OpenACC Application Programming Interface version 3.1 (2020).
[183] N. Mandell, A. Hakim, G. Hammett *et al.* Electromagnetic full-f gyrokinetics in the tokamak edge with discontinuous Galerkin methods. *arXiv:1908.05653* (2019).
[184] W. D'haeseleer, W. Hitchon, J. Callen *et al.* *Flux coordinates and magnetic field structure: a guide to a fundamental tool of plasma theory*. Springer Series in Computational Physics. Springer (1991).
[185] G. Conway, B. Scott, J. Schirmer *et al.* Direct measurement of zonal flows and geodesic acoustic mode oscillations in ASDEX Upgrade using Doppler reflectometry. *Plasma Physics and Controlled Fusion*, **47** (8), 1165 (2005).
[186] M. Cavedon, T. Pütterich, E. Viezzer *et al.* Interplay between turbulence, neoclassical and zonal flows during the transition from low to high confinement mode at ASDEX Upgrade. *Nuclear Fusion*, **57** (1), 014002 (2016).
[187] K. Itoh and S.-I. Itoh. The role of the electric field in confinement. *Plasma Physics and Controlled Fusion*, **38** (1), 1 (1996).
[188] J. F. Drake and *et al.* *Tokamak edge transport, L-H transition and generation of velocity shear layers*, volume 2. Plasma physics and controlled nuclear fusion research 1992 (Würzburg: IAEA), Vienna (1993). ISBN 9201011938.
[189] A. B. Hassam, T. M. Antonsen, J. F. Drake *et al.* Spontaneous poloidal spin-up of tokamaks and the transition to the H mode. *Phys. Rev. Lett.*, **66**, 309 (1991).
[190] G. D. Conway, E. Poli, T. Happel *et al.* Interaction of Mean and Oscillating Plasma Flows Across Confinement Mode Transitions. *Plasma and Fusion Research*, **5**, S2005 (2010).
[191] H. Biglari, P. H. Diamond and P. W. Terry. Influence of sheared poloidal rotation on edge turbulence. *Physics of Fluids B: Plasma Physics*, **2** (1), 1 (1990).
[192] T. S. Hahm and K. H. Burrell. Flow shear induced fluctuation suppression in finite aspect ratio shaped tokamak plasma. *Physics of Plasmas*, **2** (5), 1648 (1995).
[193] I. K. Charidakos, J. R. Myra, S. Parker *et al.* Analysis of equilibrium and turbulent fluxes across the separatrix in a gyrokinetic simulation. *Physics of Plasmas*, **25** (7), 072306 (2018).
[194] B. Zhu, M. Francisquez and B. N. Rogers. Up–down symmetry breaking in global tokamak edge simulations. *Nuclear Fusion*, **58** (10), 106039 (2018).
[195] H. Bufferand, C. Baudoin, J. Bucalossi *et al.* Implementation of drift velocities and currents in SOLEDGE2D–EIRENE. *Nuclear Materials and Energy*, **12**, 852 (2017).
[196] T. T. Ribeiro and B. Scott. Tokamak turbulence computations on closed and open magnetic flux surfaces. *Plasma Physics and Controlled Fusion*, **47** (10), 1657 (2005).
[197] P. Manz, A. Stegmeir, B. Schmid *et al.* Magnetic configuration effects on the Reynolds stress in the plasma edge. *Physics of Plasmas*, **25** (7), 072508 (2018).
[198] D. Galassi, G. Ciraolo, P. Tamain *et al.* Tokamak Edge Plasma Turbulence Interaction with Magnetic X-Point in 3D Global Simulations. *Fluids*, **4** (1), 50 (2019).
[199] V. Rozhansky, S. Voskoboynikov, E. Kaveeva *et al.* Simulation of tokamak edge plasma including self-consistent electric fields. *Nuclear Fusion*, **41** (4), 387 (2001).
[200] P. Manz, M. Ramisch and U. Stroth. Experimental estimation of the dual cascade in two-dimensional drift-wave turbulence. *Plasma Physics and Controlled Fusion*, **51** (3), 035008 (2009).
[201] M. Held, M. Wiesenberger, R. Kube *et al.* Non-Oberbeck–Boussinesq zonal flow generation. *Nuclear Fusion*, **58** (10), 104001 (2018).
[202] Ö. D. Gürcan, P. H. Diamond, T. S. Hahm *et al.* Intrinsic rotation and electric field shear. *Physics of Plasmas*, **14** (4), 042306 (2007).

[203] M. Wensing, J. Loizu, H. Reimerdes *et al.* X-point potential well formation in diverted tokamaks with unfavorable magnetic field direction. *Nuclear Fusion*, **60** (5), 054005 (2020).
[204] D. Tskhakaya, F. Subba, X. Bonnin *et al.* On Kinetic Effects during Parallel Transport in the SOL. *Contributions to Plasma Physics*, **48** (1-3), 89 (2008).
[205] T. Y. Xia and X. Q. Xu. Nonlinear fluid simulation of particle and heat fluxes during burst of ELMs on DIII-D with BOUT++ code. *Nuclear Fusion*, **55** (11), 113030 (2015).
[206] H. Meyer, T. Eich, M. Beurskens *et al.* Overview of progress in European medium sized tokamaks towards an integrated plasma-edge/wall solution. *Nuclear Fusion*, **57** (10), 102014 (2017).
[207] T. Eich, R. Goldston, A. Kallenbach *et al.* Correlation of the tokamak H-mode density limit with ballooning stability at the separatrix. *Nuclear Fusion*, **58** (3), 034001 (2018).
[208] B. D. Scott. Energetics of the interaction between electromagnetic ExB turbulence and zonal flows. *New Journal of Physics*, **7**, 92 (2005).
[209] U. Plank, T. Pütterich, C. Angioni *et al.* H-mode power threshold studies in mixed ion species plasmas at ASDEX Upgrade. *Nuclear Fusion*, **60** (7), 074001 (2020).
[210] P. Sauter, T. Pütterich, F. Ryter *et al.* L- to H-mode transitions at low density in ASDEX Upgrade. *Nuclear Fusion*, **52** (1), 012001 (2011).
[211] B. D. Scott. Computation of electromagnetic turbulence and anomalous transport mechanisms in tokamak plasmas. *Plasma Physics and Controlled Fusion*, **45** (12A), A385 (2003).
[212] D. L. Jassby. Transverse Velocity Shear Instabilities within a Magnetically Confined Plasma. *Physics of Fluids*, **15** (9), 1590 (1972).
[213] M. Kotschenreuther, X. Liu, D. Hatch *et al.* Gyrokinetic analysis and simulation of pedestals to identify the culprits for energy losses using 'fingerprints'. *Nuclear Fusion*, **59** (9), 096001 (2019).
[214] K. Hallatschek and A. Zeiler. Nonlocal simulation of the transition from ballooning to ion temperature gradient mode turbulence in the tokamak edge. *Physics of Plasmas*, **7** (6), 2554 (2000).
[215] G. Dif-Pradalier, G. Hornung, P. Ghendrih *et al.* Finding the Elusive E×B Staircase in Magnetized Plasmas. *Physical Review Letters*, **114** (8), 085004 (2015).
[216] P. Manz, M. Ramisch and U. Stroth. Physical Mechanism behind Zonal-Flow Generation in Drift-Wave Turbulence. *Phys. Rev. Lett.*, **103**, 165004 (2009).
[217] B. Schmid, P. Manz, M. Ramisch *et al.* Collisional Scaling of the Energy Transfer in Drift-Wave Zonal Flow Turbulence. *Phys. Rev. Lett.*, **118**, 055001 (2017).
[218] P. Manz, G. Birkenmeier, G. Fuchert *et al.* Poloidal asymmetric flow and current relaxation of ballooned transport during I-phase in ASDEX Upgrade. *Physics of Plasmas*, **23** (5), 052302 (2016).
[219] T. Stoltzfus-Dueck. Intrinsic rotation in axisymmetric devices. *Plasma Physics and Controlled Fusion*, **61** (12), 124003 (2019).
[220] J. Loizu, P. Ricci, F. D. Halpern *et al.* Intrinsic toroidal rotation in the scrape-off layer of tokamaks. *Physics of Plasmas*, **21** (6), 062309 (2014).
[221] M. Wiesenberger and M. Held. Angular momentum and rotational energy of mean flows in toroidal magnetic fields. *arXiv:2003.02707* (2020).
[222] M. Xu, G. R. Tynan, P. H. Diamond *et al.* Generation of a Sheared Plasma Rotation by Emission, Propagation, and Absorption of Drift Wave Packets. *Phys. Rev. Lett.*, **107**, 055003 (2011).
[223] I. Shesterikov, Y. Xu, C. Hidalgo *et al.* Direct evidence of eddy breaking and tilting by edge sheared flows observed in the TEXTOR tokamak. *Nuclear Fusion*, **52** (4), 042004 (2012).
[224] A. G. Peeters. Stringer spin up due to anomalous transport. *Physics of Plasmas*, **5** (6), 2399 (1998).
[225] A. Thyagaraja, F. Haas and I. Cook. Temperature fluctuations and heat transfer in tokamaks. *Nuclear Fusion*, **20** (5), 611 (1980).
[226] G. D. Dominici, G. Fuhr, P. Beyer *et al.* Flux driven pedestal formation in tokamaks: turbulence simulations validated against the isotope effect. *arXiv:1912.09792* (2019).
[227] C. S. Chang, S. Kue and H. Weitzner. X-transport: A baseline nonambipolar transport in a diverted tokamak plasma edge. *Physics of Plasmas*, **9** (9), 3884 (2002).
[228] R. W. Brzozowski, F. Jenko, R. Bilato *et al.* A geometric model of ion orbit loss under the influence of a radial electric field. *Physics of Plasmas*, **26** (4), 042511 (2019).

[229] F. Reimold, M. Wischmeier, M. Bernert *et al.* Divertor studies in nitrogen induced completely detached H-modes in full tungsten ASDEX Upgrade. *Nuclear Fusion*, **55** (3), 033004 (2015).

[230] A. Kallenbach, M. Bernert, M. Beurskens *et al.* Partial detachment of high power discharges in ASDEX Upgrade. *Nuclear Fusion*, **55** (5), 053026 (2015).

[231] L. Wang, H. Q. Wang, S. Ding *et al.* Integration of full divertor detachment with improved core confinement for tokamak fusion plasmas. *Nature Communications*, **12** (1) (2021).

[232] D. Stotler and C. Karney. Neutral Gas Transport Modeling with DEGAS 2. *Contributions to Plasma Physics*, **34** (2-3), 392 (1994).

[233] J. Romazanov, D. Borodin, A. Kirschner *et al.* First ERO2.0 modeling of Be erosion and non-local transport in JET ITER-like wall. *Physica Scripta*, **T170**, 014018 (2017).

[234] W. Fundamenski. Parallel heat flux limits in the tokamak scrape-off layer. *Plasma Physics and Controlled Fusion*, **47** (11), R163 (2005).

[235] D. Carralero, G. Birkenmeier, H. Müller *et al.* An experimental investigation of the high density transition of the scrape-off layer transport in ASDEX Upgrade. *Nuclear Fusion*, **54** (12), 123005 (2014).

[236] A. Wynn, B. Lipschultz, I. Cziegler *et al.* Investigation into the formation of the scrape-off layer density shoulder in JET ITER-like wall L-mode and H-mode plasmas. *Nuclear Fusion*, **58** (5), 056001 (2018).

[237] U. Fantz, D. Reiter, B. Heger *et al.* Hydrogen molecules in the divertor of ASDEX Upgrade. *Journal of Nuclear Materials*, **290-293**, 367 (2001).

[238] A. Kukushkin, S. Krasheninnikov, A. Pshenov *et al.* Role of molecular effects in divertor plasma recombination. *Nuclear Materials and Energy*, **12**, 984 (2017).

[239] E. Vold, A. Prinja, F. Najmabadi *et al.* The neutral diffusion approximation in a consistent tokamak edge plasma-neutral computation. *Journal of Nuclear Materials*, **176-177**, 570 (1990).

[240] A. S. Thrysøe, M. Løiten, J. Madsen *et al.* Plasma particle sources due to interactions with neutrals in a turbulent scrape-off layer of a toroidally confined plasma. *Physics of Plasmas*, **25** (3), 032307 (2018).

[241] D. P. Coster, X. Bonnin, B. Braams *et al.* Simulation of the Edge Plasma in Tokamaks. *Physica Scripta*, page 7 (2004).

[242] Y. Zhang and S. I. Krasheninnikov. Effect of neutrals on the anomalous edge plasma transport. *Plasma Physics and Controlled Fusion*, **62** (11), 115018 (2020).

[243] D. M. Fisher, B. N. Rogers, G. D. Rossi *et al.* Three-dimensional two-fluid Braginskii simulations of the large plasma device. *Physics of Plasmas*, **22** (9), 092121 (2015).

[244] Y. Zhang, S. I. Krasheninnikov, R. Masline *et al.* Neutral impact on anomalous edge plasma transport and its correlation with divertor plasma detachment. *Nuclear Fusion*, **60** (10), 106023 (2020).

[245] A. Zito, M. Wischmeier, D. Carralero *et al.* Numerical modelling of an enhanced perpendicular transport regime in the scrape-off layer of ASDEX Upgrade. *Plasma Physics and Controlled Fusion* (2021).

[246] T. D. Rognlien, M. V. Umansky, X. Q. Xu *et al.* Self-consistent simulation of turbulence and transport in tokamak edge plasmas. *Contributions to Plasma Physics*, **44** (13), 188 (2004).

[247] T. Eich, P. Manz and the ASDEX Upgrade team. The separatrix operational space of ASDEX Upgrade due to interchange-drift-Alfvén turbulence. *Nuclear Fusion*, **61** (8), 086017 (2021).

[248] R. Fischer, C. J. Fuchs, B. Kurzan *et al.* Integrated Data Analysis of Profile Diagnostics at ASDEX Upgrade. *Fusion Science and Technology*, **58** (2), 675 (2010).

[249] D. Brida, D. Silvagni, T. Eich *et al.* Role of electric currents for the SOL and divertor target heat fluxes in ASDEX Upgrade. *Plasma Physics and Controlled Fusion*, **62** (10), 105014 (2020).

[250] A. Pshenov, A. Kukushkin and S. Krasheninnikov. Energy balance in plasma detachment. *Nuclear Materials and Energy*, **12**, 948 (2017).

[251] M. Valentinuzzi. *Modélisation numérique des flux de puissances sur les composants face au plasma de Tokamak à l'aide de techniques de couplage avancées entre codes fluides et cinétiques*. Ph.D. thesis, Aix-Marseille Université (2018). Thèse de doctorat dirigée par Marandet, Yannick et Ciraolo, Guido Energie, rayonnement, plasma Aix-Marseille 2018.

[252] N. Horsten, G. Samaey and M. Baelmans. A hybrid fluid-kinetic model for hydrogenic atoms in the plasma edge of tokamaks based on a micro-macro decomposition of the kinetic equation. *Journal of Computational Physics*, **409**, 109308 (2020).

[253] W. Zholobenko, M. Rack, D. Reiter *et al.* Synthetic helium beam diagnostic and underlying atomic data. *Nuclear Fusion*, **58** (12), 126006 (2018).

[254] H. Meyer, C. Angioni, C. Albert *et al.* Overview of physics studies on ASDEX Upgrade. *Nuclear Fusion*, **59** (11), 112014 (2019).

[255] G. D. Conway, A. I. Smolyakov and T. Ido. Geodesic Acoustic Modes in magnetic confinement devices. *Nuclear Fusion* (2021).

[256] P. W. Terry. Suppression of turbulence and transport by sheared flow. *Reviews of Modern Physics*, **72** (1), 109 (2000).

[257] P. Manz, G. S. Xu, B. N. Wan *et al.* Zonal flow triggers the L-H transition in the Experimental Advanced Superconducting Tokamak. *Physics of Plasmas*, **19** (7), 072311 (2012).

[258] E. Viezzer, T. Pütterich, R. M. McDermott *et al.* Parameter dependence of the radial electric field in the edge pedestal of hydrogen, deuterium and helium plasmas. *Plasma Physics and Controlled Fusion*, **56** (7), 075018 (2014).

[259] J. Hillesheim, E. Delabie, H. Meyer *et al.* Stationary Zonal Flows during the Formation of the Edge Transport Barrier in the JET Tokamak. *Physical Review Letters*, **116** (6), 065002 (2016).

[260] B. Schweer, G. Mank, A. Pospieszczyk *et al.* Electron temperature and electron density profiles measured with a thermal He-beam in the plasma boundary of TEXTOR. *Journal of Nuclear Materials*, **196-198**, 174 (1992).

[261] M. Griener, E. Wolfrum, G. Birkenmeier *et al.* Continuous observation of filaments from the confined region to the far scrape-off layer. *Nuclear Materials and Energy*, **25**, 100854 (2020).

[262] D. Silvagni, T. Eich, T. Happel *et al.* I-mode pedestal relaxation events at ASDEX Upgrade. *Nuclear Fusion*, **60** (12), 126028 (2020).

[263] R. Pánek, J. Adámek, M. Aftanas *et al.* Status of the COMPASS tokamak and characterization of the first H-mode. *Plasma Physics and Controlled Fusion*, **58** (1), 014015 (2015).

[264] W. Gekelman, P. Pribyl, Z. Lucky *et al.* The upgraded Large Plasma Device, a machine for studying frontier basic plasma physics. *Review of Scientific Instruments*, **87** (2), 025105 (2016).

[265] A. Kendl, B. D. Scott and T. T. Ribeiro. Nonlinear gyrofluid computation of edge localized ideal ballooning modes. *Physics of Plasmas*, **17** (7), 072302 (2010).

[266] A. Cathey, M. Hoelzl, K. Lackner *et al.* Non-linear extended MHD simulations of type-I edge localised mode cycles in ASDEX Upgrade and their underlying triggering mechanism. *Nuclear Fusion*, **60** (12), 124007 (2020).

[267] T. Eich, P. Manz, R. Goldston *et al.* Turbulence driven widening of the near-SOL power width in ASDEX Upgrade H-Mode discharges. *Nuclear Fusion*, **60** (5), 056016 (2020).

[268] D. Farina, R. Pozzoli and D. Ryutov. Effect of the magnetic field geometry on the flute-like perturbations near the divertor X point. *Nuclear Fusion*, **33** (9), 1315 (1993).

[269] K. H. Burrell. Effects of E×B velocity shear and magnetic shear on turbulence and transport in magnetic confinement devices. *Physics of Plasmas*, **4** (5), 1499 (1997).

[270] P. Manz. The microscopic picture of plasma edge turbulence. Habilitation treatise (2018).

[271] M. Francisquez, B. Zhu and B. Rogers. Global 3D Braginskii simulations of the tokamak edge region of IWL discharges. *Nuclear Fusion*, **57** (11), 116049 (2017).

[272] D. R. Zhang, Y. P. Chen, X. Q. Xu *et al.* Self-consistent simulation of transport and turbulence in tokamak edge plasma by coupling SOLPS-ITER and BOUT++. *Physics of Plasmas*, **26** (1), 012508 (2019).

[273] C. Mouhot and C. Villani. On Landau damping. *Acta Mathematica*, **207** (1), 29 (2011).

[274] G. W. Hammett, W. Dorland and F. W. Perkins. Fluid models of phase mixing, Landau damping, and nonlinear gyrokinetic dynamics. *Physics of Fluids B: Plasma Physics*, **4** (7), 2052 (1992).

[275] Z. Chang and J. D. Callen. Unified fluid/kinetic description of plasma microinstabilities. Part I: Basic equations in a sheared slab geometry. *Physics of Fluids B: Plasma Physics*, **4** (5), 1167 (1992).

[276] A. M. Dimits, I. Joseph and M. V. Umansky. A fast non-Fourier method for Landau-fluid operators. *Physics of Plasmas*, **21** (5), 055907 (2014).
[277] A. G. Peeters. The bootstrap current and its consequences. *Plasma Physics and Controlled Fusion*, **42** (12B), B231 (2000).
[278] S. C. Cowley, R. M. Kulsrud and R. Sudan. Considerations of ion-temperature-gradient-driven turbulence. *Physics of Fluids B: Plasma Physics*, **3** (10), 2767 (1991).
[279] K. V. Roberts and J. B. Taylor. Magnetohydrodynamic Equations for Finite Larmor Radius. *Physical Review Letters*, **8** (5), 197 (1962).
[280] N. Tronko and C. Chandre. Second order nonlinear gyrokinetic theory : From the particle to the gyrocenter. *arXiv:1709.05222* (2017).
[281] E. L. Shi, G. W. Hammett, T. Stoltzfus-Dueck *et al.* Gyrokinetic continuum simulation of turbulence in a straight open-field-line plasma. *Journal of Plasma Physics*, **83** (3) (2017).
[282] K. Germaschewski, B. Allen, T. Dannert *et al.* Toward exascale whole-device modeling of fusion devices: Porting the GENE gyrokinetic microturbulence code to GPU. *Physics of Plasmas*, **28** (6), 062501 (2021).
[283] S. Maeyama, Y. Idomura, T.-H. Watanabe *et al.* Cross-Scale Interactions between Electron and Ion Scale Turbulence in a Tokamak Plasma. *Physical Review Letters*, **114** (25), 255002 (2015).
[284] N. Howard, C. Holland, A. White *et al.* Multi-scale gyrokinetic simulation of tokamak plasmas: enhanced heat loss due to cross-scale coupling of plasma turbulence. *Nuclear Fusion*, **56** (1), 014004 (2015).